MICROSCOPICALLY DETAILED JOINT DENSITY-FUNCTIONAL THEORY FOR THE ELECTRODE-ELECTROLYTE INTERFACE

A Dissertation

Presented to the Faculty of the Graduate School

of Cornell University

in Partial Fulfillment of the Requirements for the Degree of

Doctor of Philosophy

by

Kendra Leigh Letchworth-Weaver

February 2016

MICROSCOPICALLY DETAILED

JOINT DENSITY-FUNCTIONAL THEORY

FOR THE ELECTRODE-ELECTROLYTE INTERFACE

Kendra Leigh Letchworth-Weaver, Ph.D.

Cornell University 2016

Understanding the complex and inherently multi-scale interface between a charged electrode surface and a fluid electrolyte would inform design of more efficient and less costly electrochemical energy storage and conversion devices. Joint density-functional theory (JDFT) is an, in principle, exact theoretical framework which bridges the relevant length-scales by joining a fully *ab initio* description of the electrode with a highly efficient, yet atomically detailed classical DFT description of the liquid electrolyte structure. First, we introduce a universal approximate functional to couple any quantum- mechanical solute system with a classical DFT for any liquid and present classical density- functionals for both aqueous and non-aqueous fluids. This universal coupling functional predicts solvation energies of neutral molecules to within near-chemical accuracy of 1.5 kcal/mol and captures the qualitative and quantitative features of fluid correlation functions.

We go on to explore the suitability of JDFT to describe electrochemical systems, reviewing the physics of the underlying fundamental electrochemical concepts and identifying the mapping between commonly measured electrochemical observables and microscopically computable quantities. We then introduce a simple, computationally efficient approximate functional which we find to be quite successful in capturing *a priori* basic electrochemical phenomena, includ-

ing the capacitive Stern and diffusive Gouy-Chapman regions in the electrochemical double layer and potentials of zero charge for a series of metals. We also show that we are able to place our *ab initio* results directly on the scale associated with the Standard Hydrogen Electrode (SHE).

Leveraging the above theoretical innovations, we then predict the voltage-dependent structure and energetics of solvated ions at the interface between metal electrodes and an aqueous electrolyte, elucidating the origin of the nonlinear capacitance observed in electrochemical measurements. Finally, we discuss how JDFT calculations can determine the surface structure of a trained $SrTiO_3$ surface under operating conditions for water-splitting and explore why this structure is correlated with higher activity than an untrained surface. We predict the specular X-ray crystal truncation rods for $SrTiO_3$, finding excellent agreement with experimental measurements from the Cornell High Energy Synchrotron Source (CHESS).

BIOGRAPHICAL SKETCH

A native of Williamsburg, VA, Kendra Letchworth-Weaver attended Jamestown High School then graduated *Summa Cum Laude* from the College of William and Mary in 2007 with a Bachelors of Science in Physics and Mathematics. At William and Mary, she received the Goldwater Scholarship and the Thomas Jefferson Prize in Natural Philosophy, and was inducted into the Phi Beta Kappa honor society. She received her Ph.D from Cornell University, under the supervision of Dr. Tomás Arias and was supported by the National Science Foundation as both a Graduate Research Fellow and an Integrative Graduate Education and Research Trainee (IGERT). During her time as a graduate student, she collaborated closely with the experimentalists in the Energy Materials Center at Cornell (emc^2) to provide predictive theoretical calculations for a wide range of energy systems, including Li$^+$ batteries, SrTiO$_3$ electrodes under water-splitting conditions, and graphene-based supercapacitors. Beginning in Fall 2015, she has accepted the Aneesur Rahman Fellowship at Argonne National Laboratory, and will be working with the Center for Nanoscale Materials and the Chemical Sciences Division.

To my parents

who taught me to believe I could be anything I wanted to be

To my wonderful husband, Kirk

my partner, my support system, and my cheerleader

To my children, Adrian and Ellie

who bring me new challenges and abundant joy each day

ACKNOWLEDGEMENTS

TABLE OF CONTENTS

LIST OF TABLES

LIST OF FIGURES

CHAPTER 1

INTRODUCTION

1.1 Background

Throughout recorded history, humans have endeavored to understand the mechanisms underlying the workings of the universe. Some turned to mythology and the supernatural for explanations, while others attempted to use logic, reason, and the power of the human mind – an *ab initio* or first principles approach. As early as 600 BC, the Greek philosopher Thales proposed that water was the originating principle of nature and the source of all matter[270, 207]. According to historians, Thales noted the omnipresence of water in his daily life and drew the conclusion that "water united all things" [77]. This quest to determine the fundamental nature of matter continued with later Greek philosophers, such as Empedocles, who added air, fire, and earth to the list of indestructible elements [252, 36]. In around 400 BC, Democritus proposed atoms, meaning "uncuttable" in Greek, as the indivisible and impenetrable building blocks of nature [1]. During the scientific revolution of the 17th century, Sir Robert Boyle proposed that fundamental particles known as "corpuscles" existed in different sizes and shapes [31]. The idea that these particles could react with each other to form compounds, which produce different collective properties based upon composition, built the foundation for modern chemistry [270]. In the early 19th century, British scientist John Dalton reinstated the term atom to describe the tiny irreducible particles which constituted each chemical element [57]. Of course, modern science has shown that atoms may actually be reduced into electrons and nucleons, and the nucleons are even further divisi-

ble into quarks. However, the concept of fundamental particles which compose all matter has persisted to this day.

The concept that these fundamental particles interact with each other is equally ancient; Empedocles proposed love and strife as the forces between the four elements.[36]. In fact, it is electromagnetic attraction and repulsion which dominate the interactions between fundamental particles at the atomic scale. The first recorded description of electromagnetic force is also credited to Thales, who observed that lodestone attracts iron in 600 BC [123]. Another Greek philosopher, Theophrastus, first recorded in 300 BC that light objects were attracted to amber rubbed with wool [21]; indeed, the word electricity derives from the Greek word for amber. During the 18th century, Benjamin Franklin famously studied electricity, becoming the first to propose negative and positive charges to describe the reason for the electrostatic attraction from amber [83]. In 1770, Coulomb determined that electrostatic force is inversely proportional to the square of distance between the charged objects and directly proportional to charge, making quantitative predictions of electrostatics possible. Even more crucially to modern technology, Alessandro Volta discovered how to convert the chemical energy stored in the elements into electrical energy, which could be harnessed and stored for future use. In 1800, Volta constructed the first battery from alternating layers of zinc and silver electrodes separated by paper soaked in salt water [270].

Though Thales's proposition of water as the only fundamental constituent of matter was quickly dismissed, it is clear that water is crucial to human life, and indeed all life on Earth. Understanding the nature of water and other liquids would provide significant insight into many complex processes in the natural

world. French scientist Antoine-Laurent Lavoisier discovered in the 18th century that he could create water from oxygen and hydrogen gas, proving for the first time that water is a chemical compound rather than a fundamental unit [270]. Shortly thereafter, William Nicholson and Anthony Carlisle used Volta's newly discovered battery for the electrolysis of water, splitting the compound into oxygen and hydrogen gas using electric current [64]. This demonstration of water-splitting marks one of the first experiments in the field of electrochemistry, which studies chemical reactions at the interface between a solid electrode and a liquid electrolyte. Though the fundamental atomic components of a single water molecule were understood two centuries ago, prediction of the aggregate behavior of liquid water from the properties of its constituent molecules has proved more elusive. By the mid-19th century, collections of non-interacting point particles in the gaseous state were shown to obey the ideal gas law [49], but the strong interactions in liquids are not captured by this simple form. The van der Waals equation of state, which won the Nobel prize in 1910, improves upon the ideal gas law by including the effect of intermolecular attractions and a nonzero molecule size [288]. However, finding an accurate and predictive theory for liquids is still an active area of research today.

In 1687, Sir Isaac Newton founded classical mechanics as a unifying description of the interactions from the scale of invisible particles to the scale of cosmic bodies [270, 195]. His laws of motion revolutionized modern science and led to the development of calculus as the mathematical language of physics. Classical mechanics excels at predicting both the planetary orbits and the motion of the macroscale objects we use in our everyday lives. However, there were still some scientific mysteries that classical mechanics and electromagnetism alone could not explain. In the early 19th century Joseph von Fraunhofer found dark

lines at specific frequencies in the optical spectrum of sunlight [84]. Kirchoff and Bunsen later explained these "Fraunhofer lines" by discovering that each chemical element or compound absorbs and emits light at distinct frequencies, providing a unique spectral signature [146]. However, the rationale for these chemical fingerprints from fundamental physical principles remained elusive. It soon became clear that some assumptions of classical mechanics no longer apply at the atomic scale.

In 1896, J.J. Thomson provided a key piece of the puzzle when he discovered the electron, a new fundamental particle contained within the atom, and showed it to be around 2000 times less massive than the hydrogen atom.[278] Meanwhile, scientists were puzzled by the nature of light; was it a wave, as had been accepted by most scientists due to its ability to interfere with itself[314], or a particle, as suggested first by Newton and then again by Albert Einstein in 1905 to explain the photoelectric effect of metals [62] ? Finally, these experimental contradictions were reconciled at the beginning of the 20th century with the birth of quantum mechanics, which allowed light (and atomic-scale objects like electrons) to exhibit both particle and wave behaviors. Using Schrodinger's equation and the wavefunction formulation of quantum mechanics, [245] we can now solve atomic-scale problems to show that the unique spectral fingerprints of the chemical elements result from the quantum mechanical properties of their constituent electrons and nuclei. In principle, this quantum-mechanical theory should continue to be valid at the macroscopic scale, but the number of degrees of freedom required to construct the exact wavefunction make it practically impossible to use directly in applications. For systems of more than a few atoms, the calculations required for a fully quantum-mechanical treatment are prohibitive for humans to undertake alone.

As understanding of quantum mechanics grew, approximations such as valence bond theory [108] and linear combination of atomic orbitals [208] began to make practical calculations feasible. These approximations generally rely on the concept of single-electron orbital wavefunctions, which define the probability of finding an electron in a specific region of space around an atomic nucleus. In 1928, Bloch took the idea of quantum-mechanical orbitals and extended it to periodic arrays of atoms to study the properties of electrons in solid, crystalline materials.[26] During World War II, John Woodyard introduced the idea of modulating the electronic properties of semiconducting materials by doping them with electron donating and accepting atoms.[306] This discovery enabled computer chips to be developed from junctions of doped semiconductors[259] and spurred a technological revolution; computers shrank from the macroscale to the nanoscale in only 50 years. The first electronic computer, called ENIAC (Electronic Numerical Integrator and Computer), consisted of 18,000 vacuum tubes, weighed 30 tons, and occupied 1500 square feet. Today we can hold devices with orders of magnitude greater computing power in the palms of our hands. [270] The ubiquitous presence of computers has reshaped both modern society and modern science; the computers first developed by physics have now become essential tools for advancing the field of physics.

Just as the computer and internet revolution reshaped society in the latter half of the 20th century, a new technological revolution in renewable energy has the potential to change our lives in the first half of the 21st century. The need for energy security in a complex global economy as well as the contribution of fossil fuels to human-made climate change have made the quest for more efficient and cost-effective renewable energy sources one of the grand challenges of our modern age. Renewable energy devices such as batteries and supercapac-

itors store energy, while photoelectrochemical and fuel cells convert chemical energy and/or light into electrical energy, but they are still too inefficient and expensive to compete with gasoline and coal. Just like Volta's first battery, these electrochemical devices often consist of metal or semiconducting electrodes and a liquid electrolyte, with the chemical processes key to energy storage and conversion occurring at the interface between the solid and the liquid. This crucial electrode-electrolyte interface is inherently multiscale, requiring a theory which integrates the relevant length and time scales using both the quantum and classical mechanics descriptions relevant to each subsystem, respectively. Thus a fundamental, first principles understanding of electrochemical devices will leverage all of the above concepts, as well as rely upon computers to solve the complex equations which result from the basic physics.

In the remainder of this Introduction, we will describe the advances in computational quantum and classical physics which enable the first principles description of both solid and liquid systems through Density-Functional Theory (DFT). We will then summarize a rigorous and relatively new theory called Joint Density-Functional Theory (JDFT) which joins these regions together. In Chapter 2, we present the full realization of JDFT, which will enable atomically-detailed, first principles studies of the liquid-solid interface. In Chapter 3, we describe how to link *ab initio* computable quantities with electrochemical observables, using an approximate version of JDFT without microscopic details in the liquid region. In Chapter 4, we demonstrate the power of an atomically-detailed JDFT for predicting these electrochemical observables. In Chapter 5 we present a combined JDFT and experimental study of the structure of a strontium titanate ($SrTiO_3$) electrode under water-splitting conditions. Finally, in Chapter 6 we conclude this dissertation by discussing future opportunities for this

research.

1.2 Electronic Density-Functional Theory

Electronic density-functional theory (DFT) has become an essential tool for determining chemical and physical properties of diverse quantum mechanical systems, allowing computation of quantities from adsorption energies and bond lengths of molecules on metal surfaces to band structures of insulating semiconductors. In this section we will review the background, fundamental development, and novel extensions of DFT for electrons.

1.2.1 Quantum-Mechanical Background

The wavefunction formulation of quantum-mechanics describes the state of any physical system of N electrons and L nuclei with masses m_e and M_I and charges e and $-Z_I e$ respectively through a many-body wavefunction

$$\Psi(\{\vec{r}_i\}, \{\vec{R}_I\}) = \Psi(\vec{r}_1, \vec{r}_2, ..., \vec{r}_N, \vec{R}_1, \vec{R}_2, ..., \vec{R}_L), \tag{1.1}$$

where the position vectors $\vec{r}_i$ and $\vec{R}_I$ represent the spatial degrees of freedom for the ith electron and the Ith nucleus respectively. The time-independent Schrodinger equation [245] posits that this wavefunction must be an eigenstate of the equation

$$\hat{H}\Psi = E\Psi, \tag{1.2}$$

where E is the corresponding energy eigenvalue and $\hat{H}$ is the many-body Hamiltonian [181]

$$\hat{H} = -\frac{\hbar^2}{2m_e}\sum_i \nabla_i^2 + \frac{1}{2}\sum_{i \neq j}\frac{e^2}{|\vec{r}_i - \vec{r}_j|} - \sum_{i,I}\frac{e^2}{|\vec{r}_i - \vec{R}_I|} - \frac{\hbar^2}{2M_I}\sum_I \nabla_I^2 + \frac{1}{2}\sum_{I \neq J}\frac{Z_I Z_J e^2}{|\vec{R}_I - \vec{R}_J|}. \quad (1.3)$$

We have assumed for simplicity of discussion (as is very often the case) that non-relativistic, purely electrostatic interactions provide an extremely good description of condensed matter systems. Therefore, this Hamiltonian contains only the quantum-mechanical kinetic energy operator for both nuclei and electrons, as well as the Coulomb interaction between all bodies. We note that in the remainder of this dissertation we will employ atomic units, setting $\hbar = k_C e^2 = m_e = 1$, to simplify the equations significantly. We have also neglected electron and nuclear spin degrees of freedom as they are largely irrelevant to the work presented here.

From a cursory examination of the sheer number of nuclear and electronic degrees of freedom present in the fully rigorous Schrodinger equation, it is clear that multiple approximations will be required for any practical calculation, even with modern computers. The first modification we can make is known as the Born-Oppenheimer approximation,[30] which relies upon the assumption that the masses of the nuclei are far greater than that of the electron ($M_I \gg m_e$). In this adiabatic limit, where any motion of the nuclei is slow on the scale of electronic motion, the nuclear positions R_I are fixed for a given electronic solution of the Schrodinger equation. The Born-Oppenheimer approximation thus renders the last two terms in equation 1.3 irrelevant for a fixed configuration of nuclei, and allows the effect of the nuclei upon the electrons to be contained in an external potential

$$\hat{V}_{\text{nuc}} = -\sum_{i,I}\frac{1}{|\vec{r}_i - \vec{R}_I|}. \quad (1.4)$$

Once the corresponding electronic wavefunction is determined, the average density of electrons at position $\vec{r}$ is then

$$n(\vec{r}) = N \int d^3r_2...d^3r_n \ |\Psi(\vec{r}, \vec{r}_2, ..., \vec{r}_N)|^2. \tag{1.5}$$

Many quantum chemistry electronic structure methods, such as coupled cluster (CC) and configuration interaction (CI), are based on the full quantum-mechanical wavefunction for electronic degrees of freedom [17, 249]. However, these methods are still too expensive to compute the properties of extended systems, or even molecules with more than around ten atoms. Thus, many theoretical methods [108, 208] utilize the independent electron approximation, which assumes that one spin-up and/or one spin-down electron can exist in each noninteracting single-particle orbital $\psi_i(\vec{r})$. The orbitals then each obey the single-particle Schrodinger equation (in atomic units)

$$\frac{1}{2}\nabla_i^2 \psi_i(\vec{r}) + V_{\text{eff}}(\vec{r})\psi_i(\vec{r}) = \epsilon_i \psi_i(\vec{r}), \tag{1.6}$$

where ϵ_i is the energy eigenvalue of an electron in the ith orbital and $V_{\text{eff}}(\vec{r})$ is a local effective potential which includes the effects of both nuclear-electron and electron-electron interactions. The ground state of the system is then constructed from the bands with the lowest energy eigenvalues, filling each band with f_i ($0 \leq f_i \leq 2$) electrons by obeying the principles of exclusion [155]. The probability of finding an electron in a given location now reduces to

$$n(\vec{r}) = \sum_i f_i |\psi_i(\vec{r})|^2. \tag{1.7}$$

Of course, the independent electron approximation drastically reduces the degrees of freedom required for calculation, but suffers from a lack of a general prescription for the form of the effective potential V_{eff}. The various theo-

retical methods use different approximations for V_{eff} depending on the physical context; for example, in a solid-state context one could employ the tight-binding method[256] to calculate the band structure of a material. The Hartree approximation[105] assumes that the electron-electron interaction may be described by the mean-field interaction of the electron density $n(r)$. This assumption leads to the effective potential

$$V_{\text{eff}}(\vec{r}) = V_{nuc}(\vec{r}) + \int d^3 r' \, \frac{n(r')}{|\vec{r} - \vec{r'}|}, \tag{1.8}$$

where

$$V_{nuc}(\vec{r}) = -\sum_I \frac{1}{|\vec{r} - \vec{R_I}|} \tag{1.9}$$

is the fixed local potential from the nuclei at positions $\{R_I\}$. While the Hartree approximation misses the important physical effects of electron exchange and correlation, the form of V_{eff} in Equation 1.8 provides a straightforward prescription for solving the Schrodinger equation self-consistently because it is a *functional* of only the electron density of the ground state $n(\vec{r})$. If an exact effective potential could be found in terms of $n(\vec{r})$, that potential $V_{\text{eff}}[n(\vec{r})]$ would enable an exact solution to the many-body Schrodinger equation for electrons, with the computational cost of only the independent-electron approximation. The rigorous framework surrounding and means of discovering this exact effective potential are the domain of electronic density-functional theory (DFT).

1.2.2   Foundation of Density-Functional Theory

In the early 1960's, a theoretical physicist named Walter Kohn noted that metallurgists had employed empirical models based upon only the electron density $n(\vec{r})$ to successfully describe the properties of alloys [316]. He became curious

to discover if a rigorous theoretical justification existed for the electron density to fully determine *any* property of a many-electron system [150, 223]. His curiosity lead him to develop density-functional theory, a new theoretical framework for studying the properties of materials,for which he was co-awarded the Nobel Prize in Chemistry in 1988. The rigorous basis of density-functional theory is provided by two foundational papers authored by Walter Kohn and his coworkers. [116, 151]

The powerful Hohenberg-Kohn Theorem, published in 1964, states that any property of a system of many interacting electrons can be viewed as a functional of the ground state electron density $n(\vec{r})$ (determined from the many-body wavefunction using Equation 1.5)[116, 181]. The proof is conducted by verifying the uniqueness of the nuclear potential $\hat{V}_{\mathrm{nuc}}$ in Equation 1.4 – namely two external potentials that differ by more than a constant cannot produce the same electron density $n(\vec{r})$. The electron density therefore uniquely determines the nuclear potential in the Hamiltonian, which in turn determines all known properties of the quantum-mechanical system. The proof establishes the existence of a universal functional $F_{HK}[n(\vec{r})]$ which maps each electron density $n(\vec{r})$ to an external potential $V_{\mathrm{nuc}}[n(\vec{r})]$ and energy value $E[n(\vec{r})]$. The ground state energy E_0 of any system with fixed nuclear potential $V_{\mathrm{nuc}}(\vec{r})$ from Equation 1.9 may then be determined by a variational principle

$$E_0 = min_{n(\vec{r})} \left\{ F_{HK}[n(\vec{r})] + \int V_{\mathrm{nuc}}(\vec{r})n(\vec{r})d^3r \right\}. \tag{1.10}$$

Almost 20 years later, Levy and Lieb presented the constrained search formulation of the universal functional, which placed the above variational principle underlying DFT on rigorous mathematical underpinnings [166, 169], resolving certain mathematical issues in the original proof involving degeneracies.

Despite the revolutionary importance of the Hohenberg-Kohn theorem, its proof gives very little guidance on how to construct the functional $F_{HK}[n(\vec{r})]$ and how practical calculations may be carried out. A year later, in 1965, Kohn and his postdoctoral associate Sham claimed that the ground state electron density of an *interacting* system with many-body wavefunction Ψ is equivalent to the ground state density of a carefully chosen *non-interacting* system with single-particle orbitals $\psi_i(\vec{r})$ [151]. This ansatz comes from rewriting the Euler's equations for the variational principle in Equation 1.10 as a set of coupled single-particle Schrodinger equations (Equation 1.6). In each of these coupled equations, known as the Kohn-Sham equations, the effective potential $V_{\text{eff}}[n(\vec{r})]$ is computed from the density of the non-interacting eigenstates $\psi_i(\vec{r})$ using Equation 1.7. The prescription for determining the effective potential is straightforward – start with the Hartree approximation and add another potential $V_{xc}[n(\vec{r})]$ to account for exchange, correlation, and any other many-body effects not already captured. This formulation leads to the effective potential

$$V_{\text{eff}}[n(\vec{r})] = V_{\text{nuc}}[n(\vec{r})] + \int d^3r' \; \frac{n(r')}{|\vec{r} - \vec{r'}|} + V_{xc}[n(\vec{r})], \tag{1.11}$$

which leads to the exact solution when the exchange-correlation potential is defined as

$$V_{xc}[n(\vec{r})] = \left\langle \Psi \left| -\frac{1}{2}\sum_i \nabla_i^2 + \frac{1}{2}\sum_{i \neq j} \frac{1}{|\vec{r_i} - \vec{r_j}|} \right| \Psi \right\rangle - T_{KS}[n(\vec{r})] - \int d^3r' \; \frac{n(r')}{|\vec{r} - \vec{r'}|}. \tag{1.12}$$

The exchange-correlation potential in Equation 1.12 is framed as the difference between the exact kinetic energy and the independent electron kinetic energy $T_{KS}[n(\vec{r})]$ added to the difference between the exact electron-interaction energy and the Hartree approximation. Practical calculations require approximations to V_{xc}, but the framework is exact in principle and is therefore improvable in a rigorous way. Most importantly, the approach of Kohn and Sham offers the

computational tractability of the independent electron approximation, yet possesses the potential accuracy of the many-body wavefunction methods.

1.2.3 Density-Functionals

The earliest example of a density-functional was created long before the Hohenberg-Kohn theorem established the rigorous basis for DFT. In 1927, Thomas and Fermi developed a functional form for the electron kinetic energy based upon the electron density alone,

$$T_{TF}[n(\vec{r})] = \int d^3r \; \left(\frac{3}{10} (3\pi^2)^{\frac{2}{3}} n(\vec{r})^{\frac{5}{3}} \right),\tag{1.13}$$

which they used in conjunction with the Hartree approximation to the electron-interaction to create an energy functional [181, 277, 80]. This functional employs the *local density approximation* (LDA), which provides the exact kinetic energy for the non-interacting electron gas of constant density $n(\vec{r})$. The local approximation assumes that the electron density has little spatial variation; it idealizes the energy contained in a point $\vec{r}$ with volume d^3r and density $n(\vec{r})$ to be locally equivalent to the energy contained in volume d^3r of the non-interacting system with constant density n. However, the Thomas-Fermi energy functional is inaccurate for capturing even the qualitative features of chemical bonds and atomic shell structure. In 1930, Dirac improved upon the Thomas-Fermi functional significantly by including the local approximation for exchange,

$$E_x[n(\vec{r})] = - \int d^3r \; \left(\frac{3}{4} \left(\frac{3}{\pi} \right)^{\frac{1}{3}} n(\vec{r})^{\frac{4}{3}} \right),\tag{1.14}$$

which can be determined analytically from the homogeneous electron gas. The resulting Thomas-Fermi-Dirac approximation to $F_{HK}[n(\vec{r})]$ forms the basis of many "density-only", or "orbital-free", functionals still in use today.

Now we turn to the approximations to the exchange-correlation potential V_{xc} (Equation 1.12) within Kohn-Sham density-functional theory. The piece of the energy functional associated with the exchange-correlation potential[151] may be written within the local density approximation as

$$E_{XC}[n(\vec{r})] = \int d^3r \ n(\vec{r})\epsilon_{XC}[n(\vec{r})] \tag{1.15}$$

where $V_{xc}(r) = \epsilon_{XC}[n(r)] + n(r)\frac{\delta\epsilon_{XC}}{\delta n}$. This energy consists of the Dirac approximation to the exchange energy from Equation 1.14, as well as an LDA for the correlation energy. The correlation energy is only known exactly in the high-density (strong-correlation) and low-density (weak-correlation) limits of the homogeneous electron gas, so no analytic exact functional exists, even within the local approximation. Before the advent of DFT, Wigner [303] determined a perturbative expansion for the correlation energy which interpolates smoothly between the high-density and low-density limits of the homogeneous electron gas. In later years, Quantum Monte-Carlo simulations[42] determined the properties of the electron gas at intermediate densities. These calculations have been used to construct the various parameterizations of the LDA correlation energy used in modern DFT calculations [214].

Many forms for the exchange-correlation energy exist beyond the local density approximation, which tends to over bind both molecules and materials and leads to bond lengths and lattice constants smaller than the experimental value. The most straightforward extensions of LDA are those in terms of the spatial gradient of the electron density $|\nabla n|$, known as generalized gradient approximations (GGA) [212]. Meta-GGA functionals [271] go one step further and include second-order corrections in terms of the Laplacian $\nabla^2 n$. Hybrid functionals [260, 216] typically include a gradient-based exchange-correlation density functional in a linear combination with the Hartree-Fock exchange energy

computed from the Kohn-Sham orbitals $\psi_i(\vec{r})$. The accuracy of these hybrid functionals comes at high computational cost due to the double integral over two spatial coordinates. Other energy functionals have been formulated to better capture nonlocal dispersion effects; these van der Waals density-functionals are typically orbital-dependent and have computational cost similar to the hybrid functionals [279, 158]. This litany of exchange-correlation functionals developed over the past decades bring us ever closer to the "divine functional" [182] $F_{HK}[n(\vec{r})]$, which would be universally exact.

1.2.4 Extensions of Density-Functional Theory

Beyond Zero Temperature

Very shortly after the proof of the Hohenberg-Kohn Theorem, Mermin analogously proved thermal ensemble density-functional theory at finite temperature T by constructing the grand potential in terms of the electronic density matrix $\hat{\rho}$.[187] Within Levy's constrained search formulation, this temperature dependent functional may be written as

$$F_{HK}[n(\vec{r}), T] = \min_{\hat{\rho} \to n(\vec{r})} \text{Tr}\left(\hat{\rho}\hat{H} + k_B T \hat{\rho} \log(\hat{\rho})\right), \tag{1.16}$$

where k_B is Boltzmann's constant and $\hat{H}$ is the many-body Hamiltonian (Equation 1.3) within the Born-Oppenheimer approximation. Ensemble DFT has the obvious advantage of direct calculation of thermal equilibrium properties such as entropy, specific heat, and free energy. In addition, the smearing of the Fermi surface and shorter range of the density matrix at high temperatures could aid numerical convergence in some systems [181]. Ensemble DFT also resolves an

issue with the convexity of the Hohenberg-Kohn functional; at zero temperature, F_{HK} is not defined for all $n(\vec{r})$ because not all density fields may be obtained from some many-body wavefunction [169]. For $T > 0$, however, the functional F_{HK} is smooth and expansions of the functional around reference systems (such as the homogeneous electron gas) are not limited by singularities [223, 67].

However, the full Mermin functional does not easily lend itself to practical calculations, so most common functionals are written in terms of the single particle form for the entropy,

$$S(f_i) = - \sum_i \left[f_i \log f_i + (1 - f_i) \log (1 - f_i) \right]. \tag{1.17}$$

The grand potential for N_0 electrons is then written as

$$\Omega[n, T, \mu] = E[n, T] - \mu \left(\sum_i f_i - N_0 \right) - k_B T S(f_i). \tag{1.18}$$

This finite temperature functional allows electrons to be thermally excited to energy bands of eigenvalues ϵ_i which are unfilled in the $T = 0$ functional, with partial occupancies $f_i = \frac{1}{e^{\beta(\epsilon_i - \mu)} + 1}$ determined by the Fermi distribution at chemical potential μ [196], where $\beta = \frac{1}{k_B T}$. This functional may be minimized directly, with continuously varying occupation numbers[213], to yield exponential convergence of metallic systems.[86] This type of functional is also highly useful for performing electrochemistry calculations at fixed chemical potential μ (as in Chapter 3), where the number of electrons is treated as a continuous variable [274].

Beyond Born-Oppenheimer

Thus far, we have considered electronic DFT in which the positions of the nuclei are fixed. The nuclei can still move within the Born-Oppenheimer approxima-

tion provided the motion is adiabatic, meaning that all electrons relax to the ground state instantaneously relative to the timescale of nuclear motion. We may therefore consider a potential energy surface for the nuclei

$$U(\{\vec{R}_I\}) = E_0(\{\vec{R}_I\}) + \frac{1}{2} \sum_{I \neq J} \frac{Z_I Z_J}{|\vec{R}_I - \vec{R}_J|}, \tag{1.19}$$

which consists of the electronic ground state energy as a function of nuclear configuration $\{\vec{R}_I\}$ plus the Coulomb interaction between the nuclei (the last term of Equation 1.3). In the minimum energy (or ground state) nuclear configuration, each nucleus must therefore obey the condition

$$F_J = -\frac{dU(\{\vec{R}_I\})}{d\vec{R}_J} = 0, \tag{1.20}$$

meaning that the force F_J on the Jth nucleus must be zero. The ground state energy is formally given by $E_0(\{\vec{R}_I\}) = \langle \Psi_0 | \hat{H} | \Psi_0 \rangle$, where Ψ_0 is the ground state many-body wavefunction. In the exact ground state, $\frac{d}{dR_J} \langle \Psi_0 | \Psi_0 \rangle = 0$, so Equation 1.20 may be rewritten as

$$F_J = -\left\langle \Psi_0 \left| \frac{d\hat{H}}{dR_J} \right| \Psi_0 \right\rangle + \sum_I \frac{Z_I Z_J}{|\vec{R}_I - \vec{R}_J|^2} \tag{1.21}$$

by the Hellman-Feynman Theorem [110, 82]. Since the only term in $\hat{H}$ which depends on the nuclear positions explicitly is $\hat{V}_{nuc}$, these forces $\{F_J\}$ are straightforward to compute within the Hohenberg-Kohn theorem (Equation 1.10) as

$$F_J = -\int \frac{dV_{\mathrm{nuc}}(\vec{r})}{dR_J} n(\vec{r}) \, d^3r + \sum_I \frac{Z_I Z_J}{|\vec{R}_I - \vec{R}_J|^2}. \tag{1.22}$$

Using these Hellman-Feynman forces, many equilibrium and dynamical properties associated with the nuclei may be computed within electronic DFT: equilibrium geometries of molecules and crystals, phonons and vibrational modes, and even the motion of the nuclei over time. The latter behavior is the domain of *ab initio* molecular dynamics (AIMD) calculations, of which there

are two main flavors. The more empirical Car-Parinello molecular dynamics [38] uses a fictitious thermostat to reduce minimizing the Kohn-Sham functional to the problem of solving a set of classical equations of motion, while treating the electronic wavefunctions as a dynamical variable. The more rigorous and straightforward Born-Oppenheimer molecular dynamics [209] minimizes the Kohn-Sham functional directly and employs the Hellman-Feynman theorem to move the nuclei.

To perform calculations unrestricted by the Born-Oppenheimer approximation, Capitani, et. al. proved a multicomponent version of the Hohenberg-Kohn theorem, verifying the existence of a nonadiabatic unified density-functional in terms of both electronic and nuclear densities [37]. This unified density functional is given (in the Levy-Lieb constrained search formulation) by

$$E[n, \{N_\alpha\}] = \min_{\Psi \to n, \{N_\alpha\}} \left\langle \Psi(\{\vec{r}_i\}, \{\vec{R}_I\}) | \, \hat{H} \, | \Psi(\{\vec{r}_i\}, \{\vec{R}_I\}) \right\rangle, \qquad (1.23)$$

where $\hat{H}$ is the full many-body Hamiltonian in Equation 1.3, n is the electron density, N_α is the particle density of nuclei of type α, and $\Psi(\{\vec{r}_i\}, \{\vec{R}_I\})$ is the many-body wavefunction from Equation 1.3. The energy minimization is performed over the configuration space of all wavefunctions which yield the specified electron density n and nuclear densities $\{N_\alpha\}$. Each step of the Hohenberg-Kohn proof can also be reproduced for the unified functional in the presence of an external electric potential $\phi(\vec{r})$, yielding

$$E_\phi[n, \{N_\alpha\}] = E[n, \{N_\alpha\}] + \int d^3r \; n(\vec{r})\phi(\vec{r}) - \sum_\alpha Z_\alpha \int d^3r \; N_\alpha(\vec{r})\phi(\vec{r}) \qquad (1.24)$$

Unified DFT has been employed within the the grand-canonical ensemble to construct molecular DFT, which describes the simultaneous variation of the electron and proton distributions in a molecule to within the accuracy of Kohn-Sham DFT [293]. Molecular DFT allows electrons and nuclei numbers to fluctu-

ate, allowing one molecule to transform into another and facilitating the modeling of chemical reactions. Most crucially, unified DFT forms the basis for the rigorous Joint Density-Functional Theory framework, which is presented in detail in Section 1.4 and is utilized in all chapters of this dissertation.

1.2.5 Computational Details

In this dissertation, we will consistently employ particular theoretical, numerical, and software innovations to perform density-functional theory calculations. First, all calculations are performed using periodic boundary conditions, with a repeating real space unit cell defined by three-dimensional lattice vectors, and a corresponding Brillouin zone in reciprocal space. As such, all external potentials $V_{nuc}(\vec{r})$ in the Hohenberg-Kohn theorem respect the periodicity of the crystal unit cell, and Bloch's theorem[26] applies to the single-particle Kohn-Sham orbitals $\psi_i(\vec{r})$. Therefore, all scalar fields $f(\vec{r})$ are represented in reciprocal space using plane-wave basis functions of frequency $\vec{G}$, $e^{i\vec{G}\cdot\vec{r}}$, such that $f(\vec{r}) = \sum_{\vec{G}} f(\vec{G}) e^{i\vec{G}\cdot\vec{r}}$. Additionally, the computational cost of including all electrons within plane-wave DFT calculations is prohibitively high, namely due to the high grid resolution required to capture the core electron orbitals. Thus, we employ the pseudopotential approximation to DFT [230, 289], in which only the Kohn-Sham orbitals of valence electrons are considered. The local effect of the core electrons upon the valence electrons is folded into the potential $V_{nuc}(\vec{r})$, which then represents both the nuclei and inert core electrons. The remaining scattering properties of the ionic core are captured by additional nonlocal, angular-momentum-dependent terms in the energy functional [228]. Finally, we employ the software package JDFTx [267], based upon the original electronic

structure software DFT++ [122] but updated to leverage features in the new C++ standard and GPU parallelization through CUDA. This codebase is developed using an expressive software approach, which formulates DFT in terms of linear algebra operators while obscuring numerical and algorithmic details by leveraging templates, operator overloading, and other object-oriented features of C+. Thus, the code itself is easily readable and straightforwardly modified to introduce new physics and innovations in electronic structure calculations.

1.3   Classical Density-Functional Theory

The structure of liquids at the atomic scale critically influences the chemical reactions that drive modern technology and even the biological processes that are responsible for sustaining life. However, these systems are difficult to model because liquid phenomena result from the collective behavior of strongly interacting molecules, complicating any theoretical description. Classical density-functional theory (CDFT) has demonstrated great promise for elucidating this behavior in diverse systems such as lipids, [87] polymers, [309, 88] confined liquids, [191, 130] and electrochemical interfaces [310, 129].

Because of its ability to bridge atomic and macroscopic length scales [157, 309], CDFT is inherently a multiscale theory, but with a rigorous basis. Providing both three-dimensional microscopic detail of the liquid structure and efficient scaling to large system sizes [262, 247], CDFT is a powerful tool for modeling energy storage and conversion devices. In fact, CDFT calculations have been used to probe pore size effects [130, 129] and, thereby, hold promise to inform design of better mesoporous supercapacitor, carbon sequestration [68], and bat-

tery [168] materials. Most importantly to this work, a highly accurate and ro-
bust classical DFT for the solvent is an essential ingredient of Joint Density-
Functional Theory. Below, we will briefly discuss the concepts surrounding,
advances in, and predictions of classical DFTs which are especially relevant to
JDFT calculations.

1.3.1   Classical DFT Background

Classical density-functional theory may be derived from the fully quantum-
mechanical many-body Hamiltonian by means of the unified density-functional
theory for electrons and nuclei [37] and Mermin's finite temperature extension
of DFT [187]. Combining Equation 1.24 of Section 1.2 with Equation 1.16 yields
the unified, temperature dependent functional

$$F[n, \{N_\alpha\}, T] = \min_{\hat{\rho} \to [n, \{N_\alpha\}]} \mathrm{Tr}\left(\hat{\rho}\hat{H} + k_B T \hat{\rho} \log\left(\hat{\rho}\right)\right), \tag{1.25}$$

where $\hat{\rho}$ is the many-body density matrix for electrons and nuclei and $\hat{H}$ is the
Hamiltonian in Equation 1.3. Including an external electrostatic potential $\phi(\vec{r})$,
then minimizing over the electronic degrees of freedom leads to the classical
DFT functional

$$\Omega_\phi[\{N_\alpha\}] = \min_n \left\{F[n, \{N_\alpha\}, T] + \int d^3r \phi(\vec{r})\left(n(\vec{r}) - \sum_\alpha Z_\alpha N_\alpha(\vec{r})\right)\right\}. \tag{1.26}$$

This functional still depends upon the form of the external potential $\phi(\vec{r})$, but
weakly, since $\phi(\vec{r})$ couples to a neutral charge distribution when the fluid is
neutral. In order to construct a universal classical fluid functional $\Omega[\{N_\alpha\}] = \min_n \{F[n, \{N_\alpha\}, T]\}$, we must neglect the second term in Equation 1.26. This ap-
proximation assumes that all electrons are closely tied to the nuclei, no electron

transfer occurs, and that the fluid constituents are not highly polarizable. Unlike the universal Hohenberg-Kohn functional in electronic DFT, $\Omega[\{N_\alpha\}]$ still depends on the masses M_α and charges Z_α of each nucleus and must be redetermined for a fluid with different chemical constituents.

Classical DFT therefore requires an approximation for the free energy Ω of a particular inhomogeneous fluid directly in terms of its molecular or atomic site densities $\{N_\alpha\}$. Excellent approximations for model fluids, particularly the hard-sphere fluid, have been known for a long time [102, 16], but the development of accurate functionals for real liquids is still an area of active research.

Free-energy functional approaches for real liquids fall under two broad classes. The first class of approaches [50, 120, 315, 265] require constructing an effective short-ranged Hamiltonian for the liquid, and then theoretically approximating the free energy, typically using Wertheim's thermodynamic perturbation theory [299]. These functionals are easy to extend to other solvents and thermodynamic state points, and are remarkably accurate for the free energy of cavity formation, one of the two key contributions to solvation of electronic systems, even though they do not perfectly reproduce the pair correlations of the fluid. However, most of these functionals do not properly account for dielectric response, which is the other major contribution in solvation.

The second class of approaches [43, 44, 61, 171, 170, 319, 126, 127] is typically based on the weighted-density approximation (WDA) [55]. The weighted density-functional approach typically convolves the liquid density $N(\vec{r})$ with a weight function based on a pair potential model $w(\vec{r})$ to compute a smoothed, or coarse-grained density

$$\bar{N}(\vec{r}) = \int d^3r' \ w(|\vec{r} - \vec{r'}|)N(\vec{r}). \tag{1.27}$$

22

Classical DFT functionals based on such weighted densities rely on pair correlation functions of the fluid from molecular dynamics simulations or neutron and X-ray scattering measurements. Such methods therefore rely on experimental data available for few liquids at few state points, or the construction and testing of a pair potential model followed by extensive molecular dynamics calculations to provide the needed correlation functions. Consequently, they are not easily applicable to a new solvent or even to previously studied solvents under different conditions.

1.3.2   Construction of a Classical DFT

In this work, we will employ a classical DFT which combines the generalizability and excellent performance for cavity-formation free energies available from the perturbation-theory based approach with the simplicity and low computational cost of a weighted-density approximation [262, 266]. Furthermore, this classical functional is able to capture the nonlinear dielectric response quite accurately compared to perturbation-theory based approaches. Below, we briefly summarize the innovations required to construct a simplified, semi-empirical classical DFT functional to approximate $\Omega[\{N_\alpha\}]$.

Though many important physical effects arise from the structure and orientation of the fluid molecules, many density-functionals are constructed in terms of a single molecular density field, which places all atoms at the same site [102, 16]. Orientation-dependent density-functionals are not widely available because of the "inversion problem," which refers to the challenge of employing only atomic site densities to capture the entropy associated with the geometric

23

structure of the molecules. Recent work by Lischner et. al. [170] offers a solution to the inversion problem analogous to the Kohn-Sham formulation of electronic DFT. Lischner chooses effective atomic site potentials acting upon each atom in the noninteracting fluid (the ideal gas) as the independent variables instead of the site densities. The geometric entropy is then captured by a constraint which imposes the structure of the molecule upon the ideal gas free energy. Lischner then went on to design a "Kohn-Shamified" classical DFT for water[171] which used experimental correlation functions as input, however this preliminary water functional became numerically unstable when minimized in the presence of attractive external potentials. The preliminary work of Lischner and Petrosyan above has been generalized and extended by Sundararaman et. al. [262, 266], who chose the local electric field and local chemical potential as the independent variables in an orientation-dependent liquid functional based on the weighted-density approximation, allowing more complex interactions to be included and offering superior numerical stability.

This new class of functional leverages fundamental measure theory (FMT) [234, 272, 237], in particular the Carnahan-Starling form of FMT [39, 103], to describe the hard sphere packing of solvent molecules and prevent unphysical pileup of molecules in deep potential wells. Additional attractive interactions between molecular sites in each solvent are included through an equation-of-state-based WDA, parameterized to reproduce the properties of the bulk fluid across the phase diagram. The Jeffrey-Austin equation of state [128] forms the parameterization of the excess functional for water [262], while the Tao-Mason equation of state has been successful for non-aqueous fluids such as CCl_4 and $CHCl_3$ [266]. Sundararaman et. al. also developed a comprehensive treatment of the mean-field electrostatic interaction between atomic sites, including con-

tributions to the dielectric response from both rotations and molecular polarizability [266]. This classical DFT also employs molecular geometry and other microscopic parameters determined directly from *ab initio* calculations (through a procedure described in Section 2.4). Section 4.3.1 provides additional details about the polarizable classical DFT functional for liquid water.

1.3.3 Microscopic Properties and Energetics

In order to be appropriate for use within the JDFT framework, the classical density-functional theory for the solvent must be able to capture key microscopic properties of the liquid essential to accurate free energies. One such key property is the nonlinear dielectric response of the liquid to an applied electric field. The nonlinear dielectric response is particularly important for polar surfaces in liquids and for electrochemical cells under applied voltage. In these systems local electric fields can be quite large, and often the dielectric constant of the nearby liquid is much lower than the dielectric constant of the bulk liquid. Thus, surface energies under these conditions vary significantly from those predicted by linear solvation theories [163] and require a more advanced theory [100]. Classical DFT naturally captures nonlinear dielectric response through a competition between the ideal gas entropy and the long-range Coulomb interactions between charged sites on the solvent molecules [266].

Figure 1.1 displays the performance of the classical DFT [266] for the nonlinear dielectric response compared to molecular dynamics simulations for both nonpolar and polar solvents. Molecular dynamics simulations for water were performed using TIP4P [4] and SPCE [22] pair potentials, while molecular dy-
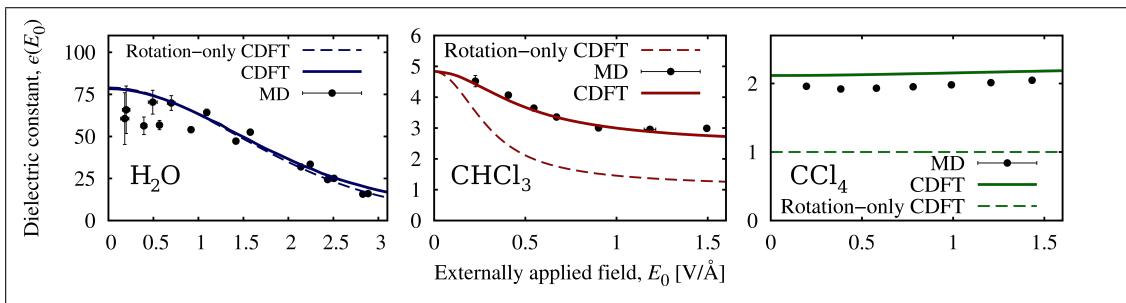
Figure 1.1: Nonlinear dielectric response to an applied electric field in polarizable (solid lines) and rotations-only CDFT (dashed lines) compared to molecular dynamics (black dots) for H_2O (blue, left), $CHCl_3$ (red, center), and CCl_4 (green, right).

namics simulations for $CHCl_3$ and CCl_4 were performed using recently developed polarizable pair potentials [156, 45]. All molecular dynamics simulations were performed within the software base LAMMPS [221] using appropriate rare event sampling techniques [85, 81]. For water, the highly polar solvent, a rotations-only classical DFT suffices to capture much of the nonlinear dielectric response, and the effect of polarizability is small. However, for the slightly polar solvent $CHCl_3$ and the nonpolar solvent CCl_4, a polarizable classical DFT is crucial to capturing the dielectric response. In fact, with a rotations-only theory, nonpolar solvents are predicted to have only the dielectric response of vacuum.

Accurate prediction of the free energy required to form a cavity or interface within the classical fluid is another essential requirement for JDFT calculations. For nonpolar or uncharged solutes, cavitation energy dominates the free energy of solvation. Computing the free energy per unit surface area required to solvate a spherical cavity $\sigma = \frac{\Delta G}{4\pi R^2}$, as a function of the cavity radius R tests the accuracy of our predictions for cavitation. For planar interfaces (large R), this free energy reflects the effect of cohesion in the liquid, and σ is simply the constant bulk surface tension. For small solutes (small R), the effect of solvent exclusion dominates instead, causing σ to vary linearly with R. Our classical DFT must be able
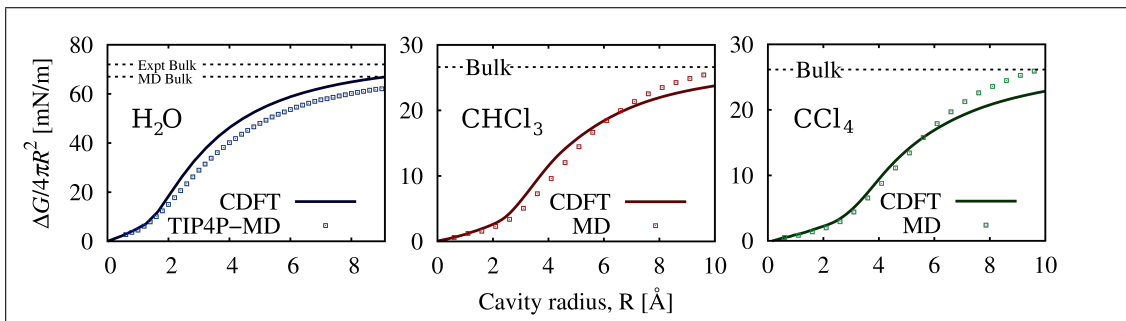
Figure 1.2: CDFT predictions of sphere cavitation energy $\sigma = \frac{\Delta G}{4\pi R^2}$ as a function of sphere radius R (solid line) compared to molecular dynamics (squares) for H_2O (blue,left), $CHCl_3$ (red,center), and CCl_4 (green,right). Bulk surface tension measured by experiment and predicted by molecular dynamics shown by dotted black lines.

to capture cavitation in both these limits, as well as in the essential crossover regime.

Figure 1.2 displays the predictions of the Polarizable CDFT for sphere cavitation, compared to molecular dynamics simulations. Clearly, the shapes of the curves predicted by MD and CDFT are in excellent qualitative agreement. One significant feature of these curves is the overprediction of bulk surface tension (asymptote of the curve as $R \to \infty$) by the molecular dynamics simulations. However, our classical density functional theories based upon an equation of state are able to reproduce the bulk experimental surface tension by construction. Polarizable CDFT's therefore offer an excellent choice for solvation of both small and large solutes (as well as planar interfaces) within the JDFT framework.

1.4   Joint Density-Functional Theory

While electronic DFT (described in Section 1.2) is a highly accurate tool for atomic scale problems in which a full quantum-mechanical treatment is neces-

sary, its computational cost is often prohibitive for systems with more than a few thousand atoms. Likewise, while classical DFT (described in Section 1.3) can efficiently treat large length scales by avoiding thermodynamic sampling of all possible configurations of the liquid, the lack of quantum-mechanics prevents any description of bonding and charge transfer. Ideally, we could combine the advantages of both theories through multiscale modeling, in which a quantum-mechanical solute is treated within electronic DFT while the fluid environment is treated classically. Joint Density-Functional Theory (JDFT) [218], described in detail in Chapter 2 provides a rigorous framework for just such a multiscale approach, enabling the study of previously intractable problems in fields ranging from biology to electrochemistry.

The proof of JDFT varies only slightly from the derivation of classical DFT presented in the previous section. The main difference is the division of the fixed nuclei of the solute system (indexed by I) from the nuclei of the environment (indexed by α). We apply a renormalization approach and hold the solute nuclei fixed while integrating over the solvent nuclear degrees of freedom so that the Coulomb interaction from the nuclei of the explicit solute system is now captured through the external potential

$$\phi(\vec{r}) = \sum_I \frac{Z_I}{|\vec{r} - \vec{R}_I|}. \tag{1.28}$$

Beginning with the temperature-dependent unified DFT functional in Equation 1.25, we now minimize over only the electron density of the liquid environment n_{lq} and leave the electrons of the solute n as the independent variable, yielding the exact (within a classical statistical-mechanical approximation for the solvent

28

nuclei) functional

$$A_\phi[n, \{N_\alpha\}, T] = \min_{n_{lq}} \Big\{ F[(n + n_{lq}), \{N_\alpha\}, T] +$$

$$\int d^3r \; \phi(\vec{r}) \Big(n(\vec{r}) + n_{lq}(\vec{r}) - \sum_\alpha Z_\alpha N_\alpha(\vec{r}) \Big) \Big\}. \tag{1.29}$$

The energy $A_\phi[n, \{N_\alpha\}, T]$ may be written as

$$A_\phi[n, \{N_\alpha\}, T] = G[n, \{N_\alpha\}, \phi, T] + \int d^3r \; \phi(\vec{r}) n(\vec{r}) \tag{1.30}$$

in terms of the semi-universal functional

$$G[n, \{N_\alpha\}, \phi, T] = \min_{n_{lq}} \Big\{ F[(n + n_{lq}), \{N_\alpha\}, T] + \int d^3r \; \phi(\vec{r}) \Big(n_{lq}(\vec{r}) - \sum_\alpha Z_\alpha N_\alpha(\vec{r}) \Big) \Big\}.$$
$$\tag{1.31}$$

As in the case of the classical DFT, this semi-universal functional still depends weakly upon the form of the external potential $\phi(\vec{r})$ and the chemical identities of the nuclei.

Some subtlety exists regarding the division of the total electron density into the solute and solvent electron densities. The indistinguishability of electrons dictates that meaningful assignment of electrons to the solvent and the solvent is not possible in an exact framework, however any real approximation will break the degeneracy. In most systems treated within JDFT, it is reasonable to assume that the liquid molecules are nonreactive and that their electrons are tightly bound and not easily polarized by the solute. Within that approxima-tion, we may neglect the right-hand side of Equation 1.31 to find a more uni-versal functional which does not depend on the nature of the solute system, communicated through the external potential $\phi(\vec{r})$.

In practice, we typically rewrite Equation 1.31 in terms of well-defined pieces as

$$A[n(r), \{N_\alpha(r)\}] = A_{HK}[n(r)] + \Omega_{lq}[\{N_\alpha(r)\}] + \Delta A[n(r), \{N_\alpha(r)\}], \tag{1.32}$$

29

where $A_{HK}[n(r)]$ is the Hohenberg-Kohn density-functional for the electrons of the solute [116], $\Omega_{lq}[\{N_\alpha(r)\}]$ is a classical density-functional for the liquid environment, and $\Delta A[n(r), \{N_\alpha(r)\}]$ is formally defined as the difference between the exact functional A and the well-known pieces A_{HK} and Ω_{lq}. Chapter 2 describes each of these pieces in additional detail and presents a successful approximation to the functional ΔA, which couples the solute system to the liquid environment. In addition, we place implicit solvation models (which depend only upon the electrons of the solute) within the rigorous framework of JDFT in Section 3.4.

CHAPTER 2

MICROSCOPICALLY ACCURATE ELECTRON-FLUID COUPLING FUNCTIONALS WITHIN EXPLICIT JDFT [1]

2.1 Introduction

Liquid water covers over 70 percent of the surface of the Earth, and is essential to the survival of a myriad of lifeforms. However, this complex liquid is far from well-understood, despite its significance. The polar nature of water, along with the strong tendency to form hydrogen bonded networks, creates strong, orientation-dependent interactions which prevent simple fluid models from successfully capturing its behavior. Even simple, nonpolar fluids such as the common chemical solvent carbon tetrachloride (CCl_4), and its slightly polar relative chloroform ($CHCl_3$) exhibit features such as molecular polarizability which are not easily captured by traditional fluid models. These molecular-scale features lead to macroscopic properties of the liquid, including dielectric response and surface tension, which can crucially impact processes occurring in a liquid environment. The greatest theoretical challenge arises when atomic-scale processes — for which a quantum-mechanical treatment is essential — occur in contact with a fluid which exhibits these microscopically driven, yet inherently large-scale and statistical phenomena.

A truly fundamental description of biological systems, such as solvated DNA and proteins, and of technological systems, such as fuel and solar cells, requires a simultaneous and complete description of the quantum-mechanical

---

[1]Co-author credits: R. Sundararaman assisted with the software implementation, the procedure for determining the microscopic parameters of the solvent molecule in Section 2.4, and preliminary benchmarking of neutral molecule calculations.

solute (broadly construed as a surface, polymer, molecule, or ion), the complex liquid environment, and the coupling between the solute and liquid. These systems also require an accurate description of the liquid-solute coupling, which captures the interaction between the liquid environment and the solute system. Moreover, to access the experimentally relevant length and time scales, this theoretical description must also be computationally efficient. The development of accurate and efficient methods to treat electronic systems in contact with liquid thus would advance basic understanding in materials physics, microbiology, pharmacology, and many other diverse fields, but despite the critical scientific importance of the solute-solvent interface, no single theory has yet overcome the inherent challenge of making solvation calculations both accurate and efficient. Instead, a variety of models have arisen, each with its own strengths and weaknesses; typically the models with sufficient accuracy are computationally prohibitive, while those with sufficient speed are highly empirical and may not generalize readily to new systems.

The common approaches to studying quantum-mechanical solvated systems may be divided into those which include explicit liquid molecules, and those which model the fluid as some type of continuum. Solvated systems may be calculated highly accurately using *ab initio* molecular dynamics[38, 209], which treat the electrons of both the ensemble of water molecules and the solute quantum-mechanically [192, 141, 147]. However, while these techniques are ideal for benchmarking properties of liquid water, they are prohibitively expensive for many applications as they require both explicit water electrons and extensive sampling over the phase-space of likely liquid configurations. A more computationally tractable method, the QM/MM approach [296, 136], employs classical molecular dynamics for the liquid, coupled to a full quantum-

mechanical calculation for the solute. In the QM/MM method, the water is modeled using empirical atomic site-potentials [22, 133, 4] and, commonly, the water-solute interaction is simulated as simply electrostatics and van der Waals repulsion for each explicit atom or functional group in the solute. Less commonly, the water-solute interaction may be treated using a density-only functional [115, 114]. While these techniques may be reasonably efficient, they require a thermodynamic average over multiple configurations of the liquid to facilitate the calculation of free energy differences.

In 2010, after the publication of JDFT, Wesolowski *et al.* [137] proposed an alternate approach which embeds a quantum-mechanical system within an integral equation description of the liquid environment through the Frozen Density Embedding (FDE) framework [302, 300]. Integral equations are often derived from pair potential models created for molecular dynamics simulations, and thus do contain microscopic information about the response of the liquid to the solute system. However, within the integral equation framework, calculation of free-energy differences is not straightforward. Indeed, significant, largely untested approximations are required to even make these computations feasible [242, 143]. Because the free-energy formalism within integral equation theory is more complicated, self consistent treatment of both the *ab initio* system and the liquid is difficult to achieve, even for a small system. Another similar solvation approach would couple a quantum-mechanical system to a perturbation theory based reference interaction site model (RISM) [48] using common force-field models [71]. This class of approach suffers from significant empiricism introduced by these force-field models into the solute-solvent coupling. Finally, no fundamental free-energy theorem undergirds the combination of integral equation theory with either the FDE framework or higher-order quantum

33

chemistry methods.

To overcome the requirement for phase-space sampling or complex integral equation formulations, some simplified, empirical solvation models replace the microscopic details of the aqueous environment with a continuum description, such as in the popular Polarizable Continuum Model (PCM). The simplest approach is to use spheres defined by the van der Waals radii of each of the solute atoms or functional groups plus an effective spherical radius for solvent molecules in order to define a solvation cavity, and then describe the fluid electrostatics by using the continuum bulk dielectric constant placed outside the cavity [281]. A more physical transition into the fluid region may be achieved using isodensity cavitation, which determines the solvation cavity from the electron density of the explicit, solute system [75]. However the cavity is defined, these models then attempt to simulate surface tension [243], dispersion,[7] and other effects deemed important[280, 180] by including *ad hoc* corrections to the free energy and fitting empirical parameters to large databases of solvation data[231]. These polarizable continuum models may be placed in a rigorous framework and made exact in principle [217], but the approximations required for practical calculations remain the same.

While the predictions made by the aforementioned continuum models may be highly accurate for those classes of systems included within the fitting database [231], these methods are not generalizable to systems like polar electrode surfaces under potential control. These simplified models do not include the molecular-scale structure of the liquid environment, and therefore cannot reliably capture nonlinear dielectric response or the complex interplay between electrostatics, cavitation, and dispersion. Ideally, each of these physical effects

should arise naturally from a full description of the thermodynamics and quantum mechanics of the system, and should be accessible through a single variational principle. Such an approach would retain the advantages of the simplified models, such as a self-consistent solution without the need for thermodynamic sampling and straightforward treatment of extended systems within a plane-wave basis, while significantly reducing the empiricism. One additional strength of a free energy approach is the direct access to thermodynamic averages from derivatives of the free energy functional.

This chapter will outline the path for coupling an in principle exact continuum model for water — a classical density-functional theory which reproduces equilibrium properties of the fluid, such as nonlinear dielectric response, cavitation energy, and shell structure, from first principles [266] — to a fully quantum-mechanical calculation of the solute system within the framework of Joint Density Functional Theory (JDFT) [218]. First, we will describe the rigorous JDFT framework for study of an explicit solute system within a continuum liquid environment. We then present a computationally tractable and microscopically accurate universal functional to couple quantum-mechanical systems with their liquid environments. Next, we provide an initial exploration of the promise of this universal coupling functional by computing solvation energies of a range of small molecules in a variety of polar and nonpolar solvents ($CHCl_3$, CCl_4, and H_2O). Finally, we test the efficacy of this theory for extended systems by determining the structuring of liquid water in the presence of a graphene sheet. The excellent performance of the JDFT approach on these test systems, compared with both experiment and state-of-the-art theory, suggests that it has matured into a predictive solvation theory which can bridge the gap between scalability and accuracy.

2.2 Theoretical Framework

Knowledge of the full equilibrium quantum-mechanical description of a solute in contact with fluid allows the free energy of the system to be exactly determined by a single variational principle through the Joint Density Functional Theory framework. Without such a framework, clearly this minimization problem can often be computationally infeasible due to the large number of liquid electronic degrees of freedom and the need for thermodynamic averaging over multiple nuclear degrees of freedom of the liquid. As described in section 1.4, Petrosyan et. al. [218] present a rigorous proof which "integrates out" the liquid electrons to construct a joint liquid-solute functional that is exact in principle. They further manipulate the functional into a form which is straightforward to approximate.

The free energy functional of the joint solute-liquid system may be constructed from well-defined quantities, leaving an unknown piece ΔA to be approximated,

$$A[n(r), \{N_\alpha(r)\}] = A_{\mathrm{HK}}[n(r)] + \Omega_{\mathrm{lq}}[\{N_\alpha(r)\}] + \Delta A[n(r), \{N_\alpha(r)\}]. \qquad (2.1)$$

In Equation 2.1, $A_{\mathrm{HK}}[n(r)]$ is the well-known Hohenberg-Kohn density-functional for the electrons of the solute with electron density $n(r)$ [116], $\Omega_{\mathrm{lq}}[\{N_\alpha(r)\}]$ is a classical density-functional for the liquid environment with atomic site densities $\{N_\alpha(r)\}$ (for water $\alpha = O, H$), and $\Delta A[n(r), \{N_\alpha(r)\}]$ is formally defined as the difference between the exact functional A and the well-known pieces A_{HK} and Ω_{lq}. In this form, JDFT makes the Born-Oppenheimer approximation for the nuclei of the explicit, quantum mechanical solute system while

the nuclei of the solvent remain fully quantum-statistical-mechanical. Additionally, due to the indistinguishability of electrons, there is no unique assignment of the electrons belonging only to the solute ($n(r)$). This lack of uniqueness implies that in principle, a large set of $n(r)$ will produce the minimum value of Equation 2.1. Of course, each of the terms in Equation 2.1 must be approximated for actual calculations, which will result in a unique decomposition of the electrons belonging to the environment from those belonging to the solute.

The term $A_{HK}[n(r)]$ in Equation 2.1 is highly studied, and is typically formulated in terms of Kohn-Sham single particle orbitals [151], with the electrostatic portion of the Coulomb interaction treated within a mean-field (Hartree) approximation. A myriad of approximate functionals for the electron exchange and correlation energy are available, including the Local-Density Approximation, multiple forms of the Generalized Gradient Approximation [212], and even van der Waals corrected functionals [311, 233]. Higher level theories such as Quantum Monte-Carlo (QMC) have also been implemented to describe highly correlated quantum-mechanical solute systems within the JDFT framework [246]. Finally, we note that when performing the decomposition of solvent and solute electrons described above, it is essential that any electrons participating in charge transfer reactions or covalent bonds be treated quantum-mechanically within A_{HK}.

Classical density-functionals for the term $\Omega_{lq}[\{N_\alpha(r)\}]$ are less widely available, likely because the typical hard-sphere reference fluid [211] is not an ideal starting point for most small molecular fluids. For highly polar molecules like water, information about the molecule orientation and geometry is required to properly capture shell structure and dielectric response. There are sev-

eral schools of thought regarding the design of orientation-dependent classical density-functionals presented in the literature; as are summarized in Section 1.3. The initial exploration of the promise of the JDFT framework by Petrosyan et. al. employed a hard-sphere density-functional theory for water in terms of only the oxygen site density $N_O(r)$, with no dependence on the hydrogen site density $N_H(r)$ [218] and therefore no sense of molecular geometry or orientation. Another weakness of this preliminary classical DFT is the *ad hoc* and empirical linear form of the dielectric function used to compute the electrostatic portion of the energy. In the present work, we use the polarizable classical DFT based on fundamental measure theory and the liquid equation of state which was recently developed by Sundararaman et al. [262, 266] and is introduced in 1.3 and described in detail for water in 4.3.1. This polarizable CDFT introduces an additional vector field $\vec{\mathcal{P}}_\alpha$, the polarization density of site α, as an independent variable in Ω_{lq}. Section 1.3.3 demonstrates that this polarizable CDFT reproduces the physical quantities relevant for free energy calculations for both polar and nonpolar solvents; predictions for nonlinear dielectric response, surface tension, and site-site correlation functions all compare favorably with experimental and molecular dynamics results.

The functional $\Delta A[n(r), \{N_\alpha(r)\}]$ which describes the coupling between a classical density-functional theory for the liquid and the electronic density-functional theory for the solute is largely unstudied, and remains an active area of research. Water-solute interaction models used to calculate coupling of quantum-mechanical systems to molecular dynamics [115, 114] may offer insight, but these models ultimately couple point particles rather than site-density fields, and so suffer the same pitfalls as classical molecular dynamics simulations, such as the need to re-calibrate for each new solvent. Simplified, implicit

solvation model approximations to JDFT, which do not consider the fluid structure explicitly, (see Section 3.4) may incorporate ideas from classical DFT, such as nonlinear dielectric response [100] and non-locality [268], but they still lack the effects of realistic structuring in the fluid.

Previous work on full, explicit JDFT for water [218, 219] employed "molecular pseudopotentials" [144] $V_{ps}(r)$ to represent the electron coupling to a single solvent molecule, resulting in a coupling functional which is linear in both solute electron density $n(r)$ and oxygen site density $N_O(r)$,

$$\Delta A = \int d^3R \int d^3r\, n(r) V_{ps}(r - R) N_O(R). \tag{2.2}$$

This molecular pseudopotential coupling functional, combined with the empirical oxygen-only classical DFT, yielded promising solvation energy results for small molecules[218], but did not yield accurate shell structure in the fluid. Furthermore, because molecular pseudopotentials do not capture the van der Waals interaction between the solvent and solute systems, they fail to reproduce correct solvation trends for noble gas atoms, the alkanes, and other nonpolar solutes [219].

When molecular pseudopotentials are employed within a classical density-functional theory for water with both oxygen and hydrogen site densities, the lack of screening from water electrons around the positively charged hydrogen sites creates too much attraction for the electrons from the explicit system, causing unphysically deep potential wells. Deep potential wells have been observed to create numerical instabilities in the minimization of the classical density-functional, limiting the practicality of JDFT coupling functionals based upon molecular pseudopotentials. In addition, these pseudopotentials are currently parameterized only for water, and are not easily generalizable to other fluids.

Construction of a molecular pseudopotential for a new solvent requires careful spectroscopic measurements of the properties of an electron in contact with that solvent, as well as empirical and largely arbitrary choices for the functional form of $V_{ps}(r)$ employed to fit the spectroscopic data. Even for water, the various molecular pseudopotentials available in the literature offer different predictions for quantities like the "volume" of the solvated electron, yielding no clear choice upon which to base a coupling functional.

Ideally, the prescription for the coupling functional should be solvent-independent and highly transferable. A coupling functional based on electronic density-functional theory would be universally applicable, but requires a reconstruction of the solvent electron density which was previously "integrated out" in the proof of JDFT. The most promising path to performing JDFT calculations with explicit molecular geometry for a general solvent therefore requires an accurate description of the electrons in the liquid and their interaction with the explicit system. Below, we present a coupling functional which captures precisely this interaction in a simple, solvent-independent form motivated from the underlying physics and basic ideas in density-functional theory.

2.3 Universal Approximate Coupling Functional

In order for JDFT to be appropriate for wide use in many diverse fields, the choice of coupling functional must not depend on the details of the particular solvent. We therefore seek to develop a universal form, which could couple any quantum-mechanical solute to any molecular solvent, given a properly parameterized classical DFT for the term $\Omega_{lq}[\{N_\alpha(r)\}]$ in Equation 2.1. To develop

such a universal coupling functional, we first divide the full system into solute and solvent *sub*systems. Then, for simplicity, we posit that a single functional $\mathcal{F}[n_S, \{N_S\}]$ may describe the interactions in each subsystem in terms of the nuclear number densities $\{N_S\}$ (and nuclear charges $\{Z_S\}$) and the electron density n_S of that subsystem. Thus, the coupling functional may be written quite generally and intuitively as

$$\Delta A = \mathcal{F}[n_{\text{tot}}, \{N_I, N_\alpha\}] - \mathcal{F}[n, \{N_I\}] - \mathcal{F}[n_{\text{lq}}[\{N_\alpha\}], \{N_\alpha\}]. \tag{2.3}$$

where the nuclei of the solute system are delta functions $N_I(r) = \delta(r - R_I)$ with charges Z_I. We note that the average electron density of the liquid, n_{lq}, should be a functional of the solvent atomic site densities $\{N_\alpha\}$, yielding the total electron density $n_{\text{tot}} = n + n_{\text{lq}}[\{N_\alpha\}]$. Section 2.3.3 describes the the specific practical approximation we employ to represent $n_{\text{lq}}[\{N_\alpha\}]$. This approximation is tantamount to assuming that each solvent electron is bound in an orientation-independent manner to a single nuclear site.

In Equation 2.3, the full coupling functional consists of the general functional $\mathcal{F}$ evaluated upon the joint system, with the individual contributions from the solute and liquid subsystems subtracted from the total (as the first two terms of Equation 2.1 consider these contributions). Of course, the particular form chosen for $\mathcal{F}$ is crucial in determining the accuracy and computational feasibility of the universal coupling functional. Section 2.3.1 describes the density-only DFT approach which we employ. Such subtraction-based approaches within orbital-free DFT are commonly used to couple high-accuracy and low-accuracy subsystems of a demanding calculation using embedding theory [53, 118] or "Frozen Density Embedding" (FDE) [302]. However, these embedding theories are formulated in a solid-state context, where all nuclei and the resulting nuclear potential are *static*, therefore the resulting frameworks are simple ex-

41

tensions of Kohn-Sham electronic DFT. Though the subsystem embedding approach has previously been employed to study liquid subsystems [137], these studies have not yet been placed on a rigorous basis because, when coupling liquid and solid regions together, one must instead consider a statistical average of nuclear positions in the liquid. In this situation, the underlying pure electronic Hohenberg-Kohn theorem in Equation 1.10 no longer applies, as the external potential acting upon the electrons is no longer constant. Thus, one may perform true liquid solvation calculations only within the free-energy framework of JDFT.

2.3.1 Approximate Local Functional

The universal subsystem functional $\mathcal{F}$ may now be approximated by any electronic DFT functional which does not depend upon the quantum-mechanical orbitals, traditionally known as density-only or orbital-free DFTs. Fortunately, an efficient and highly stable density-only functional is well-known and has been employed in the literature for a wide variety of applications [277, 80]. To produce this functional, we simply approximate the orbital-dependent kinetic energy operator from Kohn-Sham density-functional theory with the Thomas-Fermi kinetic energy T_{TF}, a functional of the electron density,

$$T_{\text{TF}}[n_S(r)] = \int d^3r \left\{ \frac{3}{10}(3\pi^2)^{\frac{2}{3}} n_S(r)^{\frac{5}{3}} + O(\nabla n_S) \right\}. \tag{2.4}$$

Among the key physical effects which this local term captures is the electron-cloud overlap due to Pauli exclusion, a physical effect which is necessary to prevent the over-attraction of solute electrons to positively charged solvent nuclear sites, and which is not well-described within the molecular pseudopotential coupling approach.

We next represent the mean-field electrostatic interactions of the total charge density $\rho_S(n_S(r), \{N_S(r)\})$ (determined for the solvent from Equation 2.19 in Section 2.4) as a multicomponent Hartree term,

$$E_H[n_S(r), \{N_S(r)\}] = \frac{1}{2} \int d^3r \int d^3r' \frac{\rho_S(r)\rho_S(r')}{|r-r'|}. \quad (2.5)$$

A more computationally feasible representation of this energy exists in fourier space as

$$E_H = \tilde{\rho}_S \hat{K} \tilde{\rho}_S \quad (2.6)$$

where $\tilde{\rho}_S$ denotes the fourier transform of the charge density and $\hat{K}$ is the Coulomb operator.

Finally, we include the effects of exchange and correlation within the local density approximation [151] as

$$E_{XC}[n_S(r)] = \int d^3r n_S(r)\epsilon_{LDA}[n_S(r)] \quad (2.7)$$

where $\epsilon_{LDA}[n_S(r)]$ is the local-density approximation for the exchange correlation potential [151, 214]. Including the generalized gradient approximation for the exchange and correlation [212] as well as gradient corrections [298] for the kinetic energy is a promising direction for future research. To date, however, our attempts at this higher level of accuracy have proved numerically unstable when combined with the classical DFT because the introduction of gradient terms results in high frequency features in the site densities N_α.

2.3.2 Beyond Local DFT

To correctly capture solvation effects, especially solvation of large, nonpolar molecules, the nonlocal effect of polarizabilities of both the liquid and the solute

must also be considered. In principle, these nonlocal effects could be included through van der Waals density-functional theory; [279, 158] however, such theories require a double integral over a nonlocal functional form and are therefore quite computationally demanding. Some promising recent approaches do reduce the computational complexity of van der Waals density-functionals[233], but these functionals are designed to use with the Kohn-sham orbital-dependent kinetic energy and may not be fully accurate with an orbital-free treatment, which overestimates electron repulsion. Thus, for this first level of approximation of the interaction between the solvent and explicit quantum-mechanical system, we employ Grimme's van der Waals pair interactions between the nuclei with a database of coefficients c_6^S and radii R_6^S derived from high-level quantum chemistry calculations [97]. The contribution to the coupling functional $\mathcal{F}$ from these pair interactions is

$$E_{\text{vdW}}[\{N_S(r)\}] = \gamma \sum_S \sum_{S'} \int d^3r \int d^3r' \frac{\sqrt{c_6^S c_6^{S'}} N_S(r) N_{S'}(r')}{|R_6^S + R_6^{S'}|^6} \qquad (2.8)$$

However, the choice of scaling prefactor γ is ambiguous – Grimme has only determined the scaling prefactor for certain approximations to the exchange and correlation (specifically 0.75 for PBE, 1.0 for TPSS, and 1.05 for B3LYP, among other GGA, meta-GGA, and hybrid functionals) [97]. There is no prefactor determined for density-only functionals or even the local density approximation. Accordingly, following [263, 268], we must adjust this parameter based upon its performance for solvation energies (see Section 2.6.1).

With the specification of the above nonlocal term, Equations 2.4, 2.5, 2.7, and 2.8 now fully prescribe our approximate density-only functional form,

$$\mathcal{F}[n_S, \{N_S\}] = T_{\text{TF}}[n_S(r)] + E_H[n_S(r), \{N_S(r)\}] + E_{\text{XC}}[n_S(r)] + E_{\text{vdW}}[\{N_S(r)\}]. \quad (2.9)$$

Note that this coupling functional is based directly upon first principles physical

effects and thus should be highly transferable. Moreover, this functional is systematically improvable as the community develops more accurate density-only functionals.

2.3.3   Convolution Electron Density Model

An accurate description of the electron density of the solvent, $n_{lq}(r)$, is necessary to properly couple an explicit electronic system to an orientation-dependent classical DFT through Equation 2.9. However, the rigorous JDFT framework integrates over the liquid electronic degrees of freedom, so that the solvent electron density $n_{lq}(r)$ must be computed efficiently from knowledge of only the nuclear degrees of freedom, $\{N_\alpha(r)\}$. The current accurate forms of the classical density-functional theory for molecular solvents available to us [262, 266] do not contain orientation information for the molecules contributing to the densities N_α. Accordingly, from a computational perspective, the electron density associated with each site α of the solvent molecule is most naturally taken as having spherical symmetry about the atomic site center. The challenge of this approach is to correctly reproduce the full electron density of a solvent molecule as a superposition of spherical site models. We therefore begin with a reference *ab initio* calculation to obtain the electron density of a quantum-mechanical solvent molecule in solution. Following the procedure of [266] (also detailed in Section 2.4) we then perform a least-squares fit of the resulting density to a parameterized set of spherical site densities.

For the water molecule, the resulting density model varies from the reference by a maximum of 0.1 a_0^{-3} and in most places is much more accurate (Fig-

ures 2.1 and 2.2). The model does underestimate the electron density somewhat in the location of the lone pair and along the oxygen-hydrogen bonds, but such features are not possible to capture using site-centered spherical models. In any event, the O-H bonds are not sterically accessible so their electron density should not overlap significantly with the quantum-mechanical system. Additionally, we have performed preliminary aqueous solvation energy calculations similar to those in Section 2.6.1 with a more detailed multi-site water model (with extra spherical sites on the lone pair and the bonds) to confirm that the details of the model within the interior the water molecule are unimportant, giving identical solvation energies to within less than 1 mH. Similar sensitivity analysis has been performed for the non-aqueous solvents CCl_4 and $CHCl_3$. As the overlap between the electron densities of the solute and solvent is generally small, capturing the asymptotic behavior of the solvent electron density should provide sufficient accuracy for calculation of free energy differences.

Though these spherical electron density models properly reproduce properties of the liquid electrons for molecules with point nuclei fixed in well-defined locations, the classical density-functional theory is written in terms of continuum density fields $N_\alpha(r)$ for the atomic sites. The effective liquid electron density $n_{lq}(r)$ may be computed simply and directly as the sum of the convolutions of each spherical site electron density $n_\alpha(r)$ with the appropriate nuclear density $N_\alpha(r)$,

$$n_{lq}[\{N_\alpha(r)\}] = \sum_\alpha N_\alpha * n_\alpha = \sum_\alpha \int d^3R N_\alpha(R) n_\alpha(r - R). \qquad (2.10)$$

The appropriate expression for n_α may be found in Equation 2.16 of Section 2.4 and the required parameters are tabulated in Table 2.1. The electron density $n_{lq}(r)$ may then be used directly in the kinetic and exchange-correlation functionals making up $\mathcal{F}$. The remaining Hartree term of the coupling functional re-

quires the total charge density of the solvent ρ_{lq}, which also includes the nuclear charge and the bound charge due to the polarizability of the liquid molecules as prescribed in Equation 2.19 of Section 2.4.

A functional form similar to the above has been employed by Kaminski et. al. for coupling integral equation theory for water to electronic DFT [137], but has not yet been applied to the calculation of free energies of solvation. While this choice of reconstructing the solvent electron density is somewhat arbitrary, we will show in Section 2.6 that using this approximation, along with Equations 2.3 and 2.9 for solute-solvent coupling within the JDFT framework, truly has predictive power for key quantities such as free energies of solvation and liquid structure.

2.4 *Ab initio* solvent-molecule parameterization

The microscopic details of the solvent impact the free energies of solvation which JDFT predicts through both the terms ΔA and Ω_{lq} in Equation 2.1. The electron-fluid coupling ΔA within JDFT, using Equations 2.3 and 2.9, employs the solvent electron density $n_{lq}[\{N_\alpha\}]$ and charge distribution $rho_{lq}[\{N_\alpha\}]$. The exponential tails of the solvent electron density overlap with the corresponding tails of the solute and therefore affect the solute-solvent interaction terms[162] in joint density-functional theory.[218] Through the parameterization in Table 2.1 of Equations 2.11 and 2.12, we reproduce these key quantities for each individual solvent molecule as faithfully as possible. We then reconstruct the charge properties of the total fluid from the nuclear number densities $\{N_\alpha\}$ and nuclear charges $\{Z_\alpha\}$ according to Equations 2.10 and 2.19.

The atomic-scale properties of the solvent molecule also impact the liquid functional Ω_{lq} through both the geometric constraint on the ideal gas free energy and the electrostatic interactions amongst the liquid atomic sites. For the liquid functional Ω_{lq}, we approximate the mean field Coulomb interaction of the fluid with itself using a different spherical shell model for the charge distribution $\rho_{MF}[\{N_\alpha\}]$ [266], designed specifically to minimize self-interaction. This mean-field self-interaction model requires accurate geometry and atomic site charges for each constituent solvent molecule, so these microscopic properties have a direct impact on both the short-range and long-range electric response of the classical fluid.

The remainder of this section establishes the procedure for determining the geometry, atomic site charges q_α, and electron site densities n_α from electronic density-functional calculations of a single solvent molecule.

2.4.1   Solvent Environment

Solvent molecules in the liquid environment differ significantly from isolated or gas phase molecules. Pair potential models created for molecular dynamics simulations of liquids are calibrated to reproduce the thermodynamic properties of the liquid state, and give strong indication of these changes. For example, the dipole moment of the SPC/E model water molecule is 2.35 Debye [22], in agreement with estimates of 2.3-2.5 Debye [89] based on cubic susceptibility measurements, and in contrast to the gas phase moment of 1.85 Debye [2].

To account for the effect of the surrounding liquid in our *ab initio* calculation, we perform calculations of a single quantum-mechanical solvent molecule

in contact with an implicit solvation model to represent the effects of the solvent environment. Specifically, we employ the nonlinear polarizable continuum model [100], which approximates solvent effects in an electronic density-functional calculation of a molecule by surrounding the molecule with a nonlinear dielectric medium. In principle, we could obtain the solvent parameters self-consistently within a solvation model which includes full microscopic detail. In practice, however, we find that the parameters determined from a properly constrained and sufficiently detailed polarizable continuum model are adequate for determining the needed microscopic details of solvent molecules in the solvent environment.

2.4.2 DFT Calculation Details

All *ab initio* calculations were performed within the DFT++ framework [122] as implemented in the open-source code JDFTx [267]. The solvent was modeled by the nonlinear polarizable continuum model GLSSA13 [100]. We employed the generalized-gradient approximation [212] using a plane-wave basis within periodic boundary conditions and a single k-point (Γ) to sample the Brillouin zone. Each molecule was computed within a supercell representation with a distance of 40 a_0 between each periodic image in each direction. All calculations presented employ optimized [230] norm-conserving Kleinman-Bylander pseudopotentials [228]. A partial core correction [172] was required for the Cl pseudopotential. A high plane-wave cutoff energy of 70 H was chosen so all details in the electron density would be fully resolved on a fourier grid of $(300)^3$ points.

2.4.3 Solvent-Molecule Geometry

Accurate structure of the solvent molecule is crucial for accurate liquid free energy calculations, as it affects the long-range electrostatics as well as the geometric contribution to the ideal gas entropy. We obtain the solvent molecule geometry directly from the relaxed nuclear positions, $\{\vec{R}_\alpha\}$, determined by the solvated electronic density-functional calculation. Table 2.1 shows that the bond lengths and angles, thus obtained, agree reasonably with popular molecular dynamics models for water, chloroform and carbon tetrachloride.

2.4.4 Determination of Solvent Site Charges

The charges q_α on each solvent atomic site impact the Coulomb interactions among the liquid molecules and between the liquid and the quantum-mechanical solute system. The mean field Coulomb kernel in the liquid functional Ω_{lq} in Equation 2.21 The norm of the liquid site electron density in Equation 2.12, which is used to compute the coupling functional ΔA, is also determined from the site charge q_α. We constrain the site charges to match the lowest multipole moments of the *ab initio* solvent molecules, employing as many moments as necessary to constrain them (up to dipole for water, quadrupole for chloroform, and octupole for carbon tetrachloride). The resulting site charges q_α are tabulated in Table 2.1.

The site charges determined by this procedure agree reasonably with those of common pair potentials for the highly polar liquid water, whose thermodynamic properties are sensitive to these parameters in molecular dynamics simulations. The site charges agree to a lesser extent for the weakly polar liquid

chloroform. However, in nonpolar fluids, the bulk thermodynamic properties do not constrain the multipole moments, since the magnitude of the Coulomb interaction is insignificant compared to the magnitude of the dispersion interaction. Thus, unsurprisingly, the empirically determined molecular dynamics site charges for carbon tetrachloride [45] differ significantly from our *ab initio* values. In fact, the octupole moment of our CCl_4 model is 13.2 Debye-$Å^2$ in much better agreement with the experimental value of (15 ± 3) Debye-$Å^2$ [73], compared to 0.5 Debye-$Å^2$ for the model of Ref. [45]

2.4.5 Spherical Charge Density Functional Forms

To be used within the JDFT coupling functional in Section 2.3 the electron and nuclear charge densities from the solvated electronic density-functional calculation must be expanded as a sum of spherical contributions around each atomic site of the solvent molecule, as in Equations 2.10 and 2.19. Accurate calculations therefore require spherically symmetric functional forms which capture the solvent electron and charge densities in the range at which they interact with the quantum-mechanical system. Because the overlap between the solvent and solute is minimal, especially in the core region of the solvent molecule, only the mid-range and asymptotic behavior of the relevant solvent densities is important. To a certain extent, we can therefore choose smoothed and simplified functions that represent the electron and nuclear charge densities within the core region to optimize representability on a Fourier grid without changing the interaction energies.

The charge due to the solvent core electrons and nuclei is confined to the

Table 2.1: Microscopic solvent parameters for water, chloroform and carbon tetrachloride from electronic density-functional theory, compared to molecular dynamics models (Ref. [133] for H_2O, Ref. [156] for $CHCl_3$ and Ref. [45] for CCl_4) wherever applicable.

Solvent	Property	Density-functional	Molecular Dynamics
H_2O	r_{OH}	0.967 Å	0.9572 Å
	θ_{HOH}	104.2°	104.52°
	q_O	-0.826	-0.8476
	q_H	+0.413	+0.4238
	Z_O^{el}, a_O^{el}	6.826, 0.37 a_0	-
	d_O^{el}, v_O^{el}	0.52 a_0, 0.37 a_0	-
	Z_H^{el}, a_H^{el}	0.587, 0.35 a_0	-
	d_H^{el}, v_H^{el}	0.0, $2a_H^{el}/\sqrt{\pi}$	-
	χ_O, a_O^{pol}	3.73 a_0^3, 0.32 a_0	-
	χ_H, a_H^{pol}	3.30 a_0^3, 0.39 a_0	-
$CHCl_3$	r_{CCl}	1.804 Å	1.79 Å
	r_{CH}	1.091 Å	1.1 Å
	θ_{HCCl}	107.8°	107.2°
	q_C	-0.256	-0.175
	q_H	+0.244	+0.211
	q_{Cl}	+0.004	-0.012
	Z_C^{el}, a_C^{el}	4.256, 0.49 a_0	-
	d_C^{el}, v_C^{el}	0.67 a_0, 0.48 a_0	-
	Z_H^{el}, a_H^{el}	0.756, 0.36 a_0	-
	d_H^{el}, v_H^{el}	0.0, $2a_H^{el}/\sqrt{\pi}$	-
	Z_{Cl}^{el}, a_{Cl}^{el}	6.996, 0.45 a_0	-
	d_{Cl}^{el}, v_{Cl}^{el}	1.01 a_0, 0.51 a_0	-
	χ_C, a_C^{pol}	6.05 a_0^3, 0.36 a_0	8.84 a_0^3, -
	χ_H, a_H^{pol}	9.13 a_0^3, 0.41 a_0	0, -
	χ_{Cl}, a_{Cl}^{pol}	15.8 a_0^3, 0.46 a_0	13.8 a_0^3, -
CCl_4	r_{CCl}	1.801 Å	1.77 Å
	q_C	-0.980	-0.1616
	q_{Cl}	+0.245	+0.0404
	Z_C^{el}, a_C^{el}	4.980, 0.61 a_0	-
	d_C^{el}, v_C^{el}	0.53 a_0, 0.37 a_0	-
	Z_{Cl}^{el}, a_{Cl}^{el}	6.755, 0.44 a_0	-
	d_{Cl}^{el}, v_{Cl}^{el}	1.04 a_0, 0.52 a_0	-
	χ_C, a_C^{pol}	5.24 a_0^3, 0.35 a_0	5.93 a_0^3, -
	χ_{Cl}, a_{Cl}^{pol}	18.1 a_0^3, 0.47 a_0	12.89 a_0^3, -

interior regions of the molecule and does not overlap with the other solvent molecules or the electronic system. For optimum Fourier resolvability, we smooth it with a gaussian distribution of standard deviation $\sigma_\alpha = R_{0\alpha}/6$. These distributions then become zero to numerical precision at the atomic van der Waals radius $R_{0\alpha}$, which is a reasonable estimate for the typical approach distance of that site to any other atom. This contribution to the charge density from the core electrons and the nuclei has norm Z_α, which is determined by the pseudopotential choice for valence/core separation.

The electron densities of the solvent molecules do overlap somewhat with the explicit quantum-mechanical system. Therefore, those functions which monotonically decrease from a maximum at the site center (such as a simple exponential or gaussian) and only provide one degree of freedom (such as a decay width a) are not sufficiently accurate to describe the valence electron densities of the solvent molecules. When a width is chosen to reproduce only the asymptotic density tails, these monotonic functional forms disagree significantly with the valence electron densities, even at atomic radii beyond the van der Waals radius. These issues are compounded for atoms represented within the pseudopotential framework, where the core electrons are missing (as in Figure 2.1). For each site, we thus require a function which smoothly increases away from the origin to account for the missing core electrons, yet has the correct asymptotic exponentially decaying behavior $\propto e^{-r/a}$.

For the valence electron density component attributed to site α, the (unnormalized) function

$$f_\alpha(\vec{r}) = \operatorname{erfc}\left(\frac{r_\alpha - d_\alpha^{\text{el}}}{v_\alpha^{\text{el}}}\right) e^{-r_\alpha/a_\alpha^{\text{el}}} \tag{2.11}$$

meets these criteria, with $r_\alpha = |\vec{r} - \vec{R}_\alpha|$ as the distance from nucleus α, a_α^{el} as the

exponential decay length scale, d_α^{el} determining the location of the peak, and v_α^{el} determining the peak width. See Figure 2.1 for an illustration of the physical meanings of these parameters a_α^{el}, d_α^{el}, v_α^{el}. For the hydrogen atom (or any other atom where all core electrons are included explicitly), we fix $d_\alpha^{el} = 0$ and $v_\alpha^{el} = \frac{2a_\alpha^{el}}{\sqrt{\pi}}$ to create a function which is cuspless at the origin. We therefore can represent the full valence electron density of the solvent molecule $n(r)$ with the model form

$$n_{\text{model}}(\vec{r}) = \sum_\alpha \frac{Z_\alpha^{el} f_\alpha(\vec{r})}{\int_V d\vec{r} f_\alpha(\vec{r})}, \tag{2.12}$$

where Z_α^{el} is the norm associated with the electron density component at site α and the denominator is present to normalize the function $f_\alpha(\vec{r})$ over the calculation unit cell volume V. The norms of the electronic site densities $Z_\alpha^{el} = q_\alpha + Z_\alpha$ are determined from the appropriate site charges q_α and ionic core charges Z_α and presented in Table 2.1.

2.4.6   Least-Squares Fit

The remaining electron density parameters a_α^{el}, d_α^{el}, v_α^{el} in Equation 2.12 are determined by a least-squares fitting procedure which minimizes the linear residual $\int d\vec{r} |n(\vec{r}) - n_{\text{model}}(\vec{r})|^2$. The core regions are included in the fit, but have a smaller effect because there are far more values of $\vec{r}$ in the exponential tails. Table 2.1 shows the electron density fit parameters for all solvents considered.

Figures 2.1 and 2.2 compare the valence electron density from the *ab initio* calculations for water to the density produced by the fitted site-spherical model. Note that the fit reproduces the electron density well in both the intermediate and tail regions, which would overlap with an explicit electronic system and
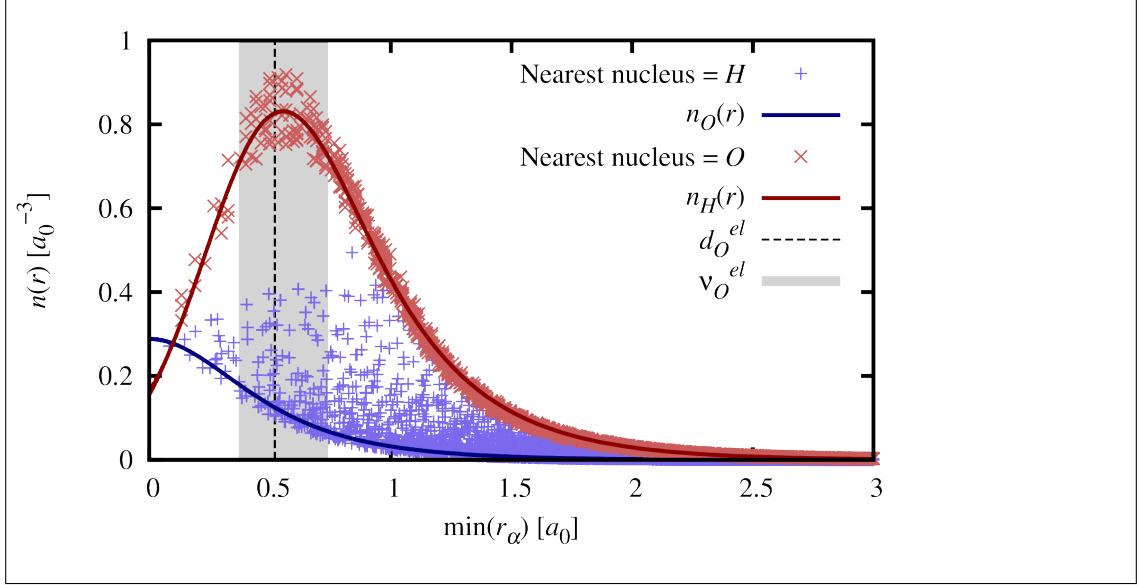
Figure 2.1: Individual site density models $n_{O,H}(\vec{r})$ with parameters given in Table 2.1 compared to the valence electron density $n(\vec{r})$ at each point in space. Parameters d_O^{el} and v_O^{el} are indicated by the dotted line and the width of the grey box.

impact the accuracy of the coupling functional ΔA. Also, the residual in the core regions has zero multipole moments to high order by construction and therefore does not contribute to the electric interaction with another non-overlapping molecule.

2.4.7 Electronic site polarizability

Finally, the electronic polarizability $\chi(\vec{r}, \vec{r}')$ in Kohn-Sham electronic density functional theory is formally related to the susceptibility of the corresponding non-interacting system,

$$\chi_{\text{NI}}(\vec{r}, \vec{r}') = -4 \sum_{c,v} \frac{\psi_c(\vec{r})\psi_v^*(\vec{r})\psi_c^*(\vec{r}')\psi_v(\vec{r}')}{\epsilon_c - \epsilon_v}, \tag{2.13}$$

by $\hat{\chi}^{-1} = \hat{\chi}_{\text{NI}}^{-1} - \delta^2 E_{HXC}[n]/\delta n^2$. Here, (ψ_v, ϵ_v) and (ψ_c, ϵ_c) are occupied and unoccupied Kohn-Sham orbital-eigenvalue pairs respectively, and $E_{HXC}[n]$ is the
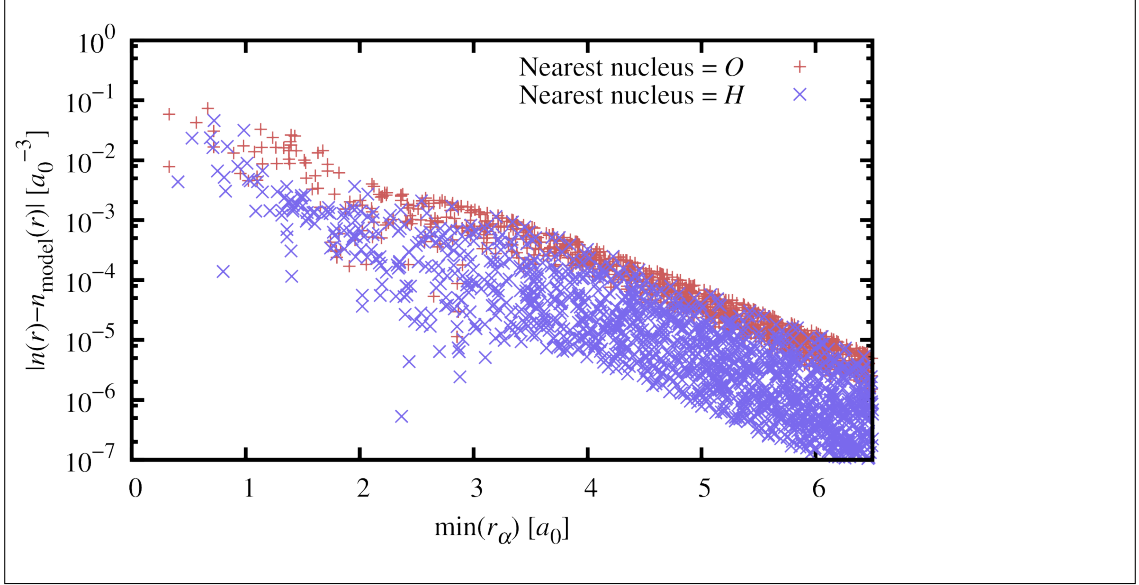
Figure 2.2: Error in the spherical density decomposition of Figure 2.1 at each point in space

sum of the Hartree term and the exchange-correlation functional. In practice, we compute a large number of unoccupied Kohn-Sham eigenpairs of the solvated solvent molecule, compute $\hat{\chi}$ from $\hat{\chi}_{\mathrm{NI}}$ as a dense matrix in the occupied-unoccupied basis ($\{\psi_c^*(\vec{r})\psi_v(\vec{r})\}$), and then diagonalize $\hat{\chi}$ to obtain an eigen-expansion $\chi(\vec{r}, \vec{r}') = \sum_i X_i \rho_i(\vec{r})\rho_i(\vec{r}')$. We find that 1000 unoccupied orbitals and 500 eigenvectors in the final expansion results in better than 1 % convergence in the total dipole polarizability of the molecule. The calculated isotropic linear dipole polarizabilities are within 5 % of the experimental values [106] for all three liquids.

The classical density functional requires the polarizability in the model form, $\hat{\chi}_{\mathrm{model}}$ given by

$$\chi_{\mathrm{model}}(\vec{r}, \vec{r}') = -\sum_{\alpha} \chi_\alpha \nabla' w_\alpha(|\vec{r}' - \vec{R}_\alpha|) \cdot \nabla w_\alpha(|\vec{r} - \vec{R}_\alpha|) \tag{2.14}$$

for one molecule with sites at positions $\vec{R}_\alpha$, with dipole polarizability strengths χ_α and normalized range functions $w_\alpha(r)$. In order to properly represent the ex-

ponential tail regions with a smooth core region, we pick a cuspless exponential form

$$w_\alpha(r) = \frac{r + a_\alpha^{\text{pol}}}{32\pi(a_\alpha^{\text{pol}})^4} \exp\left(\frac{-r}{a_\alpha^{\text{pol}}}\right) \tag{2.15}$$

for the normalized range functions. We then fit the site polarizability strengths, χ_α, and widths, a_α^{pol}, to minimize the residual $\text{Tr}\left((\hat{K}(\hat{\chi} - \hat{\chi}_{\text{model}}))^2\right)$ which effectively measures the error in the screening operator $\hat{\epsilon}^{-1} = 1 - \hat{K}\hat{\chi}$, where $\hat{K}$ is the Coulomb operator. Table 2.1 lists the thus obtained polarizability parameters for all three solvents. Note that the width parameters for a particular species are relatively similar in different solvents, while the strengths differ. Also, the empirically-fit polarizability parameters used for each atom in the pair-potential models [156, 45] compare reasonably to our *ab initio* parameters for C and Cl, but neglect the response at the H site.

2.4.8   Construction of Liquid Electron and Charge Densities

All the microscopic details required to compute the free energy of the joint solvent-solute system through JDFT may now be determined from the parameters in Table 2.1. The electron site densities $\{n_\alpha\}$ to be used in Equation 2.10 to compute the total fluid electron density n_{lq} are given by

$$n_\alpha(r) = \frac{Z_\alpha^{\text{el}} f_\alpha(\vec{r})}{\int_V d\vec{r} f_\alpha(\vec{r})}. \tag{2.16}$$

The total site charge density kernels for interactions of the classical fluid with an electronic system through JDFT (or with external potentials) are then given by

$$\rho_\alpha(r) = \frac{Z_\alpha}{(\sigma_\alpha \sqrt{2\pi})^3} \exp\left(\frac{-r_\alpha^2}{2(\sigma_\alpha)^2}\right) - n_\alpha(r). \tag{2.17}$$

The bound charge in the solvent may be computed from the polarization density of site α, $\vec{\mathcal{P}}_\alpha\}$, which is one of the independent variables in the functional $Omega_{\text{lq}}$, as

$$\rho_{\text{bound}}[\{N_\alpha, \vec{\mathcal{P}}_\alpha\}] = -\nabla \cdot \sum_\alpha w_\alpha(r) * N_\alpha \vec{\mathcal{P}}_\alpha. \tag{2.18}$$

We note that in a real system the separation of the bound charge from the electronic density is artificial. However, in the approximation of Equation 2.16 the electron density remains rigid when coupled to an external electric potential, so the inclusion of the bound charge due to dipole polarizability captures changes in the electron density in the presence of an applied electric field.

For the total charge density of the liquid, one can convolve the total site charge density $\rho_\alpha(r)$ with $N_\alpha(r)$ and add in the bound charge $\rho_{\text{bound}}(r)$, yielding

$$\rho_{\text{lq}}[\{N_\alpha\}] = \sum_\alpha N_\alpha * \rho_\alpha + \rho_{\text{bound}}. \tag{2.19}$$

Combining Equations 2.19 and 2.17 and taking the limit $\sigma_\alpha \to 0$ yields an intuitive expression for the total charge density of the fluid

$$\rho_{\text{lq}}(\vec{r}) = \sum_\alpha Z_\alpha N_\alpha(\vec{r}) - n_{\text{lq}}(\vec{r}) + \rho_{\text{bound}}(\vec{r}), \tag{2.20}$$

where the contributions from the nuclei, electrons, and bound charge in the solvent all clearly appear. For numerical purposes, we retain the slightly more complicated expression which results from the choice of $\sigma_\alpha = R_{0\alpha}/6$.

Using the convolution approach in Section 2.3.3, we also determine the analogous total charge density kernel ρ_{MF} for the mean-field self-interaction internal to the fluid. This charge density is identical to the one in Equation 2.19 above, except that it replaces both the charge density kernel $\frac{rho_\alpha}{q_\alpha}$ and the polarization range kernel w_α with a new spherical kernel w_{MF}. This spherical kernel minimizes the self-energy of the classical fluid under the constraint

$w_{MF}(r > R_{vdW}) = 0$, where $\{R_{vdW}\}$ is the molecular van der Waals radius, thus placing all the charge on the surface of the constraining sphere,

$$w_{MF}(r) = \frac{\delta(r - R_{vdW})}{4\pi R_{vdW}^2}. \tag{2.21}$$

Equivalently, we can compute $\tilde{w}_{MF}(G) = j_0(GR_{vdW})$ in Fourier space (j_0 is a spherical Bessel function). Intuitively, distributing the charge of each site onto a sphere centered on that site with a radius that is half the closest intermolecular separation minimizes the intra-molecular interaction while preserving the intermolecular interaction. The fluid charge as experienced by the fluid is thus fully specified as

$$\rho_{MF}(\vec{r}) = \sum_\alpha q_\alpha w_{MF}(r) * N_\alpha(\vec{r}) - \nabla \cdot \sum_\alpha w_\alpha(r) * N_\alpha \vec{\mathcal{P}}_\alpha(\vec{r}). \tag{2.22}$$

The procedures outlined above make specific choices for residuals and functional forms for fitting which are, of course, by no means unique. However, the parameterization developed here approximates the full *ab initio* charge distributions well for the studied solvents. As such, the above prescription enables the construction of a coupling functional for a new solvent of interest, without requiring extensive experimental or molecular dynamics data.

2.5   Computational Details

While Sections 2.2 and 2.3 fully prescribe the theory for JDFT calculations with explicit fluid structure, practical calculations require significant additional numerical, algorithmic, and software innovations.

2.5.1 Self-Consistent Joint Minimization

One key advantage of JDFT which places the theory on a stronger footing than other, more *ad hoc*, solvation theories is its formulation as a variational principle. This variational approach makes self-consistent determination of both the quantum-mechanical finite temperature ensemble state of the solute and the equilibrium structure of the solvent quite computationally feasible. Finding the minimum free-energy state is simply a matter of computing the joint free-energy functional, then minimizing this functional with respect to both the solute and solvent degrees of freedom, $n(r)$ and $\{N_\alpha(r)\}$, respectively. In practice, the Kohn-Sham single particle orbitals $\{\phi_i(r)\}$ [151] are chosen as the independent variables for representing the electron density of the solute, while the local chemical potential $\mu(r)$ and the local electric field $\vec{\epsilon}(r)$ are chosen as the independent variables for representing the density and polarization state, respectively, of the solvent [262].

While joint minimization of the full functional (Equation 2.1) with respect to both solute and solvent degrees of freedom is theoretically possible and will be implemented in the future, an alternating minimization scheme is currently more practical. Specifically, we first perform a vacuum density-functional theory calculation of the solute system. We then compute the coupling functional from the vacuum electron density $n(r)$ and charge density $\rho(r)$ and minimize the liquid and coupling functionals with respect to the site densities $\{N_\alpha(r)\}$, while the solute degrees of freedom are held fixed,

$$A = A_{\mathrm{HK}}[n(r)] + \min_{\{N_\alpha(r)\}} \left(\Omega_{\mathrm{lq}}[\{N_\alpha(r)\}] + \Delta A[n(r), \{N_\alpha(r)\}] \right)\Big|_{n(r)}. \qquad (2.23)$$

Next, the liquid degrees of freedom are held fixed while we minimize the solute

and coupling functionals with respect to the electronic density,

$$A = \Omega_{\text{lq}}[\{N_\alpha(r)\}] + \min_{n(r)} \left(A_{\text{HK}}[n(r)] + \Delta A[n(r), \{N_\alpha(r)\}]\right)|_{\{N_\alpha(r)\}}. \qquad (2.24)$$

We repeat this alternating minimization cycle until the system reaches convergence.

Because each of the above steps is variational, the total energy decreases monotonically during the minimization process. This procedure is quite similar to the "freeze and thaw" cycles used within FDE [301], but in that case the electron density is only the independent variable, whereas here we alternate between (solute) electron and (solvent) nuclear degrees of freedom. Indeed, we find minimization of the coupling functional and the solute electronic functional is straightforward and numerically stable. In fact, the electronic minimization over Kohn-Sham orbitals may be performed either by direct minimization or by using the self-consistent field (SCF) approach. However, the minimization of the liquid and coupling functionals requires a highly robust conjugate gradient algorithm [209] due primarily to the fundamental measure theory [237] term in Ω_{lq}, which causes the free energy to approach positive infinite values when the molecular density approaches the hard sphere close packing limit. This feature required us to develop a specialized control algorithm for accepting and rejecting proposed steps, as well as for adjusting the trial step size in the conjugate-gradient based line minimization. With this adjustment to the minimization algorithm, only systems with severe nonlinear behavior experience difficulty converging.

2.5.2 Software Implementation

The capability to perform JDFT calculations is fully implemented within the JDFTx software package [267], a fully functional plane-wave DFT code which works within periodic boundary conditions. JDFTx is based on the expressive DFT software framework DFT++ [122], but is written to comply with the latest C++ standard, taking full advantage of templates and other object-oriented features. Its operators are GPU-parallelized using CUDA, and the code also offers MPI-parallelization over the k-points in the electronic structure portion of the calculation and over fluid orientations in the classical DFT fluid [262]. Band structure techniques [59], auxiliary Hamiltonian minimization of partially filled bands at a constant chemical potential [86], both ultrasoft [289] and norm-conserving pseudopotentials [230], and other DFT innovations are implemented in JDFTx and are typically compatible with JDFT calculations.

The computational demands of the JDFTx implementation of JDFT are quite competitive with other solvation theories. Typically, on the order of ten alternating minimizations are required to achieve self-consistency to $10\,\mu$H. Each electronic minimization step scales linearly or quadratically with the number of solute electrons and linearly with the number of realspace gridpoints, as do typical DFT calculations. Moreover, each fluid minimization step scales only with the number of realspace gridpoints (volume of the unit cell) and *does not depend on the number of fluid molecules or electrons*. For the most computationally demanding systems in DFT (e.g. supercell surface calculations with thousands of electrons), the fluid minimization therefore comes at only a fraction the cost of an electronic minimization of the solute in vacuum. Most of the additional expense is involved with the cyclic iteration of the electronic system to self-consistency

with the fluid, thus a full JDFT calculation costs about an order of magnitude (corresponding to the need for about ten cycles to reach convergence) more than a vacuum DFT calculation of the same system. When compared to a full *ab initio* molecular dynamics calculations of the same system, which would require tens of thousands of electronic structure calculations along the molecular dynamics trajectory, this performance of JDFT is exceptionally good. Moreover, we drastically reduce the number of electrons required by "integrating out" the fluid electrons within the classical DFT. These two factors lead to a radical reduction in computational demands relative to explicit molecular dynamics.

2.6   Results

The density-only coupling functional defined through Equations 2.3, 2.9, and 2.10 has shown promising results for computing both free energies of solvation and determining the structure of liquids around both planar and molecular solutes.

2.6.1   Solvation Energies

Traditionally, free energies of solvation of small organic molecules have been used to train and benchmark solvation theories. Small molecule solvation offers an ideal training ground for new theories because all of the relevant physical effects are captured when the training set includes sufficiently diverse chemical bonds and functional groups. Physical effects such as dielectric response, dispersion, and cavity formation must work together harmoniously to provide

Table 2.2: Molecules included in the fit of Grimme scaling parameter γ to experimental solvation energies. Solvation Energy results are shown in Figures 2.3 and 2.4.

Molecule	Chemical Formula	H_2O	$CHCl_3$	CCl_4
acetamide	C_2H_5NO	✓	✓	×
acetic acid	$C_2H_4O_2$	✓	✓	✓
acetone	C_3H_6O	✓	✓	×
anisole	C_7H_8O	✓	×	✓
benzene	C_6H_6	✓	✓	✓
dimethyl ether	C_2H_6O	✓	×	×
ethane	C_2H_6	✓	×	×
ethanol	C_2H_6O	✓	✓	✓
methane	CH_4	✓	×	×
methanol	CH_4O	✓	✓	✓
methylamine	CH_5N	✓	✓	✓
phenol	C_6H_6O	✓	✓	✓
propane	C_3H_8	✓	×	×
propanol	C_3H_8O	✓	✓	✓
pyridine	C_5H_5N	✓	✓	✓
tetrahydrofuran	C_4H_8O	✓	×	×
toluene	C_7H_8	✓	✓	✓
water	H_2O	✓	✓	✓

a cohesive theory. Multi-parameter, empirical polarizable continuum models (PCM's) [180, 280] use large molecule fitting sets[231] to reproduce experimental solvation energies to high accuracy. These theories require new parameters for each new physical effect introduced, and therefore the most accurate theories are often the most empirical. JDFT offers a holistic, first-principles approach in which the only adjustable parameter is due to the black-box treatment of the van der Waals interaction using Grimme's pair potentials [97].

To benchmark the performance of JDFT, we calculate solvation energies for the series of small molecule solutes itemized in Table 2.2 in three diverse solvents: polar and hydrogen bonded water (H_2O), slightly polar chloroform

(CHCl$_3$), and nonpolar carbon tetrachloride (CCl$_4$). The benchmarking set consists of a total of N_s molecules per solvent, where $N_s = \{18, 12, 11\}$ for $s = \{$H$_2$O, CHCl$_3$, CCl$_4\}$. In these calculations, we employ the generalized gradient approximation [212] for A_{HK}, the liquid functionals by Sundararaman et. al. [262, 266] for Ω_{lq}, the coupling functional detailed in Sections 2.3 and 2.4, and the computational procedure described in Section 2.5.1. Our DFT calculations employ a 30 H plane-wave cutoff, unit cells which allow at least 15 Å of fluid between periodic solute images in each dimension, ultrasoft pseudopotentials [289], gamma point Brillouin zone sampling, and solute molecule geometries relaxed in the continuum solvation theory CANDLE [264]. Since the Hellman-Feynman forces on each solute atom of remained less than 1 mH $a_0^{-}1$ after the converged JDFT calculation, we have confidence that additional relaxation of the atomic positions would yield insignificant changes in the free energies of solvation.

We perform the full set of solvation energy calculations as a function of the scaling parameter γ in Equation 2.8, then choose the value of γ which minimizes the root-mean-square (rms) error in the solvation energy compared to experimental measurements. To find a universal value for γ across all three solvents, we minimize the following residual

$$\sigma_u(\gamma) = \frac{1}{\sqrt{\sum_s N_s}} \sqrt{\sum_s \sum_{i=1}^{s} (E_{s,i}(\gamma) - E_{s,i}^{\mathrm{exp}})^2}, \tag{2.25}$$

where N_s is the number of molecules in solvent s, $E_{s,i}(\gamma)$ is the JDFT solvation energy of the ith molecule in solvent s at parameter value γ, and $E_{s,i}^{\mathrm{exp}}$ is the corresponding experimental solvation energy from References [180] for water, [185, 92] for CHCl$_3$, and [93] for CCl$_4$. We also explore minimizing the rms error
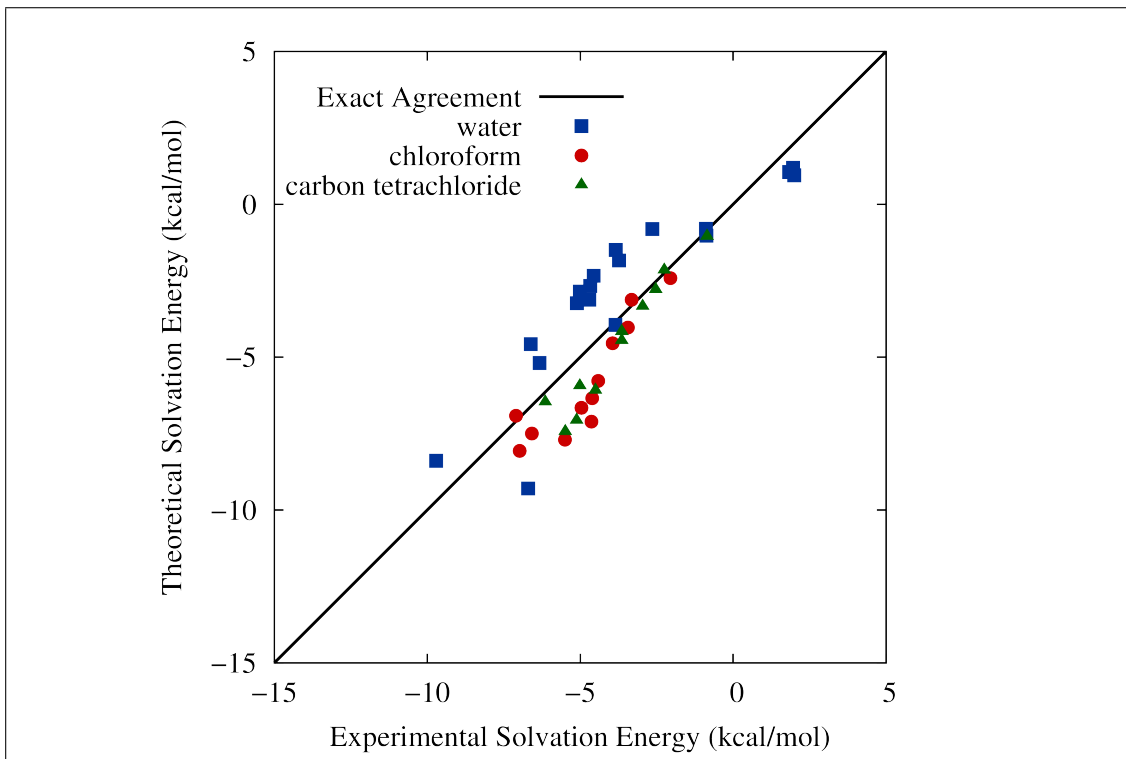
Figure 2.3: Solvation energies for H_2O (blue), $CHCl_3$ (red) and CCl_4 (green) using universal parameter $\gamma = 0.488$.

for each solvent individually, minimizing the fit residual

$$\sigma_s(\gamma_s) = \frac{1}{\sqrt{N_s}} \sqrt{\sum_{i=1}^{s} (E_{s,i}(\gamma_s) - E_{s,i}^{\text{exp}})^2}. \tag{2.26}$$

The universal fit yields $\gamma = 0.488$, while the solvent-dependent fit yields $\gamma_s = \{0.540, 0.393, 0.407\}$ for $s = \{H_2O, CHCl_3, CCl_4\}$, respectively. Table 2.3 reports the rms and mean absolute errors in both the universal and solvent-dependent cases.

Figure 2.3 shows a comparison of the calculated solvation energies for our molecular test set with their experimental values for the universal model and Figure 2.4 shows the same comparison for the solvent-specific models. Aqueous solvation calculations are represented by blue squares, while solvation calculations in $CHCl_3$ and CCl_4 are shown by red circles and green triangles, respec-
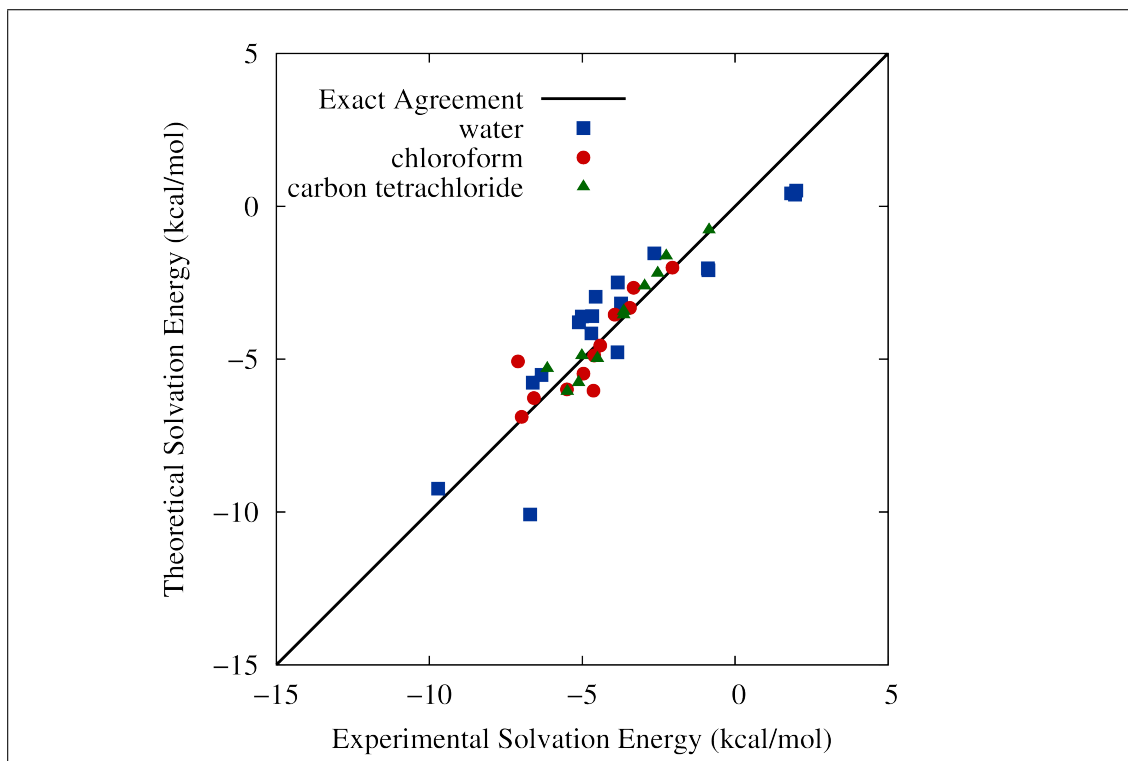
Figure 2.4: Solvation energies for H_2O (blue), $CHCl_3$ (red) and CCl_4 (green) using solvent-dependent best fit parameters $\gamma = 0.540$, $\gamma = 0.393$, and $\gamma = 0.407$ respectively.

tively. Each form of the theory agrees with the experiment to within the energy scale of thermal fluctuations (around $k_B T$=1-2 kcal/mol). Table 2.3 tabulates the precise solvation energy errors and scaling parameter γ for each solvent-specific model and for the universal model. The excellent agreement of these solvation energy results with experimental values strongly suggests that our density-only coupling functional can successfully reproduce the interaction between a quantum-mechanical solute and a classical DFT description of its liquid environment.

There are advantages to both the solvent-specific and universal coupling functionals. When the solvent under study has experimental solvation energy data to allow benchmarking, the solvent-specific model offers slightly more ac-

Table 2.3: Best fit Grimme van der Waals scaling parameters for water, chloroform and carbon tetrachloride, and a proposed universal model.

Solvent	γ	Mean Absolute Error [kcal/mol]	RMS error [kcal/mol]	Universal RMS Error [kcal/mol]
H_2O	0.540	1.23	1.38	1.64
$CHCl_3$	0.393	0.54	0.78	1.34
CCl_4	0.407	0.40	0.46	1.05
Universal	0.488	1.18	1.42	(1.42)

curate performance. The spread in Figure 2.4 is slightly better than in Figure 2.3, indicating that the use of the Grimme form in the coupling functional is not perfectly universal, requiring somewhat different values of γ to best capture higher-order multi-body screening effects in the different solvents. However, the results for the universal coupling functional based on this form with a single value for γ are still quite exceptional. We note that for the JDFT-based *implicit* solvation model SALSA, the Grimme scaling parameters for the solvents under study are vastly different [268], indicating that the implicit model is missing some underlying physics which becomes folded into γ. The simple fact that a single functional form works well for such vastly different solvents is evidence of the universality of this novel approach to solute-liquid coupling. With the universal coupling functional there is no need to perform solvation-energy calibration for each new solvent under study. This feature is especially advantageous for electrochemical studies where novel battery solvents are to be explored and experimental solvation energy data may not be available for benchmarking.

2.6.2 Real-space Liquid Structure

While continuum solvation theories can provide information about the electrostatic bound charge induced in the fluid by the solute, these theories make no direct connection to the actual structure of the liquid and spatial distribution of that charge. One clear advantage of JDFT over continuum solvation theories is the ability to predict real-space structure of liquids in contact with electronic systems. Minimization of the joint free energy functional 2.1 directly yields the thermodynamic average structure of the liquid in the form of the site densities $\{N_\alpha\}$, with no effort required beyond the JDFT calculation. Obtaining comparable information from molecular dynamics calculations requires costly thermodynamic sampling – for many systems of interest, particularly solid-liquid interfaces, such liquid structure would be heroically expensive to obtain from full *ab initio* molecular dynamics.

Figure 2.5 shows the resulting liquid structure for a variety of aqueous solutes. The features of the oxygen (red) and hydrogen (blue) liquid site-density fields reveal details about the physical effects in each case, with the quantum-mechanical subsystem depicted simply by spheres for each solute atom. The first example, methane, is an insoluble molecule and has a solvation shell similar to that of a hard sphere, with no polar response in the fluid and a rather weak peak in the shell structure. Water and methanol, by contrast, are both polar molecules and the classical densities clearly respond to this polarity with the hydrogens attracted more strongly to the positively charged sites and the oxygens attracted more strongly to the negatively charged sites. Large shell structure peaks dominate the density profiles for both polar molecules. The classical DFT description of the aqueous solution also clearly captures the presence of hy-
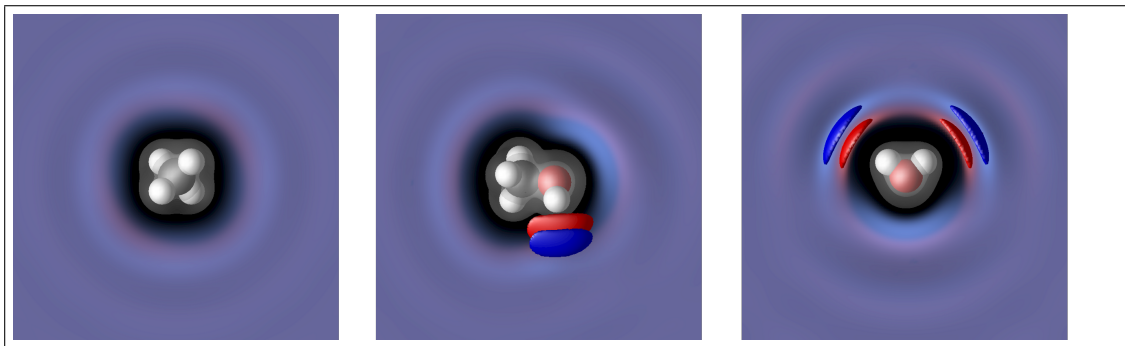
Figure 2.5: Real-space liquid structure of classical DFT water around quantum-mechanical methane (left), methanol (center), and water (right). The oxygen (red) and hydrogen (blue) density fields represent the CDFT water, while the atoms in the quantum-mechanical systems are represented by spheres (C=grey, O=red, H=white). High density contours appear at 4 times the bulk O density in water (red) and 2 times the bulk H density in water (blue). The translucent grey contours depict the electron densities of the quantum-mechanical systems at 0.4 Å^{-3} and 0.04 Å^{-3}. Each image is 14 Å on each side.

drogen bonding, with the high oxygen-density contours at the hydrogen bond locations in Figure 2.5 representing high probability that water molecules will be present at those locations.

JDFT calculations with the non-aqueous solvents chloroform and carbon tetrachloride provide similar real space structural information and Figure 2.6 shows self-solvation within these solvents. The symmetry imposed by each solute is clearly visible in the fluid density response. The high density green chlorine contour around CCl_4, for example, indicates that the solvent molecules are more ordered, with the more localized peaks perhaps due to the high symmetry of the molecule. The $CHCl_3$ self-solvation demonstrates the orientation preference of the surrounding molecules; the thin shell of blue hydrogen density around the solute molecule signifies that, at least in this particular planar slice, all the chloroform molecules point their C-H bond outwards. The reduced ordering for chloroform as compared to carbon tetrachloride is likely due to the decreased symmetry.
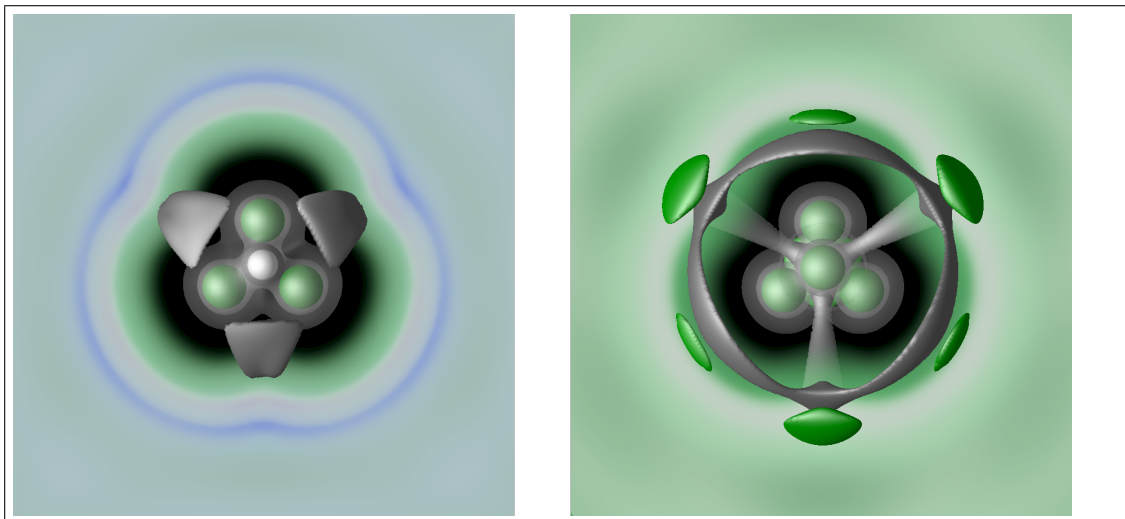
Figure 2.6: Real-space liquid structure of solvation of quantum-mechanical CHCl$_3$ in classical DFT CHCl$_3$ (left) and CCl$_4$ in CCl$_4$ (right). The carbon (light grey), chlorine (light green) and hydrogen (blue) density fields represent the CDFT water, while the atoms in the quantum-mechanical systems are represented by spheres (C=grey, Cl=green, H=white). High density contours appear at 2.6 and 3 times the bulk solvent C density (grey) in CCl$_4$ and CHCl$_3$ respectively and 1.3 times the bulk solvent Cl density (green) in the CCl$_4$ image only. The translucent grey contours depict the electron densities of the quantum-mechanical systems at 0.4 Å^{-3} and 0.04 Å^{-3}. Each image is 19.2 Å on each side.

2.6.3 Radial Distribution Functions

The spherical averages of the site densities $\{N_\alpha(r)/N_b\}$ (where N_b is the bulk solvent density) around each atomic site β correspond to the radial distribution functions (or correlation functions) $g_{\beta\alpha}(r)$. Specifically, the radial distribution functions capture the same information that is present in Figure 2.6 and in the right panel of Figure 2.5, but with a spherical average performed over the density profiles. The classical DFT representing each solvent, as a complete description of the responses of the corresponding fluid, contains within it information sufficient to derive the radial distribution functions through the Ornstein-Zernike equation [202]. One test of the universal coupling functional is to determine whether it couples an explicit, quantum-mechanical solute molecule to

71
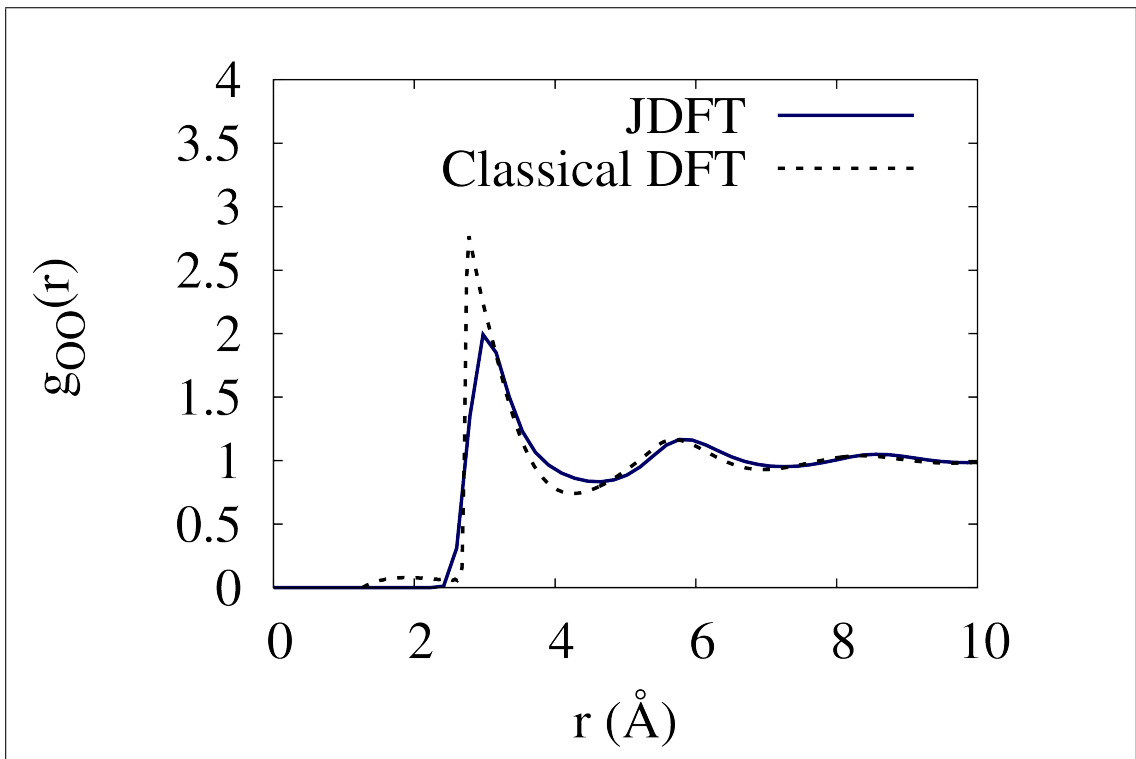
Figure 2.7: Oxygen radial distribution functions g_{OO} from a quantum-mechanical water molecule coupled to classical DFT water through JDFT (blue, solid line) and from solving the Ornstein-Zernike equation within the classical DFT water (black, dashed line).

the fluid in the same way the fluid molecules couple to themselves. Thus, we verify that self-solvation of an explicit molecule within JDFT reproduces the correlation functions of the fluid as determined by the Ornstein-Zernike equation (which describes the classical fluid's internal coupling). Figure 2.7 shows just this comparison between the spherically averaged oxygen density profiles around a quantum-mechanical water molecule solvated in a classical density-functional description of water (blue, solid line) compared to the Ornstein-Zernike correlation functions of the classical DFT water (black, dashed line). The agreement between the two is excellent, with the coupling functional reproducing both the peak locations and the integrals under each peak (coordination numbers). The main difference between the two correlation functions is the

slight spreading of the first peak in the JDFT correlation functions, an effect due to some remaining Coulomb self-interaction error within the classical DFT.

Experimental radial distribution functions typically exhibit multiple peaks from multiple solvation shells. Nonlinear PCM or any traditional continuum model for liquid form only a a spherical cavity around the solute, with no sense of this structure whatsoever. Even the liquid water classical density-functional by Lischner et. al. only captures the first peak in g_{OO} [171]. In contrast, the equation-of-state-based liquid functionals employed in this work [266] capture not only the primary but also the secondary and even tertiary solvation peaks. Figures 2.8 and 2.9 show that JDFT combined with these liquid functionals and density-only coupling captures multiple shell structure peaks for both aqueous and non-aqueous fluids, with the carbon-carbon correlation functions for chloroform and carbon tetrachloride in excellent agreement with classical molecular dynamics simulations of these fluids [156, 45].

Figure 2.8 shows the oxygen radial distribution corresponding to the solvation of water. The correlations from the model qualitatively reproduce the features in the experimental correlations; however, the location of the second oxygen peak is too far away. This discrepancy results from the fact that the fundamental measure theory employed in the classical functional tends to pack molecules in a close-packed structure rather than the tetrahedral packing expected for water. Clearly, this disagreement with experiment indicates a need to improve the liquid-water functional (as opposed to the coupling functional) because the coupling functional does reproduce the Ornstein-Zernike correlations faithfully. Another key difference between the correlation functions is that the first peak in the theoretical prediction is wider and less sharp than the ex-
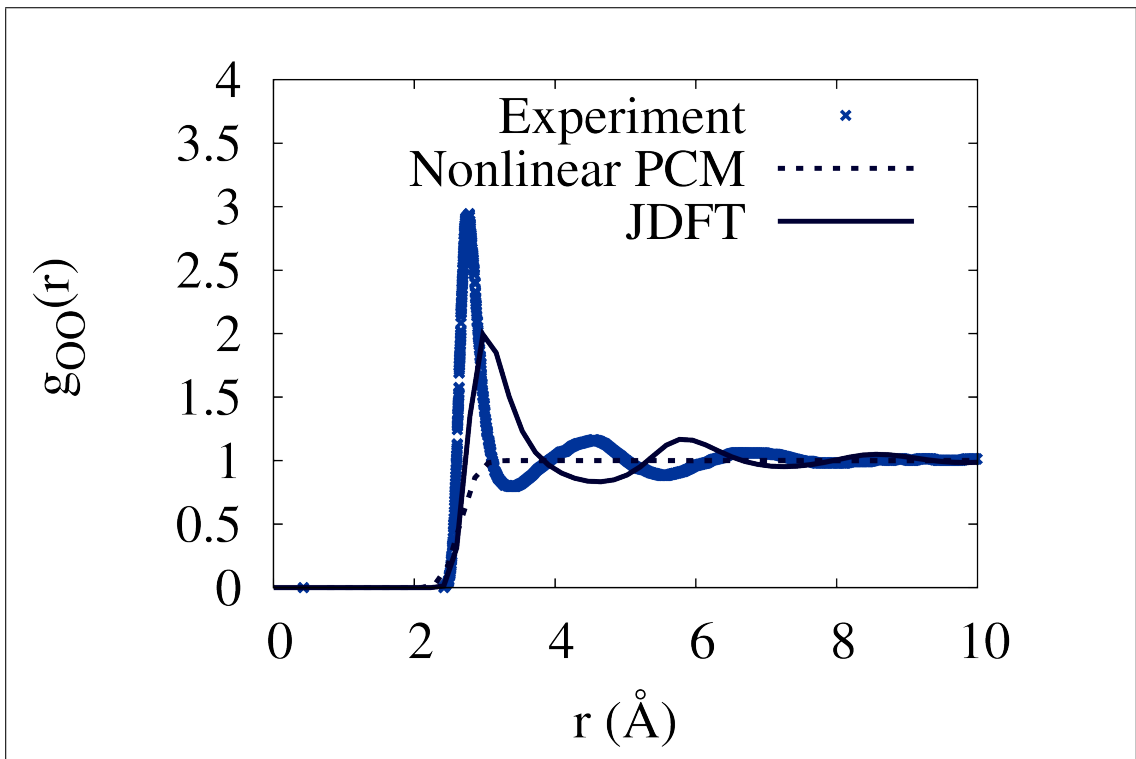
Figure 2.8: Oxygen radial distribution functions g_{OO} from a quantum-mechanical water molecule coupled to classical DFT water through JDFT (blue, solid line), coupled to a Nonlinear PCM description of water (blue, dashed line), and from experiment (blue points) [258].

perimental measurement, though the coordination number of the first solvation shell is the same. As mentioned above, this suppression of the first peak is due to the self-interaction error in the mean-field electrostatic energy of the fluid.

2.6.4 Liquid water structure next to graphene

Thus far, we have considered JDFT calculations of localized quantum-mechanical systems. However, one strength of JDFT (and its implementation in the plane-wave code JDFTx [267]) is the ability to tackle extended systems efficiently. Indeed, JDFT offers considerable advantage over molecular dynamics calculations for surface calculations because it can provide the correct spatially-
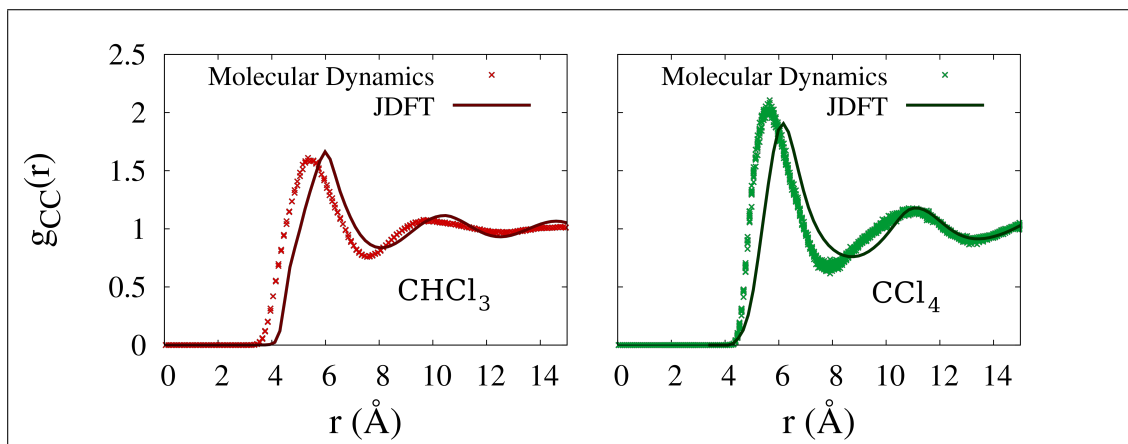
Figure 2.9: Carbon radial distribution functions g_{CC} from a quantum-mechanical molecule coupled to classical DFT solvent through JDFT (solid line) and from polarizable molecular dynamics simulations (points) for chloroform (left,red) and carbon tetrachloride (right,green) [266].

averaged liquid structure within a single, primitive unit cell of the surface. For example, we can obtain the structure of water next to a graphene sheet using a unit cell with only two carbon atoms, and thus only 8 solute electrons. Any reasonable *ab initio* molecular dynamics calculation would require a 3x3 or 4x4 surface reconstruction of the graphene sheet, requiring 9-16 times more solute electrons. Most significantly, JDFT calculations require *no* water electrons, compared to the 10-100 water molecules with 10 electrons per water molecule required to simulate just a few water layers on graphene in AIMD. These features reduce the number of electrons in even a single quantum-mechanical calculation by orders of magnitude, offering extreme computational cost savings. Finally, JDFT obtains the thermodynamic average water structure by construction, in the time required for only 10-20 DFT calculations of the solute alone, as opposed to thousands to tens of thousands of time steps needed to extract thermodynamic averages.

Figure 2.10 shows JDFT calculations of planarly-averaged oxygen (red) and hydrogen (blue) density profiles for liquid water in contact with a quantum-

mechanical graphene sheet located at z=0 Å, comparing the results to classical and Car-Parinello molecular dynamics [38] (CPMD) calculations of the same graphene system [229]. The JDFT calculations (left panel) employ a supercell representation with single primitive cell of graphene at z=0 Å and 50 Å of fluid between periodic images, spatial resolution corresponding to a 30 H plane-wave cutoff, a 72x72x1 k-point mesh to sample the Brillouin zone, and ultrasoft pseudopotentials [289]. To represent the solvent, we use the full JDFT functional described in Section 2.6.1 with the optional choice of $\gamma = 0.540$ for liquid water. (We actually find the liquid structure to be not highly sensitive to this choice.)

Figure 2.10 also provides comparison (right panel) to the oxygen density profiles from the first principles CPMD approach and a series of classical potential molecular dynamics calculations. The classical calculations allow tuning of λ, the strength of the Lennard-Jones interaction between the carbon atoms in the graphene and the oxygen atoms of the aqueous solvent. Clearly, tuning this interaction affects the density profiles significantly by changing both the heights and locations of the peaks. The value of $\lambda = 0.7$ agrees best with the CPMD calculations, indicating that interaction strength most closely mimics the CPMD. However, the CPMD uses the PBE exchange and correlation functional, which is known to under bind and does not sufficiently capture van der Waals interactions, which should contribute significantly to the graphene-water interaction.

The JDFT-calculated oxygen density profile shows excellent qualitative agreement with the molecular dynamics simulations, demonstrating the efficacy of the theory for fluid structure near planar interfaces. In particular, the peak *heights* are in excellent agreement with both the CPMD and the $\lambda = 0.7$ classical MD simulations. However, the JDFT predictions for peak *locations*

76
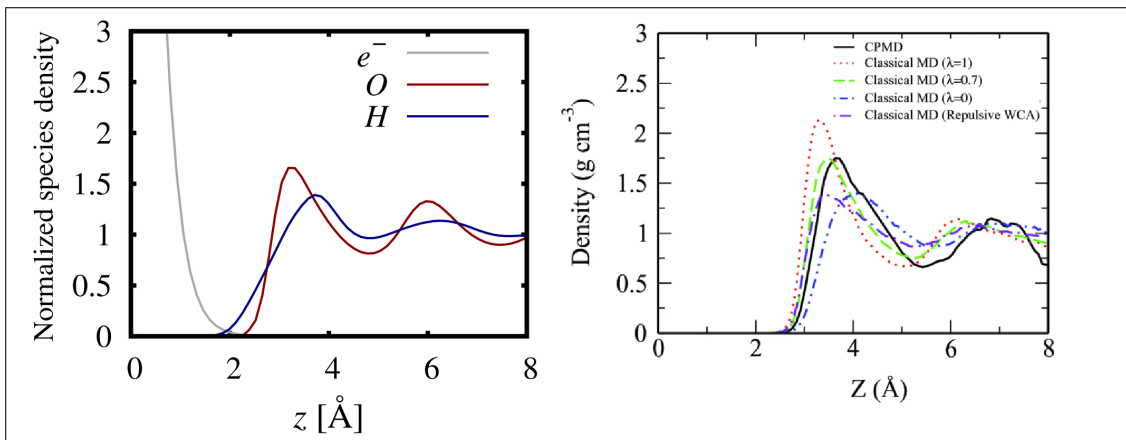
Figure 2.10: Planarly averaged oxygen (red, solid line) and hydrogen (blue, solid line) densities from a quantum-mechanical graphene sheet located at z=0 coupled to classical DFT water through JDFT (left) compared to Car-Parinello (black, solid line) and classical molecular dynamics simulations (colored, dashed lines) of the same system (right). Each dashed line represents a classical molecular dynamics simulation with a different strength (λ) of interactions between the carbon atoms in the graphene and the oxygen atoms in the water [229].

agree best with the classical MD simulations with λ = 1.0. This result likely indicates that, indeed, the CPMD simulations do not fully capture the van der Waals interaction, leading to an artificially long carbon-oxygen distance. The efficacy of JDFT for predicting water structure next to graphene allays some concerns about the discrepancy between the experimentally-measured and JDFT-predicted radial distribution functions for liquid water in Figure 2.8. Three dimensional tetrahedral packing around another tetrahedral water molecule may be harder to capture with the limitations of an FMT reference fluid than fluid structure at a planar interface. Regardless of the subtleties, the results in Figure 2.10 show that accurate liquid water structuring can be obtained at planar interfaces with JDFT and suggest that JDFT is a promising theory for the study of planar systems and interfaces in aqueous environments.

2.7 Conclusion

While much progress has been made toward improvement of implicit solvation models based upon the JDFT framework [163, 100, 268], this work represents the first fully explicit JDFT calculations with a realistic classical density-functional theory since the publication of the rigorous proof of the theorem and the accompanying preliminary results [218]. The present work offers the first realization of full JDFT with an orientation-dependent classical DFT[262, 266] used for the liquid functional, as well as the first explicit JDFT calculations in non-aqueous solvents. Unlike previous JDFT calculations, which employed water-specific and empirical molecular pseudopotentials to couple the liquid and solid regions, this work describes and benchmarks a *universal* coupling functional, appropriate to couple *any* solute to *any* solvent. We also describe the procedure and software implementation for performing self-consistent solvation calculations within the JDFT framework. We show that our implementation of the JDFT framework, used in conjunction with the orientation-dependent polarizable classical DFT and the herein developed universal coupling functional, captures aqueous and non-aqueous solvation free energies of small molecules with a near-chemical accuracy of 1-2 kcal/mol. Finally, we offer the first demonstration of full JDFT for an extended system by predicting the structure of liquid water in contact with a graphene sheet, resulting in good agreement with the liquid structuring found in both classical and quantum-mechanical molecular dynamics calculations.

While previous works have coupled liquid and solid subsystems together within orbital-free DFT [302, 137], these types of multi-scale approach do not possess a fully rigorous basis. The approximate partitioning of Kohn-Sham DFT

into subsystems relies upon fixed locations of the nuclei in all subsystems, resulting in a time-independent nuclear potential acting upon the electrons. Because the nuclei in a liquid are not fixed, additional statistical averaging over their positions must be performed and the theorems underlying embedding approaches are no longer relevant. The framework of JDFT, by contrast, provides a rigorous theorem in the case where the nuclei of the environment are not static but instead form a statistical average continuum.

Molecular dynamics simulations require sampling over all possible configurations of liquid to obtain thermodynamic averages, then costly thermodynamic integration[148] if free energies are desired. Integral equation theories for the liquid environment also suffer from pathologies associated with computation of free energies [242, 143]. In contrast, JDFT calculations obtain free energies by construction, from straightforward variational minimization of the in principle exact free-energy functional with respect to liquid and solute degrees of freedom. In addition, thermodynamic averages, such as chemical potentials and densities, may be obtained directly from derivatives of free energy functional at the minimum free energy. JDFT also provides the structure of liquid and other thermodynamic quantities, averaged over the experimentally relevant length and time scales. Section 3.8.4, for example, describes in detail how thermodynamic averages computed from the JDFT free energy functional are ideal for comparison to experimental quantities such as potentials of zero charge.[163] Finally, free energies are precisely the relevant quantities in computing free energy barriers within transition-state theory, opening up many new avenues of future study for JDFT.

Of course, there are also some limitations on the classes of systems currently

suitable for study within JDFT. Any electrons participating in charge-transfer reactions or covalent bonds must be treated within the quantum-mechanical portion of the calculation. When performing surface studies, some knowledge of the surface coverage and orientation of strongly bonded adsorbates is therefore required, though weakly bonded or hydrogen bonded adsorbates may be captured with sufficient accuracy by the classical liquid functional. In the case of strongly bonded adsorbates, the real-space liquid atomic site densities naturally provide preliminary information for the location and bonding configuration of fully quantum-mechanical explicit solvent molecules. JDFT may also fail to capture the dynamical limit, where zero-point motion of the solute is significant and the Born-Oppenheimer approximation no longer applies. When vibrational modes of the solute and solvent are strongly coupled to each other, *ab initio* molecular dynamics is required to capture the vibrational frequencies, although the potential of mean force remains well described by JDFT. Finally, the treatment of charged solute systems within full JDFT still requires an unphysical neutralizing background charge to prevent divergence of the electrostatic energy within a periodic unit cell, unless provision is made for ionic species within the classical DFT describing the solvent (as in Chapter 4).

The above limitations suggest some promising future areas for development opportunities of JDFT. An ideal treatment of charged solute systems, such as the electrode-electrolyte interface in electrochemistry, would require including charged ionic species within the solvent as mentioned above. Such electrolyte-liquid functionals would require an accurate and efficient multi-component classical DFT for the solvent which could capture both the solvent-ion correlation functions and the properties of the bulk liquid. Once we develop an appropriate classical DFT for electrolyte liquids, we would then repeat for ionic

solutes the solvation energy benchmarking already performed for neutral solute molecules. Finally, extending JDFT into the dynamical limit offers the tantalizing possibility of Joint AIMD calculations, where the solute system is treated within AIMD, while the solvent continues to be captured by the classical DFT.

The aforementioned limitations notwithstanding, the accurate and efficient JDFT coupling functional developed in this work offers a promising new approach to a wide array of scientific problems. In Surface Science, the geometry and composition of a solvated surface can differ significantly from the high-vacuum surface structures studied in traditional DFT calculations. JDFT calculations of these systems can determine the relative surface energies of different structures, and thus offer insight into surface composition and structure in solution, which is difficult to probe experimentally. In Biology, certain chemical processes occurring at the active sites of proteins depend critically on the presence and nature of the aqueous environment. In the past, such systems have been studied classically, with force fields which may not capture the relevant quantum mechanics[71] or with continuum models for the liquid, which may not capture key aqueous structures such as salt bridges. JDFT provides an ideal tool for this class of problem, with its ability to treat the active site quantum mechanically while providing the detailed microscopic structure of the solvent without the need for thermodynamic sampling. These are just a few examples of the broad scientific impact achievable with the full realization of the JDFT framework presented in this work.

CHAPTER 3

AB INITIO ELECTROCHEMISTRY

3.1   Introduction

Ab initio calculations have shed light on many questions in physics, chemistry, and materials science, including chemical reactions in solution [27, 273] and at surfaces.[225, 96, 98] However, first principles calculations have offered less insight in the complex and multi-faceted field of electrochemistry, despite the potential scientific and technological impact of advances in this field. Because the fundamental microscopic mechanisms involved in oxidation and reduction at electrode surfaces are often unknown and are difficult to determine experimentally, [250] rich scientific opportunities are available for theoretical study. From a technological perspective, practicable first principles calculations could become a vital tool to direct the experimental search for better catalysts with significant potential societal impact: as just one example, economically viable replacement of gasoline powered engines with fuel cells in personal transport systems requires systems operating at a cost of \$35/kW, whereas the current cost is \$294/kW, [12] due mostly to the expense of platinum-based catalyst materials.

The primary challenge which distinguishes theoretical study of electrochemical systems is that including the liquid electrolyte, which critically influences the functioning of the electrochemical cell, requires detailed thermodynamic sampling of all possible internal molecular configurations of the fluid. Such critical influences include (a) screening of charged systems, (b) establishment of an absolute potential reference for oxidation and reduction potentials, and (c)

voltage-dependence of fundamental microscopic processes, including the nature of reaction pathways and transition states. While there have been attempts at the full *ab initio* molecular dynamics approach to this challenge,[244, 99, 27] such calculations are necessarily of the heroic type, require tremendous computational resources, and do not lend themselves to systematic studies of multiple reactions within a series of many candidate systems. Such studies require development of an alternate approach to first-principles study of electrochemistry.

3.1.1   Previous approaches

One response to the aforementioned challenges is to avoid the issue and lessen the computational cost either by forgoing electronic structure calculation entirely or by neglecting the thermodynamic sampling of the environment. Some studies have employed classical molecular dynamics with interatomic potentials; [304, 222] however, such semi-empirical techniques often perform poorly when describing chemical reactions involving electron-transfer, which are central to oxidation and reduction reactions.

The latter approach – single configuration *ab initio* calculations – neglects key phenomena associated with the presence of an electrolyte liquid in equilibrium. The most direct single configuration *ab initio* approach pursued to date is to study the relevant reactions on a surface in vacuum and to study trends and correlations with the behavior in electrochemical systems.[199, 198] Some of these studies are done in a constant charge or constant potential ensemble[173] to allow variation of the applied electrode potential. This approach, however, does not include critical physical effects of the electrolyte such as the dielec-

tric response of the liquid environment and the presence of high concentrations of ions in the supporting electrolyte. In response, an intermediate approach is to include a layer or few layers of explicit water molecules into the calculation.[275, 125, 138, 283]

Such an approach is problematic for a number of reasons. First, actual electrochemical systems can have rather long ionic screening lengths (30 Å for an ionic concentration of 0.01 M), which would require large amounts of explicit water. Second, simulation of the actual effects of dipolar and ionic screening in the fluid requires extensive sampling of phase space, corresponding to very long run times. Indeed, in some references, only one layer of frozen water without thermal or time sampling is included. [254] Moreover, as most reactions of interest occur at potentials away from the potential of zero charge, such calculations must include a net charge, which can be problematic in typical solid-state periodic supercell calculations. One may compensate for this charge with a uniform charged background extending throughout the unit cell, both the liquid and the solid regions,[125] but this distribution does not reflect the electrochemical reality. Other methods include an explicit reference electrode with a corresponding negative surface charge to keep the unit cell neutral,[173] but this requires a somewhat arbitrary choice of where to place the compensating electrode and may not lead to realistic potential profiles. More recently, modeling the electrolyte by a layer of explicit hydrogen atoms was shown to provide a source of electrons for charged surface calculations while keeping the unit cell neutral.[255] Again, however, this approach requires either judicious choice of the locations of the corresponding protons which make up the corresponding reference electrode or computationally intensive thermodynamic sampling.

Another broad approach constructs an approximate *a posteriori* continuum model[76] for both the dielectric response of the water molecules and the Debye screening effects of the ions and performs *ab initio* calculations where the electrostatic potential is determined by solving Poisson-Boltzmann-like equations.[203, 132, 56] Explicit inclusion of a few layers of explicit water molecules and ionic species within the *ab initio* calculations can further enhance the reliability of this approach without dramatic additional computational cost. While including explicitly the most recognized physical effects of the electrolyte, such Poisson-Boltzmann-like approaches do not arise from an exact underlying theory. Thus, they may disregard physically relevant effects, such as the non-locality and non-linearity of the dielectric response of liquid water and the surface tension associated with formation of the liquid-solid interface. We note, for instance, that a typical electrochemical field strength would be a 0.1 V drop over a double layer width of 3 Angstroms, or 300 MV/m, a field at which the bulk dielectric constant of water is reduced by about one-third, strongly indicating that non-linear dielectric saturation effects are present in actual electrochemical systems, particularly near the liquid-solid interface, and ultimately should be captured naturally for an *ab initio* theory to be truly predictive and reliable.

3.1.2   Joint density-functional theory approach

This work begins by placing the aforementioned modified Poisson-Boltzmann approaches on a firm theoretical footing within an, *in principle*, exact density-functional theory formalism, and then describes the path to including all of the aforementioned effects in a fully rigorous *ab initio* density functional. The work then goes on to elucidate the fundamental physics underlying electrochemistry

and provide techniques for computation of fundamental electrochemical quantities from a formal perspective. The work then shifts focus and introduces an extremely simplified functional for initial exploration of the potential of our overall approach for practical calculations. The equations which result at this high level of simplification resemble those introduced by others[132, 56] from an *a posteriori* perspective, thus putting those works on a firmer theoretical footing and showing them in context as approximate versions of a rigorous underlying approach. We then work within this simplified framework to explore – in more depth than previously in the literature – fundamental physical effects in electrochemistry, including the microscopic behavior of the electrostatic potential near an electrode surface, the structure of the electrochemical double layer, differential capacitances, and potentials of zero charge across a series of metals. The encouraging results which we obtain even with this highly simplified functional indicate that the overall framework is sound for the exploration of physical electrochemical phenomena and strongly suggests that the more accurate functionals under present development [171] will yield accurate, fully *ab initio* results.

Section 3.2 begins by laying out our theoretical framework, Section 3.3 describes connections between experimental electrochemical observables and microscopic *ab initio* computables. Section 3.4 introduces a simple approximate functional which offers a computationally efficient means of bridging connections to experimental electrochemistry. Sections 3.5 and 3.6 include technical information regarding implementation of our functional within a pseudopotential framework. Section 3.7 provides specific details about electronic structure calculations of transition metal surfaces. Finally, Section 3.8 presents electrochemical results for those metallic surfaces obtained with our simplified functional and

Section 3.9 concludes the paper.

3.2   Theoretical Framework

As described in the Introduction, much of the challenge in performing realistic
ab initio electrochemistry calculations comes not only from the need to include
explicitly the atoms composing the environment but also from the need to per-
form thermodynamic averaging over the locations of those atoms. Recently,
however, it was proved rigorously that one can compute exact free-energies
by including the environment in a joint density-functional theory framework.
[217, 218] Specifically, this previous work shows that the free energy A of an
explicit quantum mechanical system with its nuclei at fixed locations while in
thermodynamic equilibrium with a liquid environment (including full quantum
mechanical treatment of the environment electrons and nuclei), can be obtained
by the following variational principle, [218]

$$A = \min_{n(r),\{N_\alpha(r)\}} \{G[n(r), \{N_\alpha(r)\}, V(r)]$$
$$- \int d^3 r V(r) n(r)\} \tag{3.1}$$

where $G[n(r), \{N_\alpha(r)\}, V(r)]$ is a universal functional of the electron density of the
explicit system $n(r)$, the densities of the nuclei of the various atomic species
in the environment $\{N_\alpha(r)\}$, and the electrostatic potential from the nuclei of
the explicit system $V(r)$. The functional $G[n(r), \{N_\alpha(r)\}, V(r)]$ is universal in the
sense that it depends only on the nature of the environment and that its de-
pendence on the explicit system is only through the electrostatic potential of
the nuclei included in $V(r)$ and the electron density of the explicit system $n(r)$.
With this functional dependence established, one can then separate the func-

tional into large, known portions and a smaller coupling term ultimately to be approximated,[218]

$$G[n(r), \{N_\alpha(r)\}, V(r)] \equiv A_{KS}[n(r)] + \Omega_{lq}[\{N_\alpha(r)\}]$$

$$+ \Delta A[n(r), \{N_\alpha(r)\}, V(r)] \tag{3.2}$$

where $A_{KS}[n(r)]$ and $\Omega_{lq}[\{N_\alpha(r)\}]$ are, respectively, the standard universal Kohn-Sham electron-density functional of the explicit solute system in isolation (including its nuclei and their interaction with its electrons) and the "classical" density-functional for the liquid solvent environment in isolation. The remainder, $\Delta A[n(r), \{N_\alpha(r)\}, V(r)]$ is then the coupling term between the solute and solvent.

For $A_{KS}[n(r)]$, one can employ any of the popular approximations to electronic density functional theory such as the local-density approximation (LDA), or more sophisticated functionals such as the generalized-gradient approximation (GGA). [215] On the other hand, functionals $\Omega_{lq}[\{N_\alpha(r)\}]$ for liquid solvents such as water are generally less-well developed, though the field has progressed significantly over the past few years. For example, one recent, numerically efficient functional for liquid water reproduces many of the important factors determining the interaction between the liquid and a solute, including the linear *and nonlinear* non-local dielectric response, the experimental site-site correlation functions, the surface tension, the bulk modulus of the liquid and the variation of this modulus with pressure, the density of the liquid and the vapor phase, and liquid-vapor coexistence [171]. A framework employing such a functional would be more reliable than the modified Poisson-Boltzmann approaches available to date, which do not incorporate any of these effects except for the linear local dielectric response appropriate to macroscopic fields. Inclusion of the den-

sities of any ions in the electrolyte environment among the $\{N_\alpha(r)\}$ is a natural way to include their effects into $\Omega_{lq}[\{N_\alpha(r)\}]$ and provide ionic screening into the overall framework.

Finally, developing approximate forms for the coupling $\Delta A[n(r), \{N_\alpha(r)\}, V(r)]$ in Equation 3.2 remains an open area of research. In an early attempt, Petrosyan and co-workers[218] employed a simplified $\Omega_{lq}[\{N_\alpha(r)\}]$ using a single density field $N(r)$ to describe the fluid. In that preliminary work, because such an $N(r)$ gives no explicit sense of the orientation of the liquid molecules, the tendency of these molecules to orient and screen long-range electric fields was included *a posteriori* into a simplified linear (but nonlocal) response function. In a more complete framework with explicit distributions for the oxygen and hydrogen sites among the $\{N_\alpha(r)\}$ the full non-local and non-linear dielectric response can be handled completely *a priori*.[171] Beyond long-range screening effects, the coupling $\Delta A[n(r), \{N_\alpha(r)\}, V(r)]$ must also include effects from direct contact between the solvent molecules and the solute electrons. Because the overlap between the molecular and electron densities is small, the lowest-order coupling, very similar to the "molecular" pseudopotentials of the type introduced by Kim *et al.*,[144] would be a reasonable starting point. Using such a pseudopotential approach (with only the densities of the oxygen atoms of the water molecules), Petrosyan and coworkers [218] obtained good agreement (2 kcal/mole) with experimental solvation energies, without any fitting of parameters to solvation data. Combining a coupling functional ΔA similar to that of Petrosyan and coworkers with more explicit functionals $\Omega_{lq}[\{N_\alpha(r)\}]$ for the liquid[171] and standard electron density functionals $A_{KS}[n(r)]$ for the electrons, is thus a quite promising pathway to highly accurate *ab initio* description of systems in equilibrium with an electrolyte environment.

3.3 Connections to Electrochemistry

Turning now to the topic of electrochemistry, we present a general theoretical framework to relate the results of *ab initio* calculations to experimentally measurable quantities, beginning with a brief review of the electrochemical concepts.

3.3.1 Electrochemical potential

In the electrochemical literature, the *electrochemical potential* $\bar{\mu}$ of the electrons in a given electrode is defined as the energy required to move electrons from a reference reservoir to the working electrode. This potential is often conceptualized as a sum of two terms, $\bar{\mu} = \mu_{int} - F\Phi$, where μ_{int} is the purely chemical potential (due to concentration gradient and temperature,chemical bonding, etc.), Φ is the external, macroscopic electrostatic potential, and F is Faraday's constant. (Note that $F = N_A e$ has the numerical value of unity in atomic units, where chemical potentials are measured *per particle* rather than *per mole*.) In the physics literature, this definition for $\bar{\mu}$ (when measured *per particle*) corresponds precisely to the "chemical potential for electrons," which appears for instance in the Fermi occupancy function $f = [e^{(\epsilon - \bar{\mu})/k_B T} + 1]^{-1}$.

3.3.2 Electrode potential

In a simple, two-electrode electrochemical cell, the driving force for chemical reactions occurring at the electrode surface is a voltage applied between the

reference electrode and working electrode. In the electrochemical literature, this voltage is known as the *electrode potential* $\mathcal{E}$, defined as the electromotive force applied to a cell consisting of a working electrode and a reference electrode. In atomic units (where the charge of an electron is unity), the electrode potential is thus equivalent to the energy (per fundamental charge e) supplied to transfer charge (generally in the form of electrons) from the reference to the working electrode, assuming no dissipative losses. Under conditions where diffusion of molecules and reactions occurring in the solution are minimal, this energy is completely transferred to the electrons in the system, causing a corresponding change in the electrochemical potential of the electrons in the working electrode.

An idealized two-terminal electrochemical cell controls the chemical potential of a working electrode $\bar{\mu}^{(W)}$ through application of an electrode potential $\mathcal{E}$ (voltage) between it and a reference electrode of known chemical potential $\bar{\mu}^{(R)}$ (See Figure 3.1(a)). With the application of the electrode potential $\mathcal{E}$, the energy *cost* to the electrochemical cell, under reversible (lossless) conditions, to move a single electron from the reference electrode to the working electrode is $dU = -\bar{\mu}^{(R)} + \bar{\mu}^{(W)} + \mathcal{E}$. Here, the electrode potential appears with a positive sign, because to move a negative charge from the negative to positive terminal requires a net investment of energy, and thus *cost* to the electrochemical cell, against the source of the potential $\mathcal{E}$. Under equilibrium conditions, we must have $dU = 0$, so that $\mathcal{E} = \bar{\mu}^{(R)} - \bar{\mu}^{(W)}$.

As Section 3.4 shows, the electrostatic model which we employ for ionic screening in this work establishes a fixed reference such that the microscopic *electron* potential ϕ (the Coulomb potential energy of an electron at a given point) is zero deep in the liquid environment far from the electrode (See Figure 3.1(b))

– implying that the macroscopic *electrostatic* potential Φ (which differs in over-all sign from ϕ) there is also zero. A convenient working electrode thus corresponds to electrons solvated deep in the fluid, which will have electrochemical potential $\bar{\mu}^{(R)} = \mu_{int}^{(s)} - F\Phi = \mu_{int}^{(s)}$, where $\mu_{int}^{(s)}$ corresponds to the solvation energy of an electron in the liquid. Referring the scale of the electrochemical potential to such solvated electrons (so that $\mu_{int}^{(s)} \equiv 0$), we then have $\bar{\mu}^{(R)} = 0$, so that $\mathcal{E} = -\bar{\mu}^{(W)}$. In sum, the opposite of the electronic chemical potential in our *ab initio* calculations corresponds precisely to the electrode potential relative to solvated electrons. In practice, the choice of approximate density functionals $\Omega_{lq}[\{N_\alpha(r)\}]$ and $\Delta A[n(r), \{N_\alpha(r)\}, V(r)]$ sets the potential of a solvated electron; each model fluid corresponds to a different reference electrode of solvated electrons. Section 3.8 demonstrates the establishment of the electrochemical potential of such a model reference electrode relative to the standard hydrogen electrode (SHE).

3.3.3 Potential of zero charge (PZC)

and differential capacitance.

For any given working electrode, a specific number of electrons, and thus electronic chemical potential $\bar{\mu}$, is required to keep the system electrically neutral. The corresponding electrode potential ($\mathcal{E} = -\bar{\mu}$) is known as the potential of zero charge. Adsorbed ions from the electrolyte or other contaminants on the electrode surface create uncertainty in the experimental determination of the potential of zero charge. One advantage to *ab initio* calculation is the ability to separate the contribution due to adsorbed species from the contribution of the electrochemical double layer, the latter being defined as the potential of zero free
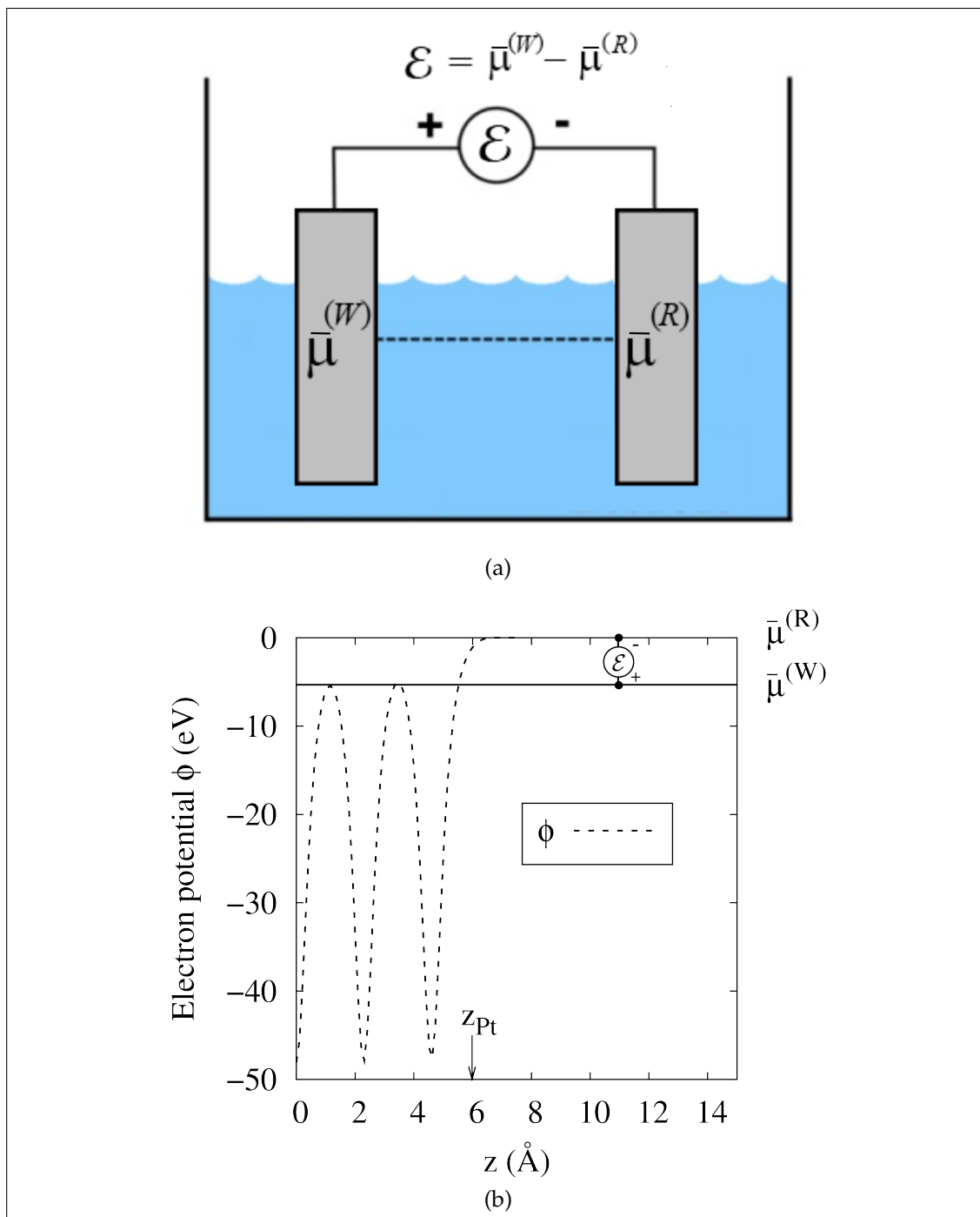
Figure 3.1: (a) Schematic of an electrochemical cell. The working electrode is explicitly modeled while the reference electrode is fixed at zero. (b) Relationship between the microscopic electron potential $\langle\phi(z)\rangle$ (averaged over the directions parallel to the surface), electrochemical potential, and applied potential for a Pt (111) surface. The large variations in potential to the left of z_{Pt} correspond to the electrons and ionic cores comprising the metal while the decay into the fluid region is visible to the right of z_{Pt}.

charge (PZFC). Experimentally, only the potential of zero total charge (PZTC), which includes the effects of surface coverage, may be measured directly, and the potential of zero free charge can only be inferred.[54] *Ab initio* approaches such as ours allow for the possibility of controlled addition of adsorbed species and direct study of these issues.

At other values of the electrode potential $\mathcal{E}$, the system develops a charge per unit surface area $\sigma \equiv Q/A$. From the relationship between these two quantities $\sigma(\mathcal{E})$, one can then determine the differential capacitance per unit area $C \equiv \frac{d\sigma}{d\mathcal{E}}$. The total differential capacitance of a metal is determined by both the density of states of the metal surface C_{DOS}, also known as the quantum capacitance,[175] and the capacitance associated with the fluid C_{fl}. These capacitances act in series, so that full differential capacitance is given by

$$C^{-1} = C_{\mathrm{fl}}^{-1} + C_{\mathrm{DOS}}^{-1}. \tag{3.3}$$

In typical systems, $C_{\mathrm{DOS}} \sim 100 - 1000 \mu F/cm^2$ is larger than the fluid capacitance (typically $C_{\mathrm{fl}} \sim 15 - 100 \mu F/cm^2$), so when the two are placed in series, the fluid capacitance dominates.

The fluid capacitance may be further decomposed into two capacitors acting in series,

$$C_{\mathrm{fl}}^{-1} = C_{\Delta}^{-1} + C_{\kappa}^{-1}, \tag{3.4}$$

as in the Gouy-Chapman-Stern model for the electrochemical double layer.[101, 46, 261] The surface charge on the electrode and the first layer of oppositely charged ions behave like a parallel plate capacitor with distance Δ between the plates. Δ indicates the distance from the electrode surface to the first layer of ions – called the outer Helmholtz layer for non-adsorbing electrolytes. The

capacitance per unit area for this simple model is $C_\Delta = \frac{\epsilon_0}{\Delta}$, analogous to the Helmholtz capacitance. For a gap size $\Delta \sim 0.5\text{Å}$, this model leads to a "gap" capacitance of about 20 $\mu F/cm^2$. Additional capacitance arises from the diffuse ions in the liquid. where the model for this capacitance $C_\kappa = \epsilon_b \epsilon_0 \kappa \cosh(\frac{e\phi(\Delta)}{2k_B T})$ is also well-known from the electrochemistry literature.[15] In the limit where most of the voltage drop is found in the outer Helmholtz layer ($\phi(\Delta) \sim k_B T$), this expression reduces to a constant value which depends only on the concentration of ions in the electrolyte and the bulk dielectric constant of the fluid ϵ_b: $C_\kappa = \frac{\epsilon_b \epsilon_0}{\kappa^{-1}}$. For water with a 1.0 M ionic concentration, the "ion" capacitance is $C_\kappa = 240$ $\mu F/cm^2$, an order of magnitude larger than the "gap" capacitance. At this high ionic concentration, the "gap" (Helmholtz) capacitance dominates not only the fluid capacitance, but also the total capacitance. For lower concentrations of ions, the magnitude of the "ion" capacitance becomes more comparable to the "gap" capacitance and voltage-dependent nonlinear effects in the fluid could become important.

3.3.4 Cyclic voltammetry

A powerful technique for electrochemical analysis is the cyclic voltammogram, in which current is measured as a function of voltage swept cyclically at a constant rate. Such data yield detailed information about electron transfer in complicated electrode reactions, with sharp peaks corresponding to oxidation or reduction potentials for chemical reactions taking place at the electrode surface. Because current is a time-varying quantity and density-functional theory does not include information about time dependence and reaction rates, careful reasoning must be employed to compare *ab initio* calculations to experimen-

tal current-potential curves. Previous work has correlated surface coverage of adsorbed hydrogen with current in order to predict cyclic voltammograms for hydrogen evolution on platinum electrodes.[138] This simple model for a cyclic voltammogram is intrinsically limited at a full monolayer of hydrogen adsorption, rather than by the more realistic presence of mass transport and diffusion effects, but nonetheless provides useful comparisons to experimental data.

Using a similar approach, our framework gives the predicted current density J directly through the chain rule as

$$J = \frac{d\sigma}{dt} = \frac{d\mathcal{E}}{dt}\frac{d\sigma}{d\mathcal{E}} \equiv KC(\mathcal{E}),$$

where $K = \frac{d\mathcal{E}}{dt}$ is the voltage sweep rate, and $C(\mathcal{E})$ is the differential capacitance per unit area at electrode potential $\mathcal{E}$, as defined above. For the bare metal surfaces with no adsorbates studied in Section 3.8 of this work, only the double layer region structure is visible, but the technique may be generalized to study chemical reactions at the electrode surface. The current density curve is simply proportional to the differential capacitance per unit area C as long as the state of the system varies adiabatically and the voltage sweep rate is significantly slower than the reaction rate. In the adiabatic limit, features in the charge-potential curves calculated for reaction intermediates and transition states can be compared directly with peaks in cyclic voltammograms to predict oxidation and reduction potentials from first principles.

3.4 Implicit Solvent Models

For computational expediency and to explore the performance of the overall framework for quantities of electrochemical interest, we now introduce a highly

approximate functional. Despite its simplicity, we find that the model below leads to very promising results for a number of physical quantities of direct interest in electrochemical systems. The first step in this approximation is to minimize with respect to the liquid nuclear density fields in the fully rigorous functional [217] so that Equation 3.1 becomes

$$\tilde{A} = \min_{n(r)}(A_{KS}[n(r), \{Z_I, R_I\}]$$
$$+ \Delta\tilde{A}[n(r), \{Z_I, R_I\}]), \tag{3.5}$$

with the effects of the liquid environment all appearing in the new term

$$\Delta\tilde{A}[n(r), \{Z_I, R_I\}] \equiv \min_{N_\alpha(r)}(\Omega_{lq}[N_\alpha(r)]$$
$$+ \Delta A[n(r), N_\alpha(r), \{Z_I, R_I\}]), \tag{3.6}$$

where Z_I and R_I are the charges and positions of the surface nuclei (and those of any explicitly included adsorbed species). This minimization process leaves a functional in terms of *only* the properties of the explicit system and incorporates all of the solvent effects implicitly. Up to this point, this theory is in principle exact, although the exact form of $\Delta\tilde{A}[n(r), \{Z_I, R_I\}]$ is unknown. For practical calculations this functional must be approximated in a way which captures the underlying physics with sufficient accuracy.

3.4.1 Approximate functional

In this initial work, we assume that the important interactions between the solvent environment and the explicit solute electronic system are all electrostatic in nature. Our rationale for this choice is the fact that most electrochemical processes are driven by (a) the surface charge on the electrode and the screening

due to the dielectric response of the liquid solvent and (b) the rearrangement of ions in the supporting electrolyte. To incorporate these effects, we calculate the *electron* potential $\phi(r)$ (the Coulomb potential energy of an electron at a given point, which equals $-e$ times the *electrostatic* potential) due to the electronic and atomic core charges of the electrode and couple this potential to a spatially local and linear description of the liquid electrolyte environment, yielding

$$
\begin{aligned}
\tilde{A}[n(r), \phi(r)] = {} & A_{TXC}[n(r)] \\
& + \int d^3r \{\phi(r)\,(n(r) - N(r, \{Z_I, R_I\})) \\
& - \frac{\epsilon(r)}{8\pi}|\nabla\phi(r)|^2 - \frac{\epsilon_b \kappa^2(r)}{8\pi}(\phi(r))^2\},
\end{aligned} \tag{3.7}
$$

where $A_{TXC}[n(r)]$ is the Kohn-Sham single-particle kinetic plus exchange correlation energy, $n(r)$ is the full electron density of the explicit system (including both core and valence electrons), and $N(r, \{R_I, Z_I\})$ is the nuclear particle density of the explicit solute system with nuclei of atomic number Z_I at positions R_I, ϵ_b is the bulk dielectric constant of the solvent, and $\epsilon(r)$ and $\kappa(r)$ are local values, respectively, of the dielectric constant and the inverse Debye screening length due to the presence of ions in the fluid. We emphasize that, despite the compact notation in Equation 3.7, in practice we employ standard Kohn-Sham orbitals to capture the kinetic energy and, as the appendices detail, we employ atomic pseudopotentials rather than direct nuclear potentials, so that $N(r, \{R_I, Z_I\})$ does not consist in practice of a set of Dirac δ-functions.

To determine local values of the quantities $\epsilon(r)$ and $\kappa(r)$ above, we relate them directly to the local average density of the solvent $N_{lq}(r)$ as

$$
\begin{aligned}
\epsilon(r) &\equiv 1 + \frac{N_{lq}(r)}{N_b}(\epsilon_b - 1) \\
\kappa^2(r) &\equiv \kappa_b^2 \frac{N_{lq}(r)}{N_b},
\end{aligned} \tag{3.8}
$$

where N_b and ϵ_b are, respectively, the bulk liquid number density (molecules per unit volume) and the bulk dielectric constant, and $\kappa_b^2 = \frac{e^2}{\epsilon_b k_B T} \sum_i N_i Z_i^2$ is the square of the inverse Debye screening length in the bulk fluid, where Z_i and $N_i = c_i N_A$ are the valences and number densities of the various ionic species. Finally, our model for the local liquid density depends on the full solute electron density $n(r)$ at each point through the relation

$$N_{lq}(n) \equiv \frac{N_b}{2} \text{erfc} \left(\frac{\ln (n/n_0)}{\sqrt{2}\gamma} \right), \tag{3.9}$$

a form which varies smoothly (with transition width γ) from the bulk liquid density N_b in the bulk solvent where the electron density from the explicit system is less than a transition value n_0 to zero inside the cavity region associated with the solute, defined as those points where $n(r) > n_0$. This form for $N_{lq}(n)$ reproduces solvation energies of small molecules in water without ionic screening to within 2 kcal/mol,[217] when the parameters in Equation 3.9 have values $\gamma = 0.6$ and $n_0 = 4.73 \times 10^{-3}$ Å^{-3}.

The stationary point of the functional in Equation 3.7 determines the physical state of the system and is actually a saddle point which is a minimum with respect to changes in $n(r)$ (or, equivalently, the Kohn-Sham orbitals) and a maximum with respect to changes in $\phi(r)$. Setting to zero the variation of Equation 3.7 with respect to the single-particle orbitals generates the usual Kohn-Sham, Schrödinger-like, single-particle equations with $\phi(r)$ replacing the Hartree and nuclear potentials and results in the modified Poisson-Boltzmann equation,

$$\nabla \cdot (\epsilon(r)\nabla\phi(r)) - \epsilon_b \kappa^2(r)\phi(r)$$
$$= -4\pi \left(n(r) - N(r, \{R_I, Z_I\}) \right). \tag{3.10}$$

Self-consistent solution of this modified Poisson-Boltzmann equation for $\phi(r)$

(a)

(b)
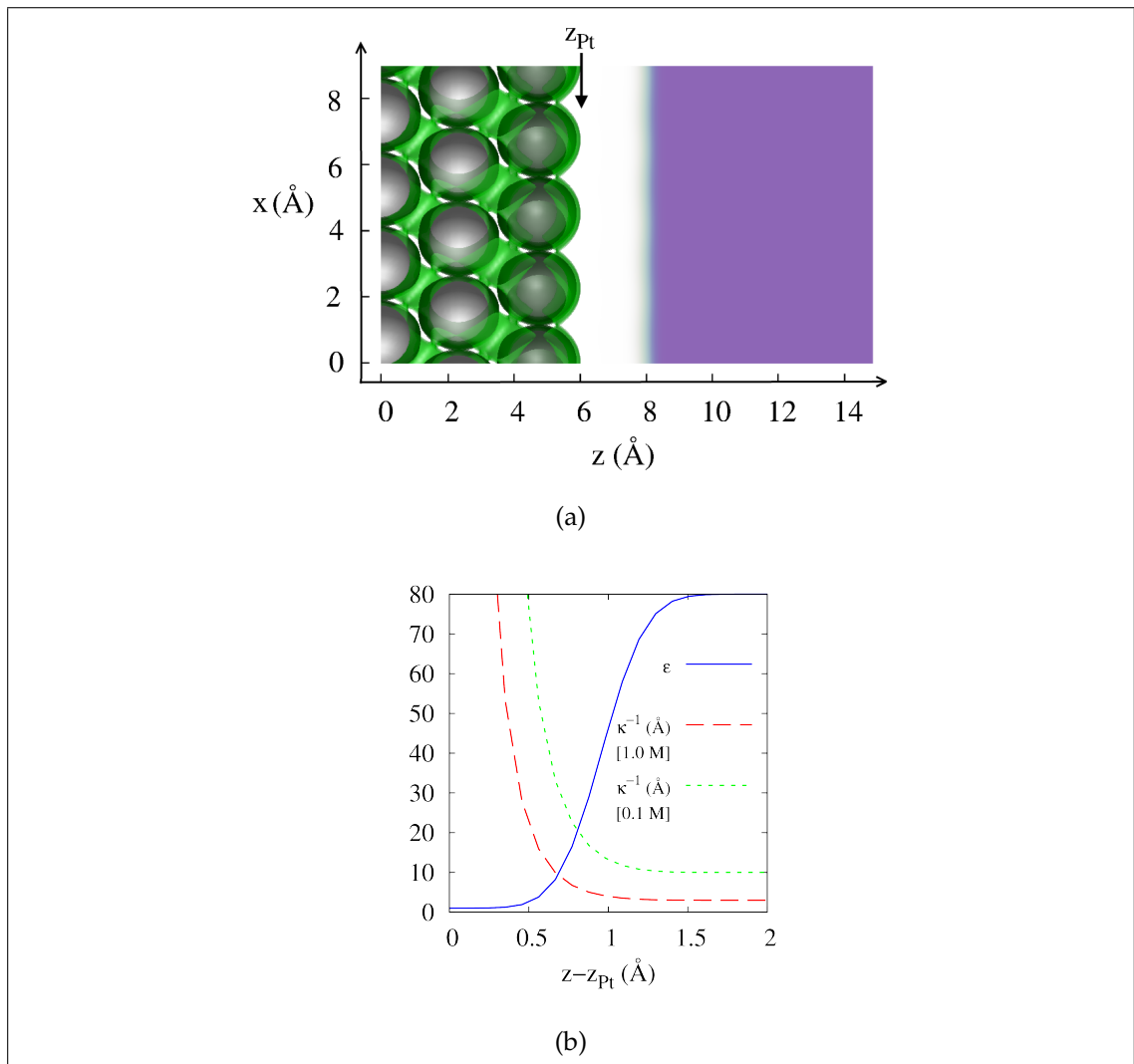
Figure 3.2: Microscopic and model quantities for Pt(111) surface in equilibrium with electrolyte: (a) Pt atoms (white), electron density $n(r)$ (green), and fluid density $N_{lq}(r)$ (blue) in a slice passing from surface (left) into the fluid (right) with $z_{Pt} = 5.95$ Å indicating the end of the metal, (b) dielectric constant $\langle \epsilon(z) \rangle$ and screening length $\langle \kappa^{-1}(z) \rangle$ (averaged over the planes parallel to the surface) for ionic concentrations of 1.0 M and 0.1 M along a line passing from surface into the fluid. Position $z - z_{Pt}$ measures distance from the end of the metal slab. (See Sections 3.7 and 3.8.)

along with solution of the corresponding traditional Kohn-Sham equations defines the final equilibrium state of the system.

Figure 3.2 illustrates the various concepts in this model using actual results from a calculation of the Pt(111) surface, described in Sections 3.7 and 3.8. Fig-

100

ure 3.2(a) shows the electron $n(r)$ and liquid $N_{lq}(r)$ densities in a slice through the system which passes through the metal (left, $z < z_{Pt}$) and the fluid (right, $z > z_{Pt}$). We define the end of the metal surface z_{metal} by the covalent radius of the last row of metal atoms ($z_{Pt} = 5.95$ Å). The ionic cores and the itinerant valence electrons in the metal are visible, as well as the gap between the surface and the bulk of the fluid. As shown in Figure 3.2(b), the local functions for the dielectric constant $\epsilon(r)$ and the *inverse* Debye screening length $\kappa(r)$ respect the correct physical limiting values: ϵ_b and κ_b in the bulk solvent and $\epsilon = 1$ and $\kappa = 0$ within the surface. The rapid increase in dielectric constant for 0 Å $< z - z_{Pt} < 1$ Å corresponds to the appearance of fluid on the right side and results in the localization of significant charge from the fluid at this location. The inverse screening length κ depends on the concentration of ions in the electrolyte through the bulk liquid value κ_b. Figure 3.2(b) shows screening length as a function of distance from the metal surface for both 0.1 and 1.0 molar bulk ionic concentrations. The large screening lengths at positions less than z_{Pt} ensure proper vacuum-like behavior within the metal surface, where all electrons are explicit and thus no implicit screening should appear.

3.4.2 Asymptotic behavior of electrostatic potential

Unlike the standard Poisson equation, which has no unique solution for periodic systems because the zero of potential is an arbitrary constant, the modified Poisson-Boltzmann equation in Equation 3.10 has a unique solution in periodic systems. To establish this, we integrate the differential equation over the unit cell. The first term, which is the integral of an exact derivative, vanishes. The

remaining terms then give the condition,

$$\int \kappa^2(r)\phi(r)dV = \frac{4\pi}{\epsilon_b}\left(Q_n - Q_N\right),$$ (3.11)

where Q_n and Q_N are the total number of electronic and nuclear charges in the cell, respectively. Any two $\phi(r)$ which differ by a constant C both can be valid solutions only if $C\int \kappa^2(r)\,dV = 0$, so that we must have $C = 0$ as long as $\kappa(r)$ is non-zero at any location in the unit cell. Thus, any amount of screening at any location in space in the calculation eliminates the usual indeterminacy of $\phi(r)$ by an additive constant, thereby establishing an absolute reference for the zero of the potential.

To establish the nature of this reference potential, we first note that deep in the fluid, far from the electronic system, the electron density approaches $n(r) = 0$ and the dielectric constant and screening lengths attain their constant bulk values $\epsilon(r) \to \epsilon_b$ and $\kappa(r) \to \kappa_b$. Under these conditions, the Green's function impulse response of Equation 3.10 to a unit point charge is

$$\phi(r) = \frac{\exp\left(-\kappa_b\, r\right)}{\epsilon_b\, r},$$ (3.12)

a Coulomb potential screened by the dielectric response of the solvent and exponentially screened by the presence of ions. Next, we rearrange Equation 3.10 so that the left-hand side has the same impulse response as the bulk of the fluid but with a modified source term,

$$\epsilon_b\nabla^2\phi(r) - \epsilon_b\kappa_b^2\phi(r) =$$
$$-4\pi\left(\rho_{\text{sol}}(r) + \rho_{\text{ext}}(r)\right)$$ (3.13)

102

where we have defined

$$\rho_{\text{sol}}(r) \equiv n(r) - N(r)$$

$$\rho_{\text{ext}}(r) \equiv -\frac{1}{4\pi}((\epsilon_b - \epsilon(r)) \nabla^2 \phi(r)$$

$$- (\nabla\epsilon(r)) \cdot (\nabla\phi(r)) + \epsilon_b \left(\kappa^2(r) - \kappa_b^2\right) \phi(r)). \tag{3.14}$$

The key step now is to note that all source terms clearly vanish in the bulk of the fluid where $\rho_{\text{sol}}(r) \to 0$, $\epsilon(r) \to \epsilon_b$ = constant, and $\kappa(r) \to \kappa_b$. From the exponential decay of the Green's function Equation 3.12 and the vanishing of $\rho_{\text{sol}} + \rho_{\text{ext}}$ in the bulk region of the fluid, we immediately conclude that $\phi(r) \to 0$ deep in the fluid region, thereby establishing that the absolute reference of zero potential corresponds to the energy of an electron solvated deep in the fluid region.

3.4.3 Future Improvements

While offering a computationally efficient and simple way to study electrochemistry, the approximate functional in Equation 3.7 is highly simplified and possesses several limitations which the more rigorous approach of Section 3.2 overcomes by coupling of an explicit solvent model for $\Omega_{lq}[N_\alpha(r)]$[171] to the electronic system through an approach similar to the molecular pseudopotentials proposed by Kim *et al.*[144] Such limitations include the fact that because we employ a linearized Poisson-Boltzmann equation, we do not include the nonlinear dielectric response of the fluid (which other approaches in the literature to date also ignore[132, 56]) or nonlinear saturation effects in the ionic concentrations, both of which become important for potentials greater than a few hundred mV. Despite these limitations, we remain encouraged by the promis-

103

ing results we obtain below for this simple functional and optimistic about the improvements that working within a more rigorous framework would provide.

3.5 Implementation Within Standard Electronic Structure Software

Here we consider the issues which arise when implementing the above framework within a pre-existing electronic-structure code. We will focus on software operating within the pseudopotential framework as this technique is commonly used for surface calculations.

Such pseudopotential calculations, for computational efficiency, include the nuclei and core electrons together as a unit and describe their combined effects on the valence electron system through effective, "pseudo"-potentials. Two subtleties now arise. First, because the pseudopotentials describe the long-range electrostatic interaction between the ionic cores and the electrons, the screening of the long-range Coulomb part of the pseudopotentials by the electrolyte environment through Equation 3.10 must be handled properly. Second, because the calculated (valence) electron density $n(r)$ in the atomic core regions tends to be relatively low in pseudopotential calculations, our definition of the liquid density $N_{lq}(n)$ as a local function of the local electron density $n(r)$ through Equation 3.9 can lead to the unphysical presence of liquid within the atomic cores if precautions are not taken.

As a matter of notation specific to this appendix, we separate conceptually the valence electron density $n_v(r)$, calculated directly with the Kohn-Sham or-

bitals, from the missing contribution $n_c(r, \{R_I\})$ due to the core electrons, which clearly varies explicitly with the locations of the centers of the ions. By including both electron and ionic (now, actually, valence-electron and ionic core) source terms, the new energy functional in Equation 3.7 naturally provides electrolyte screening of all of the relevant fields. The functional in Equation 3.7 then becomes

$$
\begin{aligned}
A[n(r), \phi(r)] = {}& A_{TXC}[n_v(r)] \\
& + E_C[n_v(r), n_c(r, \{R_I\}), \phi(r)] \\
& + U_{ps}[n_v(r), \{Z_I, R_I\}],
\end{aligned} \tag{3.15}
$$

where $A_{TXC}[n_v(r)]$ is the Kohn-Sham single-particle kinetic plus exchange-correlation energy, and

$$
\begin{aligned}
E_C[n_v(r), & n_c(r, \{R_I\}), \phi(r)] = \\
& \int d^3 r \{ \phi(r) \left(n_v(r) - N(r, \{Z_I, R_I\}) \right) \\
& - \frac{\epsilon(n_v(r) + n_c(r, \{R_I\}))}{8\pi} |\nabla \phi(r)|^2 \\
& - \frac{\epsilon_b \kappa^2 (n_v(r) + n_c(r, \{R_I\}))}{8\pi} (\phi(r))^2 \}
\end{aligned} \tag{3.16}
$$

represents the previously described electrostatic contributions to the total energy functional (with $N(r, \{Z_I, R_I\}) \equiv \sum_I Z_I \delta^{(3)}(r - R_I)$ representing point charges with the *ionic valences Z_I*), and the term

$$
\begin{aligned}
U_{ps}[n_v(r), & Z_I, R_I] = \\
& \int \left(\sum_I \Delta V_{ps}^{(I)}(r - R_I) \right) n_v(r) \, d^3 r,
\end{aligned} \tag{3.17}
$$

with

$$
\Delta V_{ps}^{(I)}(r - R_I) \equiv V_{ps}^{(I)}(r - R_I) + Z_I G(r - R_I), \tag{3.18}
$$

represents the non-Coulombic components of the pseudopotential $V_{ps}^{(I)}(r)$, with $G(r) \equiv 1/|r|$ being the Coulombic Green's function associated with a unit point

charge in free space. Note that here and henceforth in this work Z_I refers to the charges of the ionic pseudopotential cores and not the nuclear atomic numbers. Finally, Section 3.6 details how, for practical numerical reasons, we work not with mathematical point charges but rather with narrow charge distributions which we can resolve numerically.

The derivative of the functional $A[n(r)]$ with respect to $n_v(r)$ at a point r (which gives the local effective Kohn-Sham potential used for the electronic wavefunction minimization) must also be adjusted to include the new dielectric response and ionic screening terms,

$$\frac{\partial}{\partial n_v(r)} A[n(r)] = \frac{\partial}{\partial n_v(r)} A_{TXC}[n_v(r)]$$
$$+ \sum_I \Delta V_{ps}^{(I)}(r - R_I)$$
$$+ \phi(r) - \frac{1}{8\pi} (\frac{\partial \epsilon}{\partial n} |\nabla \phi(r)|^2$$
$$+ \epsilon_b \frac{\partial \kappa^2}{\partial n} \phi^2(r)). \tag{3.19}$$

Finally, Hellman-Feynman calculation of the forces on the atoms requires care because of the dependence of both the ionic core density $N(r, \{Z_I, R_I\})$ and the model core electron density $n_c(r, \{R_I\})$ on the ionic positions R_I. The final result is

$$\nabla_{R_I} A = \nabla_{R_I} E_C + \nabla_{R_I} U_{ps}, \tag{3.20}$$

where

$$\nabla_{R_I} U_{ps} = \int \left(\nabla_{R_I} \Delta V^{(I)}_{ps}(r - R_I) \right) n_v(r) \, d^3 r$$

$$\nabla_{R_I} E_C =$$

$$- \frac{1}{8\pi} \int d^3 r \left(\frac{\partial \epsilon}{\partial n} |\nabla \phi|^2 + \epsilon_b \frac{\partial \kappa^2}{\partial n} (\phi(r))^2 \right)$$

$$\times \nabla_{R_I} n_c(r, \{R_I\})$$

$$- \int d^3 r \phi(r) Z_I \nabla_{R_I} \delta^{(3)}(r - R_I) \tag{3.21}$$

While some of these derivatives have simpler analytical forms than those described above, these forms render much simpler the numerical representation of the relevant quantities, particularly the Dirac-delta functions and pseudopotentials, as described in Section 3.6.

3.6 Numerical Details

The system-dependent modified Poisson-Boltzmann equation which appears in our calculations does not have a direct analytic solution in either Fourier or real space and, thus, requires a numerical solution such that we cannot employ analytic Dirac δ functions to represent the ion-core charges. Instead, in our numerical calculations, we employ "smoothed" ion-core charge densities,

$$N^{(\sigma)}(r, \{Z_I, R_I\}) = \sum_I Z_I \delta^{(\sigma)}(r - R_I) \tag{3.22}$$

where $\delta^{(\sigma)}$ is a normalized, isotropic three-dimensional Gaussian of width σ containing a single unit change. To the extent that the smoothed distributions do not overlap with each other or the fluid regions, the replacement of the point charges with these distributions will not affect the "Ewald" energy among the

charged atomic cores or the dielectric screening effects. In practice, we find good numerical solutions by employing a relatively narrow width determined by the spatial resolution of the calculation, so that σ corresponds to a distance of 1.40 points on the Fourier grid. (Specifically, this work employs a plane-wave energy cutoff of 30 H, so that $\sigma = 0.168$ Å.) This choice of parameters ensures that there is little overlap among the Gaussians and between the Gaussians and the fluid, so that that this replacement has negligible effect on the screened interaction among the atomic cores.

These smoothed distributions, however, do overlap with the valence electrons, an effect which we must compensate. We compensate this local effect *exactly* by replacing the point-charge response $G(r)$ in the modification of the pseudopotential in Equation 3.18 with the response corresponding to the smoothed densities,

$$G^{(\sigma)}(r) \equiv \frac{\mathrm{erf}\left(|r|/\sqrt{2\sigma^2}\right)}{|r|}.$$ (3.23)

We also represent the core-electron densities in Equation 3.8 that prevent fluid penetration into the atomic cores, and whose form is thus not critical, with Gaussian distributions

$$n_c(r, \{R_I\}) = C \sum_I \delta^{(r_C)}(r - R_I).$$ (3.24)

Alternately, for this density, one could use the core-electron density from the partial core correction from an appropriately designed pseudopotential. Because the role of n_c in our framework is simply to prevent penetration of fluid into the ionic cores, the precise values of the norm C and width r_C are not critical. We find that the choice $C = 0.3$ Å^{-3}, $r_c = 0.2$ Å works well for this purpose for all the species in our calculations.

Finally, with the above definitions in place, we have taken care to make all re-

placements $\delta^3(r) \rightarrow \delta^{(\sigma)}(r)$, $G(r) \rightarrow G^{(\sigma)}(r)$ and $n_c(r, \{R_I\}) = C \sum_I \delta^{(r_C)}(r - R_I)$ in the appropriate places in the expressions for the total free energy, in the functional derivatives appearing in the effective Kohn-Sham potential of Equation 3.19, and in the expressions for the Hellman-Feynman forces on the atoms in Equation 3.20. These substitutions complete the numerical specification of the functionals employed in our calculations.

We find that standard electronic structure methods work well with our functionals. The one equation whose solution requires new algorithms is the modified Poisson-Boltzmann equation, which, unlike the standard Poisson equation, does not have a direct analytic solution in Fourier space. To solve this equation, we have, however, found a simple to implement, yet highly efficient preconditioned conjugate gradient algorithm.

The portions of the functional which depend on the potential field $\phi(r)$ appear in E_C in Equation 3.16, which is a quadratic functional whose maximum corresponds to the solution of the modified Poisson-Boltzmann equation, Equation 3.10, and whose quadratic kernel is

$$Q = (\nabla \cdot \epsilon \nabla - \epsilon_b \kappa^2)/(4\pi). \tag{3.25}$$

We chose to solve this equation in Fourier space, where the diagonal elements of this kernel have a very simple approximate form, which leads to the diagonal preconditioner,

$$K(G) = (\bar{\epsilon} G^2 + \epsilon_b \bar{\kappa^2})^{-1}, \tag{3.26}$$

where $\bar{\epsilon} = \frac{1}{\Omega} \int \epsilon(r) d^3 r$ and $\bar{\kappa^2} = \frac{1}{\Omega} \int \kappa^2(r) d^3 r$ are the average values of these parameters over the unit cell. This diagonal preconditioner completely ignores the spatial variation of the dielectric constant. A more effective preconditioner which may be obtained by building in this inhomogeneity – is calculated by

first multiplying by $\sqrt{(K(G))}$ (the square root of the diagonal preconditioner) in Fourier space, transforming to real space and dividing by $\epsilon(r)$, then returning to Fourier space and again multiplying by $\sqrt{(K(G))}$. This inhomogeneous preconditioner requires more time to evaluate for a single iteration than the diagonal preconditioner, but reduces the total number of iterations required significantly.

3.7 Electronic Structure Methodology

All calculations undertaken in this work and presented in Section 3.8 were all performed within the DFT++ framework [122] as implemented in the open-source code JDFTx. [267] They employed the local-density or generalized-gradient [215] approximations using a plane-wave basis within periodic boundary conditions. The specific materials under study in this paper were platinum, silver, copper, and gold. The (111), (110), and (100) surfaces of each of these metals were computed within a supercell representation with a distance of 10 times the lattice constant of each metal (in all cases around 30 Å) between surface slabs of thickness of 5 atomic layers. For these initial calculations, we were very conservative in employing such large regions between slabs to absolutely eliminate electrostatic supercell image effects between slabs. We strongly suspect that smaller supercells can be used in the future. All calculations presented employ optimized[230] norm-conserving Kleinman-Bylander pseudopotentials[228] with single non-local projectors in the s, p, and d channels, a plane-wave cutoff energy of 30 H, and employ a $8 \times 8 \times 1$ k-point Monkhorst-Pack[190] grids to sample the Brillouin zone.

The JDFTx-calculated lattice constants of the bulk metals within both

exchange-correlation approximations when using $8 \times 8 \times 8$ k-point grids are shown in Table 3.1. Clearly, the LDA and GGA lattice constants both agree well with the experiment. Except where comparisons are specifically made with LDA results, all calculations in this work employ GGA for exchange and correlation.

Table 3.1: Cubic lattice constant (Å) in conventional face-centered cubic unit cell

Metal	LDA	GGA	Experiment[3]
Pt	3.93	3.94	3.92
Cu	3.55	3.67	3.61
Ag	4.07	4.13	4.09
Au	4.05	4.14	4.08

3.8 Results

To evaluate the promise of our approach, we begin by studying the fundamental behaviors of transition metal surfaces in equilibrium with an electrolyte environment as a function of applied potential. We find that even our initial highly simplified form of joint density-functional theory reproduces with surprising accuracy a wide range of fundamental physical phenomena related to electrochemistry. Such transition metal systems, especially platinum, are of electrochemical interest as potential catalysts for both the oxygen reduction reaction (ORR) and th hydrogen evolution reaction (HER). Molecular dynamics studies of the platinum system in solution, both at the classical [304] and *ab initio* [244, 236] levels, to date have not fully accounted for ionic screening in the electrolyte, which is essential to capturing the complex structure of the electrochemical double layer and the establishment of a consistent reference potential.

For the initial exploratory studies presented in this manuscript, we focus on pristine surfaces without adsorbates in order to establish clearly the relationship between theoretical and experimental quantities and to lay groundwork for future systematic comparison of potential catalyst materials. Unless otherwise specified, we carry out our calculations with screening lengths of 3 Å, corresponding to monovalent ionic concentrations of 1.0 M. We employ these high concentrations because most electrochemical cells include a supporting electrolyte with high ionic concentration chosen to provide strong screening while avoiding (to the extent possible) interaction with and adsorption on the electrode. Note that, because our present model includes only ionic concentrations and no other species-specific details about the ions in the electrolyte, our results correspond to neutral pH. Future work will readily explore pH and adsorption effects by including protons and other explicit ions in the electronic-structure portions of the calculation. One great advantage of the present theoretical approach is the ability to separate the role of the non-adsorbing ions in the supporting electrolyte from the role of the adsorbing ions that interact directly with the surface.

3.8.1 Treatment of charged surfaces

in periodic boundary conditions

The application of voltage essential to the *ab initio* study of electrochemistry requires precise treatment of charged surfaces not accessible to common electronic structure approaches due to singularities associated with the Coulomb interaction. In the case of a vacuum environment, the electrostatic potential $\phi(r)$ of

even a neutral electrode approaches a physically indeterminate constant which varies with the choice of supercell. As is well-known, this difficulty compounds radically when a net charge is placed on the surface, resulting in a formally infinite average electrostatic potential in a periodically repeated system. By default, most electronic structure packages designed for use with periodic systems treat this singularity by setting the $G = 0$ Fourier component of $\phi(r)$ to zero, equivalent to incorporating a uniform, neutralizing charge background throughout the region of the computation. This solution to the Coulomb infinity is not realistic in electrochemical applications where the actual compensating charge appears in the fluid and should not be present in the interior of the electrode.

Another option which has been employed in the electrochemical context[203] is to include an oppositely charged counter-electrode located away from the working electrode in the vacuum region of the calculation. However, including an explicit density-functional electrode is often computationally prohibitive as it requires doubling the number of electrons and atoms and requires a large supercell to prevent image interaction. Implicit inclusion of a counter-electrode through either coulomb truncation or an external charge distribution [203] requires an arbitrary choice of the distribution of external charges representing the counter-electrode, and such arbitrary choices may result in unphysical electrostatic potentials, even in the presence of a few explicit layers of neutral liquid molecules. One realistic choice is to employ Debye screening as in Equation 3.10. This approach ensures that the long-range decay of $\phi(r)$ into the fluid corresponds to the behavior of the actual physical system, that the fluid response contains precisely the correct amount of compensating charge, and that the potential approaches an absolute reference, even in a periodic system.

Another more explicit, and hence computationally expensive, option employed in the electrochemical literature is to add a few layers of explicit water molecules to the surface and then include explicit counter-ions (protons) located in the first water layer.[283] This approach models some of the most important effects of the actual physical distribution of counter-ions, which really should contain both localized and diffuse components, by considering only the first layer of localized ions.

Figure 3.3(a) contrasts the potential profiles resulting from the aforementioned approaches in actual calculations of a Pt(111) electrode surface. Figure 3.3(a) displays the microscopic local electron potential energy function $\langle \phi(z) \rangle$ for a surface at applied voltage $\mathcal{E} = -1.09V$ vs PZC which corresponds to a charge of $\sigma = -18\ \mu C/cm^2$. The screened electron potentials generated by solution of Equation 3.10 at two different ionic strengths ($c = 1.0$ M and $c = 0.1$ M) are compared to potential profiles for a similarly charged surface in vacuum, with the net charge in the system neutralized either by imposing a uniform background charge or by placing an oppositely charged counter electrode at one Debye screening length from the metal surface. The two charge-compensated vacuum calculations clearly do not correspond to the electrochemical behavior, with far wider potential variations than expected. Figure 3.3(b) shows a detailed view of the macroscopic *electrostatic* potential $\langle \Phi(z) \rangle$ for the same charged surface (obtained by subtracting the microscopic *electron* potential of the neutral surface and switching the sign to reflect electrochemical convention) for the JDFT calculated charged surface at two different ionic strengths. The charge-compensated vacuum calculations would be off the scale of this figure, while the macroscopic electrostatic potential for the JDFT calculations obtains the value of the applied potential within the electrode and then approaches a well-

established reference value of zero with the correct asymptotic behavior in the fluid region.

3.8.2   Electrochemical double layer structure

The Gouy-Chapman-Stern model, described in Section 3.3.3, offers a well-known prediction of the structure of the electrochemical double layer, to which the potentials from our model correspond precisely. The electrostatic potential profiles in the standard electrochemical picture include an initial, capacitor-like linear drop in $\langle \Phi(z) \rangle$ due to the outer Helmholtz layer (the Stern region), followed by a characteristic exponential decay to zero deep in the fluid (the diffuse Gouy-Chapman region). Our model naturally captures this behavior as a result of (a) the localization of the dielectric response and screening to the liquid region as described by $N_{lq}(r)$ through Equation 3.8 and (b) the separation between the fluid and regions of high explicit electron density $n(r)$ through the definition of $N_{lq}(r) \equiv N_{lq}(n(r))$ via Equation 3.9. Both the Stern and Gouy-Chapman regions are clearly evident in Figures 3.3(b,c). We find the dielectric constant transition region appearing in Figure 3.2(b), approximately the width of a water molecule, to be essential to the accurate reproduction of the double layer structure. The potentials for charged surfaces in Figures 3.3(b,c) first show a linear decay in the region $0 \text{ Å} < z - z_{Pt} < \Delta$, corresponding to the "gap" between the end of the surface electron distribution (z_{Pt}) and the beginning of the fluid region, precisely the behavior we should expect in the Stern region. For a Pt(111) surface at applied voltage -1.09 V vs. PZC, $\Delta = 0.6$ Å, but the width of this gap is voltage-dependent (as shown in Figure 3.4(b)) and also varies with metal and crystal face. After the gap region, for $\Delta < z - z_{Pt} < \Delta + \gamma$ (where $\gamma = 0.6$ as in Equa-
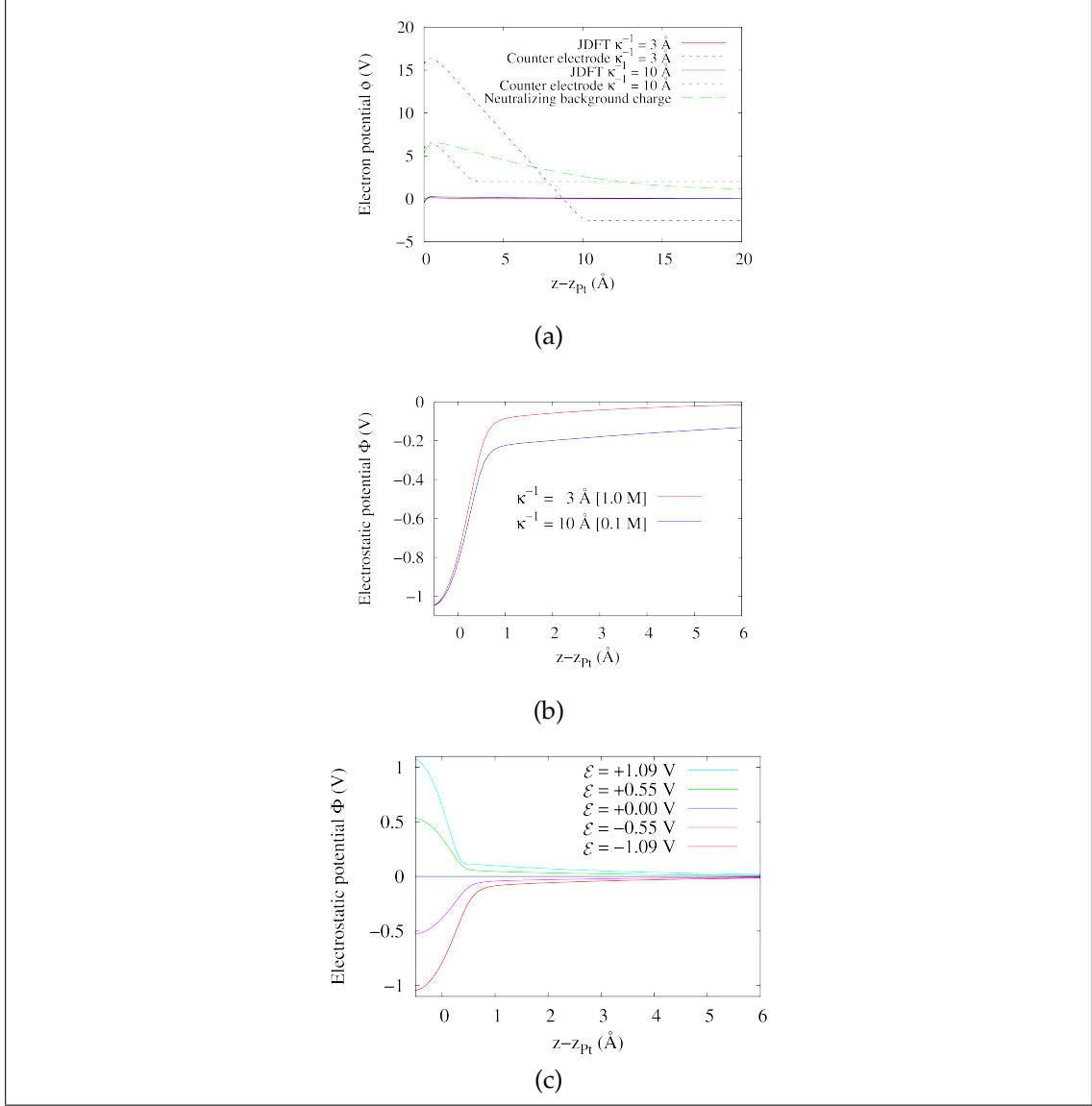
Figure 3.3: Microscopic electron potential energies $\langle\phi(z)\rangle$ and macroscopic electrostatic potentials $\langle\Phi(z)\rangle$ averaged in planes for the Pt (111) surface as a function of distance $z - z_{Pt}$ from the end of the metal surface: (a) $\langle\phi(z)\rangle$ for surface with applied voltage $\mathcal{E} = -1.09$ V vs. PZC in vacuum (green dashed) and in monovalent electrolytes of $c = 1.0$ M (red) and $c = 0.1$ M (blue) where the dotted lines represent calculations with an explicit counter-electrode and the solid lines are JDFT calculations (b) close-up view of $\langle\Phi(z)\rangle$ for JDFT calculations with $c = 1.0$ M (red) and $c = 0.1$ M (blue) and applied voltage $\mathcal{E} = -1.09$ V vs. PZC (almost indistinguishable in the previous plot) (c) Variation of $\langle\Phi(z)\rangle$ in JDFT monovalent electrolyte of $c = 1.0$ M with $\mathcal{E} = \{-1.09, -0.55, 0.0, 0.55, 1.09\}$ V vs. PZC.

116

tion 3.9), the dielectric constant in Figure 3.2(b) changes rapidly from about 10 to the bulk value $\epsilon_b \sim 80$, defining a transition region which ensures that no significant diffuse decay in the potential occurs until beyond the outer Helmholtz layer, thereby allowing proper formation of the diffuse Gouy-Chapman region for $z - z_{Pt} > \Delta + \gamma$. We emphasize that we have not added these phenomena into our calculations *a posteriori*, but that they occur naturally as a consequence of our microscopic, albeit approximate, *ab initio* approach.

3.8.3 Charging of surfaces with electrode potential

To explore the effects of electrode potential on the surface charge and electronic structure, Figure 3.4(a) shows the surface charge σ as a function of potential $\mathcal{E}$ for a series of transition metal surfaces for an electrolyte of monovalent ionic strength $c = 1.0$ M, without adsorption of ions to the surface. We find the average double layer capacitance of the Pt(111) surface – the slope of the corresponding $\sigma - \mathcal{E}$ curve in Figure 3.4(a) – to be $C=19\,\mu$F/cm^2, in excellent agreement with the experimental value of $20\,\mu$F/cm^2.[205] Indeed, we find that a significant fraction of our total capacitance is due to dielectric and screening effects in the fluid; this agreement again supports our model for the electrolyte. The remainder is associated with the "quantum capacitance" or density of states C_{DOS} of the surface slab in our supercell calculations.

Closer inspection of the charge versus potential data reveals that the slope is not quite constant as a function of voltage. Indeed, taking the numerical derivatives of the curves in Figure 3.4(a) yields values for the differential capacitance that exhibit an approximately linear dependence on voltage. This voltage-

dependence contrasts with studies performed using a different technique to produce voltage-independent constant values for the capacitance[236], which not only was limited to producing a constant value for the capacitance, but also required computationally demanding thermodynamic sampling to model the fluid.

To understand the origin of the above voltage-dependence of the capacitance, we employ the series model for differential capacitance in Equations 3.3 and 3.4, in which the total capacitance per unit area C is modeled as a series combination of the capacitance associated with the density of states of the metal, a Stern capacitance (C_Δ) across a gap of width Δ, and the (constant) Gouy-Chapman capacitance associated with the inverse screening length κ. We can then extract the "gap" capacitance as

$$\frac{\Delta}{\epsilon_0} \sim C_\Delta^{-1} \equiv C^{-1} - C_{\text{DOS}}^{-1} - \frac{\kappa^{-1}}{\epsilon_b \epsilon_0}. \tag{3.27}$$

To verify that the voltage-dependence of this contribution indeed correlates to changes in the gap associated with the Stern layer, we make an independent definition of the width of the gap as $\Delta \equiv z_c - z_{Metal}$, where z_c represents the location where the presence of our model fluid becomes significant and z_{Metal} represents the location of the surface of the metal. Specifically, we define z_c as the point where the planar average of the inverse dielectric constant has fallen by half from its value in the electrode (as in Figure 3.4(b)) since the polarization of the fluid becomes significant when $\langle \epsilon^{-1}(z_c) \rangle < 0.5$. We determine z_{Metal} from the covalent radii of the metal surface atoms, but note that the specific choice of z_{Metal} is unimportant in the analysis to follow.

Figure 3.4(c) correlates the inverse gap capacitance C_Δ^{-1} from the right hand side of Equation 3.27 with the values of Δ defined as in the previous paragraph.

There is a striking linear trend with a slope within about ten percent of ϵ_0^{-1}, validating that the primary contribution to the voltage-dependence of the differential capacitance within this model is from changes in the gap between the fluid surface and where the dielectric screening begins. The ultimate origin of this effect within the present approximation (in which the dielectric constant is determined by the electron density through Equation 3.8) can be traced to the increase in surface electrons with decreasing applied potential, which moves the location of the fluid transition further away from the metal surface. In fact, the experimentally determined capacitance of Pt(111) due to *only* the double layer[205] (after subtracting the effects of counter-ion adsorption) has a voltage-dependence quite similar to our prediction. Since the distance of closest approach of the fluid to the metal surface is determined by van der Waals interactions and the addition of more electrons could indeed strengthen the repulsion, the qualitative voltage-dependence of the "double-layer" capacitance even at this simple level of approximation may indeed be capturing some aspects of the underlying physics.

The double-layer capacitance notwithstanding, in physical systems the total capacitance is dominated by the effects of adsorption of counter-ions, and so the qualitative voltage-dependence of the capacitance at this simple level of approximation has limited practical relevance. Nonetheless, it is an important feature of the electrochemical interface for those modified Poisson-Boltzmann approaches in which the cavities are determined by contours of the electron density. Future work in this area could capture the "ion-adsorption" portion of the capacitance either by including explicit counter-ions within the electronic structure portion of the calculation or by choosing a classical fluid functional that includes a microscopic description of the counter-ions.
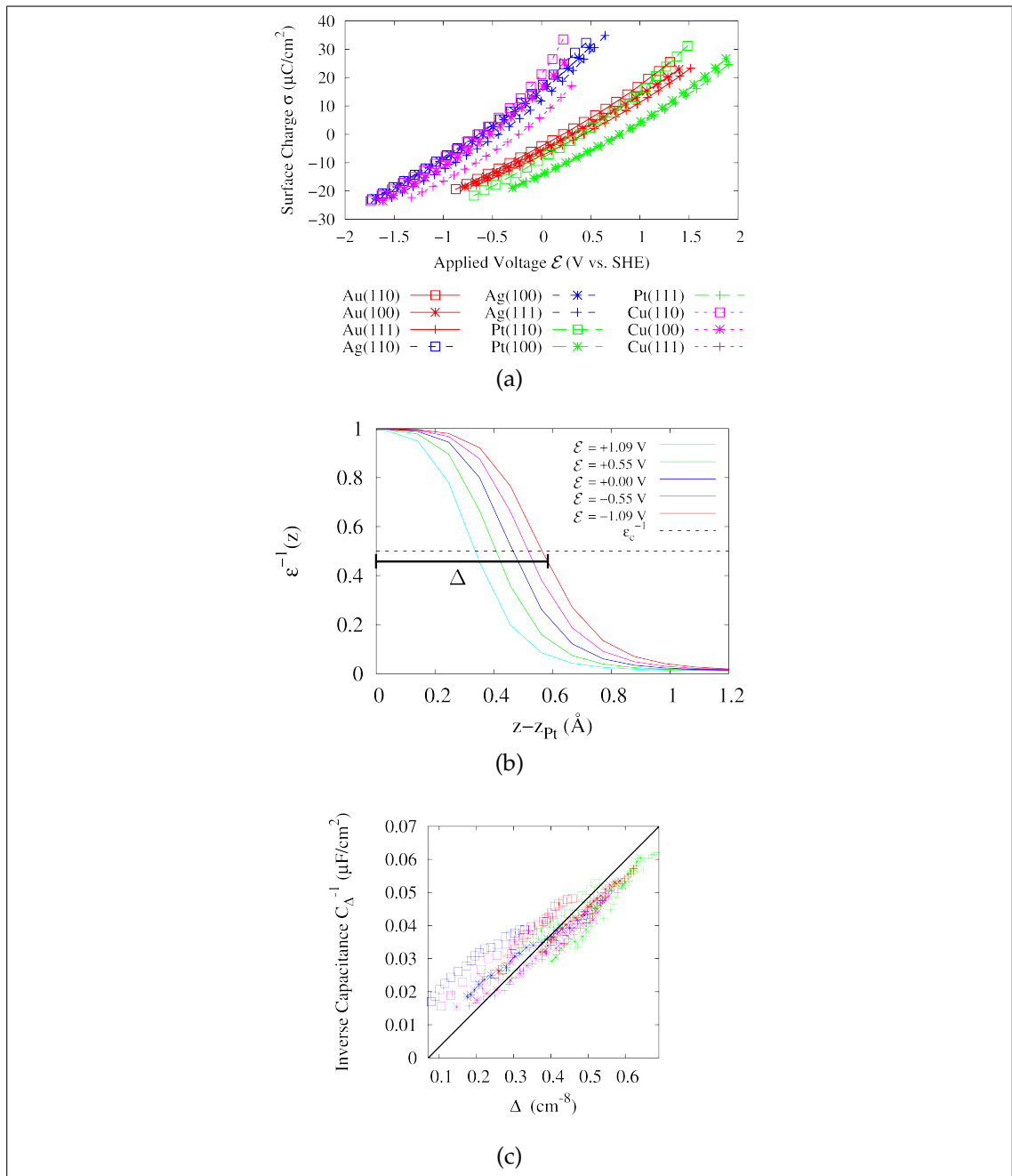
Figure 3.4: (a) Surface charge σ as a function of applied voltage $\mathcal{E}$ for a series of transition metal surfaces in an electrolyte of monovalent ionic strength $c = 1.0$ M (b) Inverse dielectric constant ϵ^{-1} as a function of distance from a Pt(111) surface for multiple values of applied voltage (c) Inverse gap capacitance C_Δ^{-1} as a function of the distance from the metal surface at which the fluid begins Δ. The solid line indicates the best fit to the data with slope constrained to ϵ_0^{-1}

3.8.4 Potentials of Zero Charge and

Reference to Standard Hydrogen Electrode

To connect our potential scale (relative to an electron solvated in our model fluid) to a standard potential scale employed in the literature and to confirm the reliability of our model, Figures 3.5(a,b) show our *ab initio* predictions for potentials of zero charge versus experimental values relative to the standard hydrogen electrode (SHE).[282] Within both the local density (LDA)[151] and generalized gradient (GGA)[215] approximations to the electronic exchange-correlation energy, we have calculated the potentials of zero charge for various crystalline surfaces of Ag, Au, and Cu, three commonly studied metals. We performed a least-squares linear fit to the intercept of our data, leaving the slope fixed at unity. (Note that the experimental data for Cu in NaF electrolyte were not included in the fit, due to concerns discussed below.) The excellent agreement between our results (with a constant offset) and the experimental data indicates that joint density-functional theory accurately predicts trends in potentials of zero charge, and encourages us that it can establish oxidation and reduction potentials in the future. The improved agreement of GGA (rms error: 0.058 V) over LDA (rms error: 0.108 V) underscores the importance of gradient-corrections to this type of surface calculation.

The strong linear correlation with unit slope between the theoretical and experimental data in Figures 3.5(a,b) indicates that the simplified Poisson-Boltzmann approach reproduces potentials of zero charge well relative to some absolute reference. The single parameter in the fit for each of the two panels (namely, the vertical intercepts of each fit line) establishes the absolute relationship between our zero of potential (implicit in each set of theoretical results)

and the zero of potential on the standard hydrogen-electrode scale (implicit in the experimental data). Specifically, we find that our zero of potential sits at -4.91 V relative to the SHE for LDA and -4.52 V relative to the SHE for GGA. Intriguingly, these values are close to the experimentally determined location of *vacuum* relative to the the standard hydrogen electrode reference (-4.44 V)[282]; in fact, the GGA reference value is within a tenth of a volt. This apparent alignment is not altogether surprising due to the following argument: (1) our method measures the difference in energy between an electron in the electrode and an electron solvated deep in our model electrolyte, so that our potentials of zero charge are measured relative to a solvated electron reference; (2) the energy of a solvated electron relative to vacuum *within the presently considered linearized Poisson-Boltzmann model* is zero because this approximation includes only electrostatic effects; and (3) because the calculated potentials of zero charge in the figures are thus *relative to vacuum*, the difference between our calculated results and the experimental results should represent the constant difference between the vacuum and SHE references.

Consideration of the breakdown of the potential of zero charge into physically meaningful quantities explains the difference between the LDA and GGA results and elucidates the apparent success of the rather simple modified Poisson-Boltzmann approach in predicting PZC's. Transferring an electron from a metal surface to a reference electrode requires, first, removal of the electron from the surface and, then, transport of the electron through the relevant interfacial layers of the liquid. The energy associated with the former process is the work function, and the energy associated with the latter relates to the intrinsic dipole of the liquid-metal interface. As is well-known, there is an approximately constant shift between the predictions of the LDA and GGA exchange

122

and correlation functionals for work functions of metals. In fact, Fall *et al.* report that GGA metal work functions are approximately 0.4 V lower than the LDA work functions,[74] corresponding well to the differences we find between the vertical intercepts of Figures 3.5(a,b). Next, to aid consideration of the intrinsic dipole of the interface, Figure 3.5(c) explicitly compares our predictions for work function with our predictions for potential of zero charge, including also the corresponding experimental data for both quantities. (To place all values on a consistent scale of potential, which we choose to be vacuum, we have added the experimentally determined 4.44 V difference between SHE and vacuum to the experimental PZC's.) The data in Figure 3.5(c) suggest that the vacuum work functions are harder to predict than potentials of zero charge, possibly due to difficulty determining the value of the reference potential in the vacuum region, an issue not present in our fluid calculations due to the screening in Equation 3.10. The figure also indicates an approximately constant shift from vacuum work function to potential of zero charge, suggestive of a roughly constant interfacial dipole for each of the metal surfaces. However, the shift is not exactly constant: both the experimental and theoretical data exhibit significant fluctuations (on the order of 0.1 V) in the shift between work function and PZC from one metal surface to another. Because the PZCs are determined to within a significantly smaller level of fluctuation (0.06 V), these data indicate that the Poisson-Boltzmann model captures not merely a constant interfacial dipole, but also a significant fraction of the fluctuation in this dipole from surface to surface.

We note that Tripkovic *et al.* have also calculated the potentials of zero charge for transition metal surfaces.[283] However, that approach requires calculation of several layers of explicit water within the electronic structure portion of the calculation, and those authors find the resulting potentials of zero charge to be

dependent on the exact structure chosen for the water layers. While differing orientations of water molecules at the interface may result in significant local fluctuations in the instantaneous PZC, the experimentally measured potential of zero charge is a temporal and spatial thermodynamic average over all liquid electrolyte configurations rather than the value from any single configuration. Direct comparison to experimental potentials of zero charge therefore should involve calculation of a thermodynamic average.

As a matter of principle, derivatives of the free energy (which the JDFT framework provides directly) yield thermodynamic averages. Therefore, an exact free-energy functional would predict the exact, thermodynamically averaged potential of zero charge, and classical liquid functionals, which capture more microscopic details of the equilibrium liquid configuration[171] than the present model, would be an ideal choice for future in-depth studies. Indeed, such functionals are capable of capturing the relevant electrostatic effects even when a single configuration of water molecules dominates the thermodynamic average. (In such cases, minimization of the free-energy functional results in localized site densities $N_\alpha(r)$ representing the dominant liquid configuration.) Of course, in cases of actual charge-transfer reactions between the surface and the liquid, the (relatively few molecules) involved in the actual transfer must be included within the explicit electronic density-functional theory, whereas the other electrolyte molecules may still be handled accurately within the more computationally efficient liquid density-functional theory.

There is also reason to be sanguine regarding the ability of the modified Poisson-Boltzmann approximation pursued in this work to capture interfacial dipole effects. The macroscopic dielectric constant contained within the present

model describes primarily the orientational polarizability of water, so that the liquid bound charges resulting from the minimization of the free energy should reflect the most dominant configurations of water molecules in the thermodynamic average, even if only a single configuration dominates. On the electrode side, the image charges corresponding to the bound charge also naturally appear, as a consequence of both the electrostatic coupling in our model and the metallic nature of the surface described within electronic density-functional theory. From an optimistic perspective, it is quite possible that a significant portion of the electrostatics of the surface dipole would be captured even at the simplified level of a Poisson-Boltzmann description. Ultimately, quantification of how much of the effect is captured may only be verified by comparison to experiment. For the systems so far considered, the excellent *a priori* agreement between experimental measurements and our theoretical predictions indicates that the relevant effects are indeed captured quite well. It appears that even a simple continuum model (which only accounts for the effects of bound charge at the interface and the corresponding image charges within the metal) can predict accurately key electrochemical observables such as potential of zero charge. Certainly, for more detailed future studies, we would recommend exploring the performance of more explicit functionals. However, the apparent accuracy and computational simplicity of the current Poisson-Boltzmann approach render it well-suited for high-throughput studies of electrochemical behavior as a function of electrode potential.

As a further example of the utility of the Poisson-Boltzmann approach, the potential of zero charge calculation for copper illustrates how this theory can be used as a highly controlled *in-situ* probe of electrochemical systems, with the ability to isolate physical effects which are not possible to separate in the exper-

(a) LDA

(b) GGA

(c) Comparison to Work Functions
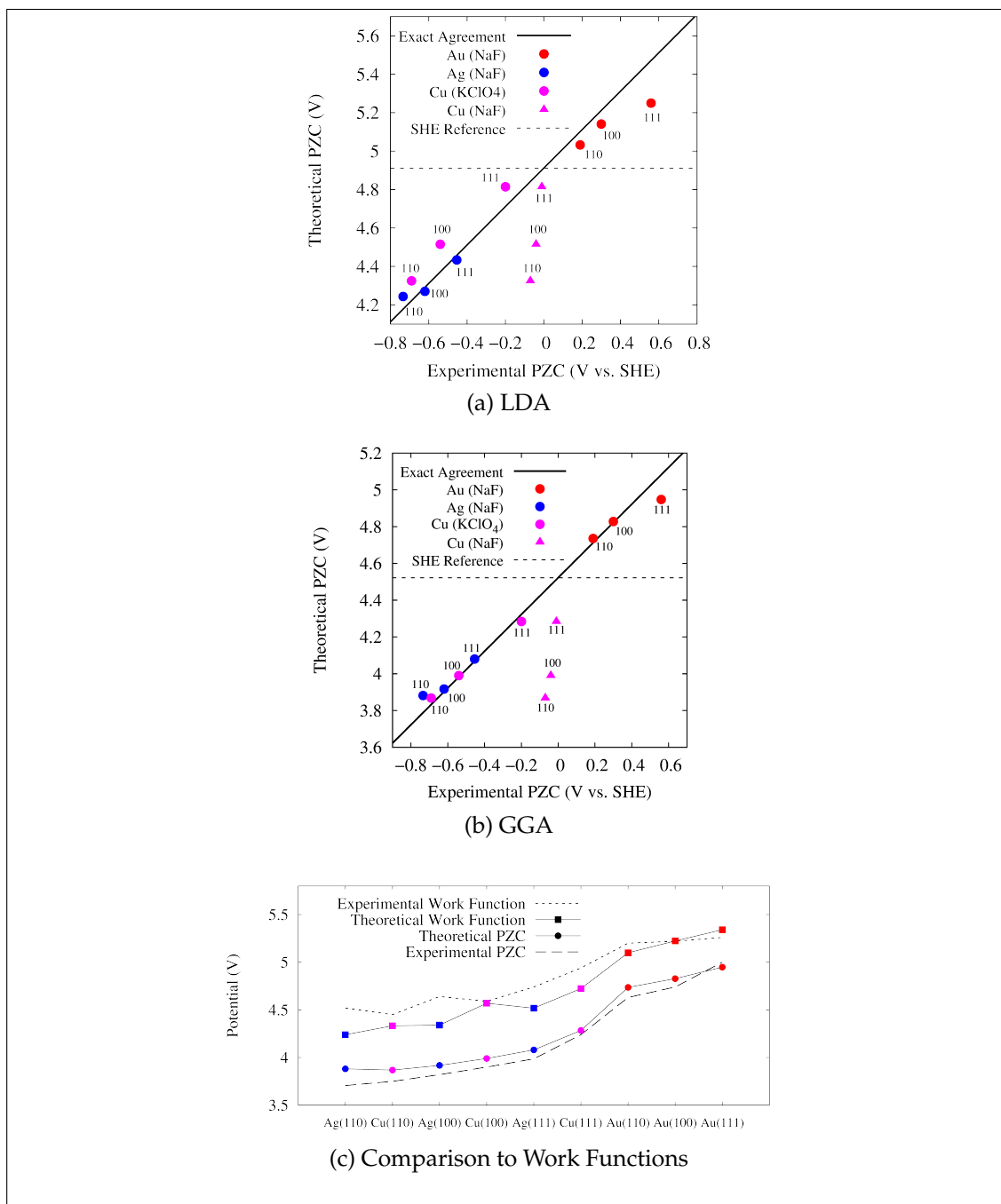
Figure 3.5: Comparisons of *ab initio* predictions and experimental data[282] for potentials of zero free charge (PZCs) and vacuum work functions: (a) *ab initio* LDA predictions versus experimental PZC relative to SHE, (b) *ab initio* GGA predictions versus experimental PZC relative to SHE, (c) *ab initio* GGA vacuum work functions (solid line with squares) and PZC's (solid line with circles), experimental work functions (dotted line) and PZC's (dashed line) versus vacuum for the same series of surfaces. Best linear fits with unit slope (dark diagonal solid lines in (a) and (b)).

iment. Specifically, in Figures 3.5 (a) and (b), for copper there are experimental values for two different electrolytes, NaF and $KClO_4$, which are both claimed to be noninteracting with the metal surface.[282] Clearly, our theoretical values, which correspond to potentials of zero *free* charge without adsorption of or chemical reaction with ions from the electrolyte, agree more favorably with experimental data for the Cu surface in $KClO_4$ than for the NaF electrolyte. Our results suggest that future experimental exploration is warranted to investigate potential interactions between the NaF electrolyte and the copper surfaces, or into other possible causes of the discrepancy in potentials of zero charge. Perhaps some polycrystalline impurities caused the experimental potentials of zero charge of the supposed single-crystalline faces to become much more similar than our calculations and the $KClO_4$ data indicate they should be. *Ab initio* calculations offer an avenue to study each of these potential causes independently and to elucidate the mechanisms underlying the apparent experimental disagreement.

Finally, although potentials of zero charge are quite readily observed in experiments for less reactive metals such as silver and gold, measurement of the potential of zero charge for platinum can be difficult because platinum is easily contaminated by adsorbates. For this reason, more convoluted methods are employed to determine an experimental value for the potential of zero charge for platinum. For instance, one may turn to ultra-high vacuum methods, where, by definition, no molecules are adsorbed on the surface, and one may then attempt to estimate the effect of the solution on the potential of zero free charge. [297] Alternately, one may employ cyclic voltammograms to estimate the charge due to adsorbates and then extrapolate the potential of zero free charge. [54] Our *ab initio* method, however, gives the values for non-contaminated potentials of

zero free charge directly, provided we establish the relation of our zero refer-ence potential relative to that of the standard hydrogen electrode, which we have done above.

For uncontaminated platinum, our method yields the potentials of zero free charge shown in Table 3.2. Compared to other references in the literature, the best agreement with our results is from an experiment which extrapolates the potential of zero charge from ultra-high vacuum, eliminating the effects of un-known adsorbates on the clean surface.[297] As with the results for Cu, the sig-nificantly better agreement of our calculations with this latter experimental ap-proach suggests that perhaps future experiments which measure potential of zero charge should reconsider the effect of possible contaminants when extrap-olating values for the potential of zero free charge.

Table 3.2: Platinum Potentials of Zero Free Charge (V vs SHE)

	(110)	(100)	(111)
LDA	0.31	0.70	0.71
GGA	0.40	0.79	0.82

3.9   Conclusion

In this work, we extend joint density-functional theory (JDFT) – which combines liquid and electronic free-energy functionals into a single variational principle for a solvated quantum system – to include ionic liquids. We describe the theo-retical innovations and technical details required to implement this framework for study of the voltage-dependence of surface systems within standard elec-tronic structure software. We establish a connection to the fundamental electro-chemistry of metallic surfaces, accurately predicting not only potentials of zero

charge for a number of crystalline surfaces for various metals but also an independent value for the standard hydrogen electrode relative to vacuum. Furthermore, we show how future innovations in free energy functionals could lead to even more accurate predictions, demonstrating the promise of the joint density-functional approach to predict experimental observables and capture subtle electrochemical behavior without the computational complexity required by molecular dynamics simulations. These advantages render joint density-functional theory an ideal choice for high-throughput screening calculations and other applications in materials design.

We have built extensively upon the framework of joint density-functional theory in the implicit solvent approximation,[217] extending it to include charged ions in a liquid electrolyte. Beginning with an implicit model for the fluid density $N_{lq}(r)$ in terms of the electronic density of the surface, $N_{lq}(r) = N_{lq}(n(r))$, we include an ionic screening length tied to the fluid density $N_{lq}(r)$ in the same way as done in previously successful models for the dielectric constant. We also solve a previously unrecognized difficulty by including model core electron densities within the surface to prevent artificial penetration of liquid density into the ionic cores, which lack electrons in typical pseudopotential treatments of the solid. Inclusion of this ionic screening allows us to provide a consistent zero reference of potential and to resolve many difficulties associated with net charges in periodic supercell calculations, thereby enabling study of electrochemical behavior as a function of applied voltage.

With the framework to include electrode potential within joint density-functional theory calculations thus in place, we then establish clear connections between microscopic computables and experimental observables. We iden-

tify the electronic chemical potential of density-functional theory calculations with the applied voltage in electrochemical cells, and thereby extract a numerical value of 4.52 V (within the GGA exchange-correlation functional) for the value of the standard hydrogen electrode relative to vacuum, which compares quite favorably to the best-accepted experimental value of 4.44 V.[282] We also show that joint density-functional theory reproduces, *a priori*, the subtle voltage-dependent behaviors expected for a microscopic electrostatic potential within the Gouy-Chapman-Stern model and we extract potentials of zero free charge for a series of metals commonly studied in electrochemical contexts, often finding agreement with experimental values to within hundredths of volts.

This qualitatively correct prediction of electrochemical behavior and encouraging agreement with experiment demonstrate the capabilities of even a simple approximation within the joint density-functional theory framework, and we expect future improvements to the free-energy functional to be able to describe more complex electrochemical phenomena. Future work should also generalize the approximate functional to include nonlinear saturation effects in ionic screening within the current modified Poisson-Boltzmann approach, with an approach along the lines of other works. [56] In electrochemical experiments, the differential capacitance of charged metal surfaces often exhibits a minimum at the potential of zero charge[15] (not seen in the linear continuum theory), and more advanced theories including such nonlinear effects should be able to capture this more subtle behavior. Additionally, recent developments in classical density functionals for liquid water [171] now can be implemented to study electrochemical systems. Such classical density functionals can be extended to include realistic descriptions of ions and are capable of capturing other essential behaviors of electrolyte fluids, including features in the ion-ion and ion-water

correlation functions due to differences in the structure of the anion and the cation. [18] Finally, in systems where electrochemical charge-transfer reactions are important or where chemical bonds of the fluid molecules are expected to break, the relatively few reactant molecules should be treated within the explicit electronic structure portion of the calculation, with the remaining vast majority of non-reacting molecules handled within the more computationally efficient liquid density-functional theory.

With advances such as those described above, joint density-functional theory holds promise to become a useful and versatile complement to the toolbox of currently available techniques for first principles study of electrochemistry. Unlike *ab initio* molecular dynamics (or any other theory involving explicit water molecules), this computationally efficient theory is not prohibitive for larger system sizes. In fact, as the system size grows, the fraction of calculation time spent solving the modified Poisson-Boltzmann equation actually decreases, meaning that for larger systems, the calculation is only nominally more expensive than calculations of the corresponding systems carried out in a vacuum environment. Also, because thermodynamic integration is not required, the joint density-functional theory approach yields equilibrium properties directly and has a clear advantage over molecular dynamics simulations for calculation of free energies. Immediate applications include the study of molecules on metallic electrode surfaces as a function of applied potential and prediction of the basic properties of novel catalyst and catalyst support materials. These calculations could inform future materials design by offering an opportunity to screen novel complex oxides and intermetallic materials in the presence of the true electrochemical environment, thereby elucidating the fundamental physical processes underlying fuel cells and liquid-phase Graetzel solar cells.

CHAPTER 4

ELECTROCHEMISTRY WITH MICROSCOPICALLY DETAILED

ELECTROLYTE THEORY [1]

4.1 Introduction

The addition of negatively charged anions and positively charged cations to liquid water introduces significant changes in the atomic-scale liquid structure and bulk properties of the water. The disruption of the hydrogen bond network in an aqueous electrolyte prompts the water molecules to form solvation shells around the ions and alters the phase diagram of the liquid [11]. Infrared spectroscopy measurements show that the influence of the electrolyte on the water structure, sometimes extending far beyond a single solvation shell, depends critically upon the type and concentration of ions and counter-ions [70] — some ions are structure-makers, enhancing the hydrogen-bonded network of the water, while others are structure-breakers [11]. The presence of ions alters the dynamics of water molecules [253], causing rotation to occur more slowly and involve more molecules.

Understanding how these phenomena depend on the presence of the ions in the electrolyte is crucial to the field of biology, where aqueous ions drive key life-sustaining processes. In biochemistry, for example, the strongly negative phosphate chain of adenosine triphosphate (ATP) attracts metal cations, especially magnesium (Mg^{2+}), which act as a cofactor to lower the transition-state barrier for the hydrolysis reaction [142]. The hydrolysis of ATP releases stored chemi-

---

[1]R. Sundararaman provided code implementation of fundamental measure theory for mixtures of hard spheres and co-developed the charge-balance framework

cal energy, which drives key processes in the human body, such as the transport of sodium and potassium ions across the cell membrane. During the process of transport, the cations and water molecules coordinate to key enzymes without forming strong chemical bonds, maintaining the delicate physiologic balance of potassium ions inside and sodium ions outside the cell [135, 251]. These basic metabolic processes depend on subtle interactions between a quantum-mechanical protein active site and an ion, all occurring in an aqueous environment. An accurate treatment of both the liquid electrolyte environment and quantum-mechanical biomolecules would provide significant insight into these chemical processes which maintain life, offering a promising avenue for future research.

In this work, however, we will focus upon the field of electrochemistry, where understanding the behavior of solvated ions at the electrode-electrolyte interface as a function of applied potential is crucial to improving energy storage and conversion devices. Batteries, solar water-splitting cells, and supercapacitors must become more efficient and less costly to ensure our future energy security. However, the complexity of the interface between the charged electrode surface and the fluid electrolyte [28] presents a challenge. In batteries, for example, the working ion (commonly Li^+) must break its shell of solvent molecules to enter the electrode, allowing the battery to charge and discharge under potential cycling. One phenomenon which underlies both batteries and supercapacitors is pseudocapacitance, which occurs at potentials where the dominant electrode process is the desolvation and adsorption of ions, without the formation of chemical bonds [5, 10]. Pseudocapacitance occurs when it is thermodynamically favorable for the charge required for progression of an electrode process, such as electrosorption or intercalation of an ion, to be a continuous function

of the applied potential [52]. Some theoretical studies have been undertaken to elucidate pseudocapacitive charging at the electrode surface [305, 167, 129], but none has satisfactorily bridged the relevant length- and time-scales.

The simplest theoretical models for the free energy of an electrolyte treat the ions and counter-ions as spherical particles then model the solvent with a continuum dielectric constant ϵ, assuming a strong, fully dissociated electrolyte. The Born model [200] estimates, from straightforward continuum electrostatics, the solvation energy ΔG of a gas-phase ion of radius R and charge q to be

$$\Delta G = -\frac{q^2}{2R}\left(1 - \frac{1}{\epsilon}\right).\tag{4.1}$$

The Born model may also be extended to capture more microscopic information by choosing the radius R to include both the size of the ion and the temperature dependent properties and dipole moment of the solvent [238]. Debye and Huckel [60] proposed a contribution to the Helmholtz free energy due to charging a liquid of point ions embedded in a continuum dielectric. Assuming a mean-field interaction of the ions with an average electrostatic field ϕ and finding the variation of the Helmholtz free energy with respect to ϕ leads to the *nonlinear* Poisson-Boltzmann equation,

$$\epsilon \nabla \cdot (\epsilon \nabla \phi) = \sum_{\gamma} -q_{\gamma} N_{\gamma}^b \exp\left(\frac{-q_{\gamma}\phi}{k_B T}\right),\tag{4.2}$$

where γ indexes over the charged species in the fluid with charge q_{γ} and bulk number density N_{γ}^b. The linearized form of the Poisson-Boltzmann equation, valid at low field strength, is given in Equation 3.10. The nonlinear Poisson-Boltzmann equation forms the mathematical basis for the Gouy-Chapman model of the electrochemical double layer, and can be extended to model time-dependent diffusion of ionic species to the electrode surface through the Nernst equation [33]. These early theories of the electrolyte often serve as the basis

for both modern implicit solvation models [174] and for equations of state for electrolyte liquids [35].

Modern models of the electrolyte liquid include perturbation-theory based equation of state descriptions, classical density-functional theory approaches, and molecular dynamics calculations with classical pair potentials. When placed in contact with a uniform charged wall to simulate the electrode surface, these electrolyte fluid theories can be employed to model the structure of the liquid at the electrochemical interface. Statistical Associated Fluid Theory (SAFT) models build upon hard sphere and chain reference fluids using perturbation theory and then fit multiple empirical parameters to reproduce experimental state and vapor pressure data [35, 109, 91, 112]. These electrolyte equations of state successfully account for the non-spherical shape of the solvent molecules and for isotropic and orientation-dependent interactions in the bulk fluid, but they do not extend easily to the non-uniform fluid. Classical density-functional approaches based on fundamental measure theory can capture much of the phenomenology associated with the electrochemical double layer, such as the interplay between close-packing and electrostatics and the effect of charge inversion [104, 149]. However, density-functional calculations of ionic liquid electrolytes (which include no solvent molecules and can be modeled by charged hard spheres) are most common [32], because the solvent-electrolyte interaction is quite hard to capture accurately. Molecular dynamics with classical pair potentials can capture interfacial structure in the fluid [167], but these calculations require thermodynamic integration to compute free energies and the results are often dependent upon the choice of model potential. Furthermore, these classical models for the fluid fail to describe specific adsorption of electrolyte, charge transfer effects, or any processes which depend on the geometry and chemical

identity of the electrode surface.

Of course, first-principles density-functional or quantum-chemical calculations of the electrode surface and any specific adsorbates can capture the relevant effects of chemical bonding and charge transfer. Typical electronic structure calculations, however, fail to describe accurately systems in contact with liquid, often neglecting entirely to include the fluid environment. In those cases where *ab initio* calculations do include the effect of the electrolyte present under typical electrochemical conditions, the atomic-scale details of the liquid are usually ignored and replaced by a continuum dielectric medium [139, 163, 56]. *Ab initio* molecular dynamics (AIMD) calculations can capture the atomic-scale details, but require computationally demanding thermodynamic sampling to predict the structure of the liquid electrolyte and require thermodynamic integration to compute free energies. To be computationally feasible, AIMD surface calculations either include only one or two layers of liquid water (without any ions) or they artificially confine the liquid between electrode surfaces in a periodic supercell representation [244, 210, 119, 290]. AIMD calculations which do include screening are restricted to only one or two ions, limiting the physical effects which can be investigated [154].

Additionally, calculations of charged systems performed under periodic boundary conditions (without ions present to neutralize the charge) will suffer from the well-known pathological divergence of the electrostatic energy. More details of the electrostatic energy divergence which occurs in typical *ab initio* calculations of charged systems are presented in Chapter 3. To prevent this divergence, most simulations include a highly unphysical constant neutralizing net background charge across the entire unit cell. In cases where small

free-energy differences can alter the qualitative predictions, such as the adsorption of molecules on a charged electrode surface, the errors introduced by such a net background charge are quite concerning. Furthermore, at the charged electrode-electrolyte interface, the lack of realistic screening from the ions may cause AIMD simulations to overestimate the polarization and structuring of the solvent molecules at the surface [305]. These challenges of treating charged systems are not confined only to first principles calculations at the atomic scale; difficulties arise at all scales and with all types of modeling [194].

In contrast to the purely classical and perturbation-theory based models for an electrolyte liquid, JDFT can capture the structural and quantum-mechanical details of the electrode surface and the influence of these atomic-scale details upon the electrochemical double-layer structure in the liquid. Unlike the traditional *ab initio* approaches used to compute the properties of the electrode, the JDFT framework (presented fully in Chapter 2) generalizes to include the screening effects of charged ions in aqueous solution upon the electrode surface, naturally preventing divergence of the electrostatic energy. JDFT also naturally captures a range of ionic concentrations which would be challenging to compute in molecular dynamics due to the discrete nature of the ions. Finally, JDFT also has the potential to capture the pseudocapacitive phenomena occurring in batteries and supercapacitors because positively charging the surface by removing an electron is equivalent to the charge transfer of an electron from a surface ion through the circuit [5, 52].

Chapter 3 connected *ab initio* computables to electrochemical observables and showed how the implicit solvent approximation to JDFT (comparable to a linearized Poisson-Boltzmann approach) is highly promising for electrochem-

ical calculations. We demonstrated how implicit JDFT calculations of charged metal surfaces in aqueous electrolyte produces microscopic electrostatic potentials which agree qualitatively with those potentials predicted by the famous Gouy-Chapman-Stern (GCS) model in electrochemistry. The implicit solvation model properly captures the linear charging regime of the GCS model, in which the charge on the metal electrode varies linearly as a function of applied potential and capacitance is constant. Implicit JDFT also captures potentials of zero charge with an accuracy better than 100 mV and establishes an absolute reference to place our calculations on the scale of the standard hydrogen electrode (SHE). However, the charging curves presented in the electrochemistry literature are often nonlinearly dependent on the applied potential, leading to a differential capacitance which also varies with potential [15, 95]. These nonlinear features are related to pseudocapacitive and potential-driven changes in the interfacial structure of the electrolyte at the electrode surface which are impossible to capture with an implicit description of the liquid.

Explicit JDFT calculations with an atomically-detailed liquid, however, should be capable of describing the structural changes in the electrolyte which give rise to the dependence of the differential capacitance upon potential. This chapter explores the ability of the JDFT framework with a classical DFT description of the liquid environment to capture complex, electrolyte-dependent electrochemical behavior, including nonlinear capacitance. Section 4.2 describes further connections between *ab initio* computables and electrochemical observables, namely differential capacitance measurements. Section 4.3 details the innovations in the JDFT classical liquid functional Ω_{lq} and the liquid-solute coupling functional ΔA required to capture the relevant physical effects in electrolyte liquid. Section 4.4 introduces a framework to perform calculations of

charged electrode surfaces under applied potential control and to relate the applied potential to standard reference electrodes in electrochemistry. Section 4.5 describes the approximations to the liquid and coupling functionals required to implement specific monovalent electrolytes within JDFT. Section 4.6 shows the predicted potentials of zero charge, interfacial liquid structure, and electrode charge as a function of applied potential for single-crystalline metallic surfaces. Section 4.7 concludes this chapter and offers future directions for the research presented herein.

4.2 Further Connections to Electrochemistry

Section 3.3 presents a careful mapping of the quantities computed in JDFT calculations to the quantities measured in electrochemical experiments. This section expands upon some of these electrochemistry concepts, specifically focusing on the structure of the electrode-electrolyte interface and on experimentally measured differential capacitances.

4.2.1 Structure of Electrode-Electrolyte Interface

At the electrode-electrolyte interface, the interplay of quantum mechanics, electrostatics, thermodynamics, and kinetics creates complex phenomena which are challenging to predict theoretically and to characterize experimentally. Figure 4.1 presents a textbook picture of the electrochemical interface between a metal electrode and an aqueous electrolyte under the influence of an applied potential [15, 28]. The textbook interfacial structure of the electrolyte consists of

two main spatial regions: the compact (inner) layer and the diffuse layer. The compact layer consists of ions which carry the opposite charge from the surface and form a plane next to the electrode surface due to electrostatic attraction. If at least one layer of water is present between the ions and the surface, the ions are in the outer Helmholtz plane (OHP), while if the ions have broken their solvation shells to associate with the electrode, the ions are in the inner Helmholtz plane (IHP). The diffuse layer consists of both positively and negatively charged ions which move to screen any charges which arise with a screening length that depends on the electrolyte concentration as described in Chapter 3. The ions in the diffuse layer typically exist within shells of solvent molecules because breaking the shells comes at a significant energy cost, and most of the electric field from the applied potential has already been screened by the compact layer.

4.2.2 Gouy-Chapman-Stern Model

As described in detail in Section 3.3, the total capacitance of the surface C may be modeled as the capacitance from the inner layer C_i in series with the capacitance from the diffuse layer C_d. Just as in Equation 3.4, the inverse capacitances are additive, yielding a total capacitance

$$C^{-1} = C_d^{-1} + C_i^{-1}. \tag{4.3}$$

In the idealized Gouy-Chapman-Stern theory[101, 46, 261] of the electrochemical double layer, the capacitance of the inner layer is a constant value,

$$C_i = \frac{\epsilon \epsilon_0}{\Delta}, \tag{4.4}$$

140
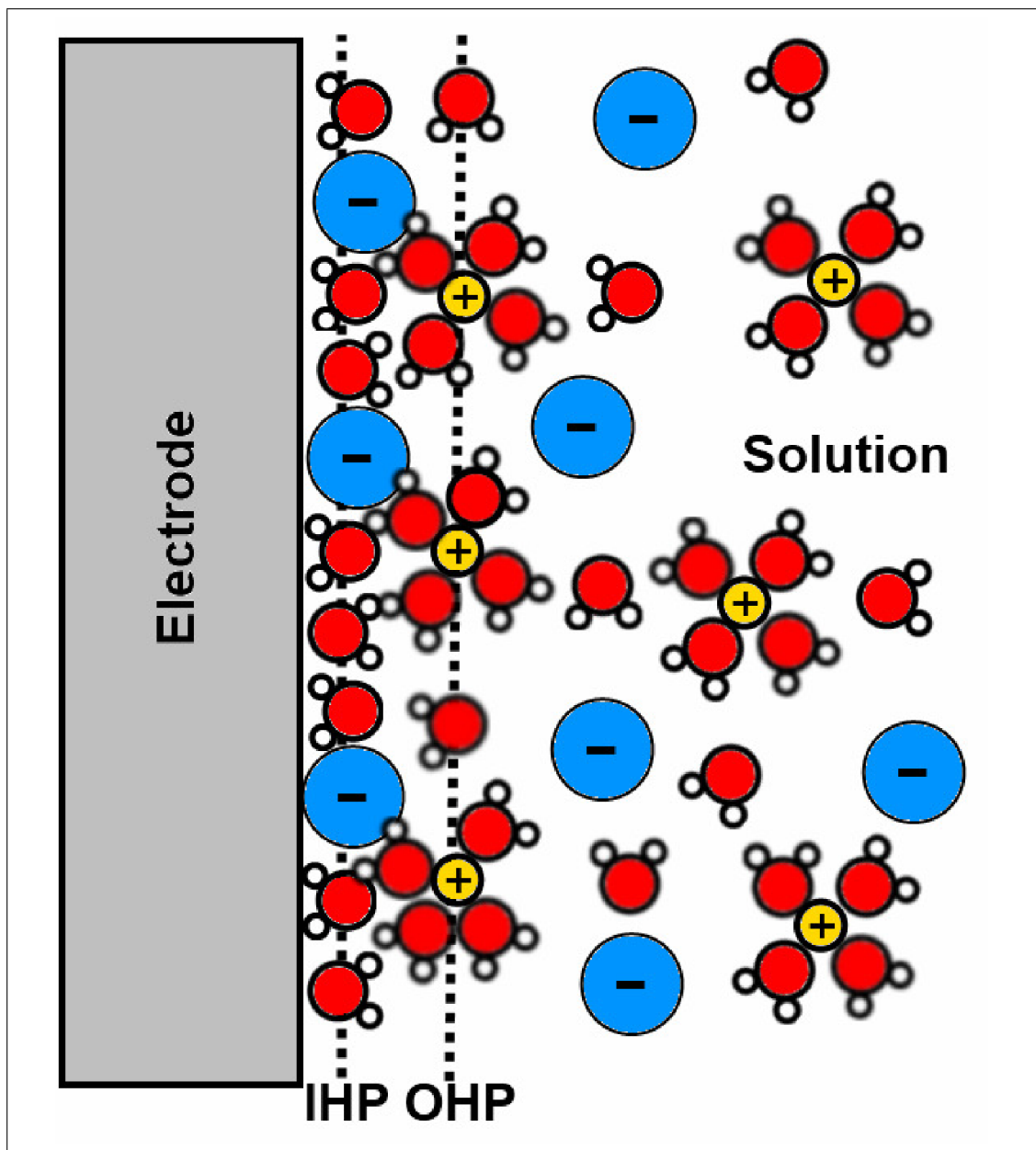
Figure 4.1: Schematic of electrochemical interface [28] with water molecules (red), cations (yellow), and anions (blue) occupying the inner Helmholtz plane (IHP) and outer Helmholtz plane (OHP).

where ϵ is the relative permittivity of the water between the electrode surface and the compact layer of ions, ϵ_0 is the permittivity of vacuum, [2] and Δ is the distance between the electrode and the layer of ions. The relative permittivity ϵ may attain any value between the bulk value in the fluid ($\epsilon_b = 78$ for water) and the vacuum value of $\epsilon = 1$, depending on whether water molecules are present between the ions and the electrode surface and whether those water molecules are free to polarize. In the compact layer, the electrostatic potential decreases linearly from the constant value in the electrode (which is equal to the applied potential as shown in Figures 3.3(c) and 4.12) to the value at the location of the outer Helmholtz plane ($\phi_\Delta = \phi(z - z_{\text{surf}} = \Delta)$). The inner layer capacitance, unlike the diffuse layer capacitance described below, is expected to be largely independent of ion concentration.

The capacitance due to the diffuse layer in the Gouy-Chapman model may be derived by assuming the ions far away from the electrode surface obey the nonlinear Poisson-Boltzmann equation in Equation 4.2. The solution to the Poisson-Boltzmann equation yields the surface charge as a function of the electrostatic potential at the outer Helmholtz plane to be

$$\sigma = \sqrt{(8k_BT\epsilon_b\epsilon_0 N_\gamma^b)}\sinh\left(\frac{\phi_\Delta}{2k_BT}\right) \tag{4.5}$$

for a 1:1 electrolyte with bulk density N_γ^b and bulk dielectric constant ϵ_b [15]. Differentiating the surface charge with respect to ϕ_Δ yields the diffuse capacitance

$$C_d = \sqrt{\frac{2\epsilon_b\epsilon_0 N_\gamma^b}{k_BT}}\cosh\left(\frac{\phi_\Delta}{2k_BT}\right) \tag{4.6}$$

By employing the identity $\sinh(x) = \sqrt{\cosh^2(x) - 1}$ and plugging in the physical constants for an aqueous electrolyte at 25° C, the diffuse capacitance C_d in $\frac{\mu F}{cm^2}$

---

[2] $\epsilon_0 = 1$ in atomic units and $\epsilon_0 = 8.85 \times 10^{-8}$ $\mu F/cm$

may be expressed in terms of the surface charge σ [206, 94] as

$$C_d = 19.46 \sqrt{(137.8C^* + \sigma^2)}, \tag{4.7}$$

where C^* is the electrolyte concentration in moles/liter and σ is the charge on the electrode surface in $\frac{\mu C}{cm^2}$.

One significant consequence of this Gouy-Chapman-Stern series capacitance model for low concentrations of the electrolyte is the emergence of a minimum in the differential capacitance at the potential of zero charge (PZC). In fact, as demonstrated in Figures 4.4 and 4.5 below, electrochemists often determine the potential of zero charge by careful measurements of the location of the differential capacitance minimum [95, 159]. Figure 4.2 shows the constant capacitance from the inner layer C_i, the capacitance from the diffuse layer C_d, and how the two capacitances combine in series to yield the total capacitance of the surface C for an ideal electrode in 0.001 M electrolyte. At potentials near the PZC the diffuse capacitance dominates the total capacitance and creates a dip centered upon the PZC, while at potentials far from the PZC the constant inner layer capacitance dominates. Figure 4.3 displays how the depth of the capacitance minimum increases with decreasing electrolyte concentration, becoming the dominant feature for concentrations below around 0.1 M. In contrast, at the higher concentration of 1.0 M the minimum is barely detectable, even in an idealized model surface.

4.2.3   Capacitance Measurements of an Ideal Electrode

Systems which adhere to the Gouy-Chapman-Stern model and exhibit a roughly constant inner layer capacitance over a wide potential range (typically more
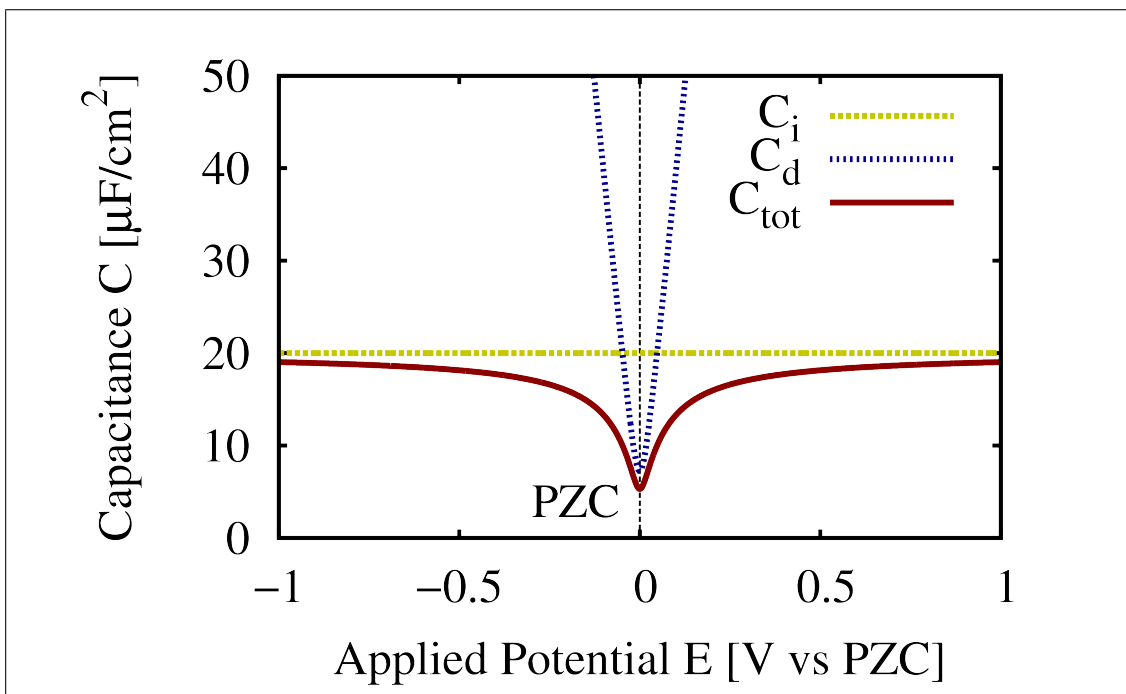
Figure 4.2: Breakdown of ideal total capacitance C (solid red line), diffuse layer capacitance C_d (dotted blue line), and constant compact layer (dashed yellow line) capacitance $C_i = 20\frac{\mu F}{cm^2}$ in a 0.001M electrolyte.

than 1 V) are considered to be ideally polarizable electrodes. In most real electrochemical systems, however, phenomena such as saturation of the dielectric in the inner layer, ions adsorbing and desorbing on the surface, and Faradaic oxidation/reduction processes introduce potential-dependence into the inner layer capacitance. The simple Gouy-Chapman-Stern model is unable to account sufficiently for these subtleties [15].

Even the liquid mercury (Hg) electrode, considered to be the standard ideally polarizable electrode, exhibits potential-dependent features in the differential capacitance [95]. The liquid nature of the mercury electrode eliminates spurious capacitance due to roughness and grain boundaries and also due to contamination of the working electrode [15], so any features in the differential capacitance are likely due to structural changes in the interfacial fluid. Figure 4.4
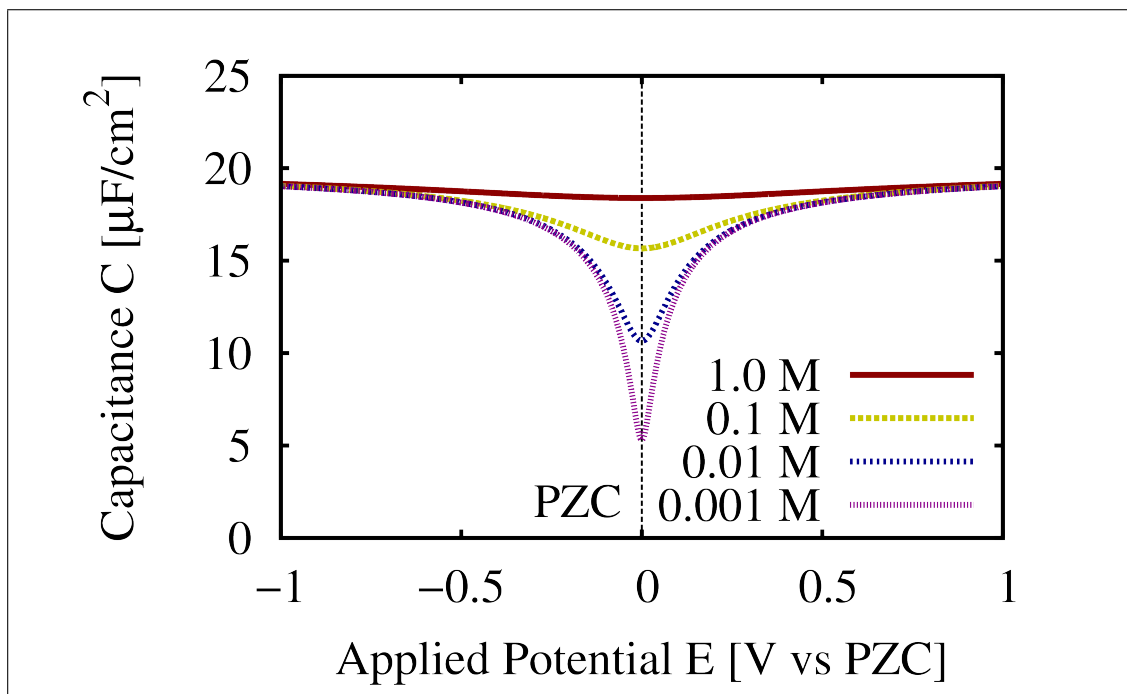
Figure 4.3: Idealized depiction of the appearance of a capacitance minimum at the potential of zero charge with decreasing concentrations of 1.0 M (solid red line), 0.1 M (dashed yellow line), 0.01 M (dotted blue line) and 0.001 M (dotted purple line) for a constant compact layer capacitance $C_i = 20 \frac{\mu F}{cm^2}$.

shows differential capacitance curves, experimentally measured by Grahame, for the mercury electrode in aqueous sodium fluoride (NaF) electrolyte at various concentrations. Grahame measured the potential of zero charge independently by determining the location of the electrocapillary maximum [94] to be -0.23 V vs SHE. [3] The PZC varies by less than 0.01 V with electrolyte concentration, indicating that no chemisorption (which would shift the PZC to lower values for higher electrolyte concentrations [94]) has occurred on the electrode surface.

In the above foundational study of the mercury electrode in a nonadsorbing NaF electrolyte, Grahame next utilized careful measurements to show that the

---

[3]Measurements were performed relative to Standard Calomel Electrode (SCE) and converted to SHE.
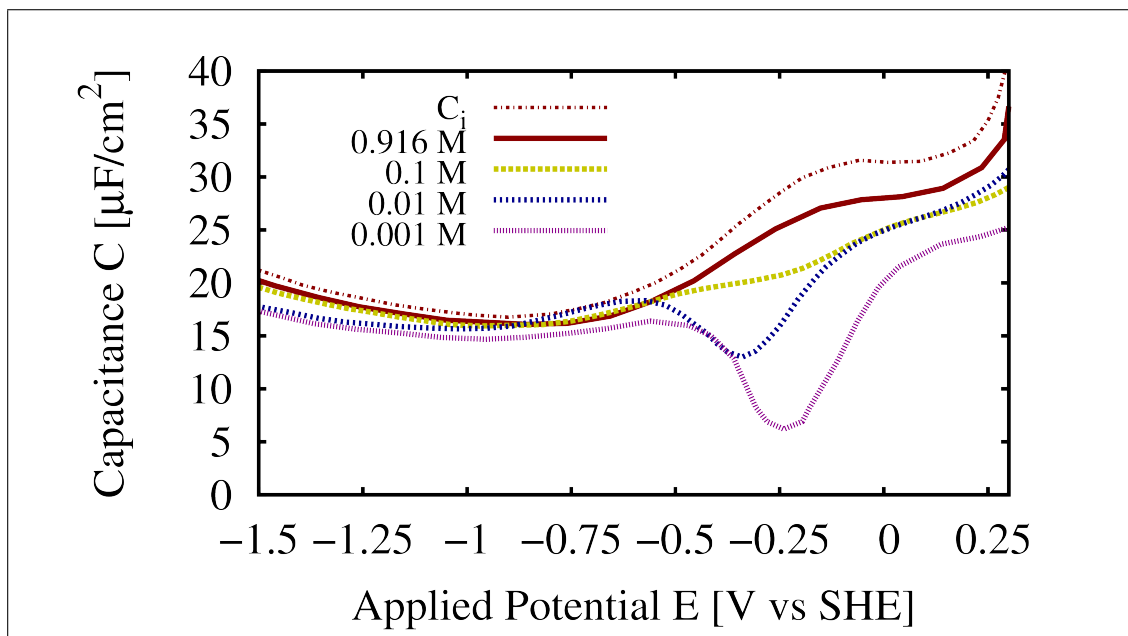
Figure 4.4: Frequency independent differential capacitance of liquid mercury electrode [95] at electrolyte concentrations 0.916 M (solid red line), 0.1 M (dashed yellow line), 0.01 M (dotted blue line), and 0.001 M (dotted purple line). The capacitance of the compact layer extracted from the 0.916 M data using Equation 4.3 and Equation 4.7 is also pictured (dashed/dotted red line).

Gouy-Chapman-Stern model is valid for an ideally polarized electrode [95]. Because the diffuse capacitance is expected to have only a small effect at high electrolyte concentration, Grahame extracted the capacitance due to the compact layer C_i from the measured total capacitance C at $C^* = 0.916$ M using the series capacitance model in Equation 4.3 and the expression in Equation 4.7 for C_d. The integrated differential capacitance provides the surface charge σ in Equation 4.7 up to a constant, and ensuring the surface charge is zero at the independently measured PZC provides the constant. The extracted inner layer capacitance C_i is pictured in Figure 4.4. Grahame proceeded to show that using the extracted C_i in the series capacitance model, with Equation 4.7 for C_d at the lower concentrations $\{C^* = 0.1\ M, 0.01\ M, 0.001\ M\}$, could almost exactly reproduce the measured capacitances shown in Figure 4.4.

One striking conclusion of Grahame's mercury electrode study is that the Poisson-Boltzmann approach which underlies the Gouy-Chapman model is quite accurate for the predicting the features of the diffuse layer, without any modifications required. An additional significant result is that, for an ideal electrode, the series capacitance model behaves as expected, indicating the structure of the inner layer has very little dependence upon the concentration of the electrolyte. The potential-dependent structure in the inner layer capacitance C_i, however, differs significantly from the constant value predicted by the Gouy-Chapman-Stern model. Not only do the features of C_i depend on potential, but the average value (25 μF/cm^2) is difficult to predict directly from Equation 4.4. Choosing the relative permittivity of the water layer to be the bulk dielectric constant of water ($\epsilon = \epsilon_b = 78$) implies that the ions in the outer Helmholtz plane are, on average, located 28 Å away. Choosing the opposite limiting case, in which no water is present between the ions and the surface ($\epsilon = \epsilon_0 = 1$), implies the ions are located a mere 0.35 Å away from the surface. Of course, reality lies in between these two extremes, but there is no *a priori* method of predicting which portion of the potential-dependent capacitance is due to dielectric saturation of the water (changes in ϵ) and which portion is due to changes in location of the first ion plane (changes in Δ). As we shall see in the remainder of this chapter, JDFT calculations can readily provide the microscopic liquid structure at the interface, allowing a complete understanding of the origins of the experimental capacitance measurements.

4.2.4 Measurement of Specific Adsorption

Despite being unable to directly probe the structure of the fluid at the electrode-electrolyte interface, electrochemists have developed analytical and experimental techniques which allow them to deduce the presence of specific adsorbates on the electrode surface.

Parsons-Zobel Plots

One analytical technique developed to probe the presence of specific adsorbates and other non-ideal conditions in the electrochemical double layer was pioneered by Parsons and Zobel [206]. These so-called Parsons-Zobel curves plot the inverse total capacitance C^{-1} as a function of the inverse diffuse capacitance C_d^{-1}, computed using the numerical formula in Equation 4.7. The plot must include a series of low to high electrolyte concentration points at a constant surface charge σ. If the electrode behaves ideally at the chosen charge σ, the constant charge curve has a constant slope with value unity and the intercept of the curve with the vertical axis (the high concentration limit) provides the value of the inverse inner layer capacitance C_i^{-1}. A constant slope with a value lower than unity indicates roughness on the electrode surface with a roughness coefficient equivalent to the the inverse of the slope [286]. A slope which deviates from a constant value for a particular charge could indicate the presence of specific adsorbates on the electrode surface. The surface charge which represents the onset of specific adsorption may be determined by plotting Parsons-Zobel curves for a series of charges and noting the lowest curve for which the slope deviates from a constant. We note that the Parsons-Zobel method is equivalent in principle to the method proposed by Grahame above [95], but provides a

much more intuitive presentation of the data.

The Parsons-Zobel method has been employed successfully to detect the adsorption of fluoride upon a polycrystalline silver surface at potentials above the PZC [159]. Silver in sodium fluoride electrolyte is often considered to be an ideally polarizable electrode because no strong chemisorption of the fluoride ion occurs in the relevant potential window. However, IR spectroscopy measurements of the Ag-O stretching frequency have indicated that the quantity of water adsorbed on the silver decreases due to co-adsorption of fluorine above the PZC [240]. Even though no chemical bond forms, the fluoride ion can still cross into the inner Helmholtz plane and physisorb, qualitatively and quantitatively altering the potential dependence of the differential capacitance.

Figure 4.5 shows the measured differential capacitance of polycrystalline silver in NaF as a function of potential for a series of electrolyte concentrations. The decreasing capacitance minimum value as a function of decreasing concentration is present in these measurements of silver in the proximity of the PZC, similar to the concentration dependence of the capacitance for the ideal mercury electrode in Figure 4.4. Unlike the measurements for mercury, however, as the applied potential increases above the PZC the silver capacitance continues to decrease significantly with decreasing concentration. On the Parsons-Zobel plot, this data forms a nonlinear curve with an onset above the surface charge $\sigma = 6\frac{\mu C}{cm^2}$, indicating a strong likelihood that fluorine specifically adsorbs on the silver surface above those charges.
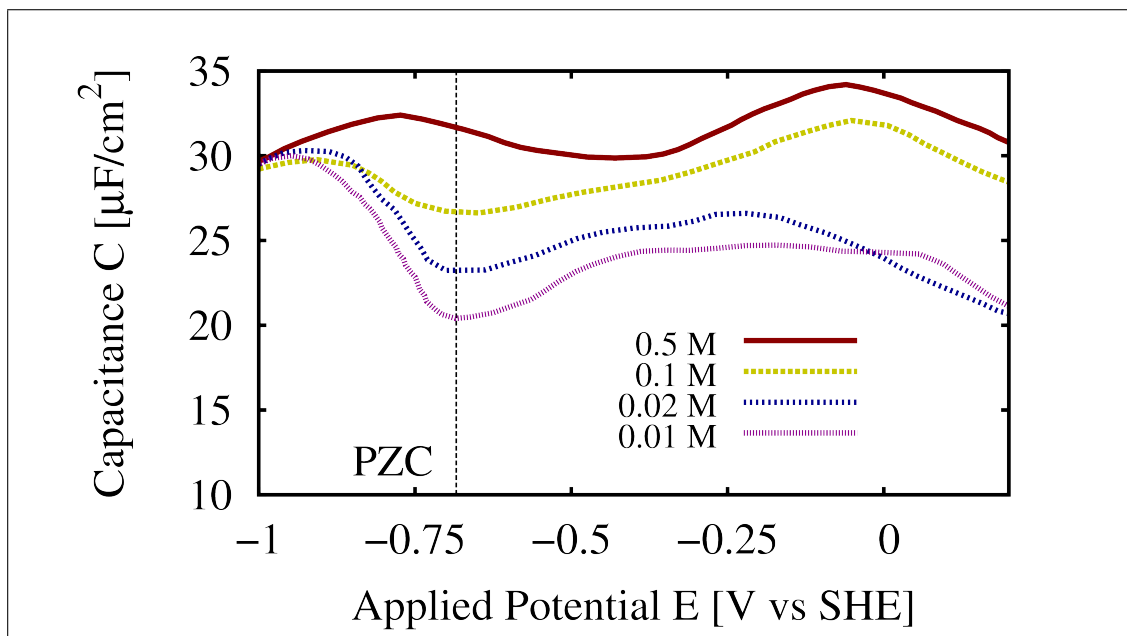
Figure 4.5: Differential capacitance of polycrystalline silver [159] measured at $\omega = 1000$ Hz and electrolyte concentrations 0.5 M (solid red line), 0.1 M (dashed yellow line), 0.02 M (dotted blue line), and 0.01 M (dotted purple line).

Frequency Dispersion of Capacitance

Impedance spectroscopy measurements of the frequency dispersion of the differential capacitance facilitate separation of the capacitance contribution of the double layer from the contribution due to specific adsorption [140]. The static definition of the differential capacitance, presented in Section 3.3 as $C = \frac{d\sigma}{dE}$, includes none of the time- or frequency-dependent behavior of the double layer. Though the capacitance measurements for mercury, an ideally polarizable electrode, in Figure 4.4 did not depend appreciably on the measurement frequency ω, the capacitance measurements for polycrystalline silver in Figure 4.5 do change significantly with frequency. At voltages near SHE, the capacitance for silver in 0.02 M NaF measured at ω=6.25 Hz is nearly twice the value of the capacitance measured at ω=1000 Hz. The capacitance measured at ω=20 Hz of the single-crystalline (111) face of silver in Figure 4.14 also exhibits higher values

above the PZC. This significant frequency dispersion of the silver capacitance provides substantial support for the presence of adsorbed F^- on the electrode surface.

Pajkossy and Kolb demonstrate [140] that comparing capacitance measurements in the high and low frequency limits allows estimation of the total capacity due to the presence of explicit adsorbates. In the high-frequency limit ($\omega \to \infty$) the electrode surface is in a frozen state and no time-dependent processes may occur, so the capacity measured is purely due to the static double layer (C_{dl}). By contrast, the total capacity ($C_{dl} + C_{ad}$) will be measured in the low-frequency, adiabatic limit ($\omega \to 0$), where the electrode surface and liquid structure reach equilibrium and all thermodynamically favored adsorption processes will occur. We note that these capacitances are distinct from the C_i and C_d above, in that they combine in parallel rather than in series. The capacitance due to adsorption may thus be measured as

$$C_{ad} = C(\omega \to 0) - C(\omega \to \infty), \tag{4.8}$$

and additional features of the impedance measurements can determine the rate at which adsorption occurs [140]. Pajkossy et. al. attribute the frequency dependence of the interfacial capacitance, even on electrodes typically considered to be ideally polarized, to the relatively slow exchange of anions between the outer and inner Helmholtz planes [204].

4.2.5 Opportunities for JDFT

Our goal is to understand the above electrochemical phenomena at the atomic scale from an *ab initio* perspective: to explain the observed nonlinearities in the

total capacitance by identifying the key structural changes in the compact layer. In principle, JDFT computes the thermodynamically favored $T > 0$ minimum energy state of the system, so it should be capable of predicting the total capacitance signal in the adiabatic limit. In practice, JDFT captures the complex interplay between electrostatics and the entropy of packing which leads to the properties of the inner and outer Helmholtz planes in the electrochemical double layer, but it would not include any of the quantum-mechanical effects of specific adsorption unless explicit adsorbed species are included in the calculations. In some cases the electrolyte could attain a lower minimum energy by forming a chemical bond, leading to additional charging capacity. Furthermore, the model electrode in JDFT calculations is also smooth, without the defects and roughness of the real surface which can increase the surface area and thus the capacitance. We therefore expect JDFT predictions with a pure classical DFT description of the adsorbates to under-predict experimental capacitances. We thus expect that in any system in which chemical bonding becomes important, the JDFT-computed capacitance should lie in between the static high-frequency capacitance measurement and the adiabatic low-frequency capacitance measurement.

Perhaps the greatest opportunity for JDFT to provide new insights lies in the fact that the separation of the interfacial fluid capacitance into two capacitors in series via the Gouy-Chapman-Stern model is an artificial construct. While such models may work well in some ideal systems, such electrochemical models lose their predictive power when the physical assumptions involved break down unexpectedly. Because JDFT treats the electrode-electrolyte interface through a holistic, first-principles approach, it remains a predictive theory, within the limits of the approximate functionals of course.

4.3 Free Energy Functionals

This section presents the functionals Ω_{lq} and ΔA which facilitate JDFT calculations of quantum-mechanical electrode surfaces in contact with an electrolyte environment.

4.3.1 Classical Water Functional

Recent work by Lischner et. al. introduced a new classical density-functional for water [170, 171], which solves the "inversion problem," which had previously kept orientation-dependent functionals from widespread use, by choosing effective site potentials as the independent variables. This work has been extended by Sundararaman et. al. [262] to allow any independent variables from which it is computationally feasible to calculate $P_\omega(\vec{r})$, the probability of a water molecule at location $\vec{r}$ to possess orientation ω. Typically, the effective local chemical potential $\mu(\vec{r})$ and the effective local electric field $\vec{\epsilon}(\vec{r})$ are the independent variables which best represent $P_\omega(\vec{r})$. This new free energy functional (in atomic units) then takes the form

$$\Omega_{lq}[P_\omega] = T \int d^3r P_\omega(\vec{r})(\log P_\omega(\vec{r}) - 1) + \int d^3r(V_\alpha - \mu)N_\alpha + F_{ex}[\{N_\alpha\}, P_\omega], \quad (4.9)$$

where the first term is the energy of a non-interacting ideal gas constrained to the molecular geometry of water, the second term describes the linear coupling of the site densities $N_\alpha(\vec{r})$ ($\alpha = O, H$) to external potentials $V_\alpha(\vec{r})$ and the chemical potential μ, and the third is an "excess" functional, including all other interactions. As these developments first focused on singles species fluids, only a single true chemical potential μ was needed in that work.

Sundararaman et. al. [262] then developed an excess functional based upon fundamental measure theory (FMT) for hard spheres [234, 272], the experimentally measured equation of state for bulk liquid water [128], and both rotational and polarizability contributions to the dielectric response [266]. This functional is given by

$$F_{ex}[\{N_\alpha, P_\omega\}] = \Phi_{FMT}[N_O] + \int d^3 r \bar{N} A_{EOS}(\bar{N} * w_{LJ}, T) + \Phi_\epsilon[\{N_\alpha\}, P_\omega], \qquad (4.10)$$

where the first term considers hard-sphere behavior, the second includes isotropic attraction constrained to the equation of state of water, and the third contains the long-range Coulomb interactions which contribute to the dielectric response of the liquid. All parameters in this classical DFT functional are completely determined by basic physics and the bulk properties of liquid water, such as surface tension, liquid-vapor coexistence, and the measured dielectric constant.

The first two terms in Equation 4.10 capture the orientation-independent short-range interactions between the water molecules, separated into a repulsive component and an attractive component. The repulsive interactions between the water molecules are computed using the White-Bear Mark II fundamental measure theory functional [103], Φ_{FMT}, with a single hard sphere of radius R_O^{HS} centered on the oxygen site. This FMT functional uses the Tarazona tensor functions of the weighted density [272] to reproduce the Percus-Yevick equation of state and the direct correlations for a hard-sphere fluid. (We note that without the tensor terms, FMT cannot describe hard-sphere freezing because the free-energy functional diverges under confinement [234], rendering it unsuitable for use within JDFT.) Sundararaman et al. constrains the FMT hard-sphere radius to reproduce the bulk liquid-vapor surface tension [262], yielding $R_O^{HS} = 1.36\text{Å}$ for water, quite close to the van der Waals radius $R_{vdW} = 1.385\text{Å}$

determined from the exclusion volume in the water equation of state [19]. The classical DFT for water thus accurately predicts the location of the first peak in the oxygen-oxygen correlation function, which FMT places at $2R^{HS}$ by construction.

Sundararaman et. al. also models the short- to mid-range attractions through the term $A_{EOS}(\bar{N} * w_{LJ}, T)$, the excess per molecule Helmholtz free energy, as determined from experimental measurements of the pressure of bulk water $p(N, T)$ as a function of the density N and temperature T [262]. To determine this excess free energy, one begins with the energy derived from the Jeffrey-Austin equation of state for liquid water [128] and then subtracts the free energy corresponding to the Carnahan-Starling hard-sphere equation of state [39], since Φ_{FMT} already accounts for the repulsive portion of the free energy. The excess free energy is then evaluated at the polarizability-weighted density

$$\bar{N} = \frac{\sum_\alpha \chi_\alpha N_\alpha}{\chi_{tot}} \tag{4.11}$$

(where χ_α is the effective dipole polarizability of site α from Table 2.1 and χ_{tot} is the total dipole polarizability of the molecule) convolved with a normalized attractive Lennard-Jones weight function [161]

$$w_{LJ}(\vec{r}) = \frac{9}{8\sqrt{2}\pi\sigma^3} \begin{cases} 1/4, & r < 2^{1/6}\sigma \\ \left(\frac{\sigma}{r}\right)^6 - \left(\frac{\sigma}{r}\right)^{12}, & r \geq 2^{1/6}\sigma \end{cases}. \tag{4.12}$$

For water, the polarizability is approximately isotropic, so most of the short-ranged attraction is attributed to the molecule center (the oxygen site). Finally, the Lennard-Jones diameter σ used in the weight function w_{LJ}, which controls the range of the intermolecular attraction, is specified to be $2R^{HS}$ as is established practice for Lennard-Jones fluids.

The long-range electrostatic interactions between the fluid molecules are captured via the last term in Equation 4.10, which is dependent on both the atomic site densities $\{N_\alpha\}$ and the orientation P_ω. Unlike the initial classical DFT functional based upon the equation of state for water [262], which employed an empirical scaling factor upon the mean-field Coulomb interaction [171] to capture the bulk dielectric constant, the polarizable classical DFT for water employs the unmodified mean-field Coulomb interaction and then includes additional terms to capture the contributions to the dielectric response from rotations and polarizability [266]. These additional terms introduce a new independent variable, the polarization density $\vec{\mathcal{P}}_\alpha(\vec{r})$, into Ω_{lq}. The total electrostatic contribution to the excess functional is thus

$$\Phi_\epsilon[\{N_\alpha\}, P_\omega] = \frac{1}{2} \int d^3r \int d^3r' \ \frac{\rho_{\text{MF}}(\vec{r})\rho_{\text{MF}}(\vec{r'})}{|\vec{r} - \vec{r'}|} + \Phi_{\text{pol}}[\{N_\alpha\}, \vec{\mathcal{P}}_\alpha] + \Phi_{\text{rot}}[\{N_\alpha\}, \vec{\mathcal{P}}_\alpha] \quad (4.13)$$

where ρ_{MF} is computed as described in Section 2.4, Φ_{pol} captures the electrostatic energy due to polarizability, and Φ_{rot} captures the electrostatic energy due to the rotations of the solvent molecules. The specific details for the two final terms are irrelevant to the present work, but they do depend on microscopic quantities, such as the site polarizabilities χ_α from Table 2.1 and the dipole moment of the solvent molecule, as well as bulk quantities such as the dielectric constant. These details are presented fully in Reference [266]. Of course, for liquid water, the dielectric response due to rotations of the molecule dominates, so the inclusion of the polarizability terms has little impact on most calculations (as demonstrated by Figure 1.1).

4.3.2 Extension to Aqueous Electrolyte

Following the above construction for pure water, the liquid free energy may be extended in a straightforward way to include the ions in the electrolyte. Specifically, we generalize Equation 4.9 as

$$\Omega_{\text{lq}} = \Omega_{\text{NI}} + \int d^3 r (V_\alpha - \mu_\alpha) N_\alpha + \int d^3 r F_{\text{ex}}[\{N_\alpha\}, P_\omega], \tag{4.14}$$

where Ω_{NI} includes the noninteracting energy of each liquid species, the second term describes linear coupling to the external potential acting on each species V_α and the individual species' chemical potentials μ_α, and the third term is the excess functional, which describes all other contributions. The noninteracting energy, $\Omega_{\text{NI}} = \Omega_{H_2O} + \sum_\gamma \Omega_{\text{NI},\gamma}$, is simply the free energy of an ideal gas of water molecules from [171], plus the free energy of an ideal gas of each ion. For a monoatomic ionic species, the *analytically exact* non-interacting free energy is

$$\Omega_{\text{NI},\gamma} = T \int d^3 r N_\gamma (\log N_\gamma - 1), \tag{4.15}$$

and the most straightforward independent variable for these calculations is the effective site potential $\psi_\gamma(\vec{r})$, which yields the given density $N_\gamma(r)$ of a non-interacting system.

Each ionic species (indexed by γ) may be approximated as a sphere of radius R_γ^{HS} with a site charge q_γ. The main interactions between the ionic species and water are thus (a) hard-sphere repulsion, captured by fundamental measure theory for a mixture of hard spheres of different sizes [103], and (b) the mean-field Coulomb interaction. Any interactions between the ions and the water not captured by the hard sphere and Coulomb terms may be grouped into a "mixing" functional F_{mix}, which depends on the oxygen site density N_O and the ion site density N_γ for ion type γ. For this initial work, we choose to forgo consideration

of N_H because N_O describes the primary center for *non-electrostatic* interactions with the water molecules. Combining these effects together, the excess functional for an aqueous electrolyte may be written as

$$F_{ex}[\{N_\alpha\}] = \Phi_{FMT}[N_O, \{N_\gamma\}] + \frac{1}{2} \int d^3r \int d^3r' \ \frac{\rho_{MF}(\vec{r})\rho_{MF}(\vec{r}')}{|\vec{r} - \vec{r}'|}$$

$$+ \sum_\gamma F_{mix}[N_O, N_\gamma] + \Delta F_{H_2O}, \qquad (4.16)$$

where ΔF_{H_2O} simply represents those parts of the excess functional for water in Equation 4.10 which are not captured by mean-field coulomb and hard-sphere interactions (the properties from the bulk water equation of state and the polarizability of water) [262, 266]. In the present work, we neglect the interactions of the ionic species with themselves and each other beyond the mean-field coulomb interaction between charged hard spheres, judging such effects to be small due to the relatively low density of ionic species compared to water molecules. We also ignore the polarizabilities of the ions within the classical DFT, though the liquid water remains polarizable.

4.3.3 Coupling Functional for Electrolyte

In order to couple the classical DFT description of an aqueous electrolyte to a solute system through JDFT, we must extend the coupling functional ΔA to include ion-solute coupling. Because the liquid-solute coupling functional in Chapter 2 was shown to be independent of the choice of neutral solvent, we choose to employ the same form for this work as well. Ideally, we should test this coupling functional on a trial set including solvated ionic species (in addition to neutral molecules) in order to verify that it performs equally well for charged systems. Indeed, benchmarking endeavors for solvated ions following the procedure of

Section 2.6.1 will be the subject of future work. Section 4.5.4 sets forth all additional specific details required to extend the coupling functional to electrolyte liquids.

4.4 Treatment of Charged Systems

In order for JDFT to be utilized for predictive calculations of electrochemical systems, we must establish a framework for computing the properties of charged systems under the influence of an applied potential. This framework must naturally handle both the balance of charge between the fluid and solute subsystems and establish the relationship of the applied potential to the standard electrochemical reference electrodes. The following subsections elucidate the mathematical and computational procedures required to determine the properties of charged systems within explicit JDFT.

4.4.1 Charge Balance Framework

To prevent energy divergence due to a net charge in a periodic unit cell of volume V, the charge present in the electrolyte fluid must exactly cancel the net charge in the explicit quantum-mechanical system, $Q_{el} = \tilde{\rho}_{el}(G = 0)$, where $\tilde{\rho}_{el}(G = 0) = \int \rho_{el} dV$ is the $G = 0$ component of the charge density of the quantum-mechanical system. Mathematically, we can write this constraint on the total charge in the unit cell Q_{tot} as

$$Q_{tot} = \sum_{\gamma} \mathcal{N}_{\gamma} q_{\gamma} + Q_{el} = 0 \tag{4.17}$$

where $\mathcal{N}_{\gamma}$ is the total number of ions of type γ with ion charge q_{γ}.

Density Scaling Procedure

However, we cannot achieve this required charge balance without an additional framework for constraining the total charge in the fluid. The number of ions of type γ (without this framework) is

$$\mathcal{N}_\gamma^0 = \int N_\gamma^0(\vec{r}) d^3r, \tag{4.18}$$

computed as the integral over the unit cell of the site density $N_\gamma^0(\vec{r})$ determined from the liquid free-energy functional Ω_{lq} and the appropriate independent variables. For single-site or monoatomic ions, the independent variables are the effective site potentials $\psi_\gamma(\vec{r})$, so the atomic site densities (and therefore the total number of atoms $\mathcal{N}_\gamma^0$) are simply computed from the ideal gas free energy as $N_\gamma^0(\vec{r}) = \frac{\delta\Omega_{NI}}{\delta\psi_\gamma(\vec{r})}$. Unfortunately, Equation 4.17 is not generally satisfied by the unscaled atomic site densities $N_\gamma^0(\vec{r})$ resulting from any naive choice of effective site potentials $\psi_\gamma(\vec{r})$.

To ensure the total charge of the fluid is equal and opposite to the charge of the solute, we introduce a fugacity factor S_γ^B (with electrochemical potential μ_0) which scales the atomic site densities according to their charges,

$$N_\gamma(\vec{r}) = N_\gamma^0(\vec{r}) \exp\left(-\beta q_\gamma \mu_0\right) = N_\gamma^0(\vec{r}) S_\gamma^B \tag{4.19}$$

where $\beta = \frac{1}{k_B T}$ for temperature T. The potential μ_0 may then be determined from the solution of Equation 4.17 with the fugacity-scaled site densities

$$Q_{\text{tot}} = \sum_\gamma \mathcal{N}_\gamma^0 q_\gamma \exp\left(-\beta q_\gamma \mu_0\right) + Q_{\text{el}} = 0. \tag{4.20}$$

In practice, we iteratively solve this equation using a Newton-Raphson algorithm. The scaled atomic site densities $N_\gamma(\vec{r})$, as opposed to the unscaled densities $N_\gamma^0(\vec{r})$, are then used to compute Ω_{lq} and ΔA.

Charge-Neutrality Constrained Minimization

The above procedure effectively performs a constrained minimization of the free-energy functional with an added Lagrange multiplier λ and the constraint given by Equation 4.20. In fact, Reference [100] describes how including the charge-neutrality constraint imposed by the Lagrange multiplier λ is formally equivalent to regularization of the divergent Coulomb energy. In this view, the Lagrange multiplier λ is computed from the Euler-Lagrange equation as the total derivative of the free energy functional A with respect to total charge on the system, $\lambda = \frac{dA}{dQ_{\text{tot}}}$. Since the the atomic density scale factors S_γ^B used in the total free energy functional depend implicitly on Q_{tot} through the potential μ_0, we employ the chain rule to compute the Lagrange multiplier as

$$\lambda = \sum_\gamma \frac{\delta A}{\delta S_\gamma^B} \frac{\delta S_\gamma^B}{\delta \mu_0} \frac{\delta \mu_0}{\delta Q_{\text{tot}}}. \tag{4.21}$$

From Equation 4.19, we compute $\frac{\delta S_\gamma^B}{\delta \mu_0} = -\beta q_\gamma S_\gamma^B$ and Equation 4.20 allows determination of $\frac{\delta Q_{\text{tot}}}{\delta \mu_0} = -\beta \sum_\gamma q_\gamma^2 \mathcal{N}_\gamma$. We may then compute the partial derivative with respect to the scaling factor as

$$\frac{\delta A}{\delta S_\gamma^B} = \frac{1}{S_\gamma^B} \int d^3 r \ \frac{\delta A}{\delta N_\gamma(\vec{r})} N_\gamma(\vec{r}). \tag{4.22}$$

Finally, combining all the above expressions yields the Lagrange multiplier

$$\lambda = \sum_\gamma \int d^3 r \ \frac{\delta A}{\delta N_\gamma(\vec{r})} N_\gamma(\vec{r}) \frac{q_\gamma}{\sum_{\gamma'} Q_{\gamma'}^2 \mathcal{N}_{\gamma'}} \tag{4.23}$$

Of course, this constrained minimization procedure also introduces some additional terms into the gradient of $\Omega_{\text{lq}} + \Delta A$ with respect to the site densities $N_\alpha(\vec{r})$. The key quantity required for computation of the gradients of the free energy with respect to the site densities is the Jacobian

$$\frac{\delta S_\gamma^B}{\delta \mathcal{N}_\alpha^0} = \frac{\delta S_\gamma^B}{\delta Q_{\text{tot}}} \frac{\delta Q_{\text{tot}}}{\delta \mathcal{N}_\alpha^0}. \tag{4.24}$$

where we use the same chain-rule expression for $\frac{\delta S_\gamma^B}{\delta Q_{tot}}$ as in Equation 4.23. The latter partial derivative can be computed from Equation 4.20 as $\frac{\delta Q_{tot}}{\delta \mathcal{N}_\alpha^0} = q_\alpha S_\alpha^B$, leading to a final expression for the Jacobian,

$$\frac{\delta S_\gamma^B}{\delta \mathcal{N}_\alpha^0} = \frac{q_\gamma q_\alpha S_\gamma^B S_\alpha^B}{\sum_{\gamma'} Q_{\gamma'}^2 \mathcal{N}_{\gamma'}}. \tag{4.25}$$

This Jacobian is then employed to compute the addition to the gradient of the free energy A with respect to $N_\alpha(\vec{r})$ due to the charge scaling procedure,

$$\frac{\delta A}{\delta N_\alpha(\vec{r})} = \frac{\delta A}{\delta N_\alpha^0(\vec{r})} + \frac{\delta A}{\delta S_\gamma^B} \frac{\delta S_\gamma^B}{\delta \mathcal{N}_\alpha^0} \frac{1}{S_\alpha^B M_\alpha}, \tag{4.26}$$

where we have utilized Equations 4.22 and 4.25 and the number of sites of type α in the molecule M_α.

The gradients of the free energy A with respect to $N_\alpha(\vec{r})$ also propagate into the gradients with respect to the independent variables ($\psi_\gamma(\vec{r})$ for a monoatomic gas). These terms are therefore essential to restricting the conjugate gradient-based minimization algorithm employed to find the minimum JDFT free energy to those solutions which are charge-balanced. We note that these terms are only significant for the charged species in the liquid; both Equations 4.25 and 4.23 vanish for uncharged species. Nonetheless, in electrolyte calculations, the neutral solvent molecules are indeed affected by these considerations indirectly through their interactions with the charged electrolyte species.

4.4.2 Establishing Potential Reference

In order to directly compare JDFT predictions to experimentally measured cyclic voltammograms, differential capacitances, and oxidation/reduction potentials we must establish a relationship between the applied potentials computed by

JDFT and the electrochemical reference electrodes, such as the Standard Hydrogen Electrode (SHE). Section 3.3 describes in detail the significance of the asymptotic value of the total electrostatic potential ϕ_{el} deep in the fluid to the establishment of a reference electrode. In this section, we will show how to ensure that the total potential acting upon the electrons deep within the fluid is zero within JDFT calculations of charged fluids.

Reference [100] shows that the constrained minimization procedure described in Section 4.4.1 above also precisely determines the $G = 0$ component of the electrostatic potential ϕ_{el} and allows the establishment of an absolute potential reference. In fact, when projecting the $G = 0$ component out for all electrostatic interactions (as is standard practice in plane-wave DFT calculations) the absolute potential far away from the electronic system is, in the case of implicit solvent models with a nonlinear Poisson-Boltzmann description of the electrolyte, exactly the Lagrange multiplier λ. Thus, choosing $-\lambda$ as the $G = 0$ component of the total electrostatic potential ensures that (in an implicit solvent) the asymptote of that electrostatic potential is zero deep in the liquid. This formal definition of the absolute potential generalizes quite cleanly to explicit JDFT, but does require several essential modifications.

Bulk Fluid Electron Potential

The first modification to the absolute potential reference required for an explicit solvent involves the potential acting upon the electrons deep within the bulk liquid, V_{el}^b. For the implicit solvent models presented in References [100] and [163], this potential is $\frac{\delta A}{\delta \rho_{el}} = 0$ in the bulk liquid. However, for an explicit JDFT calculation this electron potential is no longer negligible. We may define it pre-

cisely as

$$V_{\text{el}}^b = \left.\frac{\delta A}{\delta \rho_{\text{el}}}\right|_{\substack{\{N_\alpha\}\to\{N_\alpha^b\} \\ n\to n_{\text{lq}}^b}}, \tag{4.27}$$

where N_α^b and n_{lq}^b are, respectively, the atomic site densities and the electron density in the bulk fluid. This bulk fluid electron density may be computed simply as the sum over the bulk atomic site densities multiplied by the number of electrons on each fluid site,

$$n_{\text{lq}}^b = \sum_\alpha N_\alpha^b \int d^3r \; n_\alpha(r). \tag{4.28}$$

Of course, the atomic site and electron densities depend on the composition of the bulk fluid, and thus even in an aqueous solution different choices of electrolyte yield slightly different values for the electron potential deep in the bulk of the fluid.

When the liquid and solute are coupled via the functional ΔA presented in Chapter 2, this electron potential is

$$V_{\text{el}}^b = \left.\frac{\delta \mathcal{F}}{\delta n_S}\right|_{\substack{\{N_S\}\to\{N_\alpha^b\} \\ n_S\to n_{\text{lq}}^b}}, \tag{4.29}$$

where $\mathcal{F}$ is the density-only functional in Equation 2.9, n_S is the electron density, and N_S is the set of nuclear site densities. The most straightforward piece of the fluid electron potential comes from the kinetic energy and exchange-correlation parts of the density-only functional, $\frac{\delta T_{TF}}{\delta n_S} + \frac{\delta E_{XC}}{\delta n_S}$. However, there is an additional offset due to the mean-field Hartree term, which we discuss in Section 4.4.2 below.

For the electrolyte fluids considered in this thesis, Table 4.4 lists the values of the electron potential in the bulk of the fluid. These values are related, though not directly comparable, to the fluid-air interface potentials predicted in the literature [165]. These JDFT electron fluid potentials consider the self-consistent

164

potential acting on an electron deep in the fluid, without considering the structure of the liquid which would form at the air/liquid interface. Because the interfacial fluid structure would possess a dipole moment, the potential required to move an electron through that dipole layer must be added to the bulk potential from Equation 4.29 to allow direct comparison to the fluid-air interface potentials predicted in the literature.

Charge Density Mismatch Potential

An additional correction to the $G = 0$ component of the electrostatic potential is required due to the different representations of the fluid charge density used in the classical liquid functional Ω_{lq} and the coupling functional ΔA . The charge density of fluid site α felt by the fluid is $\rho_\alpha(r)' = q_\alpha w_{\text{MF}}(r)$, determined from the fluid site charges q_α, Equation 2.21 for water, and Equation 4.55 for ions. In contrast, the charge density felt by the electronic solute system is $\rho_\alpha(r)$ (from Equation 2.17). These mismatched charge density models are both spherically symmetric about the fluid site and they contain the same total charge, namely $\tilde{\rho}'_\alpha(0) = \tilde{\rho}_\alpha(0)$. The difference between the charge density models may thus be defined as $\Delta\rho_\alpha = \rho_\alpha - \rho'_\alpha$, which by definition has no $G = 0$ component ($\tilde{\Delta\rho}_\alpha(0) = 0$). The charge model mismatch above means the total mean-field charge density of the fluid as it interacts with itself is computed as $\rho_{\text{MF}}(\vec{r}) = \sum_\alpha N_\alpha * \rho'_\alpha$ (as in Equation 2.22) while the charge density of the fluid as it couples with the electronic system is $\rho_{\text{C}}(\vec{r}) = \sum_\alpha N_\alpha * \rho_\alpha$ (as in Equation 2.19).

The total electrostatic energy (including the Lagrange multiplier constraint upon charge neutrality from Equation 4.23) may therefore be written in terms

of the above densities as

$$U_{\text{el}} = \int d^3r \int d^3r' \left(\frac{\frac{1}{2}\rho_{\text{el}}(\vec{r})\rho_{\text{el}}(\vec{r}') + \rho_{\text{el}}(\vec{r})\rho_{\text{C}}(\vec{r}') + \frac{1}{2}\rho_{\text{MF}}(\vec{r})\rho_{\text{MF}}(\vec{r}')}{|\vec{r} - \vec{r}'|} \right)$$

$$-\lambda \int d^3r \left[\rho_{\text{el}}(\vec{r}) + \rho_{\text{MF}}(\vec{r}) \right], \qquad (4.30)$$

where $\rho_{\text{el}}(\vec{r})$ is the total charge density of the electronic system, including electrons and nuclei. At this point, it is helpful to define the total charge *felt by the fluid* due to the electronic and mean-field charges as $\rho_{\text{fl}} = \rho_{\text{el}} + \rho_{\text{MF}}$. The total electrostatic potential arising from that charge may then be found through the Poisson equation

$$\nabla^2 \phi_{\text{fl}}(\vec{r}) = -4\pi \rho_{\text{fl}}(\vec{r}), \qquad (4.31)$$

leading to the real-space form

$$\phi_{\text{fl}}(\vec{r}) = \int d^3r' \, \frac{\rho_{\text{fl}}(\vec{r}')}{|\vec{r} - \vec{r}'|}. \qquad (4.32)$$

The potential ϕ_{fl} is a solution to Poisson's equation for a neutral charge distribution, so there is no divergence or regularization required for the $G = 0$ component in Fourier space. It is also therefore straightforward to solve for this potentials in fourier space as $\tilde{\phi}_{\text{fl}}(G \neq 0) = \frac{4\pi}{G^2}\tilde{\rho}_{\text{fl}}$.

We may now rewrite Equation 4.30 in terms of ϕ_{fl} and ρ_{fl} as

$$U_{\text{el}} = \frac{1}{2} \int d^3r \, \phi_{\text{fl}}(\vec{r})\rho_{\text{fl}}(\vec{r}) + \int d^3r \int d^3r' \, \frac{\rho_{\text{el}}(\vec{r}) \sum_\alpha (N_\alpha * \Delta\rho_\alpha)(\vec{r}')}{|\vec{r} - \vec{r}'|} - \lambda \int d^3r \, \rho_{\text{fl}}(\vec{r}),$$

$$(4.33)$$

where we have made the substitution

$$\rho_{\text{C}}(\vec{r}) = \rho_{\text{MF}}(\vec{r}) + \sum_\alpha (N_\alpha * \Delta\rho_\alpha)(\vec{r}). \qquad (4.34)$$

The first term in Equation 4.33 is the mean-field self-interaction of a neutral charge density and the final term should be zero to satisfy the neutrality constraint imposed by the Lagrange multiplier. The self-interaction is straightforwardly computed by using the fourier techniques above and projecting out the

$G = 0$ component, as is standard practice within DFT calculations. The second term, which now contains all the effect of the charge model mismatch, must be dissected carefully in Fourier space to determine its $G = 0$ component.

Expressing the charge mismatch term from the electrostatic energy (second term in Equation 4.33) in fourier space rather than real-space and separating the energy due to the $G \neq 0$ terms from the energy due to the $G = 0$ terms, yields

$$U_\Delta = \sum_{G \neq 0} \frac{4\pi}{G^2} \tilde{\rho}_{el} \sum_\alpha \tilde{N}_\alpha \tilde{\Delta\rho}_\alpha + \lim_{G \to 0} \left(\frac{4\pi}{G^2} \tilde{\rho}_{el}(G) \sum_\alpha (\tilde{N}_\alpha(G) \tilde{\Delta\rho}_\alpha(G)) \right), \tag{4.35}$$

where we take the limit as $G \to 0$ to regularize the divergence of the Coulomb operator for $G = 0$. To determine the scalar value of the $G \to 0$ term, we may rewrite it as

$$U_\Delta(G = 0) = \frac{Q_{el}}{V} \sum_\alpha N_\alpha \lim_{G \to 0} \left(\frac{4\pi}{G^2} \tilde{\Delta\rho}_\alpha(G) \right), \tag{4.36}$$

in which we have used the integrals $\tilde{\rho}_{el}(0) = Q_{el}$ and $\tilde{N}_\alpha(0) = N_\alpha$ for the net electronic charge and the total number of atoms of type α with site charge q_α respectively, and included the proper volume normalization factor $\frac{1}{V}$.

If we group the remainder of Equation 4.36 into a new constant

$$\Delta C_\alpha = \lim_{G \to 0} \left(\frac{4\pi}{G^2} \tilde{\Delta\rho}_\alpha(G) \right), \tag{4.37}$$

we obtain the simple form

$$U_\Delta(G = 0) = \frac{Q_{el}}{V} \sum_\alpha N_\alpha \Delta C_\alpha. \tag{4.38}$$

However, Equation 4.37 requires careful consideration due to subtleties of the limit-taking. When $\tilde{\Delta\rho}_\alpha(G)$ is expanded about the $G \to 0$ limit, the leading term depends on G^2 because $\tilde{\Delta\rho}_\alpha(0) = 0$ and the function is spherically symmetric in real-space. The exact form of the leading term in $\tilde{\Delta\rho}_\alpha(G)$, and thus the numerical

value of ΔC_α, depends on the functional forms chosen for the site charge models $\rho_\alpha(r)$ and $\rho'_\alpha(r)$.

To determine a prescription for computing the contribution to the electrostatic energy from Equation 4.36, we define a set of electrostatic potentials due to the differences in site charge density model through the Poisson equation

$$\nabla^2 \Delta\phi_\alpha(r) = -4\pi\Delta\rho_\alpha(r), \tag{4.39}$$

and fourier solution $\tilde{\Delta\phi}_\alpha(G) = \frac{4\pi}{G^2}\tilde{\Delta\rho}_\alpha(G)$. In terms of the potential $\Delta\phi_\alpha$, the expression for C_α then becomes

$$\Delta C_\alpha = \tilde{\Delta\phi}_\alpha(0) = \int d^3r \ \Delta\phi_\alpha(r). \tag{4.40}$$

We can relate the integral of the potential $\Delta\phi_\alpha(r)$ to the charge density $\Delta\rho_\alpha(r)$ through Gauss's Law for a spherically symmetric charge distribution, resulting in the more useful expression,

$$\Delta C_\alpha = -\frac{2\pi}{3}\int d^3r \ r^2\Delta\rho_\alpha(r). \tag{4.41}$$

The above equation for ΔC_α is straightforward to compute numerically using the mean-field fluid site density ρ'_α (from Equation 2.21 and the fluid site charges q_α) and the electronic coupling fluid site density ρ_α (from Equation 2.17). We note that these $G = 0$ corrections are generally required for the charged atomic sites of both neutral and charged molecules, so corrections for the oxygen and hydrogen sites of water in an aqueous electrolyte are indeed necessary.

Finally, we may now determine the contribution to the potential offset due to the charge mismatch as the difference between the $G = 0$ component of the potential experienced by the electrons,

$$\tilde{V}_{el}(G = 0) = \frac{\delta U_{el}}{\delta\rho_{el}}(G = 0) = \sum_\alpha \frac{N_\alpha}{V}\Delta C_\alpha - \lambda, \tag{4.42}$$

and the $G = 0$ component of the sum of the potentials experienced by the fluid sites

$$\tilde{V}_{\text{fl}}(G = 0) = \sum_\alpha M_\alpha \frac{\delta U_{\text{el}}}{\delta N_\alpha}(G = 0) = \sum_\alpha M_\alpha \left(\frac{Q_{\text{el}}}{V} \Delta C_\alpha - \lambda q_\alpha \right), \tag{4.43}$$

where M_α is the number of sites of type α per molecule and $q_\alpha = \tilde{\rho}'_\alpha(0)$ is the site charge. For a monovalent electrolyte in a neutral solvent, $\sum_\alpha M_\alpha q_\alpha = 0$, so the second term in $\tilde{V}_{\text{fl}}(G = 0)$ does not contribute. Combining the charge mismatch and bulk fluid electron potentials, we find the full $G = 0$ contribution to the absolute potential for an explicit JDFT electrolyte to be

$$\Delta = -V_{\text{el}}^b + \tilde{V}_{\text{el}}(G = 0) - \tilde{V}_{\text{fl}}(G = 0). \tag{4.44}$$

Upon examination of Equation 4.33, it is also clear that the bulk fluid electron potential V_{el}^b has an additional contribution due to the charge mismatch. Namely, we must add

$$\frac{\delta U_{\text{el}}}{\delta \rho_{\text{el}}}(G = 0)\Bigg|_{\substack{\{N_\alpha\} \to \{N_\alpha^b\} \\ n \to n_{\text{lq}}^b}} = \sum_\alpha N_\alpha^b \Delta C_\alpha \tag{4.45}$$

to the kinetic energy and exchange-correlation components of the electron potential. With this new contribution, the electron potential becomes

$$V_{\text{el}}^b = \frac{\delta(T_{TF}[n] + E_{XC}[n])}{\delta n}\Bigg|_{n \to n_{\text{lq}}^b} + \sum_\alpha N_\alpha^b \Delta C_\alpha \tag{4.46}$$

and the $G = 0$ component of the absolute potential becomes

$$\Delta = -\frac{\delta(T_{TF}[n] + E_{XC}[n])}{\delta n}\Bigg|_{n \to n_{\text{lq}}^b} + \sum_\alpha \left(\frac{N_\alpha}{V} - \frac{M_\alpha Q_{\text{el}}}{V} - N_\alpha^b \right) \Delta C_\alpha - \lambda. \tag{4.47}$$

Figure 4.8 shows that the unique choice of absolute potential presented in Equation 4.47 does ensure that the microscopic electron potential deep in the fluid does indeed approach zero, allowing establishment of a reference electrode and direct comparison to electrochemical measurements.

4.5 Model Ions

We now describe the particular approximations which we utilize in this chapter for the description of the ionic species in the electrolyte.

4.5.1 Quadratic Mixing Functional Approximation

As described in Section 4.3, the interactions amongst the different fluid components (beyond hard sphere and Coulomb energy) are captured by distinct portions of the functional Ω_{lq}. We neglect both the self-interactions of the ionic species and their interactions with other types of ions because the concentration of ions is quite low (only one positive and one negative ion for every 55 water molecules in a 1.0 M aqueous solution). The mid-range attractive interaction of the water with itself is captured by the constrained weighted-density approximation in the term $\int d^3 r \bar{N} A_{\text{EOS}}(\bar{N} * w_{\text{LJ}})$ of Equation 4.10. Because of the plethora of experimental state data available for liquid water, the equation of state can be used to constrain the attractive interaction for water to physical reality. Ideally, we should also capture the mid-range interactions of the water with the ions in $F_{\text{mix}}[N_O, N_\gamma]$ with a similar weighted-density approximation constrained by the equation of state for electrolyte liquids.

The general form (ignoring ion-ion contributions beyond hard sphere and electrostatic interactions) for such a weighted-density approximation between two different density fields N_O and N_γ with free-energy functionals $A_{O,\gamma}$ and $A_{\gamma,O}$ is

$$F_{\text{mix}}[N_O, N_\gamma] = \int d^3 r N_O A_{O,\gamma}(N_\gamma * w_{\text{LJ}}) + \int d^3 r N_\gamma A_{\gamma,O}(N_O * w_{\text{LJ}}), \qquad (4.48)$$

where the Lennard-Jones weight function w_{LJ} from Equation 4.12 is normalized ($\int d^3r\ w_{\mathrm{LJ}}(r) = 1$). This normalization is necessary in order to ensure the correct bulk free energy of the liquid $A_{O,\gamma}(N_\gamma^b * w_{\mathrm{LJ}}) = A_{O,\gamma}(N_\gamma^b)$. The contribution to the free energy of the bulk fluid in volume V due to this weighted density-functional is thus

$$\Omega_\gamma^b = V\left(N_O^b A_{O,\gamma}(N_\gamma^b) + N_\gamma^b A_{\gamma,O}(N_O^b)\right). \tag{4.49}$$

In the dilute limit $N_\gamma^b \to 0$, and we can consider only the leading term of $A_{O,\gamma}(N_\gamma^b)$, reducing the bulk free energy to

$$\Omega_\gamma^b = VN_\gamma^b(N_O^b a_{O,\gamma} + A_{\gamma,O}(N_O^b)) \tag{4.50}$$

where $a_{O,\gamma}$ is a constant and $N_O^b a_{O,\gamma} + A_{\gamma,O}(N_O^b)$ is a function of only the bulk density of the water. The form of this function can, in principle, be constrained by the equation of state for the bulk electrolyte by considering $\frac{d\Omega_\gamma^b}{dN_\gamma^b} = V(N_O^b a_{O,\gamma} + A_{\gamma,O}(N_O^b))$. Experimental data for the vapor pressures and fluid densities as a function of salt concentration are available in the literature for various electrolytes (including the alkali halides) [35] and this data could be used to constrain the form of $\frac{d\Omega_\gamma^b}{dN_\gamma^b}$. Such a weighted-density approach can capture many-body effects in nonuniform fluids [145] and mixtures of fluids [58].

For this first attempt at constructing a classical DFT for an aqueous electrolyte, we consider only the leading order terms in Equation 4.48, yielding a simplified quadratic mixing functional

$$F_{\mathrm{mix}}[N_O(\vec{r}), N_\gamma(\vec{r})] = a_\gamma \int d^3r N_O(\vec{r})(w_{\mathrm{LJ}} * N_\gamma)(\vec{r}) \tag{4.51}$$

where a_γ is a constant. With the choice of $a_\gamma = 4\epsilon_\gamma \frac{8\sqrt{2}\pi\sigma_\gamma^3}{9}$, the interaction potential between the oxygen density N_O and the ion density N_γ takes on the traditional

Lennard-Jones form [161] without the repulsive core,

$$
V_{LJ}(\vec{r}) \begin{cases} -\epsilon_\gamma, & r < 2^{1/6}\sigma_\gamma \\ 4\epsilon_\gamma \left(\left(\frac{\sigma_\gamma}{r}\right)^{12} - \left(\frac{\sigma_\gamma}{r}\right)^6 \right), & r \geq 2^{1/6}\sigma_\gamma, \end{cases} \tag{4.52}
$$

where ϵ_γ is the potential energy scale and σ_γ is the interaction range. This attractive potential is shown by the solid red line in Figure 4.6 and the full Lennard-Jones potential, including the repulsive core, is shown by the dotted red line.

In Fourier space, the mixing functional in Equation 4.51 thus becomes

$$
F_{\text{mix}}[N_O, N_\gamma] = \int d^3G \ \tilde{N}_O \tilde{V}_{LJ} \tilde{N}_\gamma. \tag{4.53}
$$

This simplified form of the mixing functional captures only two-body interactions and misses higher-order interactions, such as the interplay between the water molecules in the coordination shell of an ion, which would be captured to some extent by a full WDA with non-linear terms. We thus anticipate that this first linearized approach will have difficulty exactly reproducing ion-water correlation functions. Also, lacking higher-body interactions, we expect our functional to bind too loosely the solvation shell of an ion, causing removal of an ion or water molecule from solution to occur more easily than it should. We thus anticipate that the vapor pressures of a liquid with the ion-water mixing described by Equation 4.51 will be artificially too high.

4.5.2 Solvated ion-water clusters

To mitigate some of the above concerns with a simple quadratic mixing functional, we propose treating the classical DFT ions not as bare particles, but as clusters which include the first coordination shell of water molecules. For

monoatomic ions such as the alkali cations and halide anions [227], this approx-imation is quite reasonable given the tight binding of the first solvation shell to the ion. For sodium and fluoride ions, for example, the deep first minima observed in the molecular-dynamics generated ion-water correlation functions indicate strong bonds between the ions and their coordinating water molecules [152]. Considering an ion-water cluster as a single "molecular entity" within the classical DFT captures these strong many-body interactions in the first solvation shell, which would otherwise be neglected by the approximate quadratic form of the mixing functional. The larger hard-sphere size for these clusters also pre-vents difficulties from numerical instabilities in the functional which can arise because of the number and variety of microscopic states available to small hard spheres.

Indeed, several options are available for description of an ion-water clus-ter within the liquid functional presented in Equation 4.14. As is presently the case for the water molecules, each atom in the cluster could be considered as an independent site, replacing Equation 4.15 for the ideal gas with the appropri-ate geometrically-constrained and orientation-dependent multi-site form. The independent variables for each ion would then become the local chemical po-tential $\mu_\gamma(\vec{r})$ the local electric field $\vec{\varepsilon}_\gamma(\vec{r})$. To determine the locations of the atomic sites in the ion-water cluster, we could use the *ab initio* determined minimum free energy geometry of water around the ion. However, the artificial fixing of the water molecule locations in the first solvation shell would result in over structuring of the second shell of classical water around the ion-water cluster. Also, each orientation-dependent ion adds three additional degrees of freedom to the minimization of the classical functional. To avoid these drawbacks, we instead coarse-grain each ion-water cluster as a single-site hard sphere but en-

sure the proper interactions of these coarse-grained spheres with the classical water through careful parameterization of the classical DFT functional.

4.5.3 Classical Functional Parameterization

In this section, we set forth the procedure for parameterizing the classical density-functionals for both unsolvated monoatomic ions and the coarse-grained ion-water clusters described above. The main quantities which must be determined for each electrolyte are the hard sphere radius R_γ^{HS} used in the fundamental measure theory, the range R_γ^{MF} of the mean-field Coulomb kernel in the fluid, and the range σ_γ and energy scale ϵ_γ of the attractive Lennard-Jones potential in Equation 4.51. For the present, we restrict our focus to several common alkali halide electrolytes, though the procedures described herein should be generalizable to other species and classes of electrolyte. To ensure physical behavior of the classical fluid, the values of all parameters are constrained to either theoretical calculations or experimental data for the electrolytes under consideration.

Ion hard-sphere radius

Because the hard-sphere radius R_γ^{HS} tunes the location of the repulsive potential arising from the fundamental measure theory for hard spheres and controls the closest distance of approach of the surrounding particles, we can use ion-water correlation functions predicted by molecular dynamics to establish its value. For an unsolvated ion, the location of the first maximum, $P_\gamma^{(1)}$, in the ion-water correlation function determines the hard sphere radius of the ion, ensuring proper

packing with the surrounding water. For an ion-water cluster, the first solvation shell is included within the coarse-grained sphere, so the location of the second maximum, $P_\gamma^{(2)}$, determines the hard sphere radius instead. Because the correlation function peak appears at the sum of the radii of the ion and the water, the ion hard sphere radius can be defined as

$$R_\gamma^{HS} = P_\gamma^{(m)} - R_O^{HS},$$ (4.54)

where R_O^{HS} = 1.36Å. The values of R_γ^{HS} determined from molecular dynamics predicted correlation functions of selected alkali and halide ions [152] are shown in Table 4.1 for both unsolvated ions and ion-water clusters. We note that the locations of the first correlation function peaks from molecular dynamics also compare quite favorably to the experimental values [178].

Coulomb range parameter

In our framework, the contribution to the mean-field charge density of the fluid due to an ion of type γ with site charge q_γ is

$$\rho_\gamma^{MF}(r) = \frac{q_\gamma \delta(r - R_\gamma^{MF})}{4\pi(R_\gamma^{MF})^2}.$$ (4.55)

The predictions of the classical DFT can be sensitive to the choice of R_γ^{MF}, so careful calibration is required. If the value for R_γ^{MF} is too small, the self energy of the charge distribution dominates and creates a large artificial energy cost for localization of the ions. If the value for R_γ^{MF} is too large, all the charge from the ion is placed near the exterior of the hard sphere, leading to over structuring of the fluid. We determined R_γ^{MF} by finding a mid-range value at which the solvation energy of a charged hard sphere in classical DFT water was not sensitive to the value of R_γ^{MF}. These considerations lead to the choice $R_\gamma^{MF} = \frac{R_\gamma^{HS}}{\sqrt{2}}$ rather than $R_\gamma^{MF} = R_\gamma^{HS}$, as is the case for our work with neutral fluids.

Lennard-Jones Model

To determine the parameters σ_γ and ϵ_γ used in the Lennard-Jones pair potential w_{LJ}, we simulate the solvation of a model ion within the classical DFT for pure water. The model ion located at $r = 0$ consists of a hard sphere potential which is infinite for $r < R_\gamma^{HS} + R_O^{HS}$, the mean field Coulomb kernel for the ion $\rho_\gamma^{MF}(r)$, and the attractive Lennard-Jones potential $V_{LJ}(r)$ from Equation 4.52. To maintain a neutral unit cell for our model-ion solvation, we include a spherical counter-electrode around the model ion, far from the relevant structure in the water. The model-ion potential, excluding the Coulomb interaction and counter-electrode, is shown by the dotted black line in Figure 4.6, with the separate attractive and repulsive components shown by the solid red and blue lines. Solvation of this model ion in water should reproduce ion-water interactions and correlation functions in the limit of a dilute electrolyte when σ_γ and ϵ_γ are properly constrained. By construction, the location of the first peak in the model ion-water correlation functions will agree with experiment because of the choice of R_γ^{HS} above.

Canonically, the Lorenz-Berthelot rules [29] for constructing Lennard-Jones interaction potentials prescribe that the range parameter σ_γ for the interaction between two particles should be the sum of their hard sphere radii. For the purposes of our mixing functional, we choose

$$\sigma_\gamma = \frac{R_\gamma^{HS} + R_O^{HS}}{2^{\frac{1}{6}}} \tag{4.56}$$

instead. This choice corresponds to placing the sum of the hard sphere radii at the location of the minimum of the full Lennard-Jones potential, rather than at the value where the potential crosses zero, which leads to more physical (smaller) coordination numbers in the first peak of the water-ion correlation
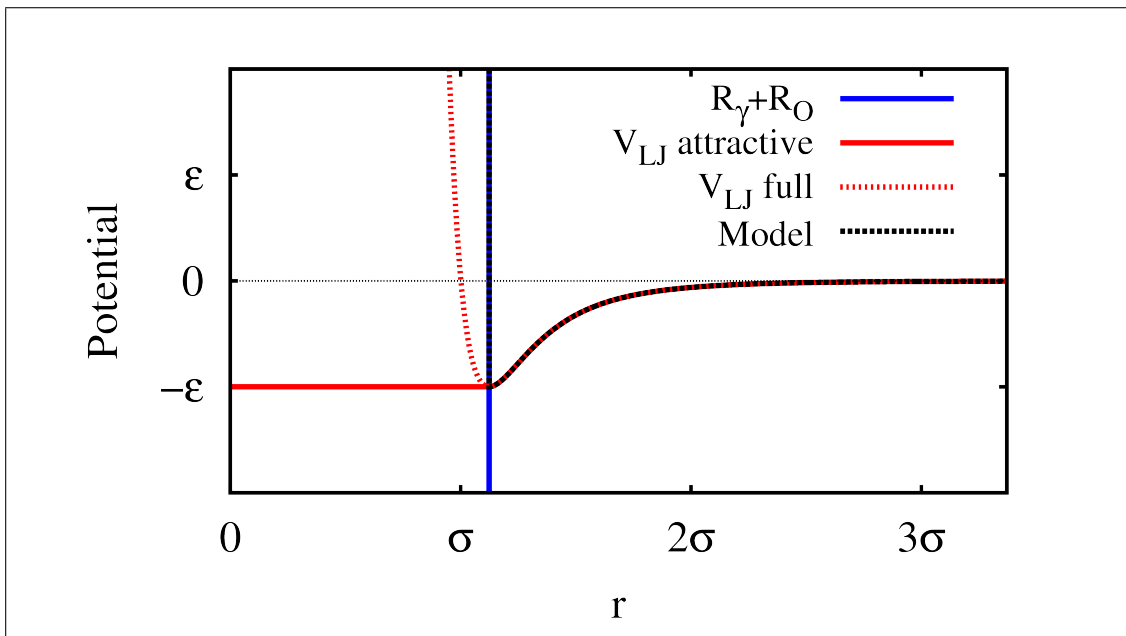
Figure 4.6: Sum of radii $R_\gamma^{HS} + R_O^{HS}$ (solid blue line), attractive Lennard-Jones potential from Equation 4.52 (solid red line) compared to full Lennard-Jones potential with the same parameters (dotted red line), and the model-ion potential excluding the Coulomb interaction (dashed black line)

function. Figure 4.6 displays the comparison between the location of the repulsive wall and the range parameter σ_γ. Table 4.1 shows the values of σ_γ and the coordination numbers predicted, both by molecular dynamics and by our model ions, for the electrolytes under study. Clearly, even for the revised definition of σ_γ, the combination of JDFT and the model ion overestimates the coordination number compared to the molecular dynamics.

The energy scale ϵ_γ dictates the strength of the ion-water interaction, so that a larger ϵ_γ leads to a higher ion solvation energy. We select the interaction strength which provides the correct experimental ion solvation energy for our model ion (or ion-water cluster) solvated in classical water [139]. (In practice, we compute the solvation energy of our model ion at discrete values of ϵ_γ and then perform an interpolation to find the value which best reproduces the experimental solvation energy.) Note that for the solvation energies we use either the bare

Table 4.1: Hard sphere radius, σ_γ, and interaction strength ϵ_γ which parameterize the classical functional for each type of ion, along with the coordination numbers and solvation energies predicted by model ion solvation in classical DFT and the corresponding target values computed in molecular dynamics [152]. [4]

Fluid	Ion	R^{HS} (Å)	σ (Å)	ϵ (H)	Pred. CN	Target CN	Pred. E_{sol} (H)	Target E_{sol} (H)
Unsolvated Ions	Na^+	0.99	2.18	0.0046	7.4	5.8	-0.166	-0.164
	K^+	1.43	2.49	0.0050	9.4	7.1	-0.140	-0.137
	F^-	1.27	2.32	0.0007	8.6	6.3	-0.172	-0.166
	Cl^-	1.84	2.85	0.0013	11.1	7.2	-0.116	-0.119
Ion-water Clusters	Na^+	3.14	4.01	0.0039	20.1	18.3	-0.112	-0.121
	K^+	3.39	4.23	0.0037	24.9	19.4	-0.111	-0.120
	F^-	3.09	3.96	0.0033	24.4	19.4	-0.116	-0.119
	Cl^-	3.64	4.45	0.0030	29.3	-	-0.113	-0.114

ion solvation energy or the solvation energy of an ion-water cluster with the number of water molecules equivalent to the molecular dynamics coordination number of the first solvation shell [152]. The best fit values for the interaction strength ϵ_γ, the experimental solvation energies, and the solvation energies of the parameterized model ion are all shown in Table 4.1.

Evaluation of Model Predictions

Figure 4.7 shows the ion-oxygen and ion-hydrogen correlation functions which our model predicts for both the unsolvated ion and the ion-water cluster models of NaF electrolyte. The locations of the maxima and minima predicted from molecular dynamics calculations are indicated by the upward triangles and the downward triangles. For the sake of consistency, we have chosen the molecular dynamics calculations of Reference [152] to provide a comparison, but we note that various experimental measurements, *ab initio* and classical molecular
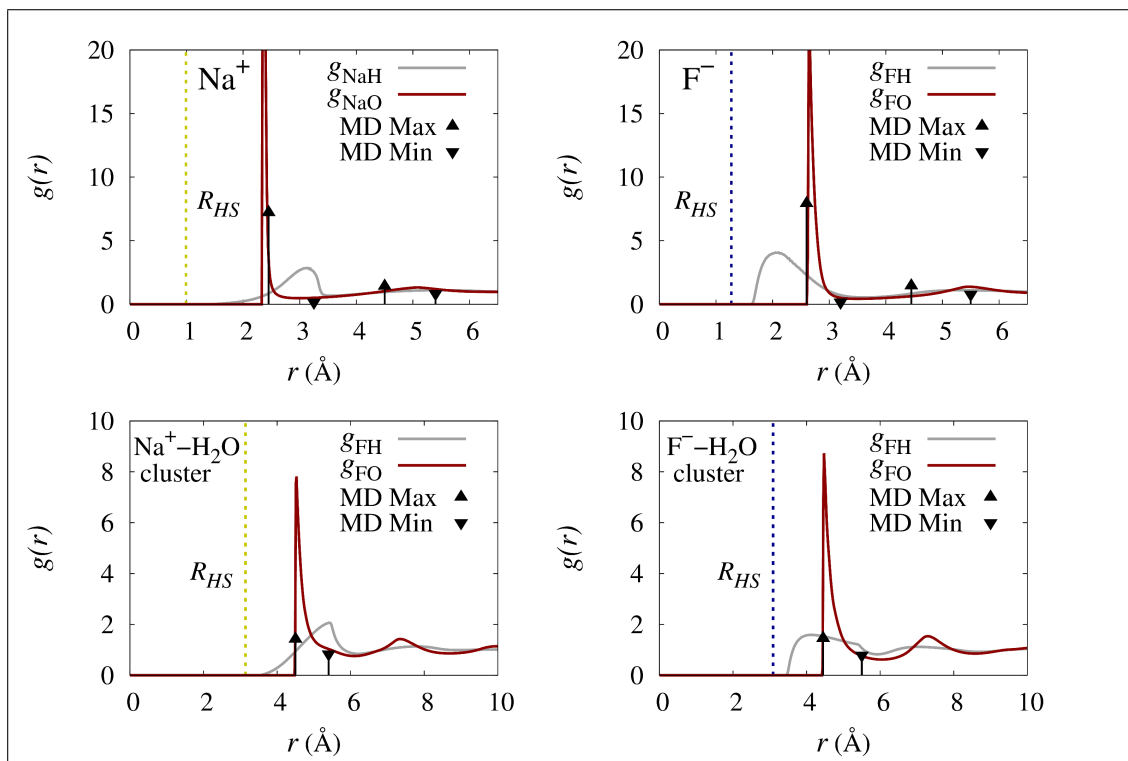
Figure 4.7: Ion-oxygen and ion-hydrogen correlation functions for Na^+ and F^- solvated in classical DFT water predicted by the unsolvated and cluster model ions, using the mixing functional parameters in Table 4.1. The points indicate the maxima (upward triangles) and minima (downward triangles) predicted from molecular dynamics calculations

dynamics predictions of these correlation function extrema provide a range of valid predictions rather than a single value [317, 241, 177, 176, 34, 47, 239]. Compared to the molecular dynamics results, the classical DFT predictions systematically overestimate the peak height and coordination number of the first solvation shell and localize the water in a strong, narrow peak at the hard sphere radius. This very strong initial peak and the known defect in the Ornstein-Zernike correlation functions for liquid water (See Section 2.6.3 for details) combine to push the location of the second solvation shell too far away from the ion.

Several possibilities exist for extending the classical DFT functional, refining our parameterization procedure, and improving the agreement of the classi-

cal DFT predictions with the molecular dynamics simulations and experimental measurements. Some of the inconsistencies between our results and the MD simulations exist because our fitting procedure assumes the model ions are point particles (delta functions with unit norm) and the model potential for point ions (shown in Figure 4.6) consists of an infinitely hard wall followed by a defined potential well. Because the classical DFT is quite sensitive to such discontinuities in the potential, the liquid functional responds by creating localized peaks. Some of this localization is a consequence of the choice to use the quadratic mixing functional in Equation 4.53 rather than a weighted density approximation. A weighted-density mixing functional based on the liquid equation of state could bring the results predicted by the model into closer alignment with the values in the literature. The expressions for the mean-field charge densities of the ion in Equation 4.55 and of the water in Equation 2.21, which contribute to the initial over structuring of the first peak and the pushing back of the second peak in the correlation functions, could also be made more physical if we developed a correction for the self-energy of the atomic sites in the liquid functional. Finally, the coordination numbers (and vapor pressures as we will see in Table 4.3) for the unsolvated anions are harder to reproduce compared to the cations, perhaps because interaction is framed as an oxygen-anion potential even though the anions are interacting most strongly with the positively charged hydrogens. Hence, we believe that introducing a dependence upon the hydrogen density into the mixing functional could potentially remedy the discrepancies between our model and the molecular dynamics predictions, especially for the anions.

4.5.4   Coupling Functional Details

Predictive JDFT calculations of a quantum-mechanical electrode surface in contact with a classical DFT liquid require a coupling functional which can capture the qualitative features of the electrode-electrolyte interface. As discussed in Section 4.2.1 and shown in Figure 4.1, the interfacial electrolyte at a charged electrode consists of a compact (Helmholtz) layer and a diffuse layer. In the diffuse layer, the ions provide exponential screening to any charges which may arise, with the amount of screening dependent on the ion concentration. In the Helmholtz layer, the oppositely charged ions move as close to the solid electrode surface as possible and form what amounts to a parallel plate capacitor. Some ions remain in the outer Helmholtz plane, with at least one layer of water in between the electrode and the ions. At some electrode potentials, the ions (especially anions) may cross the water layer into the inner Helmholtz plane and either chemisorb or physisorb on the electrode surface.

With the universal coupling functional of Chapter 2 and the unsolvated model ions, JDFT should naturally describe the capacitor-like behavior of ions near strongly charged solutes by including a close-packed layer of ions in the inner Helmholtz plane, prior to the liquid water shell structure. The diffuse exponential ionic screening region near weakly charged solutes should also naturally follow from simple electrostatics and exclusion. The van der Waals coefficients and electron density models for the unsolvated ions are described below and tabulated in Table 4.2.

However, following this same natural prescription in the case of the ion-water cluster model would be problematic for two reasons. First, the ion-water clusters described above are coarse-grained, feature spherical symmetry, and

do not possess atomic sites for the water molecules, making it impossible to include the explicit electron density of the full cluster. Second, ion-water clusters with a full description of the electron density of the first solvation shell would not be able to move into the inner Helmholtz plane, as they cannot "break" their solvation shells. In Section 4.6.4, we will show this movement into the inner Helmholtz plane to be a crucial feature for understanding the potential dependence of the differential capacitance. In light of these concerns, in our description of the coupling of ion-water clusters to the explicit electrode system, we choose to model the electron density and van der Waals interaction of the ion-water cluster as including only contributions from the ion at the center of the cluster, using the same parameterization as shown for the unsolvated ions in Table 4.2. In this description, ion-water clusters located at the inner Helmholtz plane are "partially solvated"; the classical fluid sees the solvation shell of the ion while the quantum-mechanical system does not. This choice does eliminate some of the interaction of the ion solvation shell with the electrode surface. However, this model still captures quite well the qualitative features of the electrode-electrolyte interface, as we demonstrate below.

Van der Waals Coefficients

Reference [40] describes how water physisorption at metal surfaces is highly dependent on van der Waals interactions. The coupling functional captures the van der Waals interaction between the solute and solvent through the empirical form of Grimme [97] (Equation 2.8). We choose the scaling parameter for the van der Waals interaction to be $\gamma = 0.540$, the value which performs best for computing molecular solvation energies in liquid water as shown in Section 2.6.1.

However, we still require c_6 and R_6 coefficients for charged ionic species, which are not available in the database of Grimme. For the R_6 coefficients we use the tabulated van der Waals radii of the ions [178]. We can estimate the c_6 coefficients using Grimme's formula,

$$c_6 = 0.05 N I_p \chi, \tag{4.57}$$

where N has values 2, 10, 18, 36, and 54 for atoms from rows 1-5 of the periodic table, I_p is the ionization potential (electron affinity for anions) in Hartree, and χ is the atomic polarizability in atomic units.

Hohm et. al. have extended the set of c_6 and R_6 parameters to high atomic number metal surfaces such as platinum and gold using the same procedure as Grimme. Because ion polarizability and ionization potential data are available from computational chemistry databases [2, 153] and the literature [6, 189], it should be straightforward to compute the c_6 coefficients directly according to the prescription of Grimme. However, to prevent inconsistency and unanticipated errors, we scale the coefficient which appears in the database for the neutral atom c_6^0 by the ratio of the ion properties to the neutral atom properties. Namely, for an ion of charge q, we use

$$c_6^q = \frac{I_p^q \chi^q}{I_p^0 \chi^0} c_6^0, \tag{4.58}$$

where I_p^q and χ^q are the measured or calculated properties of the ion and I_p^0 and χ^0 are the properties of the neutral atom. The values for c_6 and R_6 which we infer in this way for common monoatomic electrolytes are presented in Table 4.2.

Table 4.2: Coupling Functional: Electron Density and van der Waals parameters

Ion	Z^{el}	a^{el}	σ^{el}	r_c^{el}	c_6	R_6
Na$^+$	8.138	0.197	0.413	0.715	0.325	1.144
K$^+$	8.323	0.355	0.456	0.822	1.484	1.485
F$^-$	8.000	0.389	$2a^{el}/\sqrt{\pi}$	0.0	0.630	1.287
Cl$^-$	9.668	0.546	$2a^{el}/\sqrt{\pi}$	0.0	3.543	1.639

Ion Electron-Density Models

Finally, to compute the coupling functional for an aqueous electrolyte, the liquid electron density n_{lq} and the total charge density due to the liquid ρ_C must include contributions from the ionic species. We perform additional *ab initio* calculations of the ionic species in solution using the procedure of Section 2.4 to determine the electron site densities ρ_γ which contribute to both the electron and charge densities in the liquid. The parameterizations of ρ_γ resulting from these *ab initio* calculations are also presented in Table 4.2 for several common monoatomic electrolytes. We note that all ions have a nuclear density width $\sigma_\gamma^{nuc} = 0$ (effectively a delta function) to prevent any possible unphysical overlap between the charges.

4.6 Results

Here we examine the performance of the electrolyte liquid and coupling functionals described in Section 4.3 and the model aqueous sodium fluoride (NaF) electrolyte proposed in Section 4.5. First, we benchmark the predictions of the pure classical DFT electrolyte for key physical properties of the bulk fluid such

as bulk densities and vapor pressures. We then present JDFT calculations within the framework for charged systems in Section 4.4 for the structure and energetics of the interface of aqueous NaF electrolyte with single-crystalline metallic electrode surfaces. We compute potentials of zero charge from first principles to demonstrate how JDFT predictions of the potential-dependence of electrochemical processes such as specific adsorption of ions on the electrode surface may be placed on the scale of the Standard Hydrogen Electrode (SHE). Finally, we investigate the surface charge and capacitance as a function of applied potential for the (111) crystal face of silver, compare our predictions with the experimental measurements detailed in Section 4.2, and discuss how the structure of the fluid at the electrode surface influences the features in the differential capacitance.

4.6.1 Vapor Pressures and Densities

The excess Helmholtz free energy F_{ex} of the uniform classical fluid (Equation 4.16) at a fixed external pressure and fixed ion mole fraction fully determines the bulk densities, chemical potentials, and vapor pressures of the water and ions in the liquid. First, the bulk densities are determined by the fixed external pressure through the equation

$$p = k_B T \sum_I N_I^b - F_{\text{ex}}[N_I^b] + \sum_I N_I^b \frac{dF_{\text{ex}}}{dN_I}\bigg|_{N_I \to N_I^b}, \qquad (4.59)$$

where T is temperature and N_I^b is the bulk density of the fluid component I (where $I = \{H_2O, Na^+, F^-\}$ for aqueous NaF). The computation of the pressure assumes a fixed mole fraction of the electrolyte (roughly 1:55 for ions of concentration 1 M in water), so finding $\{N_I^b\}$ simply involves scaling all the bulk liquid densities by the same factor such that the scaled densities satisfy Equation 4.59.

The chemical potentials μ_I are determined by the derivatives of the excess free energy with respect to density as

$$\mu_I = \left.\frac{dF_{ex}}{dN_I}\right|_{N_I \to N_I^b} - \left.\frac{dF_{ex}}{dN_I}\right|_{N_I \to 0}, \tag{4.60}$$

where the left-hand term is the potential in the bulk of the fluid and the right-hand term is the potential in vacuum.

The vapor pressures P_I may be computed from the chemical potentials μ_I and bulk densities N_I as

$$P_I = k_B T N_I \exp\left(\frac{\mu_I}{k_B T}\right). \tag{4.61}$$

We note that the mean-field Coulomb term of the excess Helmholtz free energy F_{ex} in the bulk fluid is negligible since the bulk fluid is neutral by construction so the charge properties of the fluid have no influence on the vapor pressures. For the water, the terms which contribute to the vapor pressure are the fundamental measure theory, weighted-density term based on the equation of state, and the mixing functional F_{mix} between the ions and the water. For the ions, the only terms which contribute are the FMT and the mixing functional between the ions and the water. Any inaccuracies in F_{mix} would thus be expected to lead to inaccuracies in the vapor pressure of the classical liquid. Table 4.3 displays the bulk densities N_I^b, vapor pressures P_I, and chemical potentials μ_I for the water and the ions in 1 M aqueous NaF using both the unsolvated and ion-water cluster model ions, with the values for pure water presented as comparison.

Because sodium fluoride is a non-volatile electrolyte, we expect the vapor pressures P_I of the ions to be orders of magnitude smaller than the vapor pressure of the water. The vapor pressures of the sodium cations in both the unsolvated and ion-water cluster models and of the fluoride anion in the cluster model are much less than the vapor pressure of the water, as expected. How-

Table 4.3: Bulk densities of liquid components N_I^b, vapor pressures P_I, and chemical potentials μ_I of the classical DFT fluid components, alongside absolute ion solvation energies derived from experimental measurements [139].

Fluid	Component	N_I^b (Å^{-3})	P_I (kPa)	μ_I (H)	E_{sol} (H)
Pure Water	H_2O	0.0333	3.1	-0.010	-0.010
Unsolvated	H_2O	0.0336	3.0	-0.010	-0.010
NaF	Na^+	6.07×10^{-4}	3.2×10^{-7}	-0.021	-0.164
	F^-	6.07×10^{-4}	9.7×10^3	0.0013	-0.166
Ion-water	H_2O	0.0316	1.6	-0.011	-0.010
clusters	Na^+	5.72×10^{-4}	8.0×10^{-25}	-0.060	-0.121
NaF	F^-	5.72×10^{-4}	3.4×10^{-15}	-0.039	-0.119

ever, the vapor pressure of the fluoride anion in the unsolvated model is orders of magnitude higher than the vapor pressure of water. The chloride anion in the unsolvated model (not tabulated here) also exhibits a similarly high vapor pressure, suggesting a systematic error in the mixing functional for the anions.

The chemical potentials μ_I of the fluid molecules, which determine the vapor pressures, provide a better point of comparison with experimental data because we expect the chemical potentials to be reflective of the solvation energies of the molecules within the bulk liquid. As indicated by Table 4.3, the chemical potential of liquid water within the classical DFT is, as expected, within 0.001 H of its experimental solvation energy in the limit of a dilute electrolyte [180]. Both the anions and the cations modeled by ion-water clusters have chemical potentials of the right sign and order of magnitude compared to the absolute ion solvation energies derived from experimental measurements [139], though the values for the cations agree somewhat better than for the anions. In contrast, the unsolvated ion chemical potentials are smaller by at least an order of magnitude from the experimental reference, and in the case of anions, possess the incorrect sign.

The discrepancy between the model ion chemical potentials and the experimentally derived solvation energies likely appears due to the quadratic approximation to the ion-water mixing functional in Equation 4.51. Choosing to constrain the mixing functional interaction strength ϵ_γ by modeling discrete ions does not translate into the correct energetics for the ions in the bulk liquid, especially for the unsolvated ions. Because the quadratic mixing functional is a more physical approximation for the ion-water clusters (for reasons discussed in Section 4.5), the chemical potential discrepancies are less severe for the clusters. Furthermore, framing the interaction as occurring only with the oxygen atoms is not ideal for the anions, which associate with the water molecules primarily through the positively charged hydrogen atoms. Replacing the quadratic mixing functional with the weighted-density approach of Equation 4.48 would delocalize the model ions and likely capture more of the many-body interactions. A weighted density approximation based upon the equation of state for the electrolyte, would constrain the liquid vapor pressures and chemical potentials of the ions to the experimental values, just as the term A_{EOS} in Equation 4.10 does for water.

The ion chemical potentials, which are a consequence of the choice of model ion and the form of the ion-water mixing functional F_{mix}, determine how much energy must be added to the liquid in order for the ions to begin to precipitate out of solution when in thermodynamic equilibrium. Models which produce accurate values for the ion chemical potentials are thus crucial for a correct description of the electrochemical interface, where solvation and desolvation processes occur as a function of applied potential. Specifically, we expect the model-ion values for chemical potential to influence the JDFT prediction of the potential-dependent formation and structure of the compact layer next to the

electrode-electrolyte interface. We will investigate further the dependence of these structure and energy predictions upon the choice of model ion in Section 4.6.3 below.

4.6.2 Potentials of Zero Charge

Before we can predict the subtle, potential-dependent features of the electrode-electrolyte interface, we must ensure that our predictions for the electrochemical potential (μ) may be placed on the same voltage scale as the electrochemical measurements. As described in Section 3.3.2, we first establish the potential of an electron solvated deep within our model fluid as the JDFT reference electrode. Figure 4.8 displays the microscopic Kohn-Sham potential acting on the electrons for a neutral Ag(111) surface (averaged over the plane parallel to the surface) as a function of z, the distance perpendicular to the surface. For comparison, the JDFT electrochemical potential μ for the silver surface is also shown by the solid black line. This explicit JDFT result is comparable to the electron potential for Pt(111) computed from implicit JDFT and shown in Figure 3.1b, with the electrode potential applied as in Figure 3.1a. Explicit JDFT captures more features in the potential due to the structuring of the fluid at the interface, but the asymptotic value of the electron potential is still zero in the bulk fluid (dotted black line), demonstrating that the framework in Section 4.4.2 functions as intended. Therefore, just as in the implicit calculation, the applied potential E required to move an electron from the bulk of the metal to deep in the fluid is simply $E = -\mu$.

We next determine the relationship of our reference electrode to the Standard
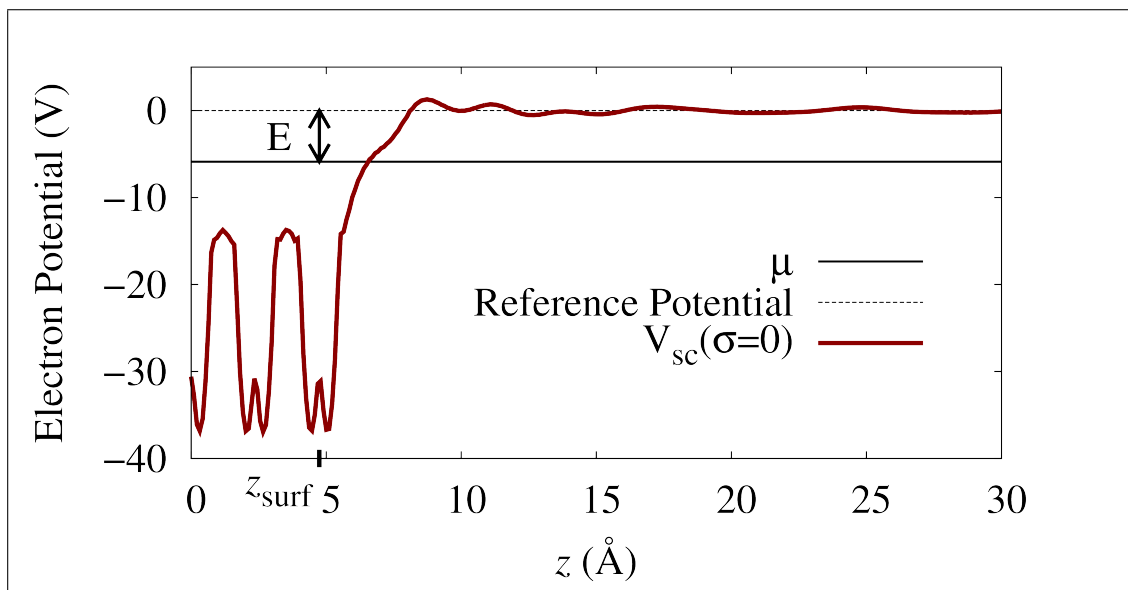
Figure 4.8: Microscopic self-consistent Kohn-Sham potential for an Ag (111) surface (solid red line) in NaF electrolyte (modeled by ion-water clusters) as a function of z, the distance perpendicular to the surface compared to the electrochemical potential μ (dotted black line).

Hydrogen Electrode (SHE) in electrochemistry, following the potential of zero charge calibration procedure set forth in Section 3.8.4. First, we compute from JDFT the values of the electrode potential for which the (100), (110), and (111) single-crystalline surfaces of copper, silver, and gold are neutral (no net charge). The metal surface calculations were performed as described in Section 3.7, using the same pseudopotentials, k-point sampling, unit cells, and energy cutoffs and the PBE exchange-correlation functional [212]. Figure 4.9 plots the JDFT-computed PZC's for both the unsolvated and cluster models in 1.0 M NaF electrolyte, versus the experimentally measured values relative to SHE [282]. We also include the PZC's for the surfaces in pure water to model the limit of a dilute electrolyte. (The electrode potentials for water are determined by subtracting the arbitrary constant asymptote of the potential in the bulk fluid from the JDFT-computed chemical potential μ, while the electrode potentials in the electrolyte are automatically computed versus the JDFT reference electrode.)
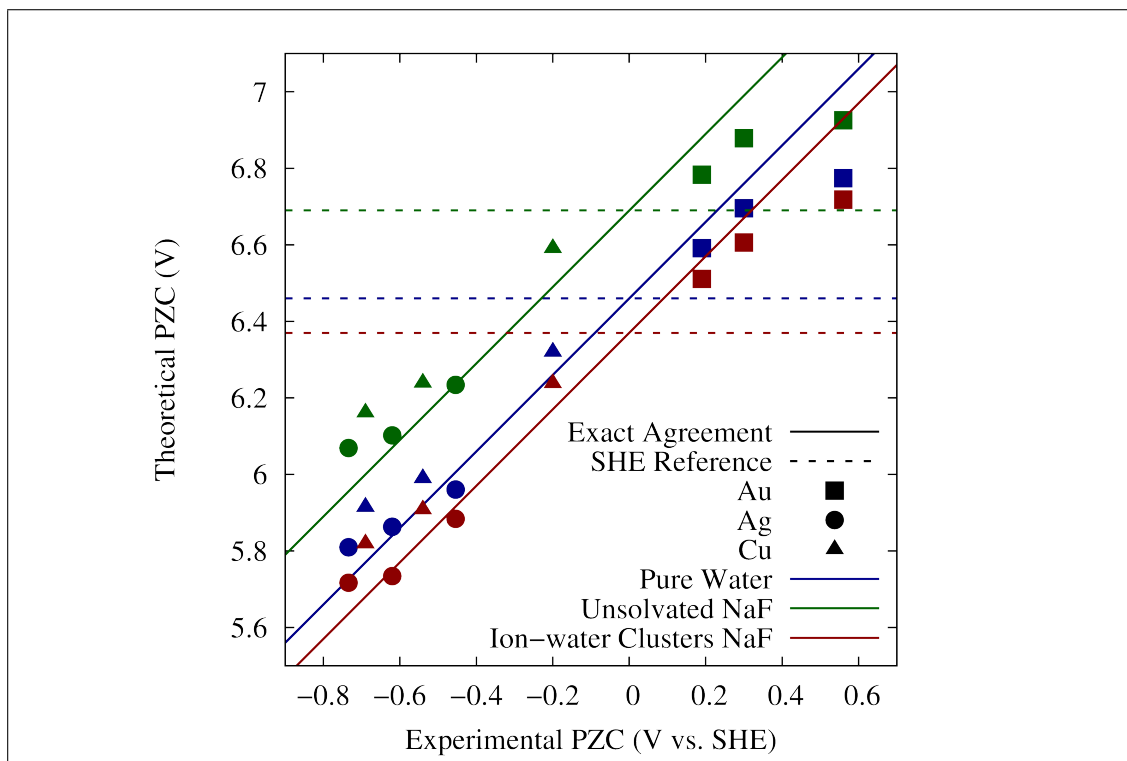
Figure 4.9: Calculated PZC's in pure water (blue points), NaF with unsolvated ions (magenta points), and NaF with ion-water clusters (red points) versus experimental measurements relative to SHE. The best linear fits to each set of theoretical predictions are shown by the diagonal solid lines and the potentials relative to SHE of the reference electrodes in each liquid model are shown by the horizontal dotted lines.

To quantify the accuracy of our predictions and place them on the scale of the SHE, we perform a least-squares linear fit to each data set with the slope constrained to unity (shown by the solid lines in Figure 4.9). The intercepts of these fits (shown by the dotted lines in Figure 4.9) establish the absolute relationship between the zero of potential in each fluid and the zero of potential on the SHE scale. Table 4.4 displays the root-mean-square error for the fit, which measures the correlation of our predictions with the experimental measurements, for each fluid model. The calculations which model the electrolyte as ion-water clusters provide the most accurate predictions compared to the experiment, while those using the unsolvated ions provide the least accurate predictions. The inaccu-

Table 4.4: RMS deviation of theoretical predictions from experimental measurements for several fluid models, the JDFT bulk fluid reference potential vs. SHE determined from least-squares fitting procedure ($E_{fl/SHE}$), the predictions for the potential of fluid relative to vacuum ($E_{fl/vac}$) from Equation 4.62, the JDFT bulk fluid electron potential (V_{el}^b) determined from Equation 4.46, and the predicted potential drop at the interface ($E_{int} = E_{fl/vac} - V_{el}^b$)

Fluid Model	RMS error (V)	$E_{fl/SHE}$ (V)	$E_{fl/vac}$ (V)	V_{el}^b (V)	E_{int} (V)
Pure Water	0.11	6.46	2.02	1.67	0.35
Unsolvated NaF	0.14	6.69	2.25	1.86	0.39
Ion-water clusters NaF	0.10	6.37	1.93	1.45	0.48

racy of the unsolvated ion model is likely due to the ions precipitating out of the liquid onto the metal surfaces. Indeed, Figure 4.11 shows that F^- is present on the metal surface at the PZC in the calculations of the Ag(111) surface using the unsolvated ion model. Table 4.4 also shows the value of the JDFT reference electrode for each fluid model relative to SHE, $E_{fl/SHE}$, allowing us to establish the absolute relationship between the applied potentials predicted by our calculations and the features in experimentally measured cyclic voltammograms and differential capacitances.

The physical meaning of zero on the scale of our reference electrode is the potential of an electron deep in the model liquid, as shown by the zero asymptote of the electron potential in Figure 4.8. To remove an electron from the JDFT model liquid to zero on the scale of the Standard Hydrogen Electrode, we must decrease its potential by $E_{fl/SHE}$, as determined by our PZC calibration procedure. That removal process occurs in two main steps. First, the electron is removed from the bulk model liquid to vacuum, decreasing its potential by the value $E_{fl/vac}$ by desolvating and passing through the air/water interface potential. Second, the electron is brought from vacuum to zero on the SHE scale,

decreasing its potential by the value $E_{\text{vac/SHE}}$. The accepted value of the potential of vacuum versus SHE is $E_{\text{vac/SHE}} = 4.44$ V [282]. The potential decreases occurring in these two steps are additive such that

$$E_{\text{fl/SHE}} = E_{\text{fl/vac}} + E_{\text{vac/SHE}}. \tag{4.62}$$

The values of the bulk fluid potential relative to the absolute potential of vacuum, $E_{\text{fl/vac}}$, determined from Equation 4.62 and the accepted value of $E_{\text{vac/SHE}}$, are shown in Table 4.4. This potential drop across the fluid-vacuum interface, $E_{\text{fl/vac}}$, may be interpreted as the energy an electron sheds as it moves through the dipole layer at the interface. The predicted values of $E_{\text{fl/vac}}$ for pure water and 1 M electrolyte are similar, suggesting that the structure of the dipole layer of water at an uncharged interface is not perturbed significantly by the presence of the ions. Figure 4.11 confirms that the structure of water changes very little upon introduction of the ions, as expected from AIMD simulations [90]. We note that our values of $E_{\text{fl/vac}}$ are reasonably close, but at least 1 V smaller than those predicted by Leung et. al., who compute the fluid-air interface potential to be $E_{\text{fl/vac}}^{\text{AIMD}} = +3.6$ V from *ab initio* molecular dynamics calculations [165]. However, pair potential models predict a significantly different value of $E_{\text{fl/vac}}^{\text{SPCE}} = -0.56$ V [257], and other values reported in the literature are highly variable [165].

The potential $E_{\text{fl/vac}}$ is also closely related to the electron potential V_{el}^b, which is determined from Equation 4.46 and also presented in Table 4.4. As discussed in Section 4.4.2, the potential V_{el}^b only includes the potential energy lost by an electron as it desolvates and does not include the potential decrease due to the interfacial dipole. The difference between the theoretical work functions and theoretical PZC's predicted from implicit JDFT in Figure 3.5c provides an estimate of $\approx 0.4 - 0.5$ V for the value of the potential drop due to interfacial

water at metal surfaces. This estimate is roughly comparable to the values of the interfacial potential $E_{\text{int}} = E_{\text{fl/vac}} - V_{\text{el}}^b$, computed for the liquid models under consideration and presented in Table 4.4.

4.6.3 Electrolyte Structure and Charged Surfaces

With the above procedure to relate the applied potential in JDFT calculations to the relevant scale for electrochemical measurements, we use JDFT to compute the properties of a charged metal surface in contact with a classical DFT description of an aqueous electrolyte. We consider the Ag(111) surface in 1.0 M sodium fluoride, specifically because silver in NaF has been reported in the literature to be ideally polarizable and free from chemisorption, as discussed in more detail in Section 4.2. The setup of the *ab initio* calculations is identical to the setup of the calculations in Chapter 3, except the unit cell size is doubled in the *z*-direction (perpendicular to the metal surface) to allow for structuring in the fluid. Figure 4.10 shows the surface charge on Ag(111) as a function of applied potential, computed with both unsolvated ions and ion-water clusters as the model electrolyte. The charging curve for the unsolvated ions appears to be somewhat less smooth, a numerical issue likely due to the grid resolution and the increased localization of the water around unsolvated ions which we observed in Figure 4.7. Clearly, the different ion models agree quite well for negatively charged surfaces (below the PZC), but the predictions diverge for positively charged surfaces (above the PZC).

The unique capability of JDFT to predict thermodynamically averaged interfacial fluid structure allows us to investigate the origin of the discrepancy
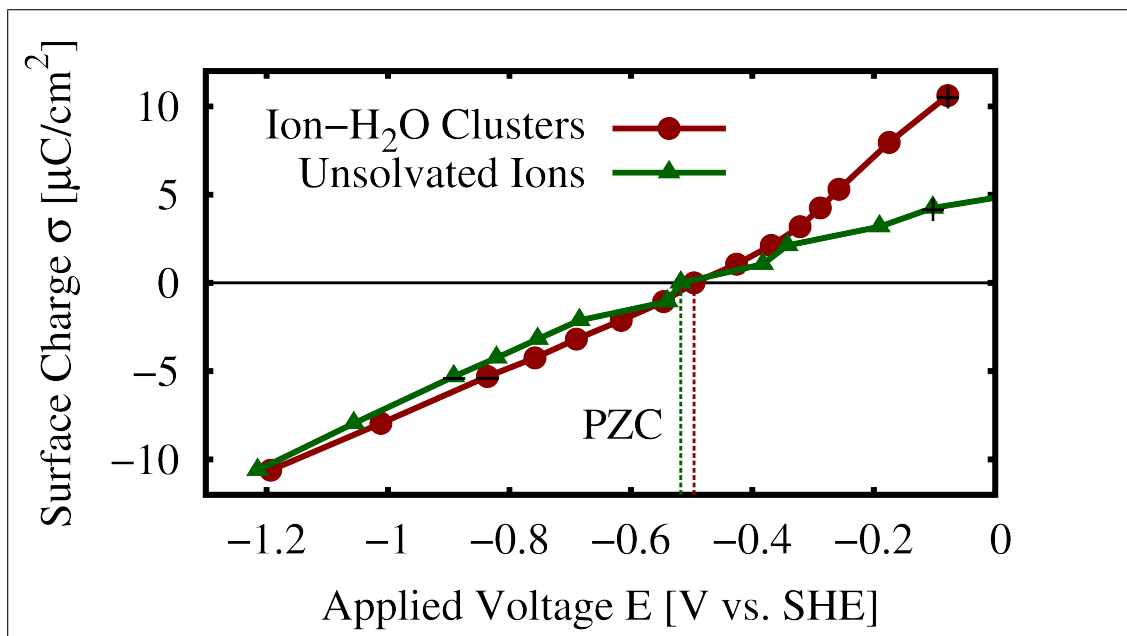
Figure 4.10: Comparison of the charge vs. potential for an Ag(111) surface in 1.0 M NaF electrolyte resulting from each choice of ion. Predictions for ion-water clusters (red circles) and unsolvated ions (green triangles) versus SHE. Interfacial liquid structure is shown in Figure 4.11 for specially marked points (-,PZC,+).

between the ion models at positive charges. For specially marked points on the charging curves in Figure 4.10 – one negative charge (-), zero charge (PZC), and one positive charge (+) – Figure 4.11 displays the density profiles of the cations (yellow), anions (blue), and oxygen atoms in the water (red) next to the surface. For reference, the density profiles of the oxygen atoms in pure water next to a neutral Ag (111) surface are shown by the dotted red line in each panel. Some similar features exist in the interfacial structure predicted for unsolvated ions and the structure predicted for ion-water clusters. As expected from the textbook picture of Figure 4.1 [28], the cations remain solvated within their water shells, even at large negative voltages, while the anions begin to move into the inner Helmholtz plane at high positive voltages. We note that the small oxygen peaks close to interface could represent a small chance of water adsorbed through the oxygen atom on the metal surface, a phenomenon which has previ-
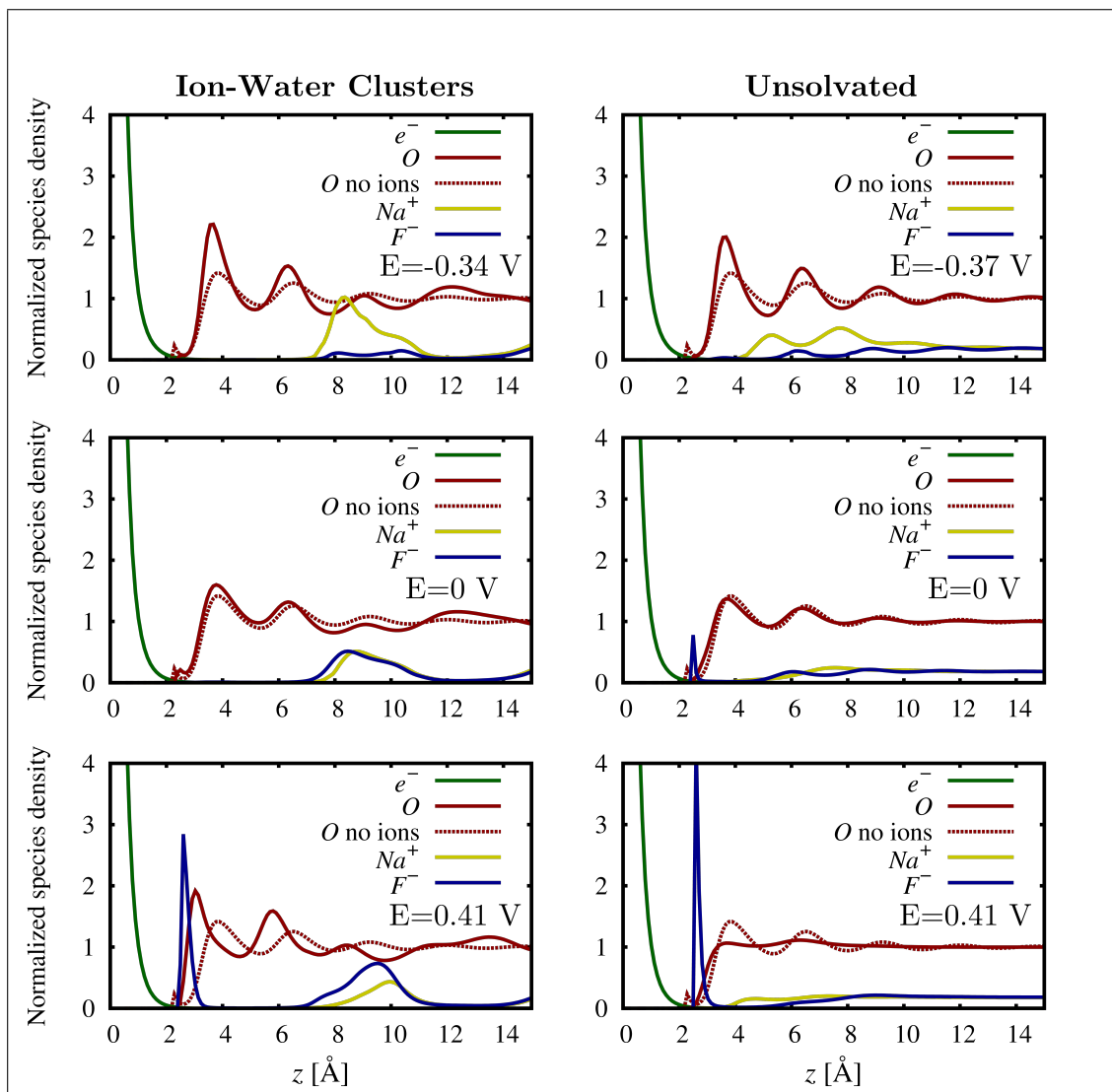
Figure 4.11: Plane-averaged oxygen (red), sodium (yellow), and fluoride (blue) densities as a function of *z*, the distance perpendicular to the surface as measured from the location of the last surface metal atom. Predictions from the ion-water cluster model (left column) are compared to those from the unsolvated ion model (right column) for positively charged, neutral, and negatively charged surfaces in 1.0 M NaF. The Na^+ and F^- site densities are magnified by an order of magnitude for visibility. Electrode potential E is reported versus PZC.

ously been observed by infrared spectroscopy [240].

Significant features also distinguish the structures predicted by the ion-water clusters from those predicted by the unsolvated ions. The ion-water clusters

exhibit a well-defined outer Helmholtz plane, localized at 8-10 Å after approximately two layers of water. In contrast, the unsolvated ions seem to behave more like a diffuse layer, penetrating closer to the surface but never forming a defined outer Helmholtz plane. As the ion-water clusters move from the outer Helmholtz plane to the inner Helmholtz plane as the potential increases, the surface charge begins to increase nonlinearly as well. As explored in Section 4.6.1 above, the unsolvated anions have an unphysically high vapor pressure, so they precipitate out of solution and into the inner Helmholtz plane, even when there is no charge on the surface. Their movement into the inner Helmholtz plane, however, is accompanied by a slight decrease in the slope of the surface charge versus applied potential. The presence of unsolvated ions in the inner Helmholtz plane at positive potentials also excludes the water from the surface and drastically suppresses the structure of the following water layers. The ion-water clusters create no such exclusion of the water from the surface – if anything the water moves closer to the surface and exhibits more structure. In Section 4.6.4 below, we discuss how these changes in the interfacial liquid structure correlate with significant features in the differential capacitance.

The interfacial liquid structure also corresponds to features in the microscopic electrostatic potential of the electrode-electrolyte interface. Figure 4.12 displays the difference between the Kohn-Sham potentials of the charged surface and the neutral surface (shown in Figure 4.8) for a series of positive and negative surface charges, with a negative sign applied to convert from *electron* potentials to *electrostatic* potentials. These potential profiles from explicit JDFT are comparable to the electrostatic potentials pictured in Figure 3.3(c) computed from the implicit solvent, with potential applied as in Figure 3.1a. In both the implicit and explicit cases, the electrostatic potential is a constant in-
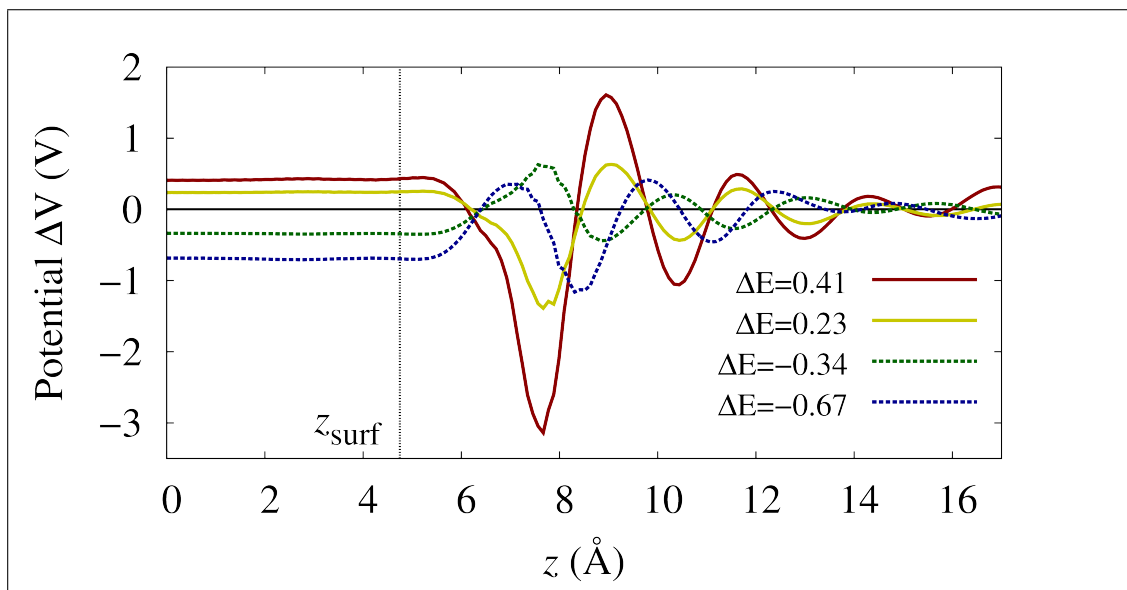
Figure 4.12: Microscopic self-consistent *electrostatic* potential difference between charged and neutral Ag (111) surfaces for surface charges of σ = $\{-10.6, -5.3, +5.3, +10.6\}\frac{\mu C}{cm^2}$ (corresponding to potentials E = $\{-0.67, -0.34, +0.23, +0.41\}$) as a function of z, the distance perpendicular to the surface. Electrolyte is 1.0 M NaF using the ion-water-cluster approximation.

side the metal surface ($z < z_{surf}$) with the value equal to the applied potential, then quickly decays outside the surface. There is a clear definition of a linearly decaying Stern region in the potential predicted by explicit JDFT. In the most positively charged case, the potential decays sharply to a strong minimum, corresponding to the anion in the inner Helmholtz layer as shown in Figure 4.11 for E = 0.41 V. All the potential profiles in Figure 4.12 possess significant structure in the fluid, but this structure does decay with an exponential envelope, reflective of the exponential decay evident in the Gouy-Chapman model for the diffuse layer. Finally, the general continuity of the curves in Figure 4.12 indicates that, unlike in the simple electrochemical model, there is no clearly defined compact layer and diffuse layer in the real electrode-electrolyte interface.

The charge as a function of potential in Figure 4.10 and associated fluid structure in Figure 4.11 indicate that, as anticipated, the ion-water cluster model ap-

pears to be more physical than the unsolvated ion model when implemented within a quadratic ion-water mixing functional. The presence of the fluoride ions in the inner Helmholtz plane, even at neutral potential, the lack of a well-defined outer Helmholtz plane, and the strong suppression of the liquid water structure at positive charges are all warning signs that the unsolvated ions, which possess unphysically high vapor pressure, also yield unphysical predictions for electrochemical systems within a simple quadratic functional description. Furthermore, the decrease in the slope of the charge vs. potential curve (capacitance) at positive potentials does not agree with the qualitative features of the experimental charging curves [286]. Thus, for the detailed study of capacitance in Section 4.6.4 below, we concentrate upon the ion-water cluster model (though we do present one capacitance result for the unsolvated ions in Figure 4.15 for reference).

4.6.4   Nonlinear Capacitance

To further explore the nonlinear features of the charge as a function of applied potential for Ag(111) for the ion-water cluster model (shown in Figure 4.10), we take the numerical derivative with respect to the potential to find the differential capacitance, resulting in the red solid curve in Figure 4.13. We now collected data on a much finer grid than in Figure 4.10 to reduce noise in computing the numeric derivative. We may then compare the structure of the interface shown in Figure 4.11 to the nonlinearities in the capacitance curves. A slight minimum appears in the capacitance curve at the potential of zero charge, a feature predicted by the Gouy-Chapman-Stern model for the electrochemical double layer set forth in Section 4.2.2 and observed in experiments as in Figure 4.5. As shown
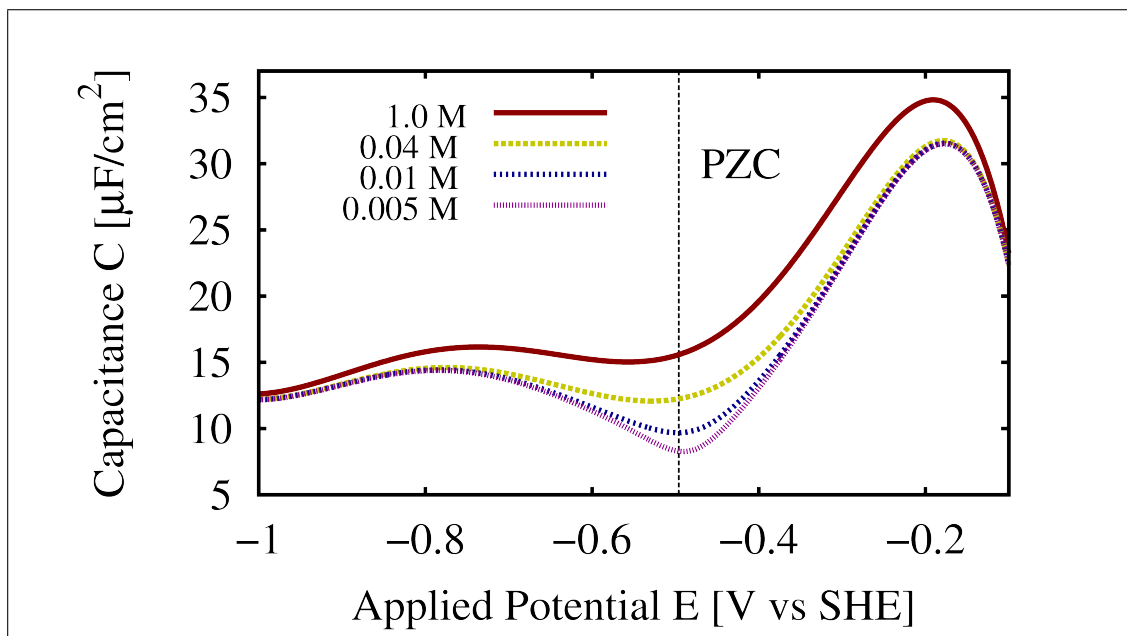
Figure 4.13: Pure *ab initio* prediction for 1.0 M (solid red) and extrapolation from the the high concentration result JDFT for low concentrations 0.04 M (dashed yellow), 0.01 M (dotted blue), and 0.005 M (dotted purple) using known expression for ideal capacitance of the diffuse layer in Equation 4.7 and the series capacitor model in Equation 4.3.

in the middle-left panel of Figure 4.11, all ions are located in the outer Helmholtz plane at the PZC, and the structure of the water is perturbed minimally from the structure of water when no electrolyte is present. Below the PZC, the capacitance rises slightly as the potential decreases, peaking at approximately 0.2 V below the PZC then falling again. This region of the capacitance curve is correlated to an increase of cations in the outer Helmholtz plane and an increase in the structure of water at the surface. At about 0.1 V above the PZC, the capacitance rises dramatically, attaining more than a factor of two increase by about 0.3 V above the PZC, and then falls again with further increasing potential. This dramatic rise in the capacitance occurs at the same potentials where fluoride anions move from the outer Helmholtz plane to the inner Helmholtz plane, as shown in the bottom-left panel of Figure 4.11.
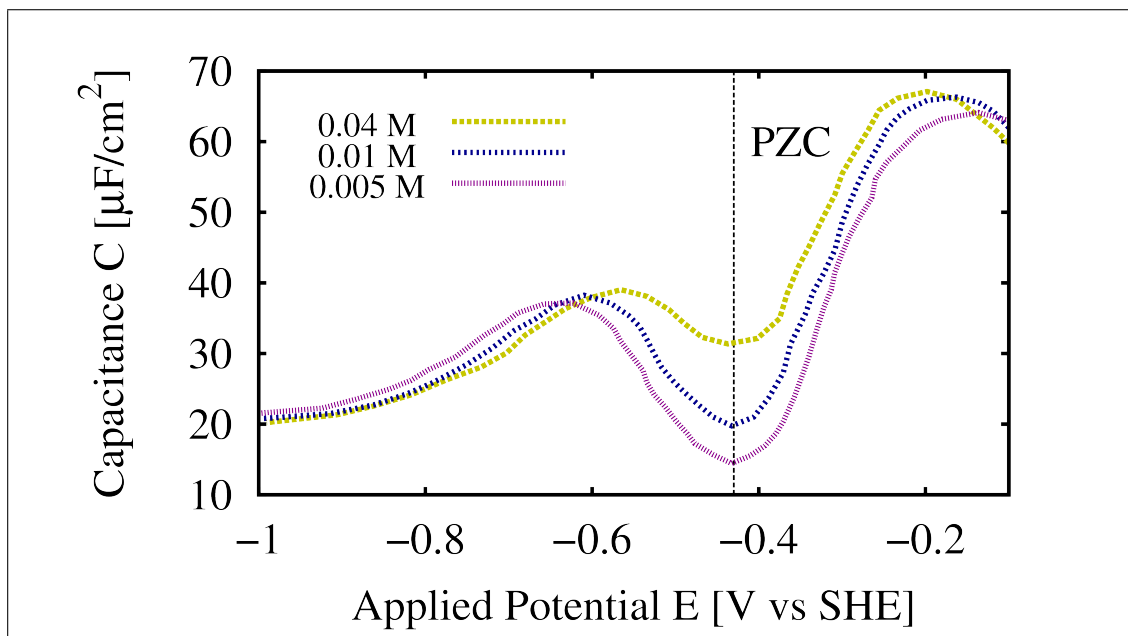
Figure 4.14: Concentrations range from 0.04 M (dashed yellow), 0.01 M (dotted blue), and 0.005 M (dotted purple) [286].

Figure 4.14 displays the experimentally measured capacitance curves for single-crystalline silver (111) in sodium fluoride [286].[5] The experimentally measured capacitance curves possess the same double-humped potential-dependence as the JDFT calculations, which predict these qualitative features *a priori*, without any input from the electrochemical models. The potential values (versus the SHE) at which the features occur are also in excellent quantitative agreement. However, the experimental curves for single-crystalline silver are measured at low electrolyte concentrations and are not directly comparable to the JDFT calculations without additional analysis.

While there is a slight capacitance minimum at the potential of zero charge in the 1.0 M JDFT predictions, the inner layer capacitance dominates over the diffuse layer capacitance at this concentration. Modeling lower concentrations in JDFT is computationally challenging due to the large unit cell required to

[5]We have scaled the experimental data by dividing by the roughness coefficient 1.10 detected by the Parsons-Zobel technique described in Section 4.2.4.

neutralize the charge on the surface. The features of the Gouy-Chapman-Stern model for the electrochemical double layer set forth in Section 4.2.2 therefore provide a useful framework for the exploration of the concentration dependence of the capacitance. Figure 4.13 displays the extrapolation of the high concentration capacitance to lower concentrations, using the series capacitance model in Equation 4.3 and the model diffuse capacitance in Equation 4.7 as described in Section 4.2.3. The JDFT results in Figure 4.13 may now be directly compared to the experimental measurements in Figure 4.14, and the excellent qualitative agreement remains.

Figure 4.15 displays our JDFT predictions for a concentration of 0.01 M simultaneously with the experimental measurements for single-crystalline silver (111) [286], polycrystalline silver [159], and the ideally polarizable mercury electrode [95]. We have also included the JDFT predictions (extrapolated to low concentration) for the unsolvated ion model as well, clearly demonstrating the superior qualitative agreement of the ion-water cluster model with the experimental measurements. Our JDFT calculations exhibit the best qualitative agreement with the Ag(111) measurements, but the quantitative values for capacitance agree best with the ideally polarizable mercury electrode. The average value of the JDFT-predicted capacitance is too low by almost a factor of two compared to the experimental measurements of silver capacitance. There are several possible explanations for this discrepancy, including the influence of kinetic processes, the presence of quantum-mechanical interactions between the fluid and the surface which are not captured by a classical fluid model, and errors in the JDFT predictions due to the primitive nature of our model ions and mixing functional.
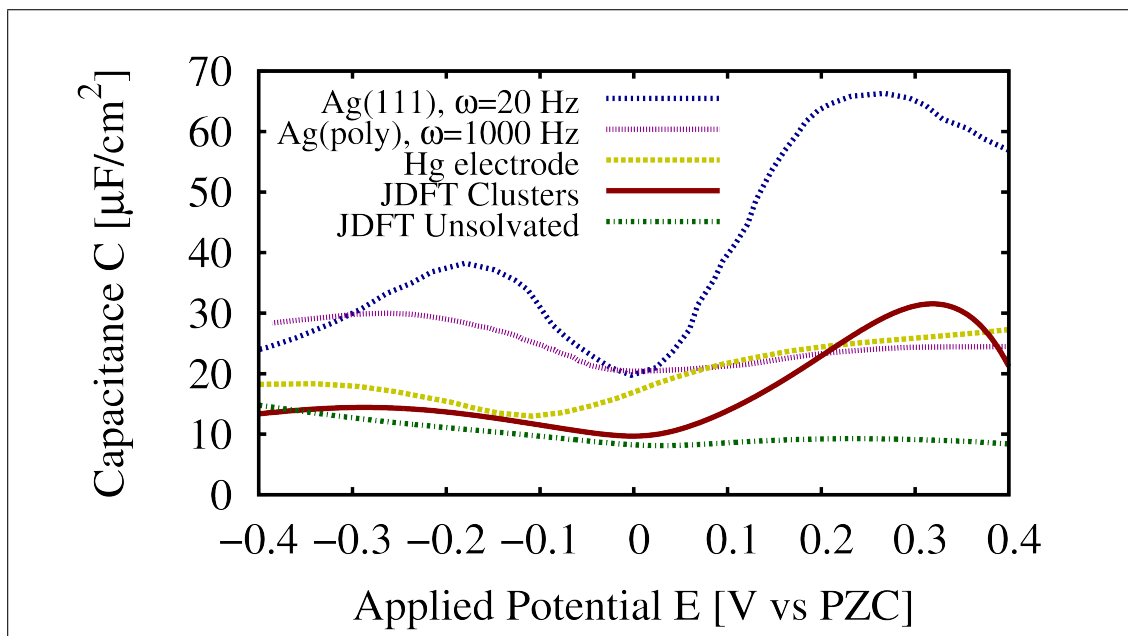
Figure 4.15: Experimentally measured capacitances vs. applied potential compared to JDFT predictions in 0.01 M NaF. Measurements include polycrystalline silver at $\omega = 1000$ Hz (purple) [159], Ag(111) at $\omega = 20$ Hz (blue) [286], and an ideally polarizable mercury electrode (yellow) [95]. JDFT-based extrapolations for both unsolvated ions (green) and ion-water clusters (red). All electrode potentials are plotted with respect to the PZC.

First, we explore the frequency-dependence of the experimental capacitance measurements to determine the influence of kinetic processes. For example, the process of an anion breaking its solvation shell and moving from the outer Helmholtz plane to the inner Helmholtz plane may be kinetically limited, leading to a frequency dependence in the capacitance measurements as discussed in Section 4.2.4 [140]. Namely, high-frequency capacitance measurements ($\omega \to \infty$) will miss kinetically limited processes like penetration through the outer layer of liquid to the electrode surface and then adsorption. In principle, JDFT predicts the structure of the liquid at thermodynamic equilibrium, capturing all energetically favorable configurations regardless of the timescale, and so should compare most directly to low-frequency capacitance measurements ($\omega \to \infty$). In practice, however, JDFT does not capture chemical bonding between the

fluid and the electrode surface (unless such species are included explicitly in the quantum-mechanical calculations), so in the cases where the kinetically-limited process is quantum-mechanical in nature the JDFT predictions will agree best with the high-frequency capacitance measurements.

Figure 4.16 shows the comparison of the renormalized JDFT predictions (scaled by a factor of two to reflect quantitative discrepancies likely due to oversimplification in our preliminary functionals) to the high-frequency (ω = 1000 Hz) [159] and low-frequency measurements (ω = 20 Hz) [286] of silver capacitance. The JDFT predictions agree best with the low-frequency measurements above the PZC and with the high-frequency measurements below the PZC. Because infrared spectroscopy measurements of the Ag-O stretching frequency suggest that the hump in the differential capacitance below the PZC is due to chemisorption of the water molecules through the oxygen atom [240], it is logical that the JDFT calculations are unable to capture this feature in the low-frequency capacitance. However, the JDFT calculations successfully predict the movement of the F^- atoms from the outer Helmholtz plane to the inner Helmholtz plane, where they physisorb on the electrode surface without transferring charge. The JDFT capacitance predictions thus agree best with the low-frequency measurements above the PZC, because the frequency dependence of interfacial capacitance in that region is attributed to the relatively slow exchange of anions between the outer and inner Helmholtz planes. [204]

Though the qualitative agreement between the JDFT predictions and the experimental measurements in Figure 4.16 is outstanding, JDFT underestimates the capacitance by a factor of two. One hypothesis for the cause of the discrepancy is that the surface area in the experiment was estimated incorrectly
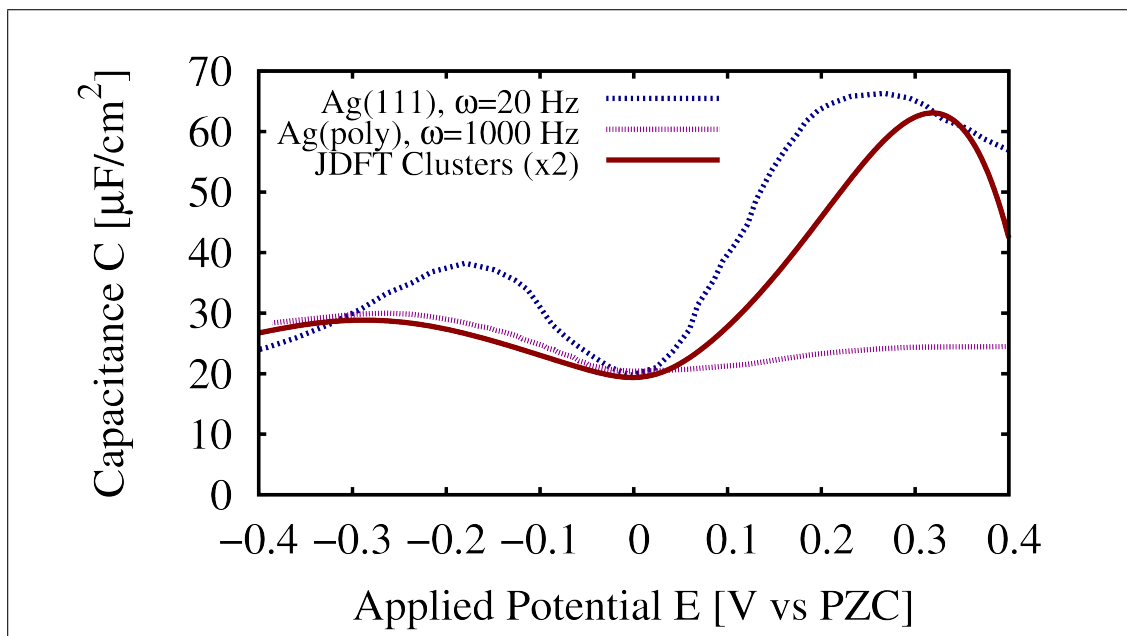
Figure 4.16: Experimentally measured capacitances vs. applied potential compared to JDFT predictions in 0.01 M NaF. Measurements include polycrystalline silver at $\omega = 1000$ Hz (purple) and Ag(111) at $\omega = 20$ Hz (blue) JDFT-based extrapolation for ion-water clusters (red) is scaled by a factor of two in order to compare to the qualitative features of the experimental measurements.

due to roughness on the surface. Because the results for Ag(111) have already been scaled by the roughness coefficient determined by the Parsons-Zobel plot ($r_{111} = 1.10$) [286], this explanation seems unlikely. To further investigate the origin of the disagreement, we consider the expression for the capacitance per unit area in a parallel plate capacitor $C_i = \frac{\epsilon_0 \epsilon}{\Delta}$, where Δ is the average distance from the metal electrode to the counter-ions and ϵ is the relative permittivity of the dielectric between the electrode and the counter-ions. Our discrepancy could thus be due either to overestimation of the dielectric saturation of the water in the inner layer (ϵ too small), or to over prediction of the distance between the water and the counter-ions (Δ too large), or to some combination of the two physical effects. Though Figure 1.1 demonstrates that the nonlinear dielectric response of the classical water is quite accurate, our ion-water cluster model implicitly assumes that the water molecules in the solvation shells of the ions

are unable to polarize in response to the electrolyte. Furthermore, the simple quadratic form of the ion-water mixing functional over-localizes the water near the ions, so it is also possible that the location of the outer Helmholtz plane is predicted incorrectly by our model. Finally, the ion-water cluster model coarse-grains the charge density due to the half solvation shell of water around the ions in the inner Helmholtz plane and the full solvation shell of water around the ions in the outer Helmholtz plane, another significant approximation. Thus, a more advanced water-ion mixing functional (such as a weighted-density approach) and a more microscopically accurate ion model will likely be required to achieve quantitative agreement with the experiment. Despite these subtleties, it remains quite impressive that a first attempt at explicit JDFT captures both the features of the nonlinear capacitance and the origins of those features in the interfacial structure of the liquid.

4.7 Conclusions

In the preceding chapter, we explored the promise of JDFT with an atomically detailed classical DFT description of the liquid electrolyte for predictive calculations of electrochemical systems, expanding upon the work presented in Chapter 3. We developed a classical liquid functional Ω_{lq} for the electrolyte and investigated the efficacy of the JDFT coupling functional ΔA from Chapter 2 for describing the interaction between a charged electrode surface and a classical liquid. We have established a framework for considering an electrode under applied potential control, ensuring the charge in the fluid balances the charge on the electrode and preventing divergence of the electrostatic energy due to a net charge in the periodic unit cell. We then demonstrated that our charge bal-

ance framework, along with the potential of an electron deep within the bulk fluid, naturally provides an absolute reference potential for comparison to electrochemical measurements. Furthermore, we establish the relationship of our reference electrode to the Standard Hydrogen Electrode, allowing the chemical potential in our JDFT calculations to be directly related to the electrode potential in differential capacitance measurements and cyclic voltammograms. Finally, we showed that Explicit JDFT can capture the qualitative features of the non-linear capacitance of metal electrodes in non-adsorbing electrolyte, connecting the increased capacitance above the PZC with movement of the anions from the outer Helmholtz layer to the inner Helmholtz layer.

The above success of JDFT at capturing the structure-driven changes in the differential capacitance of Ag(111) is especially impressive given the primitive nature of the ion-water mixing functional and the coarse-graining of the model ions. Of course, the systematic under prediction of the numerical value of differential capacitance by JDFT compared to the experimentally measured value, as clearly demonstrated in Figure 4.16, is likely due to imperfections in the relatively simple linear functional used to approximate the ion-water interaction. The clear path forward for improving the liquid functional is to return to the unsolvated ions, which caused the water to over structure and predicted an unphysically high vapor pressure in this work, and correct the mixing functional to mitigate these physical concerns. Constructing a weighted-density inspired mixing functional based upon an equation of state for the electrolyte [35] would both delocalize the water-ion interaction to prevent over structuring and reproduce the vapor pressures by construction. As the mixing functional is currently framed as an ion-oxygen interaction only, we could also include the interaction between the ions and the hydrogen atoms by evaluating our equation of state

at the polarizability weighted density in Equation 4.11. If necessary to properly capture the electrolyte equation of state, we could also add ion-ion interactions beyond the mean-field coulomb interaction and hard sphere repulsion. The long-range structure making and breaking properties of ions could also be captured by altering the effective temperature of water – structure-makers lower the effective temperature while structure-breakers raise it [179].

Because the present coupling functional was designed using solvation of neutral molecules in neutral solvents, it would be ideal to benchmark this functional's predictions for charged systems more carefully. Including large and small ionic species in the training set of Table 2.2 and then refitting the van der Waals scaling parameter to capture solvation energies of charged systems could help create a more robust and versatile coupling functional, thereby increasing the versatility of JDFT. As van der Waals interactions are crucial to capturing the attraction between water molecules and metal surfaces [40], one should also benchmark the accuracy of the procedure for extending the Grimme set of c_6 and R_6 coefficients to ions and high atomic number metals (described in Section 4.5.4). Once the accuracy of the extended Grimme set and the performance of the JDFT coupling functional has been verified for solvation of quantum-mechanical ions in pure water, JDFT calculations of the ions in Table 4.1 could be used (instead of molecular dynamics) to determine the correlation functions and solvation energies which parameterize the mixing functional.

With the improved liquid and coupling functionals, we may conduct detailed studies of other electrochemical systems which are well-characterized in the literature to benchmark our new functionals. We could investigate the capacitance of the silver surface in other electrolytes, substituting potassium for

sodium as the cation [285], and considering other halides as the anion [159, 134]. Chloride, in particular, has been shown to interact more strongly with the silver surface, providing an interesting test case for the ability of a classical functional to capture specific adsorption without quantum mechanics. Investigation of the dependence of the differential capacitance on the particular single-crystalline face exposed to the electrolyte could also reveal particularly fascinating geometry-dependent effects. Choosing to study gold electrodes offers additional exciting features to explore, including a dependence of the PZC of gold on the electrolyte due to anion adsorption [140, 51, 284]. In reactive metals, such as the Pt-group metals, and many of the other transition metals, experiments suggest that the double layer is formed mostly by the adsorbed species [204]. However, the literature also reports almost no electrolyte dependence in the differential capacitance of platinum [117], which is surprising if the double layer originates from adsorbed ions. To settle this discrepancy, one could include explicit, quantum-mechanical anions on the platinum surface within JDFT to verify the specific adsorption phenomena suggested in the literature.

After investigating the limitations and strengths of JDFT on well-characterized single-crystalline electrodes in aqueous solutions, we may next focus our attention on predictive calculations for supercapacitor and battery electrode materials in contact with novel electrolytes [5, 10, 52, 72]. In supercapacitors, pseudocapacitive charging is the main mechanism by which energy storage occurs and the amount of capacitance available in a given electrode material depends on the geometry. For example, matching the pore size to the size of the solvated ion in hierarchical carbon structures [191, 130, 129] can lead to an increase in capacitance which can be predicted by classical DFT methods. However, for novel electrode structures such as metal organic frameworks, in

which the chemical identity and quantum-mechanical effects in the electrode are important, a full JDFT approach would be required to capture such effects. In batteries, the potential dependence of the desolvation and intercalation of the working ion (usually Li^+), could be captured by using JDFT to determine the potential at which the ions begin to move into the inner Helmholtz plane. Finally, the reaction rates and kinetics of quantum-mechanical processes on the electrode surface could be captured by joining transition state theory and AIMD with JDFT to compute reaction barriers. Time-dependent electrolyte processes, such as diffusion of reactants to the electrode surface, could be captured by including dynamical info within the classical DFT in the spirit of the Nernst equation [33, 131].

CHAPTER 5

SRTIO$_3$ ELECTRODES UNDER WATER-SPLITTING CONDITIONS [1]

5.1 Overview and Motivation

5.1.1 Introduction to SrTiO$_3$

Out of a myriad of multi-featured complex oxide materials, the perovskite strontium titanate (SrTiO$_3$ or STO) is one of the most fascinating because it is known to split water under illumination with sunlight (see Figure 5.1 for the unit cell of the bulk crystal). The products of hydrolysis under either basic or acidic conditions are oxygen gas (O$_2$) and hydrogen gas (H$_2$),

$$2H_2O \rightleftharpoons 2H_2 + O_2, \tag{5.1}$$

though the reaction pathways are necessarily different in different electrolyte environments. In recent years, scientific interest in generating electricity and fuel from sunlight and water[201, 307] has grown due to concerns about energy security and climate change. STO is especially tantalizing because it performs oxygen reduction and hydrogen evolution, even without the presence of an applied voltage bias [308, 183], and yet, it is stable to dissolution under a wide range of conditions [121]. In order to split water efficiently, however, the band gap of the light-absorbing material (in this case bulk STO) should align with the peak of the solar spectrum. Unfortunately, the band gap of STO is

---

[1]Co-author credits: D. Gunceler helped perform the vacuum structure search described in section 5.4, and helped develop the hypothesis of the anatase-like structure for the activated surface. M. Plaza, X. Huang, J. Rodriguez-Lopez, and the research groups of D. Schlom, H.D. Abruña, and J.D. Brock performed the experiments. This work is under review in Nature Materials [220].
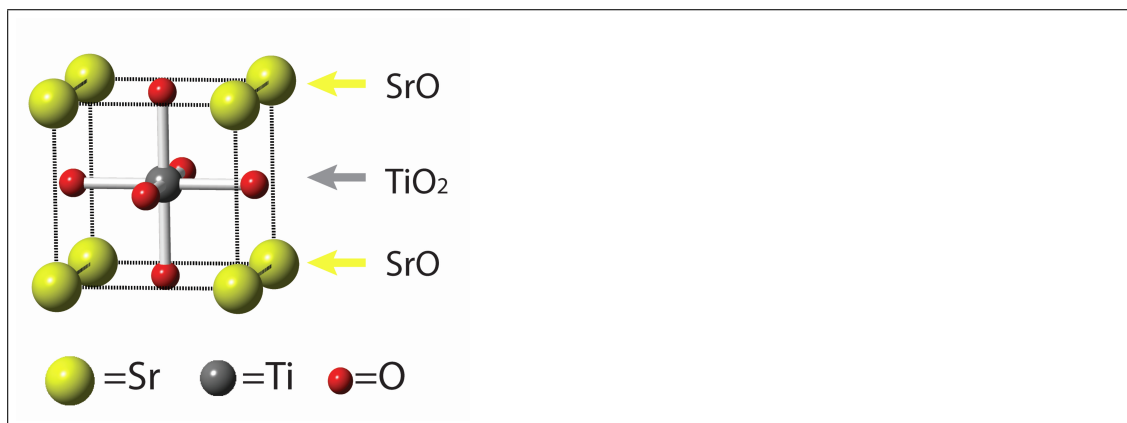
Figure 5.1: At room temperature, STO is a cubic perovskite material with a lattice constant of 3.91 Å. The Ti atom (silver) is at the body center surrounded by an octahedron of O atoms (red). The Sr atoms (yellow) are at the corners of the cube. The structure thus consists of alternating layers of SrO and TiO_2
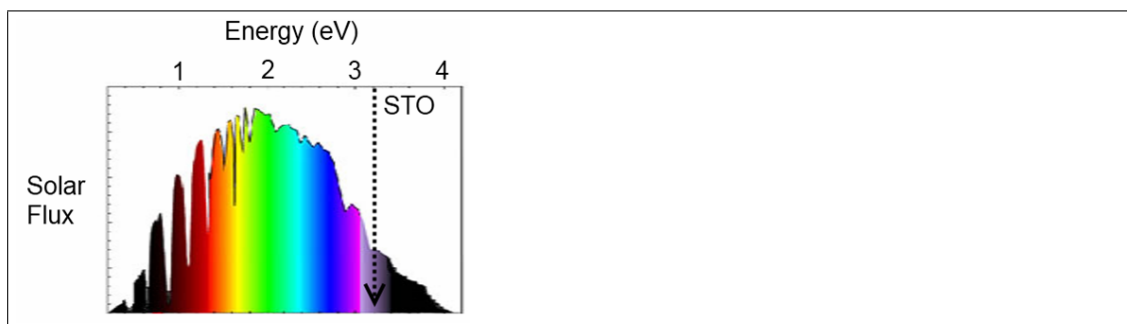
Figure 5.2: Solar Flux as a function of photon energy (eV) with peak at approximately 2 eV [25]. STO band gap (3.2 eV) falls significantly beyond the peak [63].

3.2 eV [63], which is somewhat too large for efficient absorption of the photons in sunlight (see Figure 5.2). Even though STO is not a commercially viable water-splitting material, it remains an excellent fundamental system for study of photo-catalyzed water splitting. Despite the simplicity of the STO water-splitting system, the activated surface structure and the reaction mechanisms of the STO surface in aqueous environments are largely unknown. Understanding of the fundamental physics which allows strontium titanate to split water at no applied bias would help inform the design of the energy materials of the future.

212

5.1.2 Theoretical Studies of Water-Splitting Materials

Density-functional theory (DFT) has been applied successfully to study bulk complex oxides such as STO [287, 23], and has also been instrumental in developing our understanding of physical phenomena associated with vacuum-terminated surfaces [65], materials' interfaces [9], nanomaterials [224, 291], and molecules [41]. Theoretical studies of reaction pathways for water splitting on ideal TiO_2 surfaces [235, 291] and large photo-synthetic molecules [186, 312] have been undertaken, but the literature has largely ignored fundamental surface studies on the more complex oxides, such as the perovskites. Instead, studies of STO water-splitting to date have relied upon calculating properties that correlate with high activity [292] or studying modifications to the bulk structures [69]. Many of these high-throughput studies ignore the effect of the liquid environment completely. The dissociation of water has been studied using force fields on rutile and anatase TiO_2 [226], indicating that hydrogen bonding between an explicitly adsorbed water layer and the liquid water is correlated with the extent of water dissociation. However, the effects of voltage and ionic strength are not considered in these force-field studies. Finally, X-ray measurements have been combined with DFT to calculate the structure factors of rutile (110) in liquid electrolyte [318], but these measurements did not consider the water-splitting reaction.

Fundamental mechanistic studies of water splitting in a true electrochemical environment are clearly needed to explain the nuances of photo-catalytic activity of these more complex materials. However, first principles calculations have not yet reached their full potential when applied to such systems, where the presence of a liquid electrolyte strongly influences reduction and oxida-

tion at the electrode surface. Joint density-functional theory[218] (described in Chapters 3 and 2) builds upon the proven power of electronic structure calculations for understanding physical phenomena by adding a microscopically accurate and *simultaneously* computationally tractable description of the liquid electrolyte environment. Joint density-functional theory therefore has the potential to become a vital tool for discovery of the fundamental microscopic mechanisms involved in charge transfer processes at electrode surfaces, which are quite challenging to determine, either experimentally or with any other computational method.

5.2 Experimental Background

We now review an electrochemical mystery regarding how STO behaves under water-splitting conditions and solve this mystery through a novel synthesis of theoretical and experimental techniques.[220]

5.2.1 Sample Preparation

To experimentally characterize the water-splitting properties of STO, our colleagues require a smooth, contaminant-free surface with a measurable activity for the oxygen reduction reaction in Equation 5.2. They used a commercially available $SrTiO_3$(001) single crystal wafer, which they then cleaned, etched, and annealed at high temperature. Atomic Force microscopy (AFM) measurements[24] in Figure 5.3 show the careful preparation results in a smooth surface with single-layer thick atomic terraces due to a slight mis-cut of the sam-
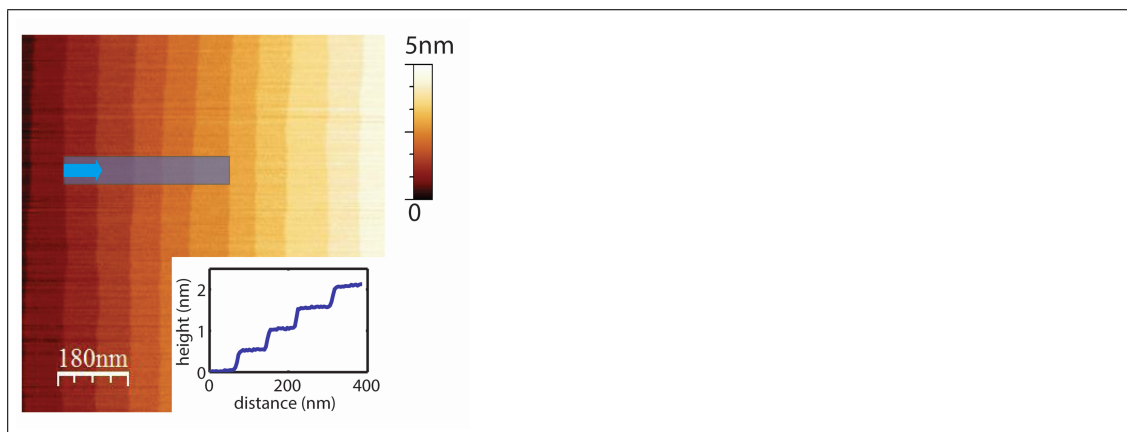
Figure 5.3: AFM image (Tapping mode AFM image of SrTiO$_3$ after surface preparation. The inset shows the height profile of the shadowed area of the AFM image. Atomic terraces were about 0.5 nm in height and 90 nm in width

ple away from the perfect (001) truncation. After the initial surface preparation, samples were annealed again at low oxygen pressure to produce oxygen vacancies, which are necessary to n-dope the sample and enhance the electrical conductivity. UV-visible reflectance measurements[78] confirm the increased conductivity of the sample after doping. Using the SECM technique descibed in Section 5.2.2 below, our colleagues found the added conductivity provided by the oxygen defects in the STO is necessary to produce water-splitting activity (the undoped surface shows no activity).

5.2.2   Measurement of Water-Splitting Activity

The water-splitting reaction (Equation 5.1) produces hydrogen (H$_2$) and oxygen (O$_2$) when an STO surface is illuminated with UV light (even when the circuit is open and no bias is applied). Our colleagues employ Scanning Electrochemical Microscopy (SECM) to determine the electrochemical activity of the STO sample. SECM [13, 14, 160] is a versatile measurement technique in which a
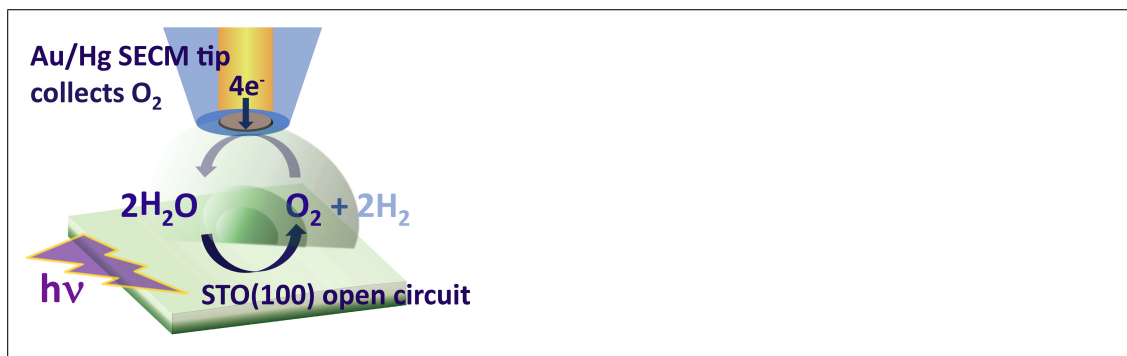
Figure 5.4: SECM in O_2 substrate collection mode. Hg/Au amalgam tip detects oxygen produced by the water splitting reaction at the $SrTiO_3$ electrode at open circuit.

specially designed micro-electrode tip is brought within microns of a substrate and biased to produce a current when specific reactions occur on the surface (Schematic in Figure 5.4). The tip composition is chosen to be sensitive to a particular product of the reaction. In this case, an Au/Hg amalgam tip can be used to detect O_2 gas [188] through the oxygen reduction reaction (ORR),

$$H_2O + 2O_2 + 4e^- \rightleftharpoons 4OH^-. \tag{5.2}$$
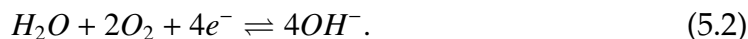
The SECM tip can remain stationary in order to measure surface composition and reactivity as a function of time, or it can be moved across the surface to determine spatial variations. SECM studies can also be carried out while the substrate is under illumination with a UV lamp, and can measure almost instantaneous changes in photo-catalyzed oxygen and hydrogen evolution as a function of the illumination.

Our collaborators used the SECM technique described above to measure the rate of generation of O_2 from the water splitting reaction on STO under a variety of experimental conditions. Figure 5.5 shows the O_2 current as a function of time, for a sequence of sample conditions with no applied bias (e.g. at open circuit potential or OCP). The dark and light stripes indicate where UV light has
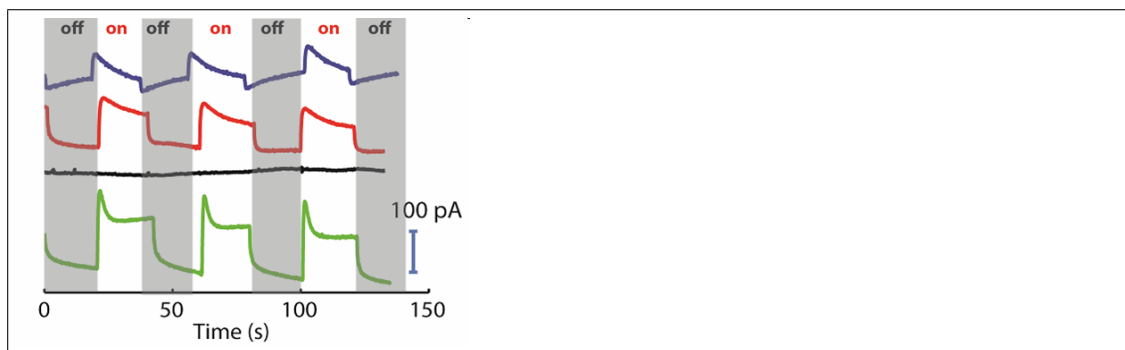
Figure 5.5: SECM collection with UV light on/off: (blue) 0.1 M NaOH before biasing potential, (red) after biasing to 0.8 V vs. Ag/AgCl for 40 minutes, (black) upon immersion in 0.1 M H_2SO_4 and (green) after returning to 0.1 M NaOH. The oxygen generation rate is proportional to the current.

been turned off and on so water splitting stops and starts. Because the oxygen generation rate is proportional to the current, these current traces relate directly to water-splitting activity. Because the instantaneous reaction rate is highly variable, the average reaction rate provides the most accurate results. Thus, the integral of the current with respect to time (corresponding to the amount of oxygen produced in a fixed time) is the best measure of water-splitting activity.

First, the STO sample, prepared using the procedure of Section 5.2.1, is freshly immersed in a basic solution of 0.1 M NaOH (top, blue curve) at OCP. Then, the electrode is biased to an oxidizing voltage of 0.8 V vs Ag/AgCl for about 40 minutes then returned to OCP. After this biasing, the activity of the electrode at OCP increases by about 260% (second, red curve). If the sample is then immersed in acid, the activity (third, black curve) vanishes because there is no OH^- intermediate to drive the reaction. However, when the sample is returned to the basic solution at OCP (last, green curve), it once again attains the enhanced activity. Therefore, it appears that biasing the sample to an oxidizing potential irreversibly *trains* the surface to exhibit a higher activity for water splitting. However, the electrochemistry alone gives no indication of the origin

of this training.

5.2.3   X-ray Reflectivity Measurements

Another tool which provides clues about this mystery is X-ray reflectivity, specifically measurement of the crystal truncation rods at the surface [8, 232]. Figure 5.7 shows the crystal truncation rods (CTR), which are a direct measurement of the amplitude of the structure factor squared versus the wavevector $\vec{q}$ in reciprocal lattice units (r.l.u.), for STO under several different conditions. An infinite perfect crystal would produce intensity only at the Bragg peaks, or at the integer values of the wavevector $\vec{q}$. When the crystal is terminated, however, signal appears between the Bragg peaks. Variations in this signal occur when the atoms at the surface are strained so they are no longer in their bulk crystalline positions, thus allowing crystal truncation rods to be used to analyze surface structures with sub-Angstrom resolution. High intensity X-rays, such as those from a synchrotron, are required in order to provide sufficient signal between the Bragg peaks, so the measurements are performed at CHESS (Cornell High Energy Synchrotron Source). Figure 5.6 shows the experimental setup for these reflectivity measurements, including a specialized area detector, a UV lamp for shining light on the sample, and an electrochemical cell for performing *operando* measurements while the water-splitting reaction is in progress.

Figure 5.7 shows the experimental data for the specular (0 0 L) truncation rods of the STO sample (a) in air, (b) freshly immersed in liquid at open circuit potential (OCP), and (c) after biasing to an oxidizing potential. The signal between the Bragg peaks differs significantly between each sample, indicating a
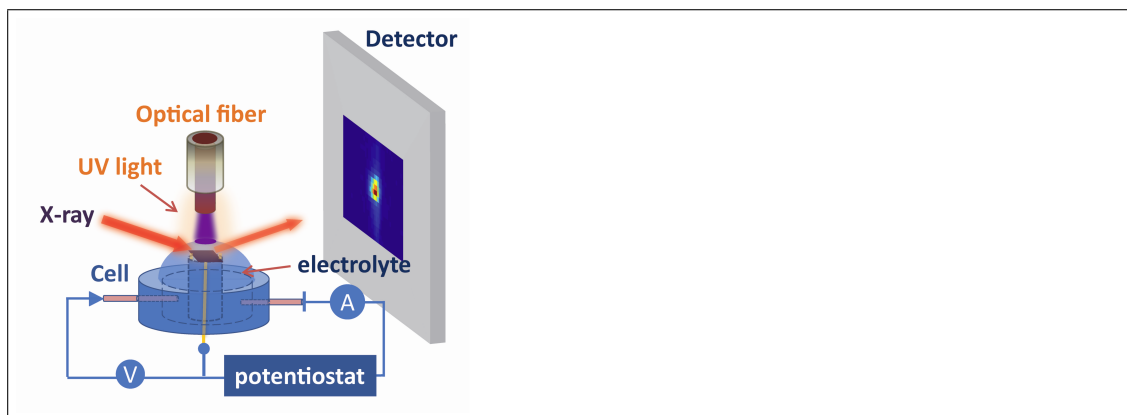
Figure 5.6: Schematic of the experimental set-up for in situ X-ray reflectivity of SrTiO$_3$ during photoassisted electrochemistry

different surface structure is present in each. In order to track these changes in the surface, we therefore define a reaction coordinate as the value of the structure factor squared at q_z = 1.5 in reciprocal lattice units and show a schematic of how the surface changes in Figure 5.8. As the surface is first put into liquid at OCP, and then again as it is biased to oxidizing potentials, the reaction coordinate increases. This reaction coordinate therefore appears to be correlated with the higher activity for water splitting. Finally, the initial CTR measurements of the immersed surface were repeated with 0.1 M CsOH to verify that the surface structure is not sensitive to the choice of cation in the electrolyte.

Because the X-ray signature of the final, trained surface (in red) is stable, despite submerging the sample in acid and removing it from the liquid, these results indicate the higher activity may be the result of a significant and irreversible structural change of the surface. Because the X-ray intensity *increases* rather than decreases as the activation of the surface proceeds, this change is not just due to increasing roughness [232], but actually indicates some increase in surface ordering. The vacuum surface has been characterized both theoretically and experimentally [65], and it has been found to be a double-terminated
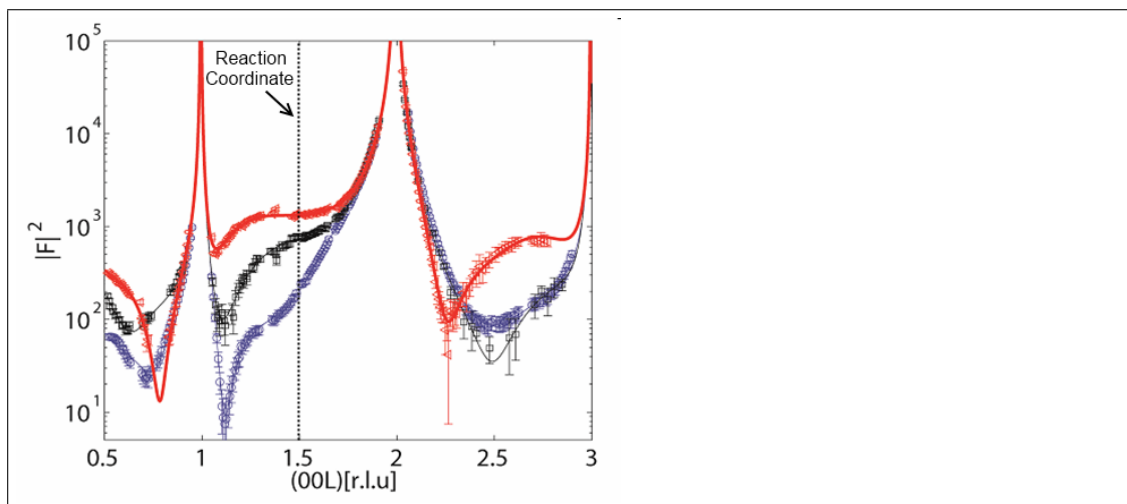
Figure 5.7: (0 0 L) structure factor of SrTiO3 in air (blue), in 0.1 M NaOH at open circuit before (black) and after (red) biasing at +0.8 V vs. Ag/AgCl. Solid lines correspond to best fits to atomic models which minimize χ^2.
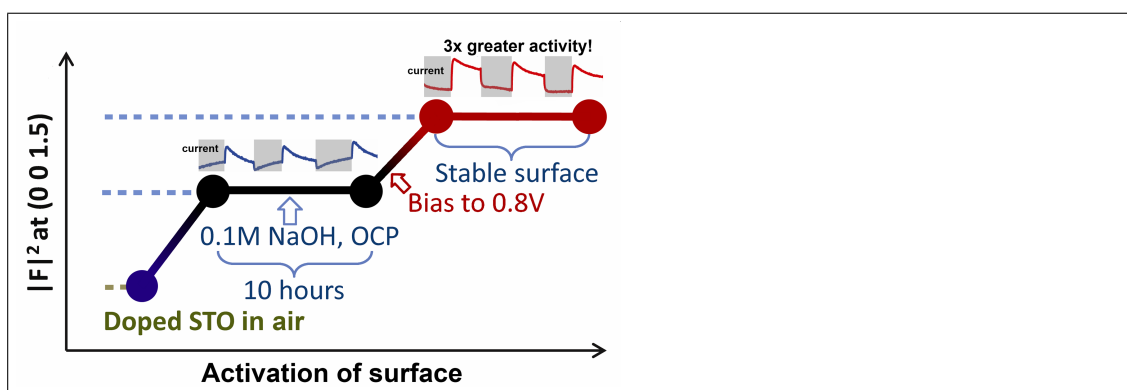
Figure 5.8: Reaction coordinate map to the evolution of $|F|^2$ at (0 0 1.5) r.l.u. of samples under different conditions: Blue, doped or undoped $SrTiO_3$ in air; Black, doped SrTiO3 in 0.1 M NaOH or 0.1 M CsOH before biasing; Red, doped $SrTiO_3$ in 0.1 M NaOH after biasing

TiO_2 surface (meaning the terminating layers are $TiO_2/SrO/TiO_2/TiO_2$) with a 2×1 reconstruction parallel to the surface. However, the exact structure of the surface under bias, and in electrolyte is heretofore undetermined. The *operando* surface (while operating and actively splitting water) could have a different termination, reconstruction, or geometry than the vacuum surface. In particular, the *operando* surface likely has molecules or reactants/products such as OH^- or H_2O adsorbing and de-adsorbing at active sites.

Typically, experimentalists determine the surface structure by non-linear least squares fitting of the locations of the lattice planes, the occupancies of the atoms in those planes, and the widths of the planes (also known as Debye Waller factors) to the experimental $|F|^2$ data. They use the reduced chi-squared parameter,

$$\chi^2 = \frac{1}{N - n - 1} \sum_{i=1}^{N} \frac{(S_i - f(q_i))^2}{\sigma_i^2},$$ (5.3)

to measure the quality of the fit to be optimized. Here, N is the total number of data points; n is the number of adjustable parameters; σ_i is the experimental error at the scattering wave vector q_i, mainly from the stochastic noise in the photon-counting statistics; S_i is the measured experimental data at q_i; and, $S(q_i)$ is the expected X-ray signal at q_i, calculated from the assumed atomic positions, vacancy concentrations, and Debye-Waller factors. The solid lines in Figure 5.7 show the fit-based interpretation of the CTR data for the STO after biasing. The choice of atomic model is not unique, and significantly different choices of surface composition can lead to comparably high levels of accuracy in the fit because of the high number of adjustable parameters available. There is also no guarantee that the structures produced from pure fitting to the X-ray data are realistic. For example, when the atoms are placed in the X-ray fit locations, the DFT-computed forces on the atoms are often quite large, indicating structures far from equilibrium. It would be far preferable to have a way to predict this structure directly from fundamental physics – without a purely empirical fitting procedure.

5.3 Theoretical Determination of Surface Structures

The JDFT framework[218], even with a simplified description of the liquid environment, has been proven reliable for mapping electrochemical observables to ab initio computables in [163] and Chapter 3. A single DFT calculation which makes specific choices for the orientation of the liquid molecules at the electrode surface [283, 132] is insufficient to predict electrochemical observables because the effects of screening from the electrolyte on the surface often depend on the spatially and temporally averaged structure of the liquid, not a single configuration. A classical liquid functional, on the other hand, captures the microscopic details of the thermodynamically averaged interfacial liquid structure and provides highly accurate predictions of solvated atomic structure and the electronic properties of solvated systems.

5.3.1 Crystal Truncation Rods from JDFT

Once the relaxed atomic positions, electron density, and fluid density profiles are determined from a JDFT calculation with a given stoichiometry and surface configuration, we may use them to compute the X-ray structure factor $F(\vec{q})$ with *no adjustable parameters*. We do not require tabulated form factors, nor is there a need to guess the relevant oxidation states of the surface atoms. The main quantity required for a completely first principles prediction of a crystal truncation rod (CTR) is the total electron density (including valence, core, and fluid electrons) averaged over the planes perpendicular to the X-ray scattering vector. In the present case of specular reflection, we compute this average over the planes parallel to the surface (the *x*- and *y*-coordinates), leaving the electron density as
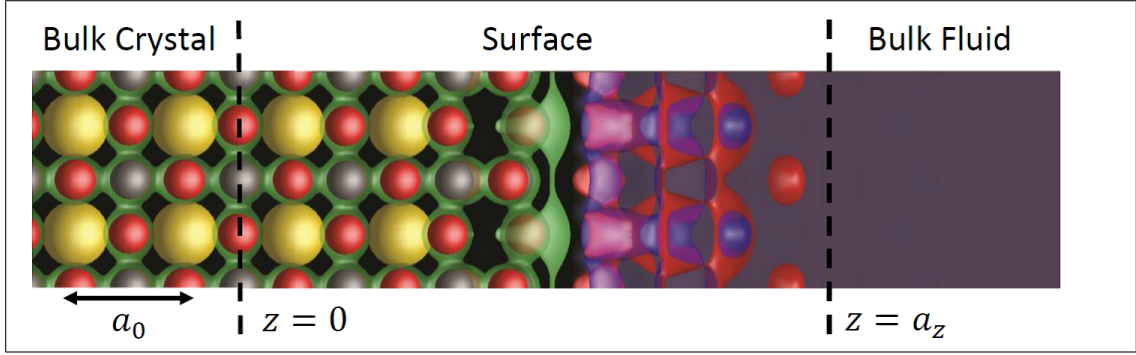
Figure 5.9: Schematic of X-ray structure calculation from first principles, with a region representing each of the 3 terms from Equation 5.4. The DFT lattice constant is a_0 and a_z is half the length of the DFT supercell in the z-direction (see Figure 5.17)

a function of the coordinate perpendicular to the surface (the z-coordinate). We thus first calculate $n_{tot}(\vec{r})$ from JDFT using Equation 2.1 from Chapter 2 and then average it over the plane parallel to the surface to find $\bar{n}_{tot}(z) = \iint n_{tot}(\vec{r})dxdy$. With this electron density profile, the structure factor for a specular X-ray CTR ($\vec{q} = q_\perp = [0\ 0\ 2\pi L/a_0]$) is then

$$F(\vec{q}) = \frac{\int_0^{a_0} \bar{n}_{bulk}(z)e^{iq_\perp z}dz}{1 - e^{iq_\perp a_0}} + \int_0^{a_z} \bar{n}_{tot}(z)e^{iq_\perp z}dz + \frac{n_{fl}^b e^{iq_\perp a_z}}{iq_\perp}. \tag{5.4}$$

Figure 5.9 displays the physical origin of each of the terms in Equation 5.4 for an STO surface with a two-layer TiO_2 termination. The first term in Equation 5.4 gives the scattering from a (semi-)infinite bulk crystal below the surface from locations $z = 0$ to $z = -\infty$, whose electron density we take to be that of an unperturbed, infinite bulk crystal. The numerator of this term represents the scattering from a single unit slab of thickness a_0, and the denominator represents the phase sum for the semi-infinite collection of layers. In practice, we obtain the planarly averaged electron density $\bar{n}_{bulk}(z)$ from an *ab initio* bulk unit cell calculation with lattice constant a_0. The last term, similarly, represents the scattering from a semi-infinite layer of bulk liquid of average electron density n_{fl}^b extending from location a_z to ∞. Because of the translational invariance of

223

the fluid far from the surface, this bulk electron density is constant.

The second term, which includes all the important interfacial effects, is simply the fourier transform of the total electron density $\bar{n}_{tot}(z)$ from the JDFT calculation of the surface. Finally, we note that this total density $\bar{n}_{tot}(z)$ includes several key components: 1) the valence electron density $n(\vec{r})$ of the quantum mechanical electrode, 2) the valence electron density $n_{fl}(\vec{r})$ of the fluid, determined by the atomic fluid density fields and a single quantum mechanical calculation for each type of fluid molecule, and 3) the core electron density $n_{core}(\vec{r})$, determined by the all electron calculations used to generate the atomic pseudopotentials. Section 5.5 describes further numerical and computational details of these calculations.

5.3.2 JDFT-guided Least-Squares Fitting

Nonlinear least-squares fitting allows the atoms to move away from their JDFT minimum energy positions to consider the effect of non-equilibrium processes and develop partial occupancies and Debye-Waller factors to account for defects and disorder. We may ensure the physicality of these fits by minimizing a residual R^2 which includes both χ^2 from Equation 5.3 and a penalty function to prevent the fit positions $\{\eta_I\}$ from varying significantly from the JDFT predicted positions $\{Z_I\}$,

$$R^2 = \chi^2 + \frac{1}{2}\frac{\kappa}{k_B T}\sum_I (\eta_I - Z_I)^2. \tag{5.5}$$

In this new residual, the tabulated form factors for the explicit atoms located at fit positions $\{\eta_I\}$ *and* the electron density of the fluid $n_{fl}(\vec{r})$ predicted from JDFT are combined to compute the structure factor $S(q_i)$ in χ^2. The constant $\frac{\kappa}{k_B T}$ in

Equation 5.5 determines the relative weight of the penalty function compared to χ^2, and may be related to an effective spring constant κ and temperature-dependent energy scale $k_B T$.

Two figures of merit characterize the quality of the resulting fit. First, the root-mean-squared displacement of the fit positions of the atoms from the JDFT-predicted positions,

$$z_{\text{rms}} = \sqrt{\frac{1}{N_I} \sum_I (\eta_I - Z_I)^2}, \tag{5.6}$$

gives a direct measure of the spatial distortion from the pure *ab initio* structure. Second, the calculated JDFT excitation energy of the fit structure gives a measure of the distortion relative to the known inaccuracies of density-functional theory. Any fit structure which has an excitation energy of only a few times $k_B T$ per fit atom (the inherent accuracy of typical approximations to density-functional theory) and a z_{rms} of around 0.1 Å (the typical extent of atomic vibrations in bulk crystals) would be considered physically realizable.

5.4   First Principles Predictions for Strontium Titanate

With the combination of the JDFT framework in Chapter 2, the recipe for calculating crystal truncation rods from first principles in Equation 5.4, and the JDFT-guided fitting procedure in Equation 5.5, we are able to make meaningful theoretical predictions for *operando* X-ray signatures. Previous work [318] has established that DFT calculations can be a valuable tool for interpreting CTR's of TiO$_2$ in a liquid environment, but that work did not include the water splitting reaction and involved theory that considered only ideal vacuum surfaces, without including the liquid environment or the relaxation of the surface in the

presence of the liquid. JDFT, on the other hand, provides a prediction of not only the interfacial liquid structure, but also the effect of the screening from the liquid environment on the electronic structure of the electrode and the positions of each atomic layer. Finally, the JDFT constrained fitting procedure allows us to consider any additional variation away from the ideal surface due to disorder, defects, and non-equilibrium processes.

JDFT does, in fact, predict hydrogen bonding and physisorption effects accurately (see Figures 2.8 and 2.10 in Chapter 2), so associative water adsorption is captured within the classical liquid functional. However, covalent bonds or charge transfer reactions between the liquid molecules and electrode must be included in the quantum mechanical portion of the calculation ($F_{KS}[n(\vec{r})]$ in Equation 2.1). For each surface termination or stoichiometry considered, we must thus consider hydroxide, water, and oxygen chemisorption explicitly within the quantum-mechanical functional. Additionally, reconstructions of the solid material parallel to the surface which result from rearrangements of the electrode atoms must be considered explicitly (though the classical DFT fluid does account for statistical averages over reconstructions of the fluid parallel to the surface, including partial coverages of water, even when working with a single unit cell of $SrTiO_3$). The extremely large phase space of possible configurations of the solid surface which must be explored makes this endeavor quite daunting, and virtually impossible to approach with molecular dynamics due to the additional complication of thermodynamically sampling the liquid. JDFT is an ideal technique for this problem because it is both computationally efficient and microscopically accurate.

To consider all potential $SrTiO_3$ surface terminations which could be partic-

ipating in the water splitting reaction, we performed a large scale JDFT search over many stoichiometries and surface compositions [124]. We explored surface structures with different number of terminating SrO or TiO_2 layers and horizontal reconstructions (1×1, 2×1 and $\sqrt{2} \times \sqrt{2}$), including several structures presented in the literature [65, 66, 248]. Adsorbed species involved in the water-splitting reaction (O^{2-}, OH^- and H_2O) were also considered on each surface. To reduce the computational demands, JDFT calculations were performed at varying levels of approximation for the liquid. We first evaluated a large number of surfaces within implicit solvation theory [100], and the promising candidates were then recalculated with explicit JDFT [266, 262]. Finally, we considered those surfaces which were stable, but not necessarily the global minimum of free energy. We chose to include local free energy minima for two reasons. First, the water splitting reaction is a non-equilibrium process with multiple intermediate states. Second, the global minimum of free energy is difficult to determine because chemical potentials for reaction constituents such as O (needed to compare free energies of non-stoichiometric surfaces) depend on the details of the particular reaction pathway and local concentration gradient, so are difficult to obtain from simple pH arguments.

5.4.1 Surface In Air

Figure 5.11 shows the CTR predictions for some of the best candidates for the surface in air found in the large-scale structure search. The three best-agreeing structures are all double TiO_2 terminated; one is the 2×1 reconstruction from the literature [65], the second has a higher symmetry 1×1 unit cell, and the third has adsorbed OH on the surface. The realspace images for these three candidates
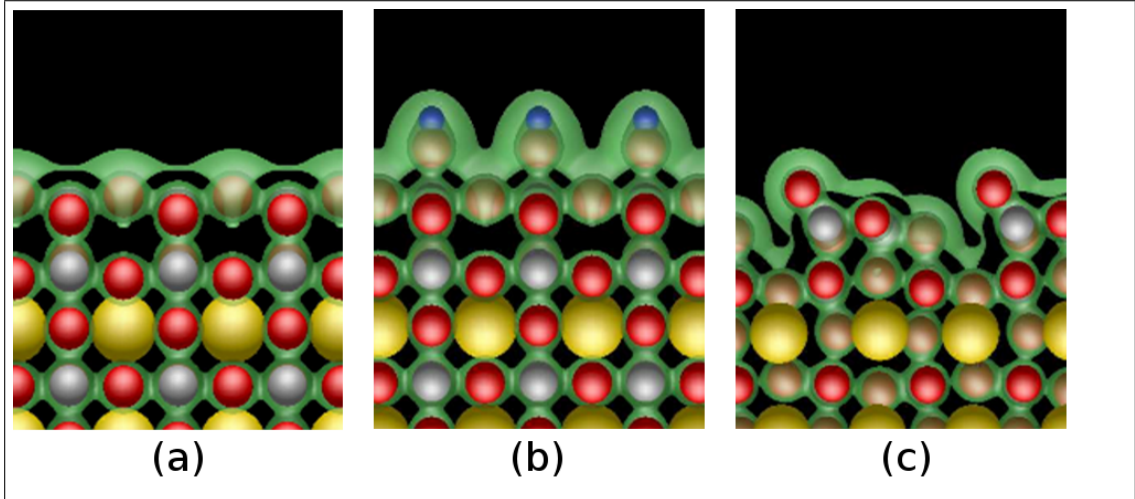
Figure 5.10: Realspace images of potential candidates for domains on STO in air: (a) 1×1 unit cell with no adsorbates; (b) 1×1 unit cell with adsorbed OH; (c) relaxed 2×1 reconstruction from the literature [65]

are shown in Figure 5.10. Some features of each CTR agree reasonably well with the experiment (blue squares), but overall none of the individual calculations reproduces the experimental X-ray signal across the full range of wavevectors. Since the experimental data does not appear to show the extra diffraction spots associated with a long-range reconstruction, STO in air likely includes a mixture of short-range reconstructed domains. This result is in agreement with the experimental interpretation for STO in air [111, 294]. One could then attempt to model the effect of the mixture of reconstructed domains by combining the calculations for individual surfaces into a weighted average with the weights fit to the experimental data. In Figure 5.12 we show a structure factor (purple dotted line) which is a linear combination of the structure factors computed for the candidate surfaces in Figure 5.10, with the 2×1 reconstruction as the most heavily weighted structure. Clearly, the agreement between the experimental data and the linear combination of structure factors is much better than the agreement for any of the pure structure factors alone.
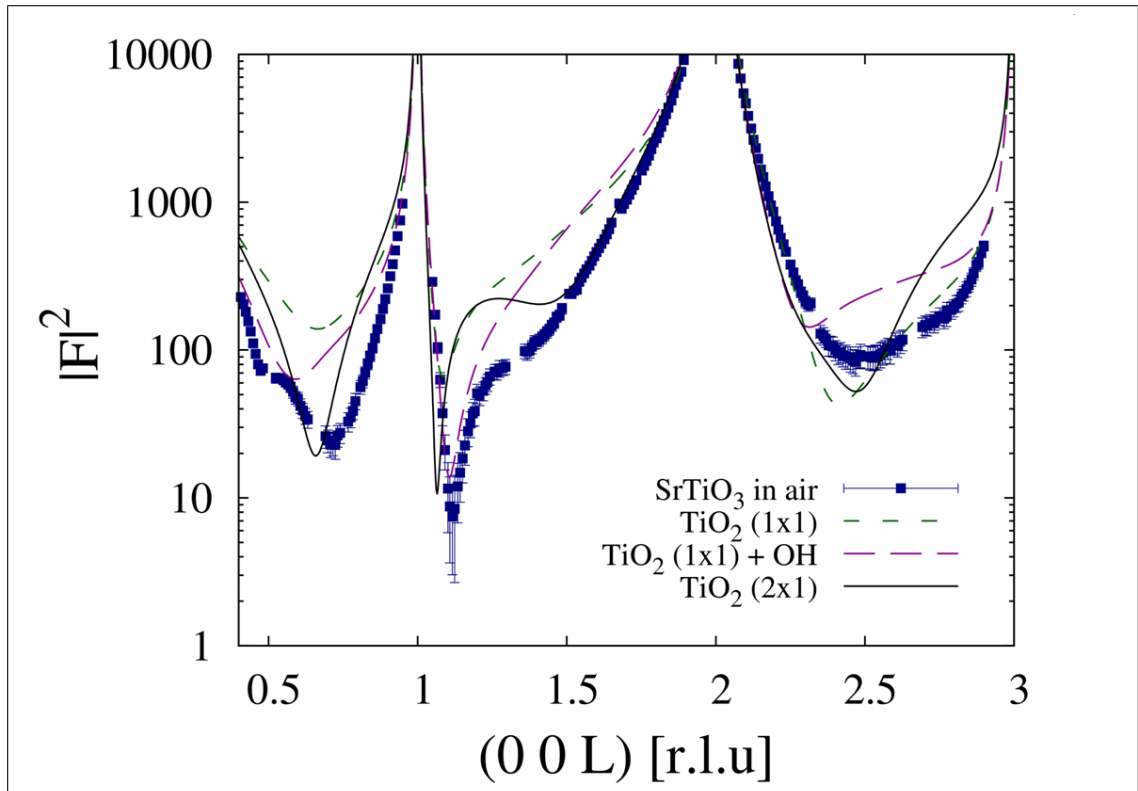
Figure 5.11: First principles CTR predictions compared to experimental X-ray signal (green squares) for the three candidate surfaces in Figure 5.10: (a) dotted green line (b) dashed purple line (c) solid black line

Alternatively, it is possible to address the imperfections in the air surface using the vacuum DFT-guided fitting procedure in Equation 5.5 with constant $\frac{\kappa}{kT} = 20$ Å^{-2}. The best fit structure in air has a total DFT-calculated excitation energy from the relaxed vacuum structure in the literature [65] of only 0.26 eV, or 0.012 eV (less than $kT/2$) per atom included in the fit. The JDFT-guided fitting procedure yields the structure factor (solid green line) in Figure 5.12, which is almost indistinguishable from the experimental data. The rms displacement in the best fit positions compared to the DFT-predicted positions is $z_{rms} = 0.035$ Å with a maximum change of 0.2 Å for a single atom.
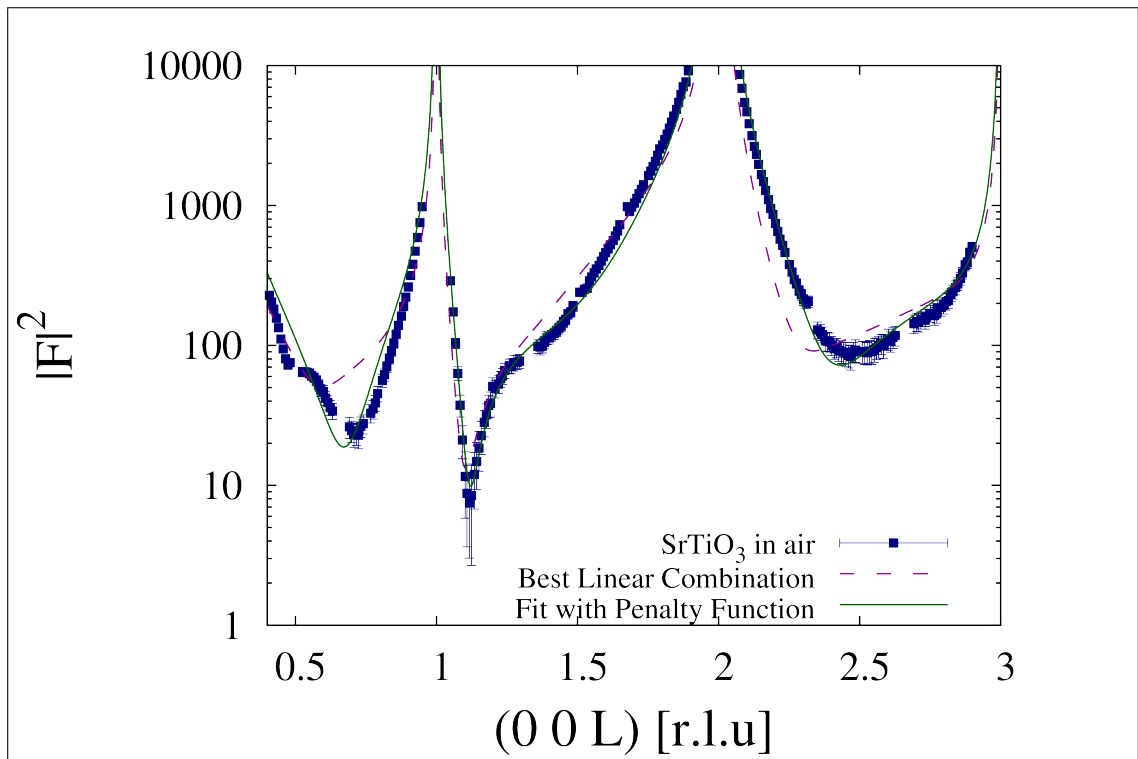
Figure 5.12: JDFT-informed CTR fits compared to experimental X-ray signal (green squares) for the STO surface in air using two different methods: linear combination of the fully *ab initio* CTR predictions in Figure 5.11 (dotted purple line) and minimizing the penalty function in Equation 5.5 to constrain the fit to the known vacuum structure[65] (solid green line).

5.4.2 Freshly Immersed Surface

For a $SrTiO_3$ surface freshly immersed in a liquid electrolyte, JDFT-calculated crystal truncation rods (CTRs) agree with X-Ray reflectivity measurements with *no parameters whatsoever* fit to the experimental X-Ray data. The surface configuration which agrees best (CTR shown by the solid black curve in Figure 5.13 and structure shown in Figures 5.14(a) and 5.17(a)) is a double TiO_2 terminated surface with no specific chemical adsorption (only physisorbed water provided automatically by the JDFT fluid). The z-positions (distance perpendicular to the interface) for each atom in this structure are presented in Table 5.1 in the lattice coordinates of the bulk STO unit cell. Because the CTRs are highly dependent

upon the slight displacements of atomic layers away from their bulk positions, the excellent agreement with the experiment indicates the high accuracy of the JDFT-predicted atomic positions and liquid structure.

Additionally, Figure 5.13 indicates the superior agreement for the CTR prediction when including the thermodynamically sampled liquid within JDFT (solid black curve), compared to including a single explicit layer of water in a vacuum calculation (dashed blue curve). The vacuum calculation includes relaxed water molecules which dissociate, covalently bond with the surface, and alter the atomic structure, while the JDFT calculation assumes liquid water with shell structure. An additional feature of the classical DFT description is that, unlike adding a layer of explicit water molecules, CDFT allows water to attain a partial coverage on the surface within a calculation of a single unit cell and is not constrained to integral numbers of water molecules within the cell.

Additional features of the STO-water interface may be discovered upon examination of the real-space images in Figure 5.14. These images are each $3a_0 = 11.82$Å by 30 Å in dimension. We include the Sr, Ti, O, and H atoms of the quantum mechanical surface as yellow, grey, red, and blue spheres with radii exactly half their van der Waals radii. The valence electron density of the quantum mechanical system is represented by dual green contours, appearing at $n(\vec{r}) = 0.1$ Å^{-3} and $n(\vec{r}) = 0.013$ Å^{-3}. The purple-blue background appears where the fluid oxygen density N_O reaches at least half the bulk density of liquid water ($N^b = 0.033$ Å^{-3}) mapped onto a plane with surface normal pointing out of the page. The red and blue contours represent the oxygen and hydrogen densities in the liquid, respectively, where $N_O(\vec{r}) = N_H(\vec{r})/2 = 1.1N^b$. Thus, contours are only present in locations with significant shell structure in the fluid.
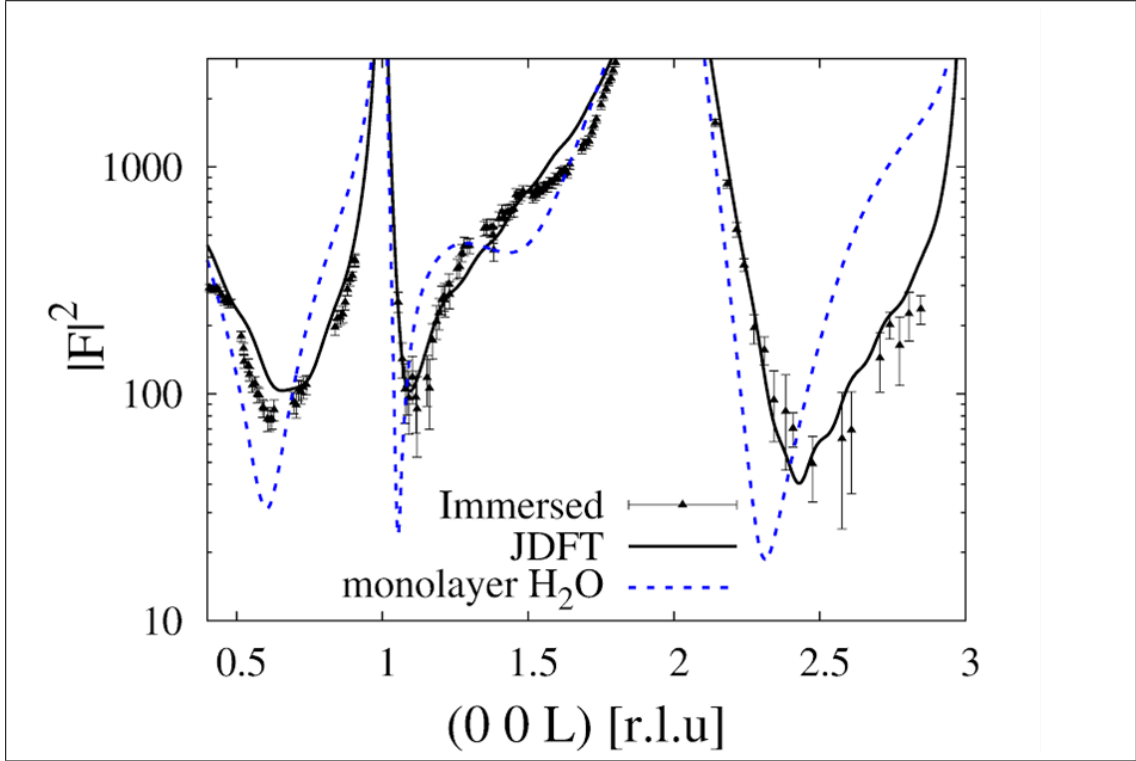
Figure 5.13: JDFT predicted CTR (solid black line) which agrees best with X-ray measurements (black triangles) for freshly immersed STO surface compared to the vacuum CTR for the same surface composition with a single water molecule per unit cell relaxed within DFT (dashed blue line).

As shown in Figure 5.14(a), the freshly immersed, "untrained" surface may be contained in a single unit cell parallel to the surface. This JDFT-predicted surface therefore possesses a higher degree of symmetry and is quite distinct from the 2×1 reconstruction which is a free-energy minimum in vacuum or air calculations presented in the literature [65, 107]. Despite its simplicity, this surface composition matches the experimental X-ray data far more closely than any of the more complicated reconstructions considered. We thus hypothesize that the screening from the liquid passivates the strong fields which drive the process of reconstruction and therefore leads to more symmetric surface. The extent of fluid density contours at the surface and extending into the bulk of the fluid also indicates noteworthy structure in the interfacial water. One potential
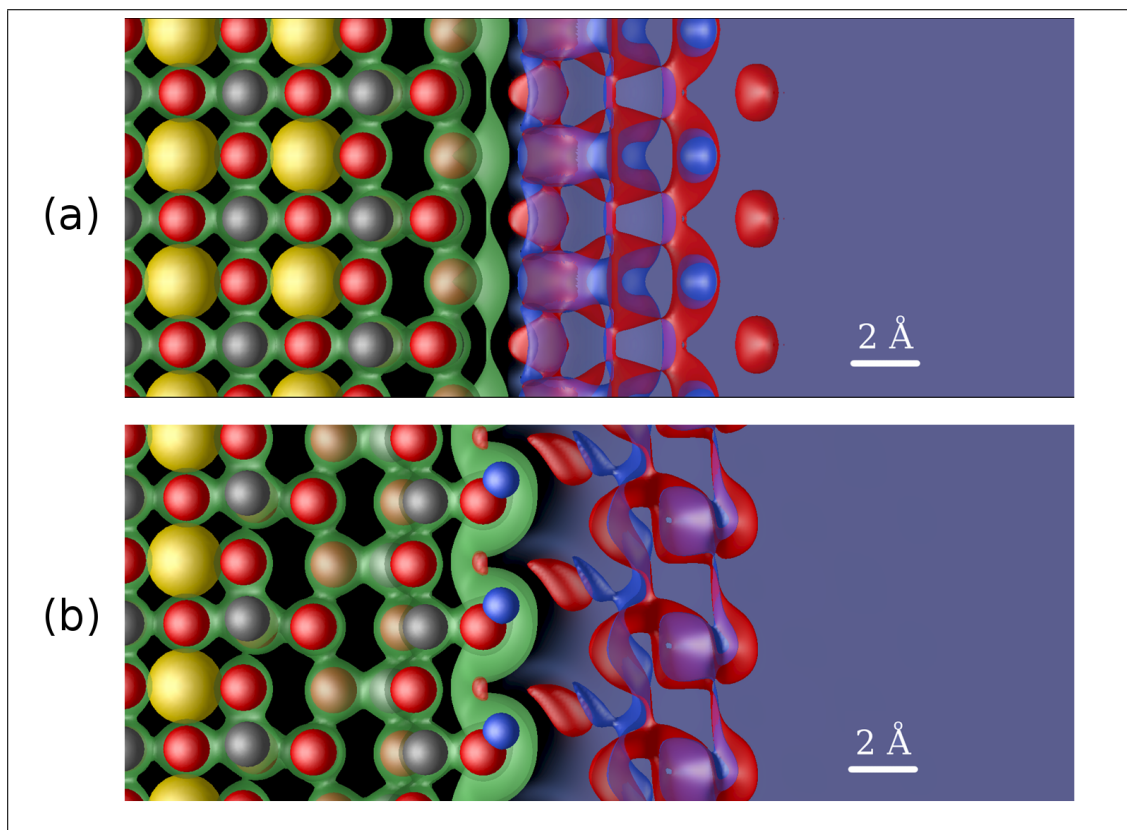
Figure 5.14: (a) The JDFT structure for the (001) surface of STO at open circuit before biasing. (b) The activated JDFT structure for the (001) surface of STO at open circuit after biasing. Yellow spheres are Sr, red are O, and silver are Ti atoms. Green, red, and blue density contours represent electron, oxygen, and hydrogen density respectively.

explanation for this highly ordered liquid structure is a match between the minimum oxygen-oxygen distance in the TiO_2 layers on STO (2.79 Å) and the same quantity in cubic ice (2.90 Å with a cubic ice lattice constant of 6.69 Å).

5.4.3   Activated surface

It was a greater challenge to identify the structure of the more complex, "trained" $SrTiO_3$ electrode surface, which reorders after biasing under water-splitting conditions. Of the approximately 100 surface topologies and

233

chemistries explored, nearly all failed to agree with the experimental CTR for the activated surface, with the difference being most striking in the middle range of scattering vectors, between the first and second Bragg peaks (as measured by the reaction coordinate $|F|^2$ at $\vec{q} = \frac{2\pi}{a_0}[001.5]$). After this intensive search, finally a structure with a triple layer Ti-rich termination yielded a promising reaction coordinate. The identified structure is anatase-like in the stacking of the Ti atoms (see Figure 5.17(b) for a clear picture of the layer stacking), but is under a strain of over 3% from the anatase lattice parameter.

Close investigation of the real-space data presented in Figure 5.14(b) provides additional information about the interfacial structure and possible function of the activated surface. This trained surface is terminated by non-stoichiometric TiO_{2-x} with $x = 0.25$, consisting of two layers of TiO_2, then a layer of Ti_2O_2, and finally one hydroxide bonded to the outermost titanium. Furthermore, comparing the trained surface in Figure 5.14(b) to the freshly immersed surface in Figure 5.14(a) reveals that at least one layer of SrO has been stripped from the surface during activation, possibly explaining the irreversibility of the training process. The fluid density profile in Figure 5.14(b) also indicates the orientation and location of the water molecules binding to the surface, therefore offering insight into potential mechanisms by which water splitting might proceed. Namely, the small pockets of fluid oxygen density shown on the trained surface in the same plane as the adsorbed hydroxide could indicate a possible active site for the water-splitting reaction.

The predicted CTR for this structure with no fit parameters is shown by the red dotted line in Figure 5.15. While this prediction is clearly not an exact match to the experimental data, our exhaustive search for alternatives (as well as the
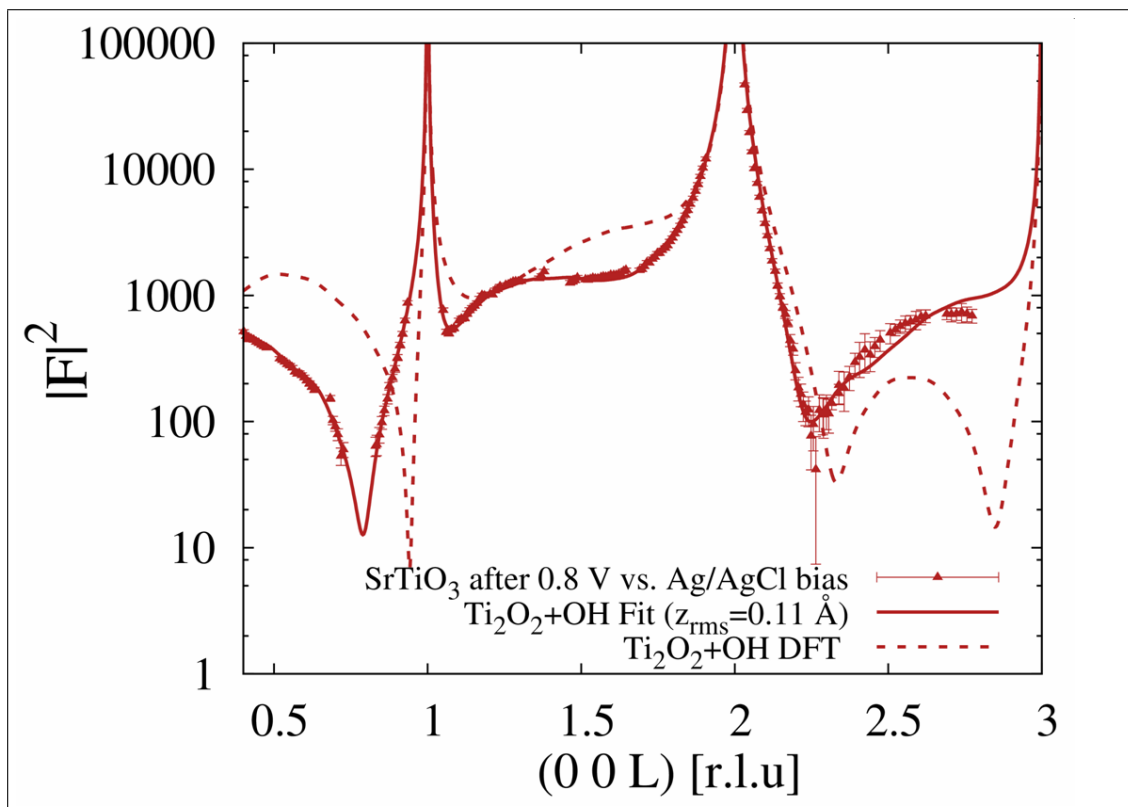
Figure 5.15: Comparison between CTR predictions for minimum energy JDFT structure with no fitted parameters whatsoever (dotted red line), the best JDFT-guided fit to that structure (solid red line), and experimental data (red triangles) for the trained surface.

success of the JDFT-guided fitting procedure described below) leaves us confident that the discrepancies are due to non-equilibrium processes during formation, defects, and disorder at the surface. To account for the aforementioned processes, we used the JDFT-guided fitting procedure and the objective function in Equation 5.5 with constant $\frac{\kappa}{kT} = 10$ Å^{-2}. Table 5.2 tabulates, for the activated surface, the best fit positions, occupancies, Debye-Waller factors, and distortions from the ideal JDFT-determined positions. The corresponding CTR prediction for the best fit structure is shown by the solid red line in Figure 5.15.

The best fit structure has a total DFT-calculated excitation energy from the *ab initio* minimum energy structure of only 0.73 eV, or 0.045 eV (less than $2kT$)

per atom of the 16 atoms included in the fit. The rms displacement in the best fit positions compared to the JDFT-predicted positions is $z_{rms} = 0.11$ Å with a maximum change of 0.22 Å for a single atom. We judge these distortions, close to the underlying uncertainties of density-functional theory, to be quite reasonable given the non-equilibrium nature of the surface. Finally, the partial occupancy (near 0.5) of the top Ti atom in the fit suggests a stoichiometry between TiO_2 and Ti_2O_2. Kinetic processes or oxygen vacancies from the n-type doping diffusing to the surface can readily account for this level of oxygen-deficiency from our idealized structure.

5.4.4 Uncertainty Analysis

There is also some resulting uncertainty in the fluid structure due to flexibility in our construction of the functional ΔA in Equation 2.1 of Chapter 2, which couples the surface and the fluid. Namely, we choose the Grimme van der Waals scaling parameter γ in ΔA based upon solvation of neutral molecules rather than polar surfaces. If we allow that parameter to vary within the physical range of $0 \leq \gamma \leq 1.0$, we obtain a range of structure factor predictions which corresponds to adjusting the strength of the van der Waals binding of water to the polar surface. In the spirit of ensemble error analysis [265, 193], Figure 5.16 indicates the corresponding range of JDFT predictions for the CTRs in Figures 5.13 and 5.15. The agreement with experimental data remains good for all plausible choices of γ.

A similar sensitivity analysis could be performed upon each of the partial occupancies, Debye-Waller factors, and atomic positions tabulated in Table 5.2 and
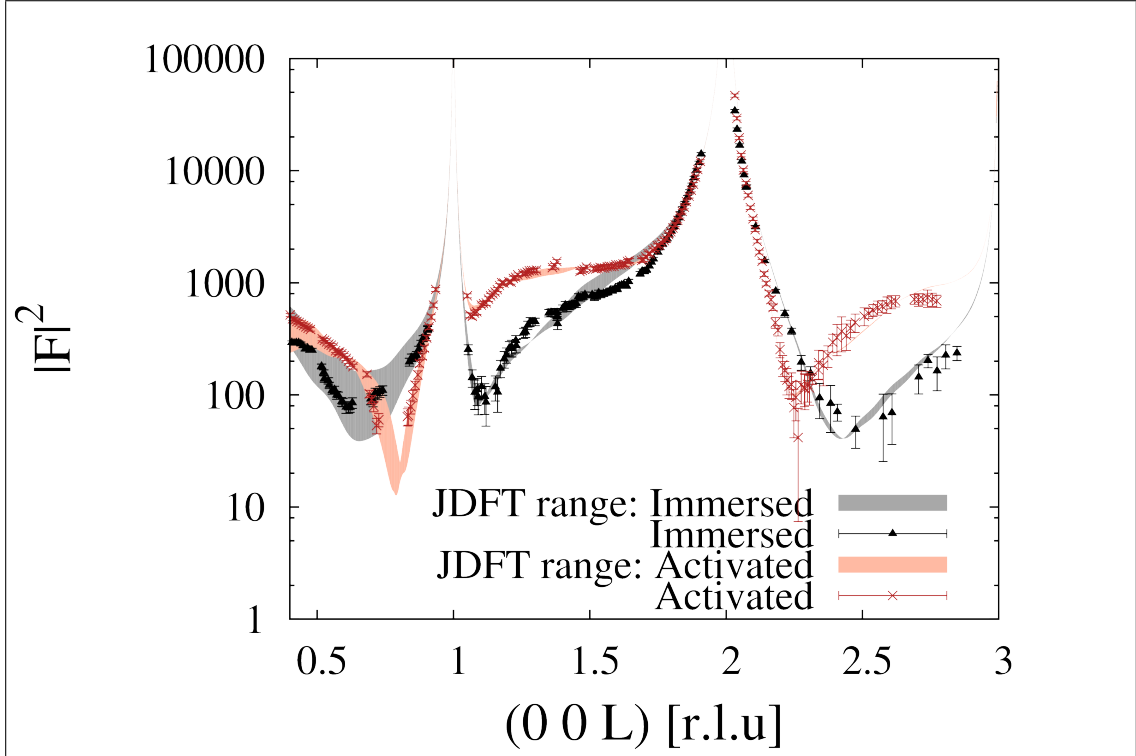
Figure 5.16: JDFT results from Figures 5.13 and 5.15 with a sensitivity analysis performed on the construction of the coupling functional (describing interactions between the fluid and the electrode). Black and red points represent the experimental data for the freshly immersed and trained surfaces respectively, while the corresponding grey and pink shaded regions represent the full range of physical predictions for the effect of a non-reacting fluid on the surface.

used to compute the JDFT-guided fit residual from Equation 5.5. Since this full analysis would be quite a significant project, we content ourselves with qualitative explorations of the response of the trained surface CTR signal in Figure 5.15 to each of these variables. The key feature which was not possible to capture fully in the set of *ab initio* calculations is the inflection point at $\vec{q} = \frac{2\pi}{a_0}[001.5]$. Another significant discrepancy between the best fully *ab initio* prediction (dotted red line) and the fit (solid red line) is the location of the minimum in the range $0.5 \leq \frac{q_z a_0}{2\pi} \leq 1.0$. In order to capture these significant features with the fit, it was not sufficient to simply introduce distortions in position compared to the *ab initio* structure. Disorder in the structure, introduced through the Debye-Waller

Table 5.1: Calculated positions z in bulk STO lattice coordinates

Atom	z
Ti	0.000
O	0.000
O	0.000
Sr	0.500
O	0.500
O	0.991
Ti	0.999
O	1.008
O	1.498
Sr	1.500
O	1.935
Ti	1.997
O	2.066
O	2.493
Ti	2.557
O	2.653

factors, and the partial occupancy of the top titanium atom were both influential variables in capturing the inflection point, allowing the predicted signal to be suppressed in the range $1.5 \leq \frac{q_z a_0}{2\pi} \leq 2.0$. In order to capture the location of the minimum in the low-q regime, distortion and disorder was required in a TiO_2 layer buried several layers beneath the surface. As the Debye-Waller factors have minimal importance below the first Bragg peak, the structure distortion was the more important factor in reproducing the features in the low-wavevector regime.

Table 5.2: Best fit positions z (bulk STO lattice coordinates), distortions from the ideal JDFT-determined positions Δz (as a fraction of the bulk lattice constant), partial occupancies, and Debye-Waller factors.

Atom	z	Δz	Occupancy	Debye-Waller Factor
Ti	0.000	0.0000	1.00	0.0037
O	0.000	0.0000	1.00	0.0048
O	0.000	0.0000	1.00	0.0048
Sr	0.500	0.0000	1.00	0.0044
O	0.500	0.0000	1.00	0.0048
Ti	1.007	0.0139	1.00	0.0037
O	0.945	-0.0566	1.00	0.0865
O	0.992	-0.0177	1.00	0.0048
Sr	1.514	0.0168	1.00	0.0044
O	1.513	0.0028	1.00	0.1689
O	1.966	0.0024	1.00	0.0263
Ti	1.998	0.0036	1.00	0.0713
O	2.077	0.0215	1.00	0.1899
O	2.561	0.0401	1.00	0.0048
Ti	2.587	0.0463	1.00	0.0037
O	2.646	-0.0365	1.00	0.0048
Ti	3.121	-0.0246	1.00	0.2276
O	3.226	-0.0107	1.00	0.0277
O	3.320	0.0017	1.00	0.0593
Ti	3.429	0.0179	0.48	0.0037
O	3.919	0.0471	1.00	0.0954
H	4.014	0.0000	1.00	0.0000

5.5 Numerical and Computational Details

5.5.1 Electronic DFT

We performed all *ab initio* calculations within the DFT++ framework[122] as implemented in the open-source code JDFTx [267]. To solve for the minimum energy electronic wavefunctions (and the corresponding independent variables in the fluid calculations) we employed direct minimization via the conjugate gradi-

ents algorithm [209]. We used fully periodic boundary conditions with a plane-wave basis and a plane-wave energy cutoff of 800 eV to sample these electronic wavefunctions. To approximate the exact Kohn-Sham exchange-correlation energy in the electronic DFT functional, we employed the generalized-gradient approximation [212]. At all times, we employ optimized norm-conserving Kleinman-Bylander pseudopotentials [230, 228] to handle the separation between the valence and core electrons. The Sr and Ti pseudopotentials require a partial core correction [172], which captures the essential features of the core electron density in the spatial region where the valence electrons are present.

We use a single unit cell of $SrTiO_3$ for the bulk crystal calculation, which was then used to construct the surface geometries and to provide the electron density $\bar{n}_{bulk}(z)$ for use in Equation 5.4. The bulk calculation also determined the DFT calculated lattice parameter of $SrTiO_3$ to be $a_0 = 3.94$ Å, less than 1% above the experimental lattice constant[287]. In order to ensure accurate results for the larger systems, we used the bulk system as a test case to check energy convergence with both plane-wave energy cutoff and k-point sampling. The choice of an 800 eV plane-wave cutoff and a 4×4×4 k-point mesh[190] (to sample the Brillouin zone) provides energy convergence in the bulk system to the accuracy of DFT calculations (around room temperature $k_B T$). All surface calculations employed this same plane-wave cutoff and a k-point set which provides sampling equivalent to a $4 \times 4 \times 4$ k-point mesh in the bulk.

The supercells for the $SrTiO_3$ surfaces were constructed as symmetric, double-surfaced periodic slab geometries. These supercell geometries are demonstrated in Figure 5.17 for the relevant surfaces in liquid. The vacuum surfaces have been shown previously in Figure 5.10 for a single side only, but

are constructed using the same symmetric slab geometry as the surfaces in liquid. We used the minimal real-space unit cell in the x and y directions (parallel to the surface) but maintained k-point sampling commensurate with the bulk calculation (A 1×1 real-space cell with $4 \times 4 \times 1$ k-point sampling for the examples shown). All unit cells were constructed to be inversion symmetric about $z = 0$ with a distance of $2 * a_z \approx 40 a_0 \approx 160$Å between the centers of the periodic surface images. Note that such a large distance was employed to allow for structuring in the fluid densities at the surface. Some of the high-throughput screening calculations in vacuum and in simplified fluid theories without shell structure[100] instead employed Coulomb truncation to prevent image interaction. We obtain the geometry of the SrTiO$_3$ surfaces directly from the relaxed nuclear positions $\{\vec{R}_I\}$ of the JDFT calculation. The total forces on the atoms were relaxed to less than 5 meV/Å, indicating highly converged calculations.

5.5.2 Joint DFT

To perform a full JDFT[218] calculation of the surface in contact with a liquid environment, we must specify the liquid functional $\Omega_{lq}[\{N_\alpha(\vec{r})\}]$ and the coupling functional $\Delta A[n(\vec{r}), \{N_\alpha(\vec{r})\}]$ in Equation 2.1 of Chapter 2. We used a classical liquid functional Ω_{lq} for water[262, 266] with only rotational contributions to the dielectric response. (Polarizability contributions to dielectric response are negligible for water and slow convergence significantly due to 3 extra degrees of freedom.) We sampled the orientation probability of the water molecules in an ideal gas representation from [262] and used 144 quadrature points over all Euler angles.
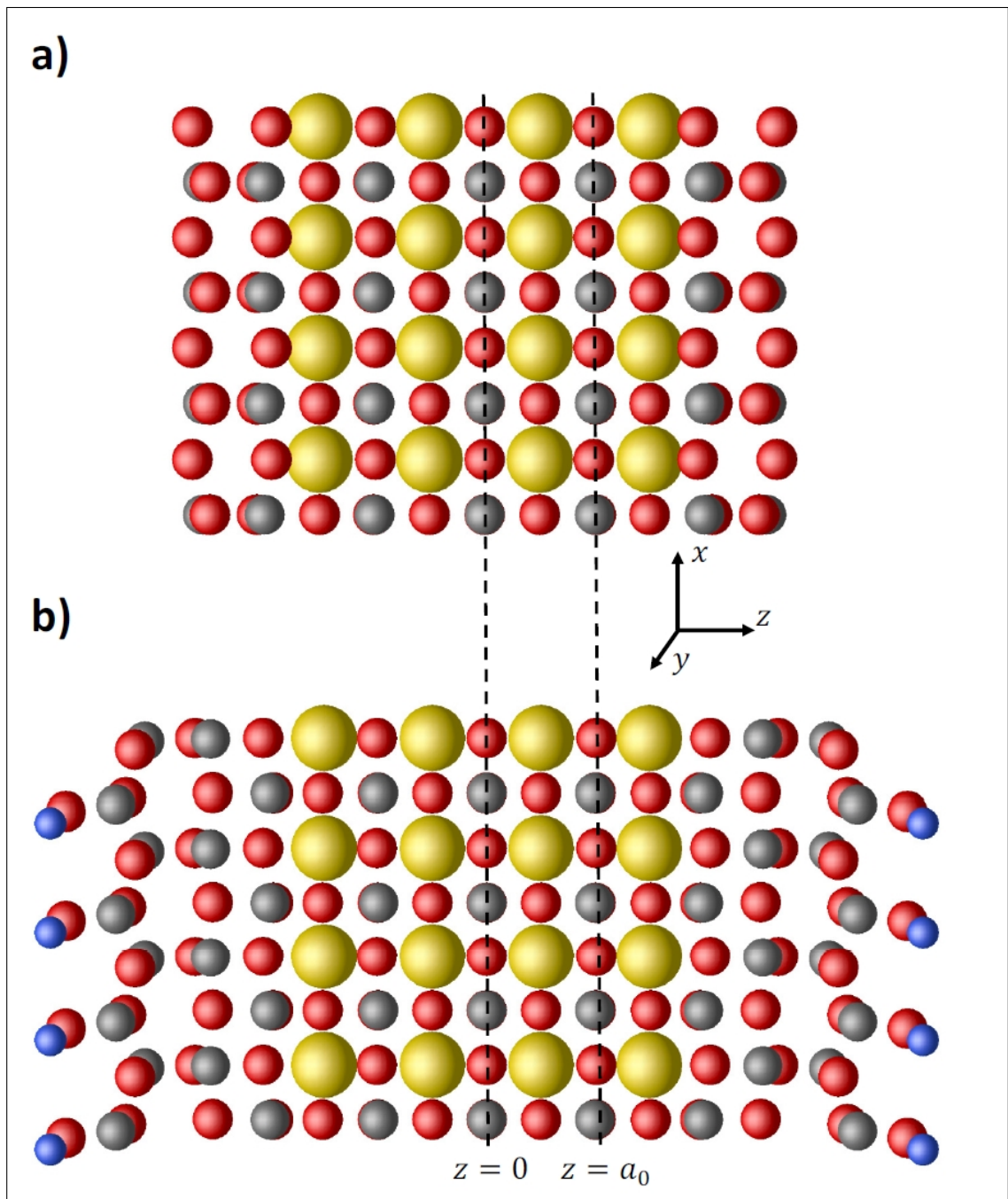
Figure 5.17: DFT supercells for the freshly immersed (a) and activated (b) surfaces. Sr, Ti,O, and H atoms are yellow, silver,red, and blue respectively. Unit cells are truncated in the z-direction and should extend to $z = \pm a_z$, where $a_z \approx 20a_0 \approx 80$Å. The activated surface (b) has been rotated 90° in the x-y plane from Figure 5.14 to better display the anatase-like stacking of the Ti atoms

To couple the fluid to the quantum-mechanical $SrTiO_3$ electrode, for ΔA we use (1) the mean-field coulomb interaction between the charge density of the surface and the charge density of the fluid and (2) density-only DFT between the valence electrons of the fluid $n_{fl}(\vec{r})$ and the valence electrons of the surface $n(\vec{r})$. As described in [162] and Chapter 2, for the density-only DFT coupling we use the Thomas-Fermi[277] orbital-free expression for the kinetic energy of the electrons and the local density approximation[151] for the exchange and correlation. Finally, in computing the coupling $\Delta A = A[n + n_{fl}] - A[n] - A[n_{fl}]$, we take the electron density of the fluid to be

$$n_{fl}(\vec{r}) = \sum_{\alpha=O,H} \int d\vec{R} N_\alpha(\vec{R}) n_\alpha(|\vec{R} - \vec{r}|), \qquad (5.7)$$

where N_α is the average density of atomic site α and the electron densities for the atomic sites n_α are determined from ab initio calculations as described in [266] and Section 2.4 of Chapter 2. Finally, we directly minimize the fluid and electron degrees of freedom in an alternating scheme using a conjugate gradients algorithm[209].

5.5.3 Core Electrons

Core electrons $n_{core}(\vec{r})$ are not included in DFT calculations performed within the pseudopotential representation, but they are essential to reproducing X-ray signatures. We determine the spherically symmetric core electron density for each atomic species S using the all-electron pseudopotential generation code Opium[230, 228], which exports $n^S_{core}(r)$ on a logarithmic radial grid. For all atoms of species S_I at positions $\vec{R}_I$ in the quantum mechanical calculation, and

243

for oxygen atoms in the fluid, we add in core electrons with a total density

$$n_{\text{core}}(\vec{r}) = \sum_{I} n_{\text{core}}^{S}(|(\vec{r} - \vec{R_I})|) + \int d\vec{R} N_O(\vec{R}) n_{\text{core}}^{O}(|\vec{R} - \vec{r}|). \qquad (5.8)$$

In practice, to avoid real-space resolution errors, we perform these operations as convolutions in fourier space.

With the core and fluid valence electron densities in place we now have a prescription to calculate $n_{\text{tot}}(\vec{r})$ and n_{fl}^{b} in Equation 5.4. The total electron density includes both valence and core electrons from the liquid and the quantum mechanical system,

$$n_{\text{tot}}(\vec{r}) = n(\vec{r}) + n_{\text{fl}}(\vec{r}) + n_{\text{core}}(\vec{r}). \qquad (5.9)$$

Finally, the bulk fluid electron density is simply determined from the bulk fluid site density N_{α}^{b} as

$$n_{\text{fl}}^{b} = \sum_{\alpha=O,H} N_{\alpha}^{b} \int d\vec{r} n_{\alpha}(r), \qquad (5.10)$$

which is, as expected, just the bulk fluid density of the water times the total number of electrons per fluid molecule.

5.6 Conclusions

5.6.1 Implications for water-splitting on SrTiO$_3$

Our successful joint theoretical and experimental study has determined a proposed geometry for the surface of strontium titanate in a basic (e.g. high pH) electrolyte, as well as the microscopic structure of water in contact with this surface. Knowledge of these structures provides key insights into the origin of

several observed phenomena. For example, the apparent irreversibility of training the surface described in Section 5.2.2 may now be understood as the loss of a layer of surface Sr atoms from the immersed surface in Figure 5.14(a) to form the structure in Figure 5.14(b). Once the positive Sr ions have been driven from the surface under applied positive bias, they are unlikely to return even after a return to open circuit potential. We can also begin to understand why this irreversibly trained surface is correlated with a near-tripled activity for water splitting compared to the freshly immersed surface – this structure exhibits anatase-like stacking of the TiO_2 layers rather than the perovskite-like stacking of the TiO_2 layers on the other surfaces. Because anatase TiO_2 is also a known catalyst for water splitting[295], it is possible that similar mechanisms dominate the reaction for anatase-terminated $SrTiO_3$.

Some questions about the exact nature of this activated surface, how it is formed, and how it facilitates the water-splitting reaction continue to remain open. The JDFT-guided fitting procedure suggests the activated surface is oxygen-deficient. Are these oxygen vacancies from actual water splitting on surface or are they bulk vacancies which have diffused to surface under applied potential? Are these defects and their associated states important for catalyzing water-splitting? To conduct future studies of this system, one should start from the JDFT-determined activated structure and corresponding fluid densities to begin investigating intermediate states involved in the water-splitting reaction. Detailed mechanistic understanding could then be gained from evolving the system from initial to intermediate to final states using transition state theory.

Finally, this study lends promise to the idea of creating a device with a strained perovskite oxide as a light-absorbing substrate with a few monolay-
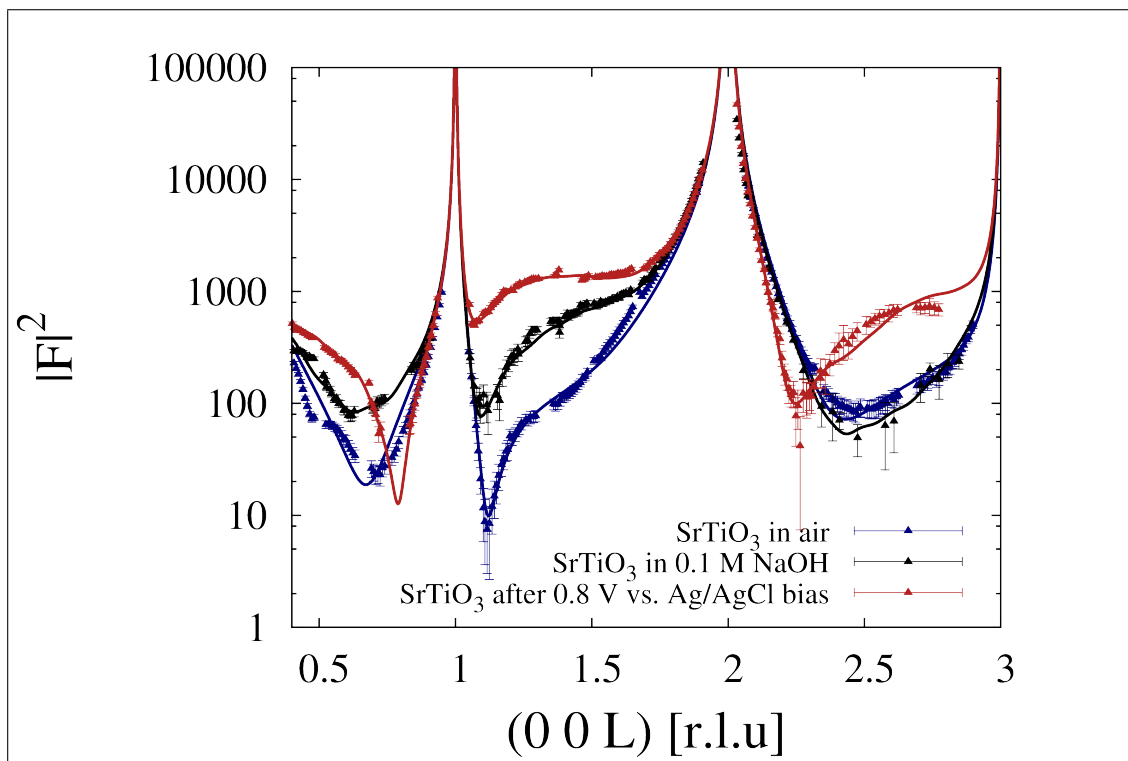
Figure 5.18: JDFT-guided fits (solid lines) for experimental CTR data from Figure 5.7 (points): STO surface in air (blue); after immersion in basic solution (black); and after biasing to oxidizing potential (red). The JDFT-guided fitting can reproduce experiment as well as pure fitting, but ensures physically realizable surface structure.

ers of epitaxial TiO_2 to catalyze the water-splitting reaction. Perovskite oxides are highly tunable both by strain[23] and cation substitution, and so it may be possible to create a material with a band-gap well matched to the solar spectrum. Detailed investigation into oxygen evolution on perovskites [184, 269] indicates that this type of device might actually be physically realizable.

5.6.2 Future Outlook

The novel synthesis of joint density-functional theory and X-ray reflectivity presented in this work also offers great promise for elucidating surface structure of

any crystalline material in any environment – with potential impact in many diverse fields. JDFT can predict X-ray structure factors with absolutely no fitted parameters, while least squares fitting offers the flexibility to account for disorder, defects, non-equilibrium processes and the errors of DFT. As shown in Figure 5.18, the JDFT-guided fits for all three surfaces are almost indistinguishable from the experimental data, with chi-squared values comparable to the fitting to atomic models typically done to analyze X-ray data. The JDFT-guiding, however, ensures that the resulting structures are physically realizable, thus providing critical additional information, particularly for surface structure studies in which the X-ray data is limited and thus may have hundreds of poorly constrained fit parameters and no unique choice of model. When the theoretical predictions and structural information are combined with novel electrochemical methods for measurement of reaction rates, an almost full characterization of a novel material is possible. The synthesis between advanced electrochemical measurements, X-ray determined *operando* structural information, and JDFT may well create new paradigm for close collaboration between experiment and theory in surface science.

CHAPTER 6

OUTLOOK

In this dissertation, we have developed and benchmarked a microscopically accurate theory which captures the physics underlying the electrode-electrolyte interface. We first presented an overview of the rigorous theoretical framework of JDFT (Section 1.4), which enables predictive and efficient multi-scale calculations by joining an electronic density functional theory for a solute system (Section 1.2) with a classical liquid environment. We reviewed recent advances in the classical liquid functionals for aqueous and non-aqueous solvents (Section 1.3) and extended these liquid functionals to capture aqueous electrolyte solutions in both continuum implicit (Section 3.4.1) and atomically-detailed explicit (Section 4.3) theories. We developed a universal approximation for the coupling between the quantum-mechanical solute and the classical liquid and demonstrated the accuracy of this coupling functional for computing both free energies of solvation and liquid structure (Chapter 2). We constructed a framework for considering charged systems in JDFT, both in the implicit solvent approximation (Section 3.8.1) and with the microscopically-detailed classical DFT electrolyte functionals (Section 4.4). We connected *ab initio* computable quantities with electrochemical measurements (Sections 3.3 and 4.2), bridging the gap between the electrochemistry terminology and the underlying physical effects. Finally, we offered a variety of JDFT predictions relevant to electrochemistry, including the structure of water at a graphene surface (Section 2.6.4), potentials of zero charge for single-crystalline metallic surfaces (Sections 3.8.4 and 4.6.2), the nonlinearity in the differential capacitance of the Ag(111) surface in sodium fluoride electrolyte (Section 4.6.4), and the structure of a $SrTiO_3$ electrode under water-splitting conditions (Section 5.4).

The development of a computationally efficient, yet microscopically accurate theory for the solid-liquid interface opens many new avenues for future research. The existing classical liquid and coupling functionals may be improved by the inclusion of additional physical effects, allowing an even more accurate description of the microscopic details and energetics of solvation. We may also construct classical liquid functionals for new solvents and electrolytes, following the procedure set forth in Reference [266], Section 2.4 and Section 4.3. Even within the present level of approximation, JDFT is poised to offer predictive calculations for a variety of electrochemical and biological systems. JDFT calculations of the electrode-electrolyte interface can provide invaluable insight into the physical processes and thermodynamics underlying high-precision basic research studies of model electrode surfaces. In addition, JDFT can offer an efficient, high throughput computational technique for screening novel electrolytes and electrode materials, eliminating the need for costly and time-consuming experimental synthesis and characterization. In biological systems, JDFT can become a key tool for computational drug design and fundamental studies of the the active sites in proteins and DNA, offering an atomically detailed description of the fluid without the need for thermodynamic sampling. Finally, JDFT-guided fitting procedures allows us to combine input from theory and experiment to account for the disorder, defects, and non-equilibrium processes which are present in real electrochemical devices and under physiological conditions.

Further benchmarking and development of the classical liquid and coupling functionals within JDFT would enhance the accuracy of the theory and extend its applicability, creating even more opportunities for future research. Though the coupling functional in Chapter 2 can accurately describe the interactions

between a variety of solutes and several common solvents, suggesting it may be universally applicable, additional study of the generalizability of this functional is warranted and further improvements are possible. The training set of molecules in Section 2.6.1 employed to fit the Grimme scaling parameter and benchmark the solvation energy performance of JDFT is quite small compared to the training sets of molecules commonly employed by popular quantum-chemical solvation models and it includes only neutral molecules. To provide a direct comparison with other universal solvation models (with more empirical parameters and no microscopic structure [180]), we could benchmark the performance of JDFT on a larger, more diverse set of neutral solute molecules and charged ions. To avoid the need for fitting the Grimme scaling parameter altogether, we could implement and test a van der Waals density-functional [233] within our orbital-free DFT coupling functional. We could also calibrate and benchmark our coupling functional for joining the explicit classical DFT to higher level quantum-chemistry calculations, leveraging the JDFT framework developed for Quantum Monte-Carlo calculations [246]. Finally, our form of the coupling functional effectively excludes all extended states from the explicit liquid, preventing a correct treatment of excited states. Ideally, we should develop a frequency-dependent coupling functional, which only excludes low-energy extended states but allows the higher-energy scattering states to penetrate into the liquid.

To accurately capture the structure and dynamics of the liquid environment, we should also consider additional development of the classical liquid functionals, both for the pure solvent and for mixtures of the solvent with electrolyte. To improve the classical DFT for the solvent, we should consider reference fluids beyond fundamental measure theory, which assumes all fluid components pack

as hard spheres. As shown in Section 2.6.3, while the hard-sphere approxima-
tion leads to accurate fluid structure in chloroform and carbon tetrachloride,
FMT does not capture the tetrahedral packing of water molecules. We thus re-
quire a reference fluid with a tetrahedral or chain reference which still possesses
the stability of FMT to joint minimization with an electronic system. To improve
the classical DFT for electrolytes, we could develop a weighted density form of
the ion-water mixing functional in Section 4.5, based upon the equation of state
data for an aqueous electrolyte [35]. Such a weighted density form would per-
haps enhance the stability and physicality of the model ions by constraining
the vapor pressure to experimental values, capturing more of the many-body
effects in the first solvation shell, and rendering the ion-water cluster approxi-
mation for the ions to be unnecessary.

At present, all the explicit JDFT calculations have ignored time-dependence
and other dynamical effects, focusing on only thermodynamically favored, min-
imum energy states. Extension of JDFT to Joint *ab initio* molecular dynamics
(J-AIMD) would allow the quantum-mechanical solute system to evolve over
time while in contact with the classical liquid. However, several practical and
theoretical challenges to the implementation of J-AIMD remain. In principle,
transition state theory should allow prediction of phenomena such as energy
barriers for chemical reactions and diffusion of particles on an electrode surface
from equilibrium JDFT calculations. JDFT calculations can also predict vibra-
tional motion of the solute in contact with the solvent in the adiabatic limit, for
low frequency modes where the water is able to reorient on a shorter timescale
than the vibrations. However, in situations where the vibrational modes of the
fluid interact significantly with the vibrational modes of the solute, JDFT free
energies and potential energy surfaces for the explicit solute atoms may be in-

accurate. The above inaccuracy may prove a challenge for performing predictive J-AIMD calculations. Extending the classical DFT to the dynamical limit, using techniques similar to Reference [131], alongside a frequency-dependent coupling functional could provide a way forward for generally applicable J-AIMD calculations.

Some disadvantages to microscopically detailed JDFT calculations include the increased computation time compared to vacuum DFT for large systems and the significant effort required to extend these calculations to new fluids. The implicit approximation to JDFT presented in Chapter 3, which possesses a computational cost similar to vacuum DFT and is easily generalizable to new solvents, is therefore an excellent tool for high-throughput screening. This efficient implicit fluid model enables rapid, voltage-dependent screening of novel supercapacitor and battery electrolytes (and screening of the electrode materials in contact with these solvents), in order to identify desired attributes for performance and stability. Furthermore, an implicit JDFT calculation which relaxes the nuclear positions of the electronic system can be a useful first step in studies of large systems which may be far away from the minimum energy configuration. For example, electrode surfaces with adsorbed reactant molecules or biomolecule structures predicted from classical MD or X-ray crystallography may benefit from an initial implicit JDFT calculation before a more accurate explicit JDFT study.

JDFT calculations of the electrode-electrode interface in a variety of systems, ranging from model graphene electrodes in aqueous solution to complex oxide electrodes in novel battery electrolytes will provide unique insights into the structure and energetics of electrochemical devices. For example,

.
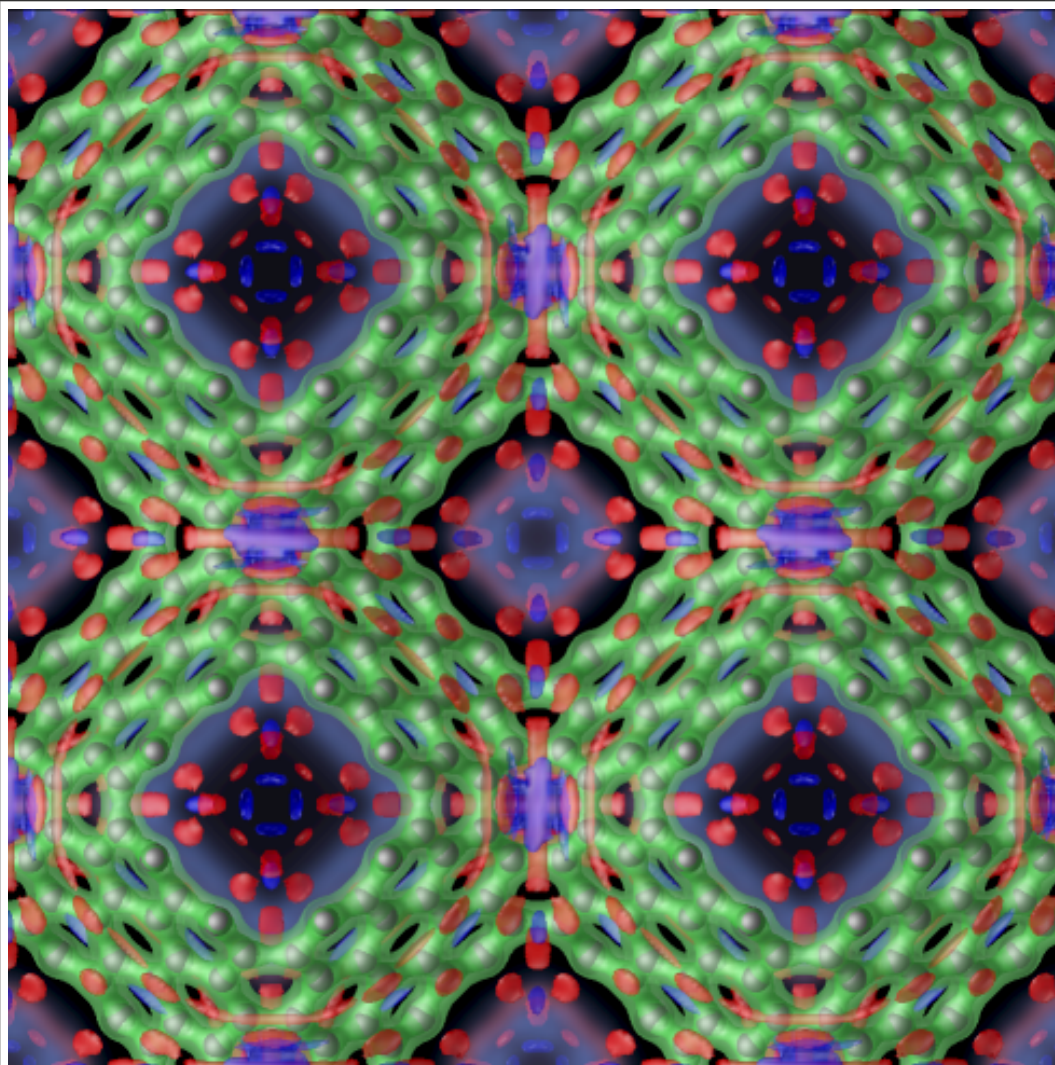
Figure 6.1: Nanostructured carbon with pores of diameter 10 Å, computed in contact with classical DFT for water (Section 4.3.1) using the coupling functional in Chapter 2

explicit JDFT calculations allow the study of confinement effects of liquids in nanoporous electrode materials. Figure 6.1 displays a model for a three-dimensional nanoporous carbon electrode material with classical DFT liquid confined within. Unlike local implicit solvation model calculations [163, 100], explicit JDFT includes information about the size of the fluid molecules, leading to the formation of discrete structure within the confined liquid. Develop-

ing classical DFT functionals for novel supercapacitor electrolytes and considering them within this nanoporous electrode structure as a function of pore size will enable predictions of the optimum combination of pore size and electrolyte composition which maximizes the energy storage capacity of the supercapacitor.

JDFT will also enable fundamental studies of ion solvation and desolvation at model graphene surfaces in conjuction with X-ray reflectivity measurements performed at Argonne National Laboratory. Batteries with multivalent working electrolytes like Mg^{2+} or Al^{3+}, which carry double or triple the charge of Li^+, could theoretically store much more energy. Experimental characterization of multivalent ion plating on a model electrode surface silicon carbide (SiC) coated with epitaxial graphene [197] is already underway. We plan to use JDFT calculations of ions at such a well-defined graphene interface to help interpret data from X-ray diffraction based techniques [79], which can resolve atomic positions with sub-Angstrom resolution. Because low atomic number ions (Li^+ etc.) are difficult to image, they are replaced with heavier, but chemically similar ions like Rb^+, Sr^{2+}, and Y^{3+}, and the behavior of the lighter ions must be extrapolated from trends. We will therefore use JDFT-calculated solvation structure and free energies to validate these trends, and predict the plating behavior of ions onto the model electrode surface. Each working ion must also break its surrounding shell of solvent molecules in order to plate onto the cathode and transfer charge. We will use transition state theory within JDFT to predict reaction pathways for ion de-solvation, yielding fundamental insight into rate-limiting processes in electrodeposition, corrosion, and even ion transport through cellular membranes.

In the complex and multi-faceted field of electrochemistry, an ideal theory is not always sufficient — we must account for disorder, defects, and non-equilibrium processes. Ideally, we should combine all available theoretical and experimental information and synthesize it to form a complete picture. Following the JDFT-guided fitting procedure in Section 5.3.2 we can begin with a pure JDFT description of a model system and find adjustable parameters which describe physical sources of uncertainty. We can then fit those parameters to the experimental data, with a penalty function to prevent unphysical deviation from the theoretical predictions and quantify sources of error. This concept can be extended to experimental characterization techniques from X-ray diffraction to spectroscopy, therefore developing a toolbox of available software to provide synergy between theory and experiment.

Using JDFT guided by experimental X-ray measurements conducted at Argonne National Laboratory, we will elucidate fluid structure and reaction pathways on complex oxide electrodes. Using the well-known $LiMn_2O_4$ spinel cathode material [276] as a model system, JDFT will address the complex problems of ion intercalation [313] and formation of the solid electrolyte interphase (SEI) [113] in batteries, probing the interfacial structure and reactivity of complex oxide battery cathodes. Unique X-ray reflectivity and related spectroscopy techniques [79] will be used to characterize the cathode surface in vacuum/air [20] and in liquid before/after cycling [113]. JDFT-guided fitting will predict the chemical composition, geometry, and termination of the electrode surface as in Chapter 5. JDFT will also provide an atomic-scale description of the chemical pathways driving Mn-dissolution and novel electrolyte decomposition [164] at high potentials, processes which ultimately limit the capacity and lifetime of batteries.

The pioneering work we have undertaken in this dissertation to obtain a microscopically-detailed, yet efficient, theoretical description of solid-liquid interfaces offers significant reward and impact. Though we have focused in this work upon the use of JDFT to elucidate phenomena in electrochemical systems, the theory itself will find application far beyond electrochemistry. One significant outcome of this work is a range of methods and software, enabling collaboration between theory and experiment on future problems related (or unrelated) to the electrode-electrolyte interface. Cross-disciplinary combination of JDFT with experimental measurements will broaden basic understanding of fundamental processes in materials science, biochemistry, and many other fields.

BIBLIOGRAPHY

[1] Democritus (460370 b.c.e.). http://www.iep.utm.edu. Accessed July 10, 2015.   p.1

[2] Nist computational chemistry comparison and benchmark database, nist standard reference database, number 101, release 16a. http://cccbdb.nist.gov/.   p.48, 183

[3] *CRC Handbook of Chemistry and Physics, 92nd Edition*. Taylor and Francis Group, LLC, 2012.   p.111

[4] J. L. F. Abascal and C. Vega. *J. Chem. Phys.*, 123:234505, 2005.   p.25, 33

[5] H. D. Abruna, Y. Kiya, and J. C. Henderson. Batteries and electrochemical capacitors. *Phys. Today*, 12:4347, 2008.   p.133, 137, 209

[6] T. Andersen, H.K. Haugen, and H. Hotop. Binding energies in atomic negative ions. *J. Phys. Chem. Ref. Data*, 28:1511, 1999.   p.183

[7] O. Andreussi, I. Dabo, and N. Marzari. *J. Chem. Phys*, 136:064102, 2012. p. 34

[8] S. R. Andrews and R. A. Cowley. Scattering of x-rays from crystal-surfaces. *J Phys C Solid State*, 18:6427–6439, 1985.   p. 218

[9] A. Annadi, Q. Zhang, X. Renshaw Wang, N. Tuzla, K. Gopinadhan, W. M. La, A. Roy Barman, Z. Q. Liu, A. Srivastava, S. Saha, Y. L. Zhao, S. W. Zeng, S. Dhar, E. Olsson, B. Gu, S. Yunoki, S. Maekawa, H. Hilgenkamp, T. Venkatesan, , and Ariando. Anisotropic two-dimensional electron gas at the laalo3/srtio3 (110) interface. *Nature Communications*, 4:1838, 2013. p.213

[10] Veronica Augustyn, Jeremy Come, Michael A. Lowe, Jong Woung Kim, Pierre-Louis Taberna, Sarah H. Tolbert, Hector D. Abruna, Patrice Simon, and Bruce Dunn. High-rate electrochemical energy storage through li+ intercalation pseudocapacitance. *Nature Materials*, 12:518522, 2013. p.133, 209

[11] H. J. Bakker. Structural dynamics of aqueous salt solutions. *Chemical Review*, 108:1456–1473, 2008.   p. 132

[12] Isa Bar-On, Randy Kirchain, and Richard Roth. Technical cost analysis for pem fuel cells. *Journal of Power Sources*, 109(1):71 – 75, 2002.   p. 82

[13] A. J. Bard, F.-R. F. Fan, and M. V. Mirkin. *Electroanalytical Chemistry: A Series of Advances*, volume 18. Marcel Dekker, New York, 2001.   p. 215

[14] A. J. Bard, M. V. Mirkin, P. R. Unwin, and David O. Wipf. Scanning electrochemical microscopy. 12. theory and experiment of the feedback mode with finite heterogeneous electron-transfer kinetics and arbitrary substrate size. *The Journal of Physical Chemistry*, 96:1861–1868, 1992. p. 215

[15] Allen J. Bard and Larry R. Faulkner. *Electrochemical methods : fundamentals and applications*. Wiley, New York, 1980.   p. 95, 130, 138, 139, 142, 144

[16] J. A. Barker and D. Henderson. *Rev. Mod. Phys.*, 48:587, 1976.   p. 22, 23

[17] R J Bartlett. Many-body perturbation theory and coupled cluster theory for electron correlation in molecules. *Annual Review of Physical Chemistry*, 32(1):359–401, 1981.   p. 9

[18] Martin Z. Bazant, Mustafa Sabri Kilic, Brian D. Storey, and Armand Ajdari. Towards an understanding of induced-charge electrokinetics at large applied voltages in concentrated solutions. *Advances in Colloid and Interface Science*, 152(12):48 – 88, 2009.   p. 131

[19] D. Ben-Amotz and K. G. Willis. *J. Phys. Chem.*, 97:7736, 1993.   p. 155

[20] R. Benedek and M. M. Thackeray. Simulation of the surface structure of lithium manganese oxide spinel. *Physical Review B*, 83:195439, 2011. p. 255

[21] P. Benjamin. *The Age of Electricity: From Amber–soul to Telephone*. C. Scribners Sons, 1886.   p. 2

[22] H. J. C. Berendsen, J. R. Grigera, and T. P. Straatsma. *J. Phys. Chem.*, 91:6269, 1987.   p. 25, 33, 48

[23] R.F. Berger, C.J. Fennie, and J.B. Neaton. Band gap and edge engineering via ferroic distortion and anisotropic strain: The case of srtio3. *Phys. Rev. Lett.*, 107:146804, 2011.   p. 213, 246

[24] G. Binnig, C. F. Quate, and Ch. Gerber. Atomic force microscope. *Phys. Rev. Lett.*, 56:930–933, 1986.   p. 214

[25] R.E. Bird and L.J. Lewis R.L. Hulstrom. Terrestrial solar spectral data sets. *Solar Energy*, 30:563, 1983.   p. xv, 212

[26] F. Bloch. ber die quantenmechanik der elektronen in kristallgittern. *Z. Physik*, 52:555600, 1928.   p. 5, 19

[27] Jochen Blumberger, Yoshitaka Tateyama, and Michiel Sprik. Ab initio molecular dynamics simulation of redox reactions in solution. *Computer Physics Communications*, 169(13):256 – 261, 2005.   p. 82, 83

[28] J. O'M. Bockris, M. A. V Devanthan, and K. Mueller. *Proc. Roy. Soc, Ser. A.*, 274:55, 1963.   p. 133, 139, 141, 195

[29] Dezso Boda and Douglas Henderson. The effects of deviations from lorentzberthelot rules on the properties of a simple mixture. *Molecular Physics*, 106:23672370, 2008.   p. 176

[30] M. Born and J. R. Oppenheimer. Zur quantentheorie der molekeln [on the quantum theory of molecules]. *Annalen der Physik*, 389:457–484, 1927. p. 8

[31] R. Boyle. *The Sceptical Chymist*. 1661. reprinted by Dover Books on Chemistry, Courier Corporation (2013).   p. 1

[32] Konrad Breitsprecher, Peter Kosovan, and Christian Holm. Coarse-grained simulations of an ionic liquid-based capacitor: I. density, ion size, and valency effects. *Journal of Physics: Condensed Matter*, 26(28):284108, 2014.   p. 135

[33] Timothy R. Brumleve and Richard P. Buck. *Journal of Electroanalytical Chemistry and Interfacial Electrochemistry*, 90:1–31, 1978.   p. 134, 210

[34] Christian J. Burnham, Matt K. Petersen, Tyler J. F. Day, Srinivasan S. Iyengar, and Gregory A. Votha. The properties of ion-water clusters. ii. sol-

vation structures of na+, cl, and h+ clusters as a function of temperature. *Journal of Chemical Physics*, 124:024327, 2006.   p.179

[35] L. F. Cameretti, G. Sadowski, and J.M. Mollerup. *Ind. Eng. Chem. Res.*, 44:3355–3362, 2005.   p.135, 171, 207, 251

[36] G. Campbell. Empedocles (c. 492432 b.c.e.). http://www.iep.utm.edu. Accessed July 10, 2015.   p.1, 2

[37] J. F. Capitani, R. F. Nalewajski, and R. G. Parr. *J. Chem. Phys.*, 76:568, 1982. p.18, 21

[38] R. Car and M. Parrinello. *Phys. Rev. Lett.*, 55:2471, 1985.   p.18, 32, 76

[39] N. F. Carnahan and K. E. Starling. *J. Chem. Phys.*, 51:635, 1969.   p.24, 155

[40] Javier Carrasco, Ji Klime, and Angelos Michaelides. The role of van der waals forces in water adsorption on metals. *J. Chem. Phys.*, 138, 2013.   p. 182, 208

[41] Mark E. Casida. Time-dependent density-functional theory for molecules and molecular solids. *Journal of Molecular Structure: THEOCHEM*, 914:3– 18, 2009.   p. 213

[42] D. M. Ceperley and B. J. Alder. Ground state of the electron gas by a stochastic method. *Phys. Rev. Lett.*, 45:566, 1980.   p.14

[43] D. Chandler, J. McCoy, and S. Singer. *J. Chem. Phys.*, 85:5971, 1986.   p.22

[44] D. Chandler, J. McCoy, and S. Singer. *J. Chem. Phys.*, 85:5978, 1986.   p.22

[45] T.-M. Chang, K. A. Peterson, and L. X. Dang. *J. Chem. Phys.*, 103:7502, 1995.   p.26, 51, 52, 57, 73

[46] D.L. Chapman. *London, Edinburgh, Dublin Philos. Mag. J. Sci. Ser.*, 6(25):475, 1913.   p.94, 140

[47] Snehasis Chowdhuri and Amalendu Chandra. Molecular dynamics simulations of aqueous nacl and kcl solutions: Effects of ion concentration on the single-particle, pair, and collective dynamical properties of ions and water molecules. *The Journal of Chemical Physics*, 115:3732, 2001.   p.179

[48] Gennady N. Chuev, Marat Valiev, and Marina V. Fedotova. Integral equation theory of molecular solvation coupled with quantum mechanical/molecular mechanics method in nwchem package. *Journal of Chemical Theory and Computation*, 8(4):1246–1254, 2012. p.33

[49] E. Clapeyron. Mmoire sur la puissance motrice de la chaleur. *Journal de l'cole Polytechnique*, XIV:15390, 1834. p.3

[50] G. N. I. Clark, A. J. Haslam, A. Galindo, and G. Jackson. *Molecular Physics*, 104:3561, 2006. p.22

[51] J. Clavilier and N. Van Huong. *Electroanalytical Chemistry and Interfacial Electrochemistry*, 41:193–199, 1973. p.209

[52] B.E. Conway, V. Birss, and J. Wojtowicz. The role and utilization of pseudocapacitance for energy storage by supercapacitors. *Journal of Power Sources*, 66(12):1 – 14, 1997. p.134, 137, 209

[53] P. Cortona. *Phys. Rev. B*, 44:8454–8458, 1991. p.41

[54] Angel Cuesta. Measurement of the surface charge density of co-saturated pt(111) electrodes as a function of potential: the potential of zero charge of pt(111). *Surface Science*, 572(1):11 – 22, 2004. p.94, 127

[55] W. A. Curtin and N. W. Ashcroft. *Phys. Rev. A*, 32:2909, 1985. p.22

[56] I. Dabo, E. Cances, Y. Li, and N. Marzari. ArXiv. http://arxiv.org/abs/0901.0096v3, 2010. p.85, 86, 103, 130, 136

[57] J. Dalton. *A New System of Chemical Philosophy*. William Dawson and Sons, 1808. p.1

[58] R.L. Davidchack and B.B. Laird. Weighted-density approximation for general nonuniform fluid mixtures. *Physical Review E*, 60:3417–20, 1999. p.171

[59] E.R. Davidson. *Methods in Computational Molecular Physics*, volume 113. Plenum, 1983. p.62

[60] P. Debye and E. Hckel. The theory of electrolytes. i. lowering of freezing point and related phenomena. *Physikalische Zeitschrift*, 24:185206, 1923. p.134

[61] K. Ding, D. Chandler, S. J. Smithline, and A. D. J. Haymet. *Phys. Rev. Lett.*, 59:1698, 1987.   p. 22

[62] A. Einstein. *Ann. Phys.*, 17:132–148, 1905.   p. 4

[63] Chinedu E. Ekuma, Mark Jarrell, Juana Moreno, and Diola Bagayoko. First principle electronic, structural, elastic, and optical properties of strontium titanate. *AIP Advances*, 2:012189, 2012.   p. xv, 212

[64] V. Engelhardt. *The Electrolysis of Water: Processes and Applications*. Chemical Publishing Company, 1904.   p. 3

[65] N. Erdman, K. R. Poeppelmeier, M. Asta, O. Warschkow, D. E. Ellis, and L. D. Marks. The structure and chemistry of the tio2-rich surface of srtio3(001). *Nature*, 419:55–58, 2002.   p. xvi, 213, 219, 227, 228, 229, 230, 232

[66] R. Erdogan and I. Onal. An oniom and dft study of water and ammonia adsorption on anatase tio2 (001) cluster. *International Journal of Quantum Chemistry*, 111:21492159, 2011.   p. 227

[67] H. Eschrig. $t > 0$ ensemble–state density functional theory via legendre transform. *Phys. Rev. B*, 82:205120, 2010.   p. 16

[68] L. Estevez, R. Dua, N. Bhandari, A. Ramanujapuram, P. Wang, and E. P. Giannelis. *Energy Environ. Sci.*, 6:1785, 2013.   p. 20

[69] H.-C. Chen et al. *J. Phys. Chem. C*, 116:7897–7903, 2012.   p. 213

[70] K. J. Tielrooij et al. Cooperativity in ion hydration. *Science*, 328:1006, 2010.   p. 132

[71] W.D. Cornell et. al. A second generation force field for the simulation of proteins, nucleic acids, and organic molecules. *J. Am. Chem. Soc.*, 117:51795197, 1995.   p. 33, 81

[72] V. Etacheri, R. Marom, R. Elazari, G. Salitraa, and D. Aurbach. Challenges in the development of advanced li-ion batteries: a review. *Energy Environ. Sci.*, 4:3243–3262, 2011.   p. 209

[73] K. M. Ewool and H. M. Strauss. *J. Chem. Phys*, 58:5835, 1973.   p. 51

[74] C. J. Fall, N. Binggeli, and A. Baldereschi. Work-function anisotropy in noble metals: Contributions from d states and effects of the surface atomic structure. *Phys. Rev. B*, 61:8489–8495, 2000.   p. 123

[75] J.-L. Fattebert and F. Gygi. *Int. J. Quant. Chem.*, 93:139, 2003.   p. 34

[76] Jean-Luc Fattebert and Franois Gygi. Density functional theory for efficient ab initio molecular dynamics simulations in solution. *Journal of Computational Chemistry*, 23(6):662–666, 2002.   p. 85

[77] A. Feldman. *The Classical Journal*, 1:4–6, 1945.   p. 1

[78] Zhi Qiang. Feng, Takamasa. Sagara, and Katsumi. Niki. Application of potential-modulated uv-visible reflectance spectroscopy to electron transfer rate measurements for adsorbed species on electrode surfaces. *Analytical Chemistry*, 67(19):3564–3570, 1995.   p. 215

[79] P. Fenter, S. Kerisit, P. Raiteri, and J. D. Gale. Is the calcitewater interface understood? direct comparisons of molecular dynamics simulations with specular x-ray reflectivity data. *J. Phys. Chem. C*, 117(10):50285042, 2013.   p. 254, 255

[80] Enrico Fermi. Un metodo statistico per la determinazione di alcune priopriet dell'atomo. *Rend. Accad. Naz. Lincei*, 6:602–607, 1927.   p. 13, 42

[81] A. M. Ferrenberg and R. H. Swendsen. *Phys. ReV. Lett.*, 63:1195, 1989.   p. 26

[82] R. P. Feynman. Forces in molecules. *Phys. Rev.*, 56:340, 1939.   p. 17

[83] B. Franklin. *Experiments and Observations on Electricity*. E. Cave, at St. John's Gate, 1751.   p. 2

[84] Joseph Fraunhofer. Determination of the refractive and color–dispersing power of different types of glass, in relation to the improvement of achromatic telescopes. *Memoirs of the Royal Academy of Sciences in Munich*, 5:193–226, 1814.   p. 4

[85] D. Frenkel and B. Smit. *Understanding Molecular Simulation: From Algorithm to Applications.* Academic Press: San Diego, CA, 1996.   p. 26

[86] Christoph Freysoldt, Sixten Boeck, and Jörg Neugebauer. Direct minimization technique for metals in density functional theory. *Phys. Rev. B*, 79:241103, 2009.   p.16, 62

[87] L. J. D. Frink, A. L. Frischknecht, M. A. Heroux, M. L. Parks, and A. G. Salinger. *J. Chem. Theory Comp.*, 8(4):393–1408, 2012.   p.20

[88] A. L. Frischknecht, J.D. Weinhold, A. G. Salinger, J. G. Curro, L. J. D. Frink, and J. D. McCoy. *J. Chem. Phys.*, 117(22):10385–97, 2002.   p.20

[89] R. L. Fulton. *J. Chem. Phys.*, 130:204503, 2009.   p.48

[90] Alex P. Gaiduk, Cui Zhang, Franois Gygi, and Giulia Galli. Structural and electronic properties of aqueous nacl solutions from ab initio molecular dynamics simulations with hybrid density functionals. *Chemical Physics Letters*, 604:8996, 2014.   p.193

[91] A. Galindo, A. Gil-Villegas, G. Jackson, and A. N. Burgess. *J. Phys. Chem. B*, 103:10272–10281, 1999.   p.135

[92] David J. Giesen, Candee C. Chambers, Christopher J. Cramer, and Donald G. Truhlar. Solvation model for chloroform based on class iv atomic charges. *J. Phys. Chem. B*, 101:2061–2069, 1997.   p.65

[93] Paulo F. B. Goncalves and Hubert Stassen. Free energy of solvation from molecular dynamics,simulations for low dielectric solvents. *J Comput. Chem.*, 24:1758–1765, 2003.   p.65

[94] David C. Grahame. The electrical double layer and the theory of electrocapillarity. *Chemical Reviews*, 41:441, 1947.   p.143, 145

[95] David C. Grahame. Differential capacity of mercury in aqueous sodium fluoride solutions. i. effect of concentration. *Journal of the Americal Chemical Society*, 76:4819, 1954.   p.xv, 138, 143, 144, 146, 148, 202, 203

[96] J Greeley, JK Norskov, and M Mavrikakis. Electronic structure and catal-

ysis on metal surfaces. *Annual Review of Physical Chemistry*, 53:319–348, 2002.   p. 82

[97] Stefan Grimme. Semiempirical gga-type density functional constructed with a long-range dispersion correction. *Journal of Computational Chemistry*, 27(15):1787–1799, 2006.   p. 44, 64, 182

[98] A Gross. The virtual chemistry lab for reactions at surfaces: Is it possible? will it be useful? *Surface Science*, 500(1-3):347–367, 2002.   p. 82

[99] Axel Gross. Ab initio molecular dynamics simulations of the adsorption of h(2) on palladium surfaces. *Chem. Phys. Phys. Chem.*, 11(7):1374–1381, 2010.   p. 83

[100] D. Gunceler, K. Letchworth-Weaver, R. Sundararaman, K.A. Schwarz, and T.A. Arias, 2013.   p. 25, 39, 49, 78, 161, 163, 227, 241, 253

[101] G. Guoy. *J. Phys. Theor. Appl.*, 9:457, 1910.   p. 94, 140

[102] J.-P. Hansen and I. R. McDonald. *Theory of Simple Liquids, Third Edition*. Academic Press, 3 edition, 2006.   p. 22, 23

[103] H. Hansen-Goos and R. Roth. *J. Phys.: Cond. Matt.*, 18:8413, 2006.   p. 24, 154, 157

[104] Andreas Hartel, Mathijs Janssen, Sela Samin, and Rene van Roij. Fundamental measure theory for the electric double layer: implications for blue-energy harvesting and water desalination. *Journal of Physics: Condensed Matter*, 27(19):194129, 2015.   p. 135

[105] D. R. Hartree. *Proc. Cambridge Philos. Soc.*, 24:89, 1928.   p. 10

[106] W. M. Haynes, editor. *CRC Handbook of Physics and Chemistry 93rd ed*. 2012. p. 56

[107] E. Heifets, S. Piskunov, E. A. Kotomin, Y. F. Zhukovskii, and D. E. Ellis. Electronic structure and thermodynamic stability of double-layered srtio3(001) surfaces: Ab initio simulations. *Physical Review B*, 75, 2007. p. 232

[108] W. Heitler and F. London. Wechselwirkung neutraler atome und homopolare bindung nach der quantenmechanik. *Zeitschrift fr Physik*, 44:455–472, 1927.   p. 5, 9

[109] C. Held, L. F. Cameretti, and G. Sadowski. *Fluid Phase Equilibria*, 270:87–96, 2008.   p. 135

[110] H. Hellmann. *Einfhrung in die Quantenchemie*. Franz Deuticke, 1937. p. 17

[111] R. Herger, P. R. Willmott, O. Bunk, C. M. Schleputz, B. D. Patterson, B. Delley, V. L. Shneerson, P. F. Lyman, and D. K. Saldin. Surface structure of srtio(3)(001). *Physical Review B*, 76, 2007.   p. 228

[112] S. Herzog, J. Gross, and W. Arlt. *Fluid Phase Equilibria*, 297:23–33, 2010. p. 135

[113] M. Hirayama, H. Ido, K. Kim, W. Cho, K. Tamura, J. Mizuki, and R. Kanno. Dynamic structural changes at limn2o4/electrolyte interface during lithium battery reaction. *J. Am. Chem. Soc.*, 132(43):15268–15276, 2010.   p. 255

[114] M. Hodak, Chisnell, Lu, and J. Bernholc. *PNAS*, 106:11576, 2009. p. 33, 38

[115] M. Hodak, Lu, and J. Bernholc. *J. Chem. Phys.*, 128:014101, 2008. p. 33, 38

[116] P. Hohenberg and W. Kohn. *Phys. Rev.*, 136:B864, 1964.   p. 11, 30, 36

[117] Yongdan Hou, Koichi Jeremiah Aoki, Jingyuan Chen, and Toyohiko Nishiumi. Invariance of double layer capacitance to polarized potential in halide solutions. *Universal Journal of Chemistry*, 1:162–169, 2013. p. 209

[118] Chen Huang and Emily A. Carter. Potential-functional embedding theory for molecules and materials. *J. Chem. Phys.*, 135:194104, 2011.   p. 41

[119] Patrick Huang, Tuan Anh Pham, Giulia Galli, and Eric Schwegler. Alumina(0001)/water interface: Structural properties and infrared spectra from first-principles molecular dynamics simulations. *J. Phys. Chem. C*, 118:89448951, 2014.   p. 136

[120] J. Hughes, E. J. Krebs, and D. Roundy. *J. Chem. Phys.*, 138:024509, 2013. p. 22

[121] Nobuo Ishizawa, Hidekuni Banno, Motoo Hayashi, Seung Eul Yoo, and Masahiro Yoshimura. Preparation of batio3 and srtio3 polycrystalline thin films on flexible polymer film substrate by hydrothermal method. *Japanese Journal of Applied Physics*, 29(11R):2467, 1990.   p.211

[122] Sohrab Ismail-Beigi and T.A. Arias. New algebraic formulation of density functional calculation. *Computer Physics Communications*, 128(12):1 – 45, 2000.   p.20, 49, 62, 110, 239

[123] P. Iversen and D. J. Lacks. A life of its own: The tenuous connection between thales of miletus and the study of electrostatic charging. *Journal of Electrostatics*, 70:309–311, 2012.   p.2

[124] A. Jain, S. P. Ong, G. Hautier, W. Chen, W. D. Richards, S. Dacek, S. Cholia, D. Gunter, D. Skinner, G. Ceder, and K. A. Persson. The materials project: A materials genome approach to accelerating materials innovation. *APL Mat*, 1:011002, 2013.   p.227

[125] Michael Janik, Christopher Taylor, and Matthew Neurock. First principles analysis of the electrocatalytic oxidation of methanol and carbon monoxide. *Topics in Catalysis*, 46:306–319, 2007.   p. 84

[126] G. Jeanmairet, M. Levesque, and D. Borgis. *J. Chem. Phys.*, 139:154101, 2013.   p.22

[127] G. Jeanmairet, M. Levesque, R. Vuilleumier, and D. Borgis. *J. Phys. Chem. Lett.*, 4:619–624, 2013.   p.22

[128] C. A. Jeffery and P. H. Austin. *J. Chem. Phys*, 110:484, 1999.   p.24, 154, 155

[129] D. Jiang, Z. Jin, D. Henderson, and J. Wu. *J. Phys. Chem. Lett.*, 3:1727–1731, 2012.   p.20, 134, 209

[130] D. Jiang, Z. Jin, and J. Wu. *Nano Lett.*, 11:5373–5377, 2011.   p.20, 209

[131] Jian Jiang, Dapeng Cao, De en Jiang, and Jianzhong Wu. Time-dependent density functional theory for ion diffusion in electrochemical systems. *Journal of Physics: Condensed Matter*, 26(28):284102, 2014.   p.210, 252

[132] Ryosuke Jinnouchi and Alfred B. Anderson. Electronic structure calculations of liquid-solid interfaces: Combination of density functional theory

and modified poisson-boltzmann theory. *Phys. Rev. B*, 77:245417, 2008. p. 85, 86, 103, 222

[133] W. L. Jorgensen, J. Chandrasekhar, J. D. Madura, R. W. Impey, and M. L. Klein. *J. Chem. Phys.*, 79:926, 1983.   p. 33, 52

[134] V.D. Jovic and B.M. Jovic. Eis and differential capacitance measurements onto single crystal faces in different solutions part i: Ag(111) in 0.01 m nacl. *Journal of Electroanalytical Chemistry*, 541:1–11, 2003.   p. 209

[135] Morth JP, Pedersen BP, Toustrup-Jensen MS, Sorensen TLM, Petersen J, Andersen JP, Vilsen B, and Nissen P. Crystal structure of the sodium-potassium pump. *Nature*, 450:1043–1049, 2007.   p. 133

[136] S. C. L. Kamerlin, M. Haranczyk, and A. Warshel. *J. Phys. Chem. B*, 113:1253, 2009.   p. 32

[137] Jakub W. Kaminski, Sergey Gusarov, Tomasz A. Wesolowski, and Andriy Kovalenko. Modeling solvatochromic shifts using the orbital-free embedding potential at statistically mechanically averaged solvent density. *The Journal of Physical Chemistry A*, 114(20):6082–6096, 2010.   p. 33, 42, 47, 78

[138] G. S. Karlberg, T. F. Jaramillo, E. Skulason, J. Rossmeisl, T. Bligaard, and J. K. Norskov. Cyclic voltammograms for h on pt(111) and pt(100) from first principles. *Phys. Rev. Lett.*, 99:126101, 2007.   p. 84, 96

[139] Casey P. Kelly, Christopher J. Cramer, and Donald G. Truhlar. Aqueous solvation free energies of ions and ion-water clusters based on an accurate value for the absolute aqueous solvation free energy of the proton. *J. Phys. Chem. B*, 110:16066–16081, 2006.   p. 136, 177, 187

[140] Zsolt Kerner and Tamas Pajkossy. Measurement of adsorption rates of anions on au(111) electrodes by impedance spectroscopy. *Electrochimica Acta*, 47:2055–2063, 2002.   p. 150, 151, 203, 209

[141] Rustam Z. Khaliullin and Thomas D. Kuhne. Microscopic properties of liquid water from combined ab initio molecular dynamics and energy decomposition studies. *Phys. Chem. Chem. Phys.*, 15:15746–15766, 2013.   p. 32

[142] I. V. Khavrutskii, B. Grant, S. S. Taylor, and J. A. McCammon. A transition

path ensemble study reveals a linchpin role for mg2+ during rate-limiting adp release from protein kinase. *A. Biochemistry*, 48:11532–11545, 2009. p. 132

[143] Kentaro Kido, Daisuke Yokogawa, and Hirofumi Sato. A modified repulsive bridge correction to accurate evaluation of solvation free energy in integral equation theory for molecular liquids. *The Journal of Chemical Physics*, 137(2):024106, 2012. p.33, 79

[144] Kwang S. Kim, Ickjin Park, Sik Lee, K. Cho, Jin Yong Lee, Jongseob Kim, and J. D. Joannopoulos. The nature of a wet electron. *Phys. Rev. Lett.*, 76:956–959, 1996. p.39, 89, 103

[145] Soon-Chul Kim. Weighted-density approximations for non-uniform classical fluids and their applications. *Journal of Physics: Condensed Matter*, 4(48):9517, 1992. p.171

[146] G. Kirchhoff and R. Bunsen. Chemische analyse durch spectralbeobachtungen. *Annalen der Physik*, 180:161189, 1860. p. 4

[147] B Kirchner, PJ di Dio, and J. Hutter. Real-world predictions from ab initio molecular dynamics simulations. *Top Curr Chem*, 307:109–53, 2012. p.32

[148] J. G. Kirkwood. Statistical mechanics of fluid mixtures. *J. Chem. Phys.*, 3:300–313, 1935. p.79

[149] Roland Kjellander. Intricate coupling between ionion and ionsurface correlations in double layers as illustrated by charge inversioncombined effects of strong coulomb correlations and excluded volume. *Journal of Physics: Condensed Matter*, 21(42):424101, 2009. p.135

[150] W. Kohn. Nobel lecture: Electronic structure of matter, wave functions, and density functionals. *Rev. Mod. Phys.*, 71:1253–1266, 1999. p.11

[151] W. Kohn and L. Sham. *Phys. Rev.*, 140:A1133, 1965. p.11, 12, 14, 37, 43, 60, 121, 243

[152] S. Koneshan, Jayendran C. Rasaiah, R. M. Lynden-Bell, and S. H. Lee. Solvent structure, dynamics, and ion mobility in aqueous solutions at 25 c. *J. Phys. Chem. B*, 102:4199, 1998. p.173, 175, 178

[153] A. Kramida, Yu. Ralchenko, J. Reader, and and NIST ASD Team. NIST Atomic Spectra Database (ver. 5.2),http://physics.nist.gov/asd National Institute of Standards and Technology, Gaithersburg, MD., 2014. p. 183

[154] Heather J. Kulik, Eric Schwegler, and Giulia Galli. Probing the structure of salt water under confinement with first- principles molecular dynamics and theoretical xray absorption spectroscopy. *J. Phys. Chem. Lett.*, 3:26532658, 2012. p. 136

[155] W. Kutzelnigg and III Morgan, J.D. Hund's rules. *Zeitschrift fr Physik D Atoms, Molecules and Clusters*, 36(3-4):197–214, 1996. p. 9

[156] G. Lamoureux, J. D. Faraldo-Gomez, S. Krupin, and S. Y. Noskov. *Chem. Phys. Lett.*, 468:270, 2009. p. 26, 52, 57, 73

[157] J. Landers, G. Y. Gor, and A. V. Neimark. *Colloids and Surfaces A: Physicochem. Eng. Aspects*, 437:3–32, 2013. p. 20

[158] D. C. Langreth, M. Dion, H. Rydberg, E. Schrder, P. Hyldgaard, and B. I. Lundqvist. Van der waals density functional theory with applications. *International Journal of Quantum Chemistry*, 101(5):599–610, 2005. p. 15, 44

[159] D. Larkin, K. L. Guyer, J. T. Hupp, and M. J. Weaver. Determination of specific adsorption of some simple anions at polycrystalline silver - aqueous interface using differential capacitance and kinetic probe techniques. *Journal of Electroanalytical Chemistry*, 138:401, 1982. p. xv, 143, 149, 150, 202, 203, 204, 209

[160] C. Lefrou and R. Cornut. Analytical expressions for quantitative scanning electrochemical microscopy (secm). *Chem Phys Chem*, 11:547–556, 2010. p. 215

[161] J. E. Lennard-Jones. On the determination of molecular fields. *Proc. R. Soc. Lond. A*, 106:463–477, 1924. p. 155, 172

[162] K. Letchworth-Weaver, R. Sundararaman, and T.A. Arias. Microscopically informed ab initio jdft framework: Free energies of solvation to chemical accuracy. *In Preparation*, 2015. p. 47, 243

[163] Kendra Letchworth-Weaver and T. A. Arias. Joint density functional the-

ory of the electrode-electrolyte interface: Application to fixed electrode potentials, interfacial capacitances, and potentials of zero charge. *Physical Review B*, 86:075140, 2012. p. 25, 78, 79, 136, 163, 222, 253

[164] K. Leung. First principles modeling of the initial stages of organic solvent decomposition on lixmn2o4 (100) surfaces. *J. Phys. Chem. C*, 116(18):9852–9861, 2012. p. 255

[165] Kevin Leung. Surface potential at the airwater interface computed using density functional theory. *The Journal of Physical Chemistry Letters*, 1(2):496–499, 2010. p. 164, 193

[166] M. Levy. Universal variational functionals of electron densities, first–order density matrices, and natural spin–orbitals and solution of the v–representability problem. 76(12):6062–6065, 1979. p. 11

[167] Song Li, Guang Feng, and Peter T Cummings. Interfaces of dicationic ionic liquids andgraphene: a molecular dynamics simulation study. *Journal of Physics: Condensed Matter*, 26(28):284106, 2014. p. 134, 135

[168] X. Li, Y. Cao, W. Qi, L. V. Saraf, J. Xiao, Z. Nie, J. Mietek, J-G. Zhang, B. Schwenzer, and J. Liu. *J. Mater. Chem.*, 21:16603, 2011. p. 21

[169] E. H. Lieb. Density functionals for coulomb systems. *International Journal of Quantum Chemistry*, 24(3):243–277, 1983. p. 11, 16

[170] Johannes Lischner and T. A. Arias. Kohn-sham-like approach toward a classical density-functional theory of inhomogeneous polar molecular liquids: An application to liquid hydrogen chloride. *Phys. Rev. Lett.*, 101:216401, 2008. p. 22, 24, 153

[171] Johannes Lischner and T. A. Arias. Classical density-functional theory of inhomogeneous water including explicit molecular structure and nonlinear dielectric response. *The Journal of Physical Chemistry B*, 114(5):1946–1953, 2010. p. 22, 24, 73, 86, 88, 89, 103, 124, 130, 153, 156, 157

[172] S. G. Louie, S. Froyen, and M. L. Cohen. *Phys. Rev. B*, 26(4):1738, 1982. p. 49, 240

[173] Alexander Y. Lozovoi and Ali Alavi. Reconstruction of charged surfaces: General trends and a case study of pt(110) and au(110). *Phys. Rev. B*, 68:245416, 2003.   p. 83, 84

[174] B. Z. Lu, Y. C. Zhou, M. J. Holst, and J. A. McCammon. Recent progress in numerical methods for the poisson-boltzmann equation in biophysical applications. *Commun. Comput. Phys.*, 3(5):9731009.   p. 135

[175] Serge Luryi. Quantum capacitance devices. *Appl. Phys. Lett.*, 52(6), 1988. p. 94

[176] Haibo Ma. Hydration structure of na+, k+, f-, and cl- in ambient and supercritical water: A quantum mechanics/molecular mechanics study. *International Journal of Quantum Chemistry*, 114:1006–1011, 2014.   p. 179

[177] Johan Mahler and Ingmar Persson. A study of the hydration of the alkali metal ions in aqueous solution. *Inorg. Chem.*, 51:425438, 2012.   p. 179

[178] Yizhak Marcus. Ionic radii in aqueous solutions. *Chem. Rev.*, 88:1475–1498, 1988.   p. 175, 183

[179] Yizhak Marcus. Effect of ions on the structure of water: Structure making and breaking. *Chem. Rev.*, 109:13461370, 2009.   p. 208

[180] A. V. Marenich, C. J. Cramer CJ, and D.G. Truhlar. Universal solvation model based on solute electron density and on a continuum model of the solvent defined by the bulk dielectric constant and atomic surface tensions. *J. Phys. Chem. B.*, 113:6378–96, 2009.   p. 34, 64, 65, 187, 250

[181] R.M. Martin. *Electronic Structure: Basic Theory and Practical Methods*. Cambridge University Press, 1 edition, 2004.   p. 8, 11, 13, 15

[182] Ann Mattson. Density functional theory: In pursuit of the "divine" functional. *Science*, 298:759–760, 2002.   p. 15

[183] J. G. Mavroides, J. A. Kafalas, and D. F. Kolesar. Photoelectrolysis of water in cells with srtio3 anodes. *Applied Physics Letters*, 28:241–243, 1976. p. 211

[184] K. J. May, C. E. Carlton, K. A. Stoerzinger, M. Risch, J. Suntivich, Y. L. Lee,

A. Grimaud, and Y. Shao-Horn. Influence of oxygen evolution during water oxidation on the surface of perovskite oxide catalysts. *J Phys Chem Lett*, 3:3264–3270, 2012. p. 246

[185] N. A. McDonald, H. A. Carlson, and W. L. Jorgensen. Free energies of solvation in chloroform and water from a linear response approach. *Journal of Physical Organic Chemistry*, 10:563–576, 1997. p. 65

[186] J. McEvoy, J. A. Gascon, V.S. Batista, and G.W. Brudvig. *Photochem. Photobiol. Sci.*, 4:940–949, 2005. p. 213

[187] N. D. Mermin. *Phys. Rev.*, 137:A1441, 1965. p. 15, 21

[188] A. Minguzzi, M. A. Alpuche-Aviles, J. R. Lopez, S. Rondinini, and A. J. Bard. Screening of oxygen evolution electrocatalysts by scanning electrochemical microscopy using a shielded tip approach. *Anal Chem*, 80:4055–4064, 2008. p. 216

[189] J. Mitroy, M. S. Safronova, and Charles W. Clark. Theory and applications of atomic and ionic polarizabilities. *Journal of Physics B: Atomic, Molecular and Optical Physics*, 43:202001, 2010. p. 183

[190] H. J. Monkhorst and J. D. Pack. *Phys. Rev. B*, 13:5188, 1976. p. 110, 240

[191] P.A. Monson. *Microporous and Mesoporous Materials*, 160:47–66, 2012. p. 20, 209

[192] J. A. Morrone and R. Car. *Phys. Rev. Lett.*, 101:017801, 2008. p. 32

[193] J. J. Mortensen, K. Kaasbjerg, S. L. Frederiksen, J. K. Norskov, J. P. Sethna, and K. W. Jacobsen. Bayesian error estimation in density-functional theory. *Phys. Rev. Lett.*, 95:216401, 2005. p. 236

[194] R R Netz. Theoretical approaches to charged surfaces. *Journal of Physics: Condensed Matter*, 16(26):S2353, 2004. p. 137

[195] I. Newton. *The Principia: Mathematical Principles of Natural Philosophy*. University of California Press, 1999. p. 3

[196] D. M. C. Nicholson, G. M. Stocks, Y. Wang, W. A. Shelton, Z. Szotek, and W. M. Temmerman. Stationary nature of the density-functional free energy: Application to accelerated multiple-scattering calculations. *Phys. Rev. B*, 50:14686–14689, 1994.   p. 16

[197] W. Norimatsu and M. Kusunoki. Epitaxial graphene on sic0001: advances and perspectives. *Phys. Chem. Chem. Phys.*, 16:3501–3511, 2014.   p. 254

[198] J. K. Norskov, T. Bligaard, J. Rossmeisl, and C. H. Christensen. Towards the computational design of solid catalysts. *Nat. Chem.*, 1(1):37–46, 2009. p. 83

[199] J. K. Norskov, J. Rossmeisl, A. Logadottir, L. Lindqvist, J. R. Kitchin, T. Bligaard, and H. Jonsson. Origin of the overpotential for oxygen reduction at a fuel-cell cathode. *The Journal of Physical Chemistry B*, 108(46):17886–17892, 2004.   p. 83

[200] A. Onufriev, D. Bashford, and D.A. Case. Effective born radii in the generalized born approximation: The importance of being perfect. *Journal of Computational Chemistry*, 23:12971304, 2002.   p. 134

[201] B. Oregan and M. Gratzel. A low-cost, high-efficiency solar-cell based on dye-sensitized colloidal tio2 films. *Nature*, 353:737–740, 1991.   p. 211

[202] L. S. Ornstein and F. Zernike. Accidental deviations of density and opalescence at the critical point of a single substance. *Proc. Acad. Sci. Amsterdam*, 17:793–806, 1914.   p. 71

[203] M. Otani and O. Sugino. First-principles calculations of charged surfaces and interfaces: A plane-wave nonrepeated slab approach. *Phys. Rev. B*, 73:115407, 2006.   p. 85, 113

[204] T. Pajkossy and D. M. Kolb. Anion-adsorption-related frequency-dependent double layer capacitance of the platinum-group metals in the double layer region. *Electrochimica Acta*, 53:7403–7409, 2008.   p. 151, 204, 209

[205] T. Pajkossy and D.M. Kolb. Double layer capacitance of pt(111) single crystal electrodes. *Electrochimica Acta*, 46(2021):3063 – 3071, 2001.   p. 117, 119

[206] R. Parsons and F. G. R. Zobel. The interphase between mercury and aqueous sodium dihydrogen phosphate. *J. Electroanal. Chem.*, 9:333, 1965.   p. 143, 148

[207] K. Paul. *Thales:The First Philosophers of Greece*. 1898.   p.1

[208] L. Pauling. The principles determining the structure of complex ionic crystals. *Journal of the American Chemical Society*, 51(4):1010–1026, 1929. p.5, 9

[209] M.C. Payne, M.P. Teter, D.C. Allan, T.A. Arias, and J.D. Joannopoulos. Iterative minimization techniques for ab initio total energy calculations: molecular dynamics and conjugate gradients. *Reviews of Modern Physics*, 64:1045–1097, 1992.   p.18, 32, 61, 240, 243

[210] Luana S. Pedroza, Adrien Poissier, and M.-V. Fernndez-Serra. Local order of liquid water at metallic electrode surfaces. *The Journal of Chemical Physics*, 142:034706, 2015.   p.136

[211] Jerome K. Percus and George J. Yevick. Analysis of classical statistical mechanics by means of collective coordinates. *Phys. Rev.*, 110, 1958. p.37

[212] J. P. Perdew, K. Burke, and M. Ernzerhof. *Phys. Rev. Lett.*, 77:3865, 1996. p. 14, 37, 43, 49, 65, 190, 240

[213] J. P. Perdew, R. G. Parr, M. Levy, and J. L. Balduz. Density-functional theory for fractional particle number: Derivative discontinuities of the energy. *Phys. Rev. Lett.*, 49:1691–1694, 1982.   p.16

[214] J. P. Perdew and Alex Zunger. Self-interaction correction to density-functional approximations for many-electron systems. *Phys. Rev. B*, 23:5048, 1981.   p.14, 43

[215] John P. Perdew, J. A. Chevary, S. H. Vosko, Koblar A. Jackson, Mark R. Pederson, D. J. Singh, and Carlos Fiolhais. Atoms, molecules, solids, and surfaces: Applications of the generalized gradient approximation for exchange and correlation. *Phys. Rev. B*, 46:6671–6687, 1992.   p.88, 110, 121

[216] J.P. Perdew, M. Ernzerhof, and K. Burke. Rationale for mixing exact exchange with density functional approximations. *The Journal of Chemical Physics*, 105:9982, 1996.   p.14

[217] S. Petrosyan, A.A. Rigos, and T.A. Arias. *J. Phys. Chem B.*, 109(32):15436–15444, 2005.   p. 34, 87, 97, 99, 129

[218] S. A. Petrosyan, J.-F. Briere, D. Roundy, and T .A. Arias. *Phys. Rev. B*, 75:205105, 2007.   p. 28, 35, 36, 38, 39, 47, 78, 87, 88, 89, 214, 222, 241

[219] Sahak A. Petrosyan, David Roundy, Jean-Francois Briere, and Tomas A. Arias. Classical density-functional theory for water. 2010.   p. 39

[220] M. Plaza, X.Huang, J.Y.P. Ko, Joel Brock, M. Shen, B. H. Simpson, J. Rodriguez-Lopez, N. L. Ritzert, H.D. Abruna, K. Letchworth Weaver, D. Gunceler, T.A. Arias, and D.G. Schlom. Enhanced photocatalytic activity induced by surface structural changes in strontium titanate electrodes: An operando study. *Nature Materials, Under Revision*, 2014.   p. 211, 214

[221] S. Plimpton. *J Comp Phys*, 117:1, 1995.   p. 26

[222] M Pounds, S Tazi, M Salanne, and P A Madden. Ion adsorption at a metallic electrode: an ab initio based simulation study. *Journal of Physics: Condensed Matter*, 21(42):424109, 2009.   p. 83

[223] E. Prodan. Viewpoint: Raising the temperature on density–functional theory. *Physics*, 3:99, 2010.   p. 11, 16

[224] A. Puzder, A. J. Williamson, F. A. Reboredo, and G. Galli. Structural stability and optical properties of nanomaterials with reconstructed surfaces. *Physical Review Letters*, 91:157405, 2003.   p. 213

[225] MR Radeke and EA Carter. Ab initio dynamics of surface chemistry. *Annual Review of Physical Chemistry*, 48:243–270, 1997.   p. 82

[226] M. Raju, S. Y. Kim, A. C. T. van Duin, and K. A. Fichthorn. Reaxff reactive force field study of the dissociation of water on titania surfaces. *Journal of Physical Chemistry C*, 117:10558–10572, 2013.   p. 213

[227] Lavanya M. Ramaniah, Marco Bernasconi, and Michele Parrinello. Density-functional study of hydration of sodium in water clusters. *The Journal of Chemical Physics*, 109:6839, 1998.   p. 173

[228] N. J. Ramer and A. M. Rappe. *Phys. Rev. B*, 59:12471, 1999.   p. 19, 49, 110, 240, 243

[229] M. K. Rana and A. Chandra. *J. Chem. Phys.*, 138:204702, 2013. p. xiii, 76, 77

[230] A. M. Rappe, K. M. Rabe, E. Kaxiras, and J. D. Joannopoulos. *Phys. Rev. B*, 41:1227, 1990.   p. 19, 49, 62, 110, 240, 243

[231] R. C. Rizzo, T. Aynechi, D. A. Case, and I. D. Kuntz. *J. Chem. Theory Comput.*, 2:128, 2006.   p. 34, 64

[232] I. K. Robinson. Crystal truncation rods and surface roughness. *Physical Review B: Condensed Matter*, 33:3830–3836, 1986.   p. 218, 219

[233] Guillermo Román-Pérez and José M. Soler. Efficient implementation of a van der waals density functional: Application to double-wall carbon nanotubes. *Phys. Rev. Lett.*, 103:096102, 2009.   p. 37, 44, 250

[234] Y. Rosenfeld. *Phys. Rev. Lett.*, 63:980, 1989.   p. 24, 154

[235] J. Rossmeisl, Z. W. Qu, H. Zhu, G. J. Kroes, and J. K. Norskov. Electrolysis of water on oxide surfaces. *Journal of Electroanalytical Chemistry*, 607:83–89, 2007.   p. 213

[236] Jan Rossmeisl, Egill Skulason, Marten E. Bjorketun, Vladimir Tripkovic, and Jens K. Norskov. Modeling the electrified solidliquid interface. *Chemical Physics Letters*, 466(13):68 − 71, 2008.   p. 111, 118

[237] R. Roth. *J. Phys. Cond. Matt.*, 22:063102, 2010.   p. 24, 61

[238] Benoit. Roux, Hsiang Ai. Yu, and Martin. Karplus. Molecular basis for the born model of ion solvation. *The Journal of Physical Chemistry*, 94(11):4683–4688, 1990.   p. 134

[239] Christopher N. Rowley and Benoit Roux. The solvation structure of na+ and k+ in liquid water determined from high level ab initio molecular dynamics simulations. *J. Chem. Theory Comput.*, 8:35263535, 2012.   p. 179

[240] Andrea E. Russell, Andrew S. Lin, and William E. O'Grady. In situ far-infrared evidence for a potential dependence of silver-water interactions. *J. Chem. Soc: Faraday Trans.*, 89:195–198, 1993.   p. 149, 196, 204

[241] Alberto De Santis and Dario Rocca. Radial distribution functions of molecular systems at low density. *Chemical Physics*, 208, 1996.   p. 179

[242] H. Sato. *Phys. Chem. Chem. Phys.*, 15:7450–7465, 2013.   p. 33, 79

[243] D. A. Scherlis, J.-L. Fattebert, F. Gygi, M. Coccocioni, and N. Marzari. *J. Chem. Phys*, 124:074103, 2006.   p. 34

[244] Sebastian Schnur and Axel Gross. Properties of metalwater interfaces studied from first principles. *New Journal of Physics*, 11(12):125003, 2009. p. 83, 111, 136

[245] E. Schrdinger. An undulatory theory of the mechanics of atoms and molecules. *Physical Review*, 28:1049–1070, 1926.   p. 4, 7

[246] K. A. Schwarz, R. Sundararaman, K. Letchworth-Weaver, T. A. Arias, and R. G. Hennig. *Phys. Rev. B., Rapid Comm.*, 85:201102, 2012.   p. 37, 250

[247] M.P. Sears and L.J.D. Frink. *J. Comp. Phys.*, 190(1):184–200, 2003.   p. 20

[248] H. Seo, A. B. Posadas, C. Mitra, A. V. Kvit, J. Ramdani, and A. A. Demkov. Band alignment and electronic structure of the anatase tio2/srtio3(001) heterostructure integrated on si(001). *Phys. Rev. B*, 86:075301, 2012. p. 227

[249] C. David Sherrill and Henry F. Schaefer III. The configuration interaction method: Advances in highly correlated approaches. 34:143 – 269, 1999. p. 9

[250] Zheng Shi, Jiujun Zhang, Zhong-Sheng Liu, Haijiang Wang, and David P. Wilkinson. Current status of ab initio quantum chemistry study for oxygen electroreduction on fuel cell catalysts. *Electrochimica Acta*, 51(10):1905 – 1916, 2006.   p. 82

[251] et al. Shinoda, T. Crystal structure of the sodium-potassium pump at 2.4 resolution. *Nature*, 459:446–451, 2009.   p. 133

[252] Simplicius. *Simplicius: On Aristotle, Physics 1.5-9*. Bristol Classical Press, 2012.   p. 1

[253] James L. Skinner. Following the motions of water molecules in aqueous solutions. *Science*, 328:985, 2010.   p. 132

[254] Egill Skulason, Gustav S. Karlberg, Jan Rossmeisl, Thomas Bligaard, Jeff Greeley, Hannes Jonsson, and Jens K. Norskov. Density functional theory calculations for the hydrogen evolution reaction in an electrochemical double layer on the pt(111) electrode. *Phys. Chem. Chem. Phys.*, 9:3241–3250, 2007.   p. 84

[255] Egill Skulason, Vladimir Tripkovic, Marten E. Bjorketun, Sigridur Gudmundsdottir, Gustav Karlberg, Jan Rossmeisl, Thomas Bligaard, Hannes Jonsson, and Jens K. Norskov. Modeling the electrochemical hydrogen oxidation and evolution reactions on the basis of density functional theory calculations. *The Journal of Physical Chemistry C*, 114(42):18182–18197, 2010.   p. 84

[256] J. C. Slater and G. F. Koster. Simplified lcao method for the periodic potential problem. *Phys. Rev.*, 94:1498–1524, 1954.   p. 10

[257] D.J. Sokhan, V.P.; Tildesley. The free surface of water: Molecular orientation, surface potential, and nonlinear susceptibility. *Mol. Phys.*, 92:625, 1997.   p. 193

[258] A. K. Soper. *Chem. Phys.*, 258:121, 2000.   p. xiii, 74

[259] M. Sparks and G. K. Teal. Method of making p–n junctions in semiconductor materials. U.S. Patent 2,631,356. filed 1950, granted 1953.   p. 5

[260] P.J. Stephens, F.J. Devlin, C.F. Chabalowski, and M.J. Frisch. *J. Phys. Chem.*, 98:11623–11627, 1994.   p. 14

[261] O. Stern. *Z. Elektrochem.*, 30:508, 1924.   p. 94, 140

[262] R. Sundararaman and T.A. Arias. Efficient classical density-functional theories of rigid-molecular fluids and a simplified free energy functional for liquid water. *Computer Physics Communications*, 185:818–825, 2014.   p. 20, 23, 24, 38, 45, 60, 62, 65, 78, 153, 154, 155, 156, 158, 227, 241

[263] R. Sundararaman, D. Gunceler, and T. A. Arias. Weighted-density func-

tionals for cavity formation and dispersion energies in continuum solvation models. *The Journal of Chemical Physics*, 141:134105, 2014.   p. 44

[264] R. Sundararaman and W.A. Goddard III. The charge-asymmetric nonlocally determined local-electric (candle) solvation model. *Journal of Chemical Physics*, 142:064107, 2015.   p. 65

[265] R. Sundararaman, K. Letchworth-Weaver, and T. A. Arias. *J. Chem. Phys.*, 137:044107, 2012.   p. 22, 236

[266] R. Sundararaman, K. Letchworth-Weaver, and T.A. Arias. A recipe for free energy functionals of polarizable molecular fluids. *Journal of Chemical Physics*, 140:144504, 2014.   p. xiii, 23, 24, 25, 35, 38, 45, 48, 65, 73, 75, 78, 154, 156, 158, 227, 241, 243, 249

[267] R. Sundararaman, K. Letchworth-Weaver, Deniz Gunceler, K.A. Schwarz, Yalcin Ozhabes, and T. A. Arias. JDFTx. `http://jdftx.` `sourceforge.net`, 2015.   p. 19, 49, 62, 74, 110, 239

[268] R. Sundararaman, K. A. Schwarz, K. Letchworth-Weaver, and T. A. Arias. Spicing up continuum solvation models with salsa: The spherically averaged liquid susceptibility ansatz. *The Journal of Chemical Physics*, 142:054102, 2015.   p. 39, 44, 68, 78

[269] J. Suntivich, K. J. May, H. A. Gasteiger, J. B. Goodenough, and Y. Shao-Horn. A perovskite oxide optimized for oxygen evolution catalysis from molecular orbital principles. *Science*, 334:1383–1385, 2011.   p. 246

[270] C. Suplee. *Milestones of Science*. National Geographic Society, 2000. p. 1, 2, 3, 5

[271] J. Tao, J.P. Perdew, V. N. Staroverov, and G. E. Scuseria. Climbing the density functional ladder: Nonempirical generalized gradient approximation designed for molecules and solids. *Phys. Rev. Lett.*, 91:146401, 2003. p. 14

[272] P. Tarazona. *Phys. Rev. Lett.*, 84:694, 2000.   p. 24, 154

[273] Yoshitaka Tateyama, Jochen Blumberger, Michiel Sprik, and Ivano Tavernelli. Density-functional molecular-dynamics study of the redox reactions

of two anionic, aqueous transition-metal complexes. *The Journal of Chemical Physics*, 122(23):234505, 2005. p. 82

[274] I. Tavernelli, R. Vuilleumier, and M. Sprik. *Ab Initio* molecular dynamics for molecules with variable numbers of electrons. *Phys. Rev. Lett.*, 88:213002, 2002. p. 16

[275] Christopher D. Taylor, Sally A. Wasileski, Jean-Sebastien Filhol, and Matthew Neurock. First principles reaction modeling of the electrochemical interface: Consideration and calculation of a tunable surface potential from atomic and electronic structure. *Phys. Rev. B*, 73:165402, 2006. p. 84

[276] M. M. Thackeray. Manganese oxides for lithium batteries. *Progress in Solid State Chemistry*, 25:1–71, 1997. p. 255

[277] L. H. Thomas. The calculation of atomic fields. *Mathematical Proceedings of the Cambridge Philosophical Society*, 23:542–548, 1927. p. 13, 42, 243

[278] J.J. Thomson. Cathode rays. *The Electrician*, 39:104, 1897. p. 4

[279] A. Tkatchenko and M. Scheffler. Accurate molecular van der waals interactions from ground-state electron density and free-atom reference data. *Phys. Rev. Lett.*, 102:73005. p. 15, 44

[280] J. Tomasi, B. Mennucci, and R. Cammi. *Chem. Rev.*, 105:2999, 2005. p. 34, 64

[281] J. Tomasi and M. Persico. *Chem. Rev.*, 94:2027, 1994. p. 34

[282] S. Trasatti. *Modern Aspects of Electrochemistry*, (33), 1999. p. xiv, 121, 122, 126, 127, 130, 190, 193

[283] Vladimir Tripkovic, Marten E. Bjorketun, Egill Skulason, and Jan Rossmeisl. Standard hydrogen electrode and potential of zero charge in density functional calculations. *Phys. Rev. B*, 84:115452, 2011. p. 84, 114, 123, 222

[284] R. I. Tucceri and D. Posadas. A surface conductance study of the anion adsorption on gold. *J. Electroanal. Chem.*, 191:387–399, 1985. p. 209

[285] R.I. Tucceri and D. Posadas. The effect of surface charge on the surface conductance of silver in surface inactive electrolytes. *J. Electroanal. Chem.*, 283:159–166, 1990.   p. 209

[286] Georges Valette and Antoinette Hamelin. *Electroanalytical Chemistry and Interfacial Electrochemistry*, 45:301–319, 1973. p. xv, 148, 199, 201, 202, 203, 204, 205

[287] K. van Benthem, C. Elsässer, and R. H. French. Bulk electronic structure of srtio3: Experiment and theory. *J. Appl. Phys.*, 90:6156, 2001. p. 213, 240

[288] J.D. van der Waals. The equation of state for gases and liquids. *Nobel Lectures in Physics*, pages 254–265, 1910.   p. 3

[289] David Vanderbilt. Soft self-consistent pseudopotentials in a generalized eigenvalue formalism. *Phys. Rev. B, Rapid Comm.*, 41:7892, 1990. p. 19, 62, 65, 76

[290] Peter Vassilev, Rutger A. van Santen, and Marc T. M. Koper. Ab initio studies of a water layer at transition metal surfaces. *The Journal of Chemical Physics*, 122:054701, 2005.   p. 136

[291] A. Vittadini, M. Casarin, and A. Selloni. Chemistry of and on tio2-anatase surfaces by dft calculations: a partial review. *Theoretical Chemistry Accounts*, 117:663–671, 2007.   p. 213

[292] A. Vojvodic and J. K. Norskov. Optimizing perovskites for the water-splitting reaction. *Science*, 334:1355–1356, 2011.   p. 213

[293] O.A. von Lilienfeld and M. E. Tuckerman. Molecular grand–canonical ensemble density functional theory and exploration of chemical space. *The Journal of Chemical Physics*, 125(15):154104, 2006.   p. 18

[294] V. Vonk, S. Konings, G. J. van Hummel, S. Harkema, and H. Graafsma. The atomic surface structure of srtio3(001) in air studied with synchrotron x-rays. *Surf Sci*, 595:183–193, 2005.   p. 228

[295] F. T. Wagner, S. Ferrer, and G. A. Somorjai. Surface aspects of hydrogen photogeneration on titanium oxides. *Nature*, 146:159–178, 1981.   p. 245

[296] A. Warshel and M. Levitt. *Journal of Molecular Biology*, 103:227–249, 1976. p. 32

[297] Michael J. Weaver. Potentials of zero charge for platinum(111)aqueous interfaces: a combined assessment from in-situ and ultrahigh-vacuum measurements. *Langmuir*, 14(14):3932–3936, 1998. p. 127, 128

[298] C. F. v. Weizscker. Zur theorie der kernmassen. *Zeitschrift fr Physik*, 96:431–458, 1935. p. 43

[299] M. S. Wertheim. *J. Chem. Phys.*, 87:7323, 1987. p. 22

[300] T. Wesolowski and A. Warshel. Ab initio free energy perturbation calculations of solvation free energy using the frozen density functional approach. *The Journal of Physical Chemistry*, 98(20):5183–5187, 1994. p. 33

[301] T. A. Wesolowski and J. Weber. *Chem. Phys. Lett.*, 248:71–76, 1996. p. 61

[302] Tomasz Adam Wesolowski and Arieh Warshel. Frozen density functional approach for ab initio calculations of solvated molecules. *The Journal of Physical Chemistry*, 97(30):8050–8053, 1993. p. 33, 41, 78

[303] E. Wigner. On the interaction of electrons in metals. *Phys. Rev.*, 46:10021011, 1934. p. 14

[304] Adam P. Willard, Stewart K. Reed, Paul A. Madden, and David Chandler. Water at an electrochemical interface-a simulation study. *Faraday Discuss.*, 141:423–441, 2009. p. 83, 111

[305] Brandon C. Wood, Tadashi Ogitsu, Minoru Otani, and Juergen Biener. First-principles-inspired design strategies for graphene-based supercapacitor electrodes. *J. Phys. Chem. C*, 118:4–15, 2014. p. 134, 137

[306] J. R. Woodyard. Nonlinear circuit device utilizing germanium. US Patent No. 2,530,110. filed 1944, granted 1950. p. 5

[307] M. S. Wrighton. Photoelectrochemical conversion of optical-energy to electricity and fuels. *Accounts Chem Res*, 12:303–310, 1979. p. 211

[308] M. S. Wrighton, A. B. Ellis, P. T. Wolczanski, D. L. Morse, H. B. Abrahamson, and D. S. Ginley. Strontium-titanate photoelectrodes - efficient photoassisted electrolysis of water at zero applied potential. *J Am Chem Soc*, 98:2774–2779, 1976.   p.211

[309] J. Wu. *Amer. Instit. Chem. Eng. J*, 52:1169–1193, 2006.   p.20

[310] J. Wu, T. Jiang, D. Jiang, Z. Jin, and D. Henderson. *Soft Matter*, 7:11222, 2011.   p.20

[311] Jun Wu and Franois Gygi. A simplified implementation of van der waals density functionals for first-principles molecular dynamics applications. *The Journal of Chemical Physics*, 136(22):224107, 2012.   p.37

[312] X. Yang and M. B. Hall. *J. Am. Chem. Soc.*, 132:120–130, 2010.   p.213

[313] W. Yoon, K. Chung, K. H. Oh, and K. Kim. Changes in electronic structure of the electrochemically li-ion deintercalated limn2o4 system investigated by soft x-ray absorption spectroscopy. *Journal of Power Sources*, 119-121:706–709, 2003.   p.255

[314] T. Young. Bakerian lecture: Experiments and calculations relative to physical optics. *Philosophical Transactions of the Royal Society*, 94:1–16, 1804.   p. 4

[315] Y.-X. Yu and J. Wu. *J. Chem. Phys.*, 117:2368, 2002.   p.22

[316] Andrew Zangwill. The education of walter kohn and the creation of density functional theory. arXiv:1403.5164v1, 2014.   p. 10

[317] Cui Zhang, Tuan Anh Pham, Franois Gygi, and Giulia Galli. Electronic structure of the solvated chloride anion from first principles molecular dynamics. *The Journal of Chemical Physics*, 138:181102, 2013.   p.179

[318] Z. Zhang, P. Fenter, N. C. Sturchio, M. J. Bedzyk, M. L. Machesky, and D. J. Wesolowski. Structure of rutile tio2 (110) in water and 1 molal rb+ at ph 12: Inter-relationship among surface charge, interfacial hydration structure, and substrate structural displacements. *Surface Science*, 601:1129–1143, 2007.   p.213, 225

[319] S. Zhao, Z. Jin, and J. Wu. *J. Phys. Chem. B*, 115:6971, 2011.